Quantitative MRI and EMG study of the Brachial Plexus

Zaid Bin Mahbub

Thesis submitted to the University of Nottingham

for the Degree of Doctor of Philosophy

June 2014

Dedication

TO

MY BELOVED MOTHER AND FATHER

ACKNOWLEDGEMENT

Abstract

Abstract

This thesis describes the development and applications of quantitative MRI and combined EMG and MRI study of Brachial Plexus. The protocols developed in this thesis have been used on normal healthy subjects, aiming at characterizing the tissues based on their MR and EMG parameters.

The Brachial Plexus is the upper portion of the peripheral nervous system and controls the movements of shoulder and arms. Neurological disorders in the brachial plexus can result from cervical spondylotic neuropathy due to compression of nerve roots exiting from vertebra or compression of the spinal cord due to bulging discs. MRI provides the opportunity to obtain precise information on the location of these disorders and to provide quantitative biomarkers. EMG in the form of the distribution of F-latency (DFL) is a recently introduced nerve conduction parameter that can detect functional symptoms with such disorders.

To study the brachial plexus the diffusion weighted MRI with body signal suppression (DWIBS) technique was used to highlight the nerves from surrounding tissues. This technique was then used to investigate the diffusivity of water molecules in the peripheral nerve axon. The diffusion time dependency of the diffusion coefficient was used to study the presence of restricted diffusion in the brachial plexus. A clear reduction of the apparent diffusion coefficient was observed with long diffusion times and confirmed the restricted diffusion in nerves and cord. The T_2 relaxation was used to investigate the properties of intercellular and intracellular space in peripheral nerves. Diffusion weighting dependency of T_2 and echo time dependency of apparent diffusion coefficient (ADC) was observed in initial studies. The magnetisation transfer (MT) and z-spectra were used to study macromolecular characteristics and exchange mechanisms. Asymmetry in z-spectra both for nerves and spinal cord was observed, this relates to possible detection of the nuclear overhauser effect (NOE) in the brachial plexus. Quantitative MRI studies showed that these parameters can be used as important biomarkers for neurological studies in the brachial plexus. The DFL, representing the motor nerve fibres conduction characteristics, was measured for normal healthy nerves and combined with MR parameters. Correlation between DFL and MR parameters was observed for the first time.

Introduction

Accurate investigation and diagnosis is invaluable in the management of many diseases. Therefore different techniques that can probe into the human body and can detect various body functions are continuously being developed around the world.

The brachial plexus, the upper portion of the peripheral nervous system, is commonly involved in degenerative conditions of the cervical spine such as cervical spondylosis, radiculopathy and myelopathy, and distinguishing these disorders is necessary to ensure proper treatment (Nurjck 1972, Shedid *et al.* 2007). Diagnosis of these disorders can be made accurately and easily using Computed Tomography (CT) or Magnetic Resonance Imaging (MRI). CT scans can show enlargement of the facet joints, which could indicate spondylosis (Iwasaki *et al.* 1985). But MRI is especially good at showing when there is abnormality in a disc, ligament, or nerve root (Hackney 1994). Electromyogram (EMG) studies show abnormalities in response shapes and help to differentiate such disorders (Preston 2012). This thesis will discuss development of combined MRI and EMG techniques for locating such disorders.

MRI is a versatile technique, Qualitative MRI can produce high resolution images of the biological tissues (Modic *et al.* 1986), while Quantitative MRI provides potential biomarkers that are able to study microstructure and are sensitive to microscopic changes in tissues. MRI has the advantage of providing absolute and normative values that can be used for diagnosis, prognosis, multiple site studies, and clinical trials (Stroman *et al.* 2014). This thesis focused on diffusion weighted MRI, T2 relaxation, and magnetization transfer MRI measurements for quantitative MRI study of the brachial plexus.

Diffusion Weighted MRI (DW-MRI) came into existence in the mid-1980s. During the last two decades important methodological and conceptual developments of diffusion MRI have been made and successfully used for different studies of neurological disorder. DW-MRI is appealing as an imaging technique for several reasons. Firstly, the imaging can be performed relatively quickly and thus has the potential to be widely generalized and adopted. Secondly, the technique does not

require the administration of exogenous contrast agents, which is attractive in the light of potential serious adverse effects of gadolinium-based contrast media. Thirdly, the technique yields both qualitative and quantitative information, the latter being of particular importance as development of quantitative imaging techniques is now acknowledged to be critical to the future of radiology. DW-MRI yields unique information that reflects microstructural and functional alterations in tissues. DW-MR is becoming an essential tool in the management of stroke patients and other clinical disorders. In 2004, a new technique to acquire DW-MRI of the whole body, called DWIBS (diffusion-weighted whole-body imaging with background body signal suppression) (Takahara *et al.* 2004) was first described. Applying the principles of DWIBS allows us to acquire thin-section datasets, which make it possible to produce three-dimensional images of peripheral nerves in virtually any part of the body. This thesis demonstrated the potential applications of DWIBS for brachial plexus imaging for highlighting the peripheral nerves and spinal cord.

Restricted motion of molecules in complex structures is important in many areas of science, engineering, and medicine. Examples can be taken from biology (intracellular and extracellular water molecule motions, perfusion, membrane function), catalysis, foodstuff, materials (concrete, cement, polymer networks, self-organizing materials), and geology (fluid movement in hydrocarbon reservoirs, ground water migration, contamination). Where the local geometry leaves a fingerprint, so to say, on the diffusion coefficient; changing it from the bulk D time independent value to a time-dependent $D(t)$. Measurements of time dependence of diffusion coefficients thus give us an opportunity to obtain detailed information about the nature of the dynamics of the molecules through selective pathways, the nature of the membrane or restriction boundaries and its permeability. From the perspective of biological tissues, the degree of restriction to diffusion is inversely correlated to the tissue cellularity and integrity of cell membranes. The motion of water molecules is more restricted in tissues with a high cellular density. By contrast, motion is less restricted in areas of low cellularity. Thus experimentally observing the time dependency of diffusion coefficients reveals unique information of tissues. This thesis describes the restricted diffusion of the brachial plexus to extract information about the confining geometry of the axons.

T_2 weighted images here played a key role in clinical applications from early days of MRI showing sensitive changes with the pathological conditions. T_2 relaxation measures and quantifies the intercellular and intracellular content of nerves. There is an opportunity to extract quantitative information about the spinal cord and brachial plexus nerves (Cohen-Adad *et al.* 2014). This thesis provides an overview of T_2 relaxation measurements.

Magnetization transfer (MT) was first used in MR imaging by Wolff and Balaban (Balaban *et al.* 1992); it generates contrast dependence upon the phenomenon of magnetization exchange between semi-solid macromolecular protons and water protons. This technique has the ability to image indirectly semi-solids, such as protein matrices and cell membranes, whose signals decay too rapidly to be imaged directly (Henkelman *et al.* 1993). Since its introduction, in vitro and in vivo results suggest that MT quantification allows characterization of the pathologically heterogeneous lesions of multiple sclerosis (MS) by providing a measure of demyelination (Henkelman *et al.* 2001, Schmierer *et al.* 2004). The z-spectra created by different offset frequencies of MT can detect and quantify the macromolecules and other solutes in the tissues and mechanisms of different exchange processes. The nuclear overhauser effect (NOE) has recently been observed in the brain (Mougin *et al.* 2010, Liu *et al.* 2013, Mougin *et al.* 2013) which principally provides information about MT between aliphatic protons situated in proteins, peptides and lipids and the water pool. This thesis records detectable NOE in the brachial plexus for the first time.
All these Quantitative MR measurements provide significant opportunities in clinical studies, but despite this are expensive, and are not available widely internationally.

Electro-neurophysiology studies started in the early 20th century for diseases in the peripheral nervous system. With steady improvement and standardization of electrodiagnosis methods, electromyogram (EMG) and nerve conduction studies (NCS) became reliable tests in clinical settings and vast knowledge has been accumulated from these methods concerning neurological disorders. EMG using needle electrode and NCS using the surface electrodes over skeletal muscles, both techniques are based on evoked responses, and are used for the studies of various peripheral neuropathies and have the attraction that they are potentially low cost, and thus can be made available widely (Preston *et al.* 2012). Recently, a group in Dhaka

University, Bangladesh conceived and developed a new nerve conduction technique in the form of Distribution of F-Latency (DFL), measured from peripheral nerves, found a distinctive pattern of DFL for cases of neuropathy in cervical spondylosis (Rabbani *et al.* 2007, Alam *et al.* 2010). Through agreement with X-ray and MRI investigations, it was shown that the DFL can be used as a screening test for brachial plexus and lumbar plexus neuropathies such as carpal tunnel syndrome, spondylotic disorders and differentiation between these disorders. Hypotheses have been proposed to explain the distinctive DFL patterns such as more than one peak and/or changes in widths with such neurological disorders based on neurophysiology. Therefore it seems this technique has potential in the diagnosis of cervical spondylotic neuropathy and also for lumbo-sacral region. An early diagnosis at an affordable cost will help the management and recovery of patients in less time with reduced cost. As such the DFL technique for the diagnosis of neurological disorders will be beneficial for a wide section of population Globally and particularly in my home country, Bangladesh, where it could be of direct relevance to national development, as it could provide an easily accessible health care service. This thesis intended to combine the DFL and MRI as two complimentary techniques for brachial plexus and study their correlation.

Scope of the Thesis:

This thesis was planned to develop quantitative MRI for brachial plexus and to evaluate the findings from the new study of DFL, in order to produce a new investigation technique in the peripheral nervous system.

Chapter 1 describes an overview of NMR and MRI physical basis and applications and discusses the pulse sequences used in this thesis.

Chapter 2 describes a brief description of human nervous system, and discusses overview of anatomical and physiological description of brachial plexus and neuropathies in brachial plexus.

Chapter 3 presents background information of the research work used in this thesis. It sequentially describes the anatomical MRI of brachial plexus; the basics and applications of diffusion MRI, diffusion MRI for body imaging and DWIBS sequence, restricted diffusion MRI and different models to explain the biological microstructures; the T2 relaxation time measurements; the magnetization transfer

imaging and z-spectrum study in MRI and finally basics of EMG studies for brachial plexus.

Chapter 4 describes the diffusion weighted MRI application for brachial plexus in two sections, the first section describes development of the diffusion weighted imaging with body signal suppression (DWIBS) application for brachial plexus, and the second section describes the optimization of DWIBS for restricted diffusion study in brachial plexus and diffusion time dependency of apparent diffusion coefficient (ADC) study.

Chapter 5 describes the T2 relaxation measurements for brachial plexus using the diffusion sensitized pulse sequences and the role of diffusion weighting with T2 measurements.

Chapter 6 describes the magnetization transfer and z-spectrum study for brachial plexus using the diffusion sensitized pulse sequences. Also the study of possible asymmetry in z-spectra and detectable NOE in brachial plexus nerves and cord are presented.

Chapter 7 describes combining the DFL and MRI studies in brachial plexus, observing the effects of head movement in DFL, anatomical MRI and quantitative MRI measurements.

Conclusion provides a general summary and key feature of chapters 4, 5, 6 and 7; it also presents possible future directions for clinical applications.

References:

Alam, M. and K. Rabbani (2010). "Possible detection of cervical spondylotic neuropathy using Distribution of F-latency (DFL), a new neurophysiological parameter." BMC Research Notes **3**(1): 112.

Balaban, R. S. and T. L. Ceckler (1992). "Magnetization transfer contrast in magnetic resonance imaging." Magnetic resonance quarterly **8**(2): 116-137.

Cohen-Adad, J. and C. Wheeler-Kingshott (2014). Quantitative MRI of the Spinal Cord, Academic Press.

Hackney, D. B. (1994). "Magnetic resonance imaging of the spine. Edited by Michael T. Modic, MD, Thomas J. Masaryk, MD, and Jeffrey S. Ross, MD St Louis, Mo: Mosby, 1994. $135.00; pp 442; hundreds of illustrations, 38 in color." Journal of Magnetic Resonance Imaging **4**(3): 250-250.

Henkelman, R. M., X. Huang, Q.-S. Xiang, G. J. Stanisz, S. D. Swanson and M. J. Bronskill (1993). "Quantitative interpretation of magnetization transfer." Magnetic Resonance in Medicine **29**(6): 759-766.

Henkelman, R. M., G. J. Stanisz and S. J. Graham (2001). "Magnetization transfer in MRI: a review." NMR in Biomedicine **14**(2): 57-64.

Iwasaki, Y., H. Abe, T. Isu and K. Miyasaka (1985). "CT myelography with intramedullary enhancement in cervical spondylosis." Journal of neurosurgery **63**(3): 363-366.

Liu, D., J. Zhou, R. Xue, Z. Zuo, J. An and D. J. Wang (2013). "Quantitative characterization of nuclear Overhauser enhancement and amide proton transfer effects in the human brain at 7 tesla." Magnetic Resonance in Medicine **70**(4): 1070-1081.

Modic, M. T., T. Masaryk and D. Paushter (1986). "Magnetic resonance imaging of the spine." Radiologic Clinics of North America **24**(2): 229-245.

Mougin, O., M. Clemence, A. Peters, A. Pitiot and P. Gowland (2013). "High-resolution imaging of magnetisation transfer and nuclear Overhauser effect in the human visual cortex at 7 T." NMR in Biomedicine **26**(11): 1508-1517.

Mougin, O. E., R. C. Coxon, A. Pitiot and P. A. Gowland (2010). "Magnetization transfer phenomenon in the human brain at 7 T." Neuroimage **49**(1): 272-281.

Nurjck, S. (1972). "The pathogenesis of the spinal cord disorder associated with cervical spondylosis." Brain **95**(1): 87-100.

Preston, D. C. and B. E. Shapiro (2012). Electromyography and Neuromuscular Disorders: Clinical-Electrophysiologic Correlations (Expert Consult-Online), Elsevier Health Sciences.

Rabbani, K., M. Alam and M. Salam (2007). "Frequency Distribution of F-Latencies (DFL) has physiological significance and gives Distribution of Conduction Velocity (DCV) of motor nerve fibres with implications for diagnosis." J of Biol Phys **33**: 291 - 303.

Schmierer, K., F. Scaravilli, D. R. Altmann, G. J. Barker and D. H. Miller (2004). "Magnetization transfer ratio and myelin in postmortem multiple sclerosis brain." Annals of Neurology **56**(3): 407-415.

Shedid, D. and E. C. Benzel (2007). "CERVICAL SPONDYLOSIS ANATOMY: PATHOPHYSIOLOGY AND BIOMECHANICS." Neurosurgery **60**(1): S1-7-S1-13 10.1227/1201.NEU.0000215430.0000286569.C0000215434.

Stroman, P. W., C. Wheeler-Kingshott, M. Bacon, J. M. Schwab, R. Bosma, J. Brooks, D. Cadotte, T. Carlstedt, O. Ciccarelli, J. Cohen-Adad, A. Curt, N. Evangelou, M. G. Fehlings, M. Filippi, B. J. Kelley, S. Kollias, A. Mackay, C.

A. Porro, S. Smith, S. M. Strittmatter, P. Summers and I. Tracey (2014). "The current state-of-the-art of spinal cord imaging: Methods." <u>NeuroImage</u> **84**(0): 1070-1081.

Takahara, T., Y. Imai, T. Yamashita, S. Yasuda, S. Nasu and M. Van Cauteren (2004). "Diffusion weighted whole body imaging with background body signal suppression (DWIBS): technical improvement using free breathing, STIR and high resolution 3D display." <u>Radiation medicine</u> **22**(4): 275-282.

Chapter 1
Basics of NMR and MRI

This chapter presents the basic NMR and MRI principles necessary to form the framework of this thesis. This chapter is divided into two sections: the first section describes the origins of nuclear magnetisation and the behaviour of a system under the applied magnetic field and the second section describes the overview of MRI, all these discussions are based on the references (Brown *et al.* , Haacke *et al.* , Hashemi *et al.* , Morris 1986, Callaghan 1993, Haacke *et al.* 1999, Bernstein *et al.* 2004, McRobbie 2007).

1.1 Nuclear Magnetic Resonance (NMR): signal observation

1.1.1 The physical basis of NMR

Nuclear magnetic resonance (NMR) is a chemical analytical technique that has been used for over 50 years. The NMR phenomena were independently discovered by Bloch and Purcell in 1946 by measuring the spin angular momentum of the nucleus and explaining its interaction with an external magnetic field. It is the basis of magnetic resonance imaging (MRI).

NMR relies on magnetic properties of nucleons, protons and/or neutrons that make up the *atomic nuclei*. All the elementary particles are characterized by a variety of properties such as mass, charge, angular momentum, spin and magnetic moment. The spin angular momentum **J** of any such particle is a vector quantity and is quantized. It is expressed as, $|\boldsymbol{J}| = \hbar\sqrt{I(I+1)}$, where $\hbar$ is the Planck's constant divided by 2π and I is the spin quantum number and it can take integral and half integral values. It is a characteristic property of the atomic nuclei. Some examples are;

^{1}H, I=1/2; ^{2}H, I =1; ^{13}C, I =1/2; ^{15}N, I =1/2

The *magnetic moment,* represented as a vector in units [A.m^{2}], describes the magnetic characteristics of the nucleus. If the total number of both protons (P) and neutrons (N) is even, the magnetic moment is essentially zero. However, if P is odd and N is even, or N is odd and P is even or N and P are odd, then net non-integer nuclear spin creates a magnetic moment.

In fact the magnetic moment and spin angular momentum are proportional and colinear with each other, as schematically shown in Figure 1.1. Expressed as,

$$\mu = \gamma \mathbf{J} \tag{1.1}$$

where the scalar proportionality constant is known as the gyrometric ratio, γ. The γ is a constant in unit [rads^{-1}], for specific nucleus and depends on the charge-to-mass ratio $= e/m$.
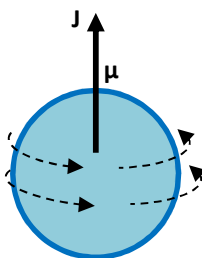
Figure 1.1 *Magnetic dipole moment and spin angular momentum of spinning proton.*

In magnetic resonance, the magnetic field is characterized by the magnetic induction **B**, which includes the magnetic properties of the medium such that, $\mathbf{B} = \mu_m \mathbf{H}$ where μ_m is the permeability of the medium unit [V.s/A.m] and **H** is the magnetic field strength unit [Am^{-1}]. The unit of B is [V.s/m^2 or Tesla, T], and 1.0 T is approximately 20,000 times stronger than the earth magnetic field.

1.1.2 Nucleus in magnetic field

From the classical mechanics approach, when a bar magnet is placed in a uniform magnetic field, a torque (τ) will act on the magnet to align it with the field. Similarly, when a nucleus with magnetic moment is placed in a magnetic field **B$_0$,** it will experience a torque tending to align it with the direction of **B$_0$**. However, due to spin angular momentum **J** the nuclear motion will be precessional like gyroscopic motion. This is because from electricity and magnetism, the torque and magnetic moment in a magnetic field are related by,

$$\boldsymbol{\tau} = \boldsymbol{\mu} \times \boldsymbol{B_0} \tag{1.2}$$

So **μ** turns in a direction perpendicular to **B**. From classical mechanics,

$$\boldsymbol{\tau} = \frac{d\mathbf{J}}{dt} \tag{1.3}$$

where **J** is the angular momentum.

From Equation (1.2) and (1.3)

$$\frac{d\mathbf{J}}{dt} = \boldsymbol{\mu} \times \boldsymbol{B_0} \tag{1.4}$$

9

Therefore $\frac{d\mathbf{J}}{dt}$ is perpendicular to $\boldsymbol{\mu}$ and $\boldsymbol{B_0}$.

As $\boldsymbol{\mu}$ is parallel to $\mathbf{J}$ from equation (1.1), therefore $\frac{d\mathbf{J}}{dt}$ is working in a direction that is perpendicular to $\mathbf{J}$, which causes the gyroscope precession of the nucleus in much the same way that a spinning top precesses due to the force of gravity. The precessional angular frequency (ω) is proportional to the magnetic field strength $\mathbf{B_0}$ (schematically shown in Figure 1.2). The Larmor equation describes the relation as,

$$\boldsymbol{\omega} = \gamma\mathbf{B_0} \tag{1.5}$$

ω is known as the Larmor frequency.
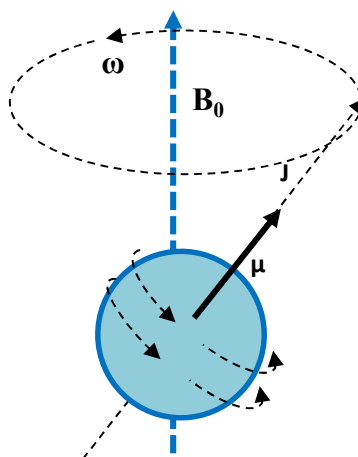
Figure 1.2 *Single proton gyroscopic precession due to external magnetic field.*

The Larmor equation is the fundamental relationship of NMR and states that the precessional frequency is directly proportional to the magnetic field. The potential energy of a moment in a field is given by,

$$E = -\boldsymbol{\mu}.\boldsymbol{B_0} \tag{1.6}$$

Thus minimum energy is obtained when $\boldsymbol{\mu}$ and $\mathbf{B_0}$ are parallel, while maximum energy is obtained when they are antiparallel. Also the energy is proportional to the magnetic field strength. Now from the quantum mechanical approach, for a particular spin quantum numbers I, there are $(2I+1)$ possible spin states related to the magnetic spin quantum number, m_i. This can be expressed as,

for integral I: $m_I = I, (I-1), (I-2), ...,0,...., -I$ and,

for half integral I: $m_I = I, (I-1), (I-2), ...,\frac{1}{2}, -\frac{1}{2}, ..., -I$

In the absence of any perturbation such as magnetic field there is degeneracy; they all possess the same energy. When a magnetic field is applied to the system there will be Zeeman coupling between the nuclear magnetic moment and the magnetic field. Due to

the Zeeman effects the energy levels splits to ($2I$ +1) possible spin states. For example, the proton spin is I=1/2 thus when it is placed in a magnetic field $\mathbf{B}_0$, it will have 2 possible states namely, $m_I = \pm$ ½. Considering the projection of the magnetic moment in the z-direction, $\mu_z = \gamma J_z$ and spin angular momentum, $J_z = \hbar m_I$. The corresponding magnetic moments are $\mu_{z+} = \gamma\hbar/2$ and $\mu_{z-} = -\gamma\hbar/2$. Therefore, the potential energies at the two energy levels are,

$E_{+1/2} = \gamma\hbar\mathbf{B}_0/2$ and $E_{-1/2} = -\gamma\hbar\mathbf{B}_0/2$

which parallel and anti-parallel to the applied field respectively. Thus the difference between the energy levels is,

$\Delta E = |\gamma\hbar\mathbf{B}_0|$

which is the Zeeman splitting due to the magnetic field $\mathbf{B}_0$. In order to excite a transition from one Zeeman state to another it is necessary to supply an energy quantum,

$$\Delta E = \hbar\omega = |\gamma\hbar\mathbf{B}_0| \tag{1.7}$$

where $\omega = \gamma\mathbf{B}_0$ is the Larmor frequency. For protons, the Larmor frequency is 41.58 MHz in a 1.0 T magnetic field. NMR is concerned with applying electromagnetic radiation at the Larmor frequency (ω) to cause transitions between the two energy levels and changes in magnetization. For a net absorption or emission of energy there must be a difference in population between the two energy levels. The magnetization $\mathbf{M}$ is defined as the sum of individual magnetic moments in a unit volume,

$$\boldsymbol{M} = \sum_i \boldsymbol{\mu_i} \quad [\text{Am}^{-1}] \tag{1.8}$$

In thermal equilibrium with surroundings, the Zeeman energy levels separated by ΔE are populated according to the Boltzmann distribution:

$$\frac{n\downarrow}{n\uparrow} = \exp\left(-\frac{\Delta E}{kT}\right) = \exp\left(-\frac{\gamma\hbar B_0}{kT}\right) \tag{1.9}$$

where $n\uparrow$ is the number of spins in the **low** energy, 'up'(+1/2) state, parallel to B_0; $n\downarrow$ is the number of spins in the **higher** energy, 'down' (-1/2) state, antiparallel to B_0; k is the Boltzmann's constant and T is the absolute temperature, schematically this is shown in Figure 1.3.
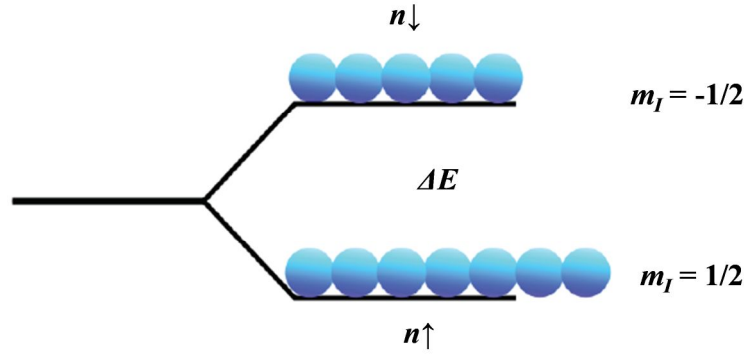
Figure 1.3 *Zeeman energy levels for protons in thermal equilibrium, showing difference in population.*

As there are only two states, the total number of spins N in the system is given by

$$N = n\uparrow + n\downarrow$$

It can be shown that the population difference is

$$n\uparrow - n\downarrow = N\frac{\left\{1-\exp\left(-\frac{\gamma\hbar B_0}{kT}\right)\right\}}{\left\{1+\exp\left(-\frac{\gamma\hbar B_0}{kT}\right)\right\}} = N tanh(\frac{\gamma\hbar B_0}{2kT}) \tag{1.10}$$

At body temperature (310K), $kT \gg \gamma\hbar B_0$ so equation (1.10) can be reduced to,

$$n\uparrow - n\downarrow \cong N(\frac{\gamma\hbar B_0}{2kT}) \tag{1.11}$$

Then the nuclear net magnetization M_0 is given by,

$$M_0 = (n\uparrow - n\downarrow)\gamma\hbar m = \frac{\gamma^2\hbar^2 N B_0}{4kT} \tag{1.12}$$

Since the energy difference ΔE is very small compared to body temperature kT the number of excess protons in the low energy state is very small, about 3 spins per million at field strength 1.0 T. It is the population difference $(n\uparrow - n\downarrow)$ that gives rise to a net, bulk, magnetisation within the material that can be detected by NMR. This small population difference is one of the fundamental factors determining the basic NMR signal. Therefore NMR has inherently low sensitivity.

While the quantum mechanical approach is the only way to fully describe the evolution of a spin system, a classical approach describing the bulk magnetization at the macroscopic scale is surprisingly effective and intuitively easier to follow. By using the Equations (1.1- 1.4) and (1.7) and considering a single value of γ, one can express the equation of motion for bulk magnetization **M**,

$$\frac{d\boldsymbol{M}}{dt} = \gamma\boldsymbol{M} \times \boldsymbol{B_0} \tag{1.13}$$

This implies that the magnetization **M** precesses about **B** at the Larmor frequency.

NMR uses a large, static magnetic field to 'polarise' the nuclear spins and hence causes a difference in the populations of the two energy levels; this field is known as the main static magnetic field generally in the range of 1.0~3.0T and created by superconducting magnets. Energy in the form of a pulse of radio frequency electromagnetic radiation at the precessional frequency or Larmor frequency related to ΔE is absorbed and flips the spins from the low-energy parallel direction to the higher energy antiparallel direction. When the perturbed system goes back to its equilibrium, the MR signal is produced.

1.1.3 Frame of reference

By convention, the applied magnetic field $\mathbf{B_0}$ is defined as parallel to the z-axis of the 3D Cartesian coordinate axis system, where the *x* and *y* axes are perpendicular to the *z* direction. For convenience, two frames of reference are used: the laboratory frame and rotating frame. The laboratory frame is a stationary frame from the observer point of view. The rotating frame spins about the z-axis with the precessional frequency of the protons (for resonating spins it is actually equal to the RF frequency). In this frame, the spins appear to be stationary, schematically shown in Figure 1.4. If a slightly higher precessional frequency occurs, a slow clockwise rotation is observed; for a slightly lower precessional frequency, counter clockwise rotation is observed.
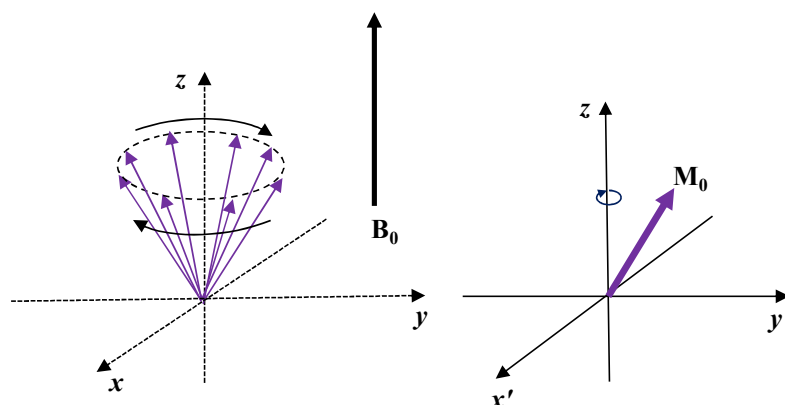
Figure 1.4 *The laboratory frame of reference uses stationary three dimensional Cartesian coordinates. The magnetic moment precesses around the z-axis at the Larmor frequency. The rotating frame of reference uses Cartesian coordinates which rotate about the z-axis at the Larmor precessional frequency and the other axes are denoted by x´ and y´.*

The net magnetization vector, $\mathbf{M_0}$, is described by two components; M_z is the component parallel to the applied magnetic field and is known as longitudinal

magnetization and M_{xy} is the component perpendicular to the applied magnetic field and is known as transverse magnetization. At equilibrium, the longitudinal magnetization is maximum $M_z = M_0$, where M_0 is determined by the excess number of protons in the low energy state from equation 1.12. At equilibrium, M_{xy} is zero, due to random orientations of the vector components in the x-y plane that cancel each other. Both magnetizations are schematically shown in Figure 1.5
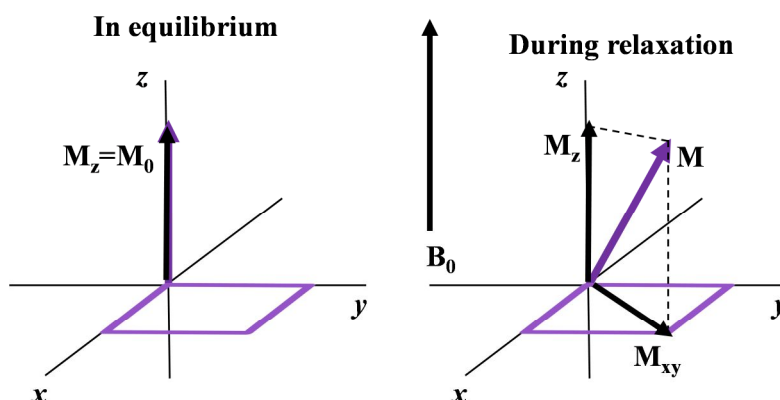
Figure 1.5 *Longitudinal magnetization, M_z, is the vector component of the total magnetization in the z direction. Transverse magnetization, M_{xy}, is the vector component of the total magnetization in the x-y plane and M_0 is the net magnetization.*

1.1.4 RF pulses in NMR

To probe the nuclear magnetisation, RF magnetic fields, also known as $\mathbf{B_1}(t)$ fields, with precisely matched precessional frequency to the protons are applied to the sample. $\mathbf{B_1}(t)$ is much smaller than the $\mathbf{B_0}$, in the range of micro Tesla (μT). The RF pulses excite the transitions between the Zeeman energy levels. The RF pulse induces transitions between the two permitted spin states (precession cones) until the occupation numbers are either identical (90^0 pulse) or inverted (180^0 pulse). A special coil (antenna) is used to produce the RF field; the coil is tuned to the appropriate resonant frequency.

From the perspective of the rotating frame (x', y', z) that is rotating at Larmor frequency about the z-axis, the RF field $\mathbf{B_1}$ appears as stationary and $\mathbf{B_0}$ transforms to zero and the magnetization vector $\mathbf{M_0}$ now precesses around the $\mathbf{B_1}$ from its equilibrium position. The gyroscopic motion, Equation (1.13), can now be written as,

$$\frac{d\boldsymbol{M}}{dt} = \gamma \boldsymbol{M} \times (\boldsymbol{B_0} + \boldsymbol{B_1}) \tag{1.14}$$

The angle α by which the $\mathbf{M_0}$ is tipped depends on the duration and amplitude of the B_1 field.

$$\alpha = \gamma \int_0^T B_1(t)dt \tag{1.15}$$

where T is the duration of RF pulse.

A 90^0 pulse flips the $\mathbf{M_0}$ into the $x'y'$ plane and results in phase synchronization of the spin magnetic moments of the sample, which yields a macroscopic transverse magnetization M_{xy}, the magnitude of which is equal to that of the equilibrium magnetization M_0 (largest possible transverse magnetization with no longitudinal magnetization). An 180^0 pulse inverts $\mathbf{M_0}$ into the –z axis. Figures 1.6 and 1.7 show the schematic diagrams of RF field effects at different flip angles.
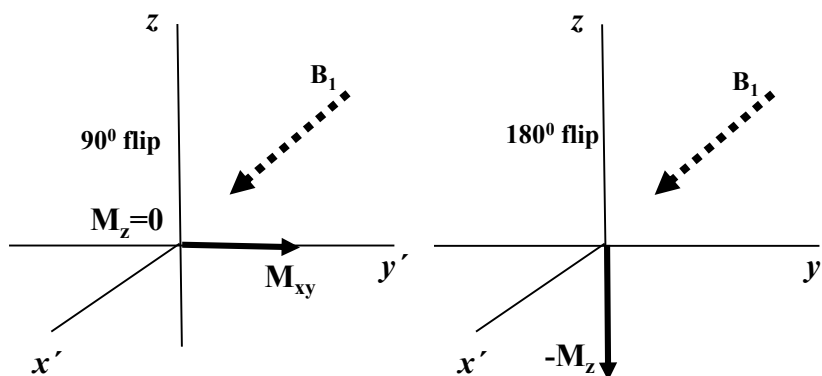
Figure 1.6 *RF pulse with 90^0 flip angle reduces M_z to zero and creates the maximum M_{xy} and a 180^0 pulse inverts M_z to $-M_z$.*
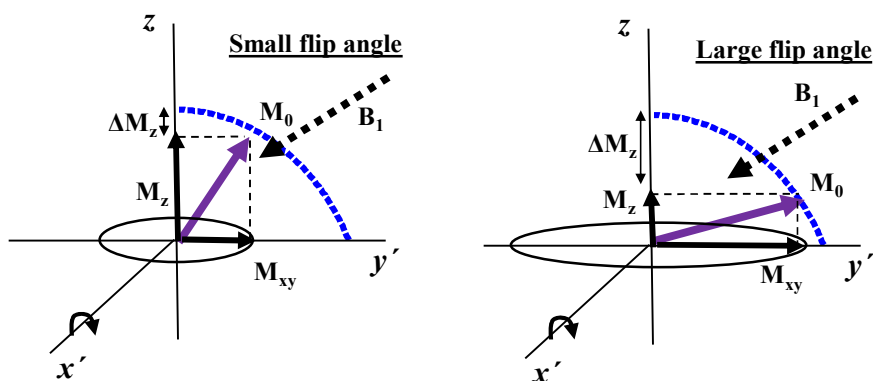
Figure 1.7 *Flip angles describe the angular displacement of the longitudinal magnetization (M_z) vector from the equilibrium position. The rotation angle of the magnetic moment vector about the x´ direction depends on the duration and amplitude of the $\mathbf{B_1}$ field at the Larmor frequency. Small flip angle (~30^0) and large flip angle (~90^0) produces small and large transverse magnetizations (M_{xy}) respectively.*

For a given $\mathbf{B_1}$ amplitude the time required to flip the magnetization depends on the displacement angle. For the same $\mathbf{B_1}$ strength, a 90^0 takes half the time to produce that

an 180^0 does. The time required to implement a rotation is of the order of 1 to 10 of microseconds. On the other hand, by using a long RF pulse it is also possible to saturate the magnetization. In fact with sufficiently long RF irradiation the spin system settles into a steady state condition that equalizes the superposition of the two states, thus momentarily nulling the net magnetization.

In the rotating frame, $\mathbf{B}_1$ is stationary and $\Delta\mathbf{B}_0$ is zero on resonance condition. If the RF pulse is not applied at the Larmor frequency, spins are not stationary in the rotating frame such condition is called off-resonance. Magnetization in this case precesses about the vector $\mathbf{B}_{eff} = \mathbf{B}_1 + \Delta\mathbf{B}_0$, where $\Delta\mathbf{B}_0 (= \Delta\omega/\gamma)$ is the field offset from the resonance. Figure 1.8 shows the off-resonance condition.
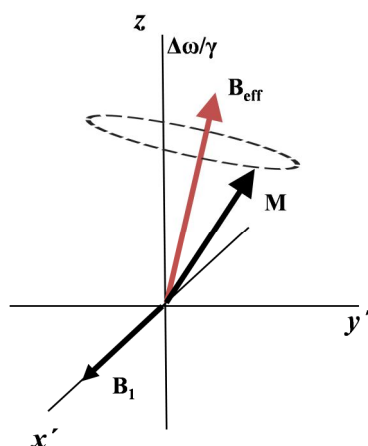
Figure 1.8 *Off-resonance condition, creating slightly tilted precession of the spins with respect to the effective field $\mathbf{B}_{eff}$.*

1.1.5 FID: free induction decay and signal detection

As explained above, after a 90° pulse the bulk magnetisation has been tipped into the x-y plane where all the spins come into phase coherence with no net population difference between the up and down states and thus generate the maximum possible transverse magnetization for a given sample volume. Once the RF pulse is switched off, the xy magnetisation created by a pulse, will now precess about the main field $\mathbf{B}_o$ at the frequency difference between the Larmor frequency and the frequency of rotating frame or frequency of spectrometer. Figures 1.9 shows schematic diagrams of the FID in the laboratory and rotating frame of references.
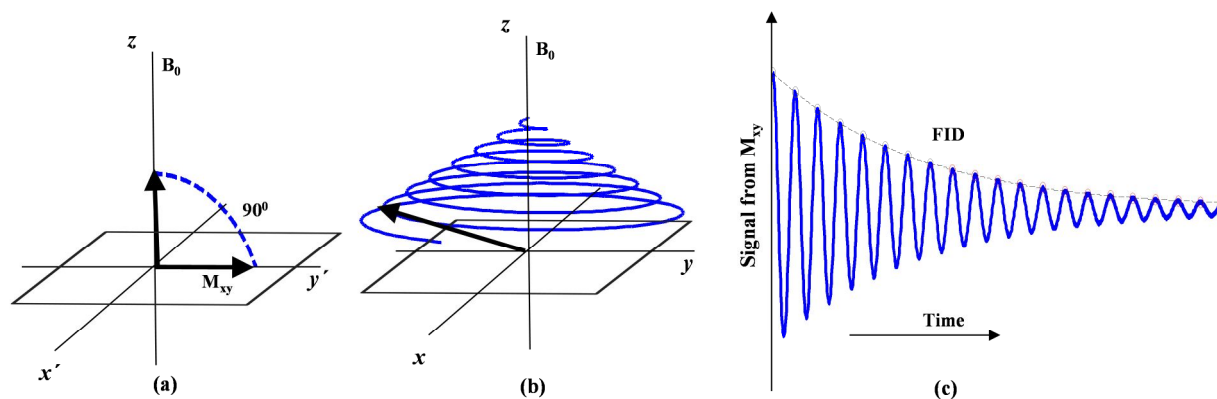
Figure 1.9a *Precession of transverse magnetization in the laboratory frame of reference. After the 90^0 RF pulse M_{xy} spiralling to the centre of x-y plane and creating the free induction decay (FID).*
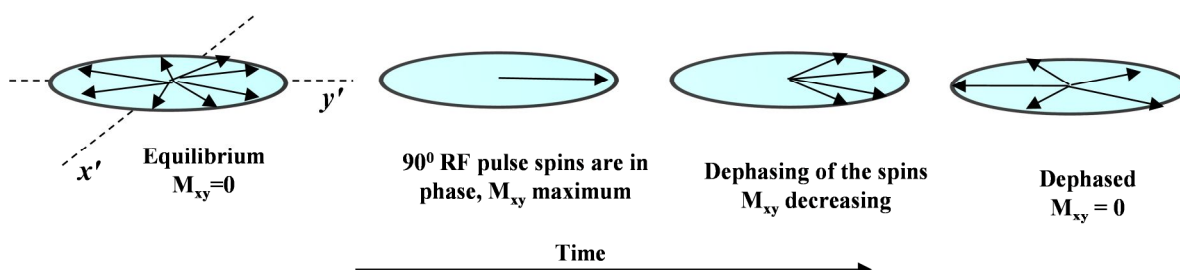
Figure 1.9b *Changes in transverse magnetization in the rotating frame of reference.*

This rotating magnetisation induces an oscillating e.m.f. in a receiver coil (in the laboratory frame) that is tuned to RF frequencies to produce a damped sinusoidal electronic signal known as the free induction decay (FID) signal. Generally the same coil works as a receiver that was used to produce the RF field to excite the magnetisation. The measured voltage is amplified, filtered, digitalized and fed to the computer of the system. The FID signal has the following characteristics:

- It oscillates with the difference between the Larmor frequency of the excited nuclei and the frequency of the spectrometer
- It decays in time with a time constant (T2*) determined by the microenvironment of the excited nuclei
- Its initial amplitude is proportional to the number of excited nuclei or spins in the system, $N=\rho V$, where ρ is the spin density and V is the volume of the sample.

In the next section, the Bloch equations and principles of relaxation processes of magnetization are reviewed.

1.1.6 Bloch equations and magnetization relaxation

In 1940 Felix Bloch derived a set of equations describing the phenomenological behaviour of bulk magnetization. Experimentally, application of an RF pulse reduces the longitudinal magnetization (M_z) by causing transitions between energy levels by spins flipping. It also causes the spins to come into phase with each other and hence creates a transverse magnetisation (M_{xy}). The rate of change of the magnetisation is described by the Bloch equations:

$$\frac{dM_z}{dt} = \frac{M_0 - M_z}{T_1} \tag{1.16a}$$

$$\frac{dM_x}{dt} = -\frac{M_x}{T_2} + \gamma(\boldsymbol{M} \times \boldsymbol{B_0})_x \tag{1.16b}$$

$$\frac{dM_y}{dt} = -\frac{M_y}{T_2} + \gamma(\boldsymbol{M} \times \boldsymbol{B_0})_y \tag{1.16c}$$

Equation (1.16a) describes rate of recovery of M_z to the equilibrium, M_0, after an excitation, where T_1 is the longitudinal magnetization relaxation time. Equations (1.16b) and (1.16c) describe the change of transverse magnetization M_x and M_y decaying to zero, in a static magnetic field B_0, and T_2 is the transverse magnetization relaxation time. When M_z relaxes towards its equilibrium, M_0, the transverse components M_x and M_y must decay to zero. Solutions to these equations give rise to the graphs and equations shown in Figure 1.10 using the appropriate boundary conditions, t = 0, M_{xy}= M_0 and M_z = 0, after a 90° RF pulse with M_z and M_{xy} returning to their equilibrium states.
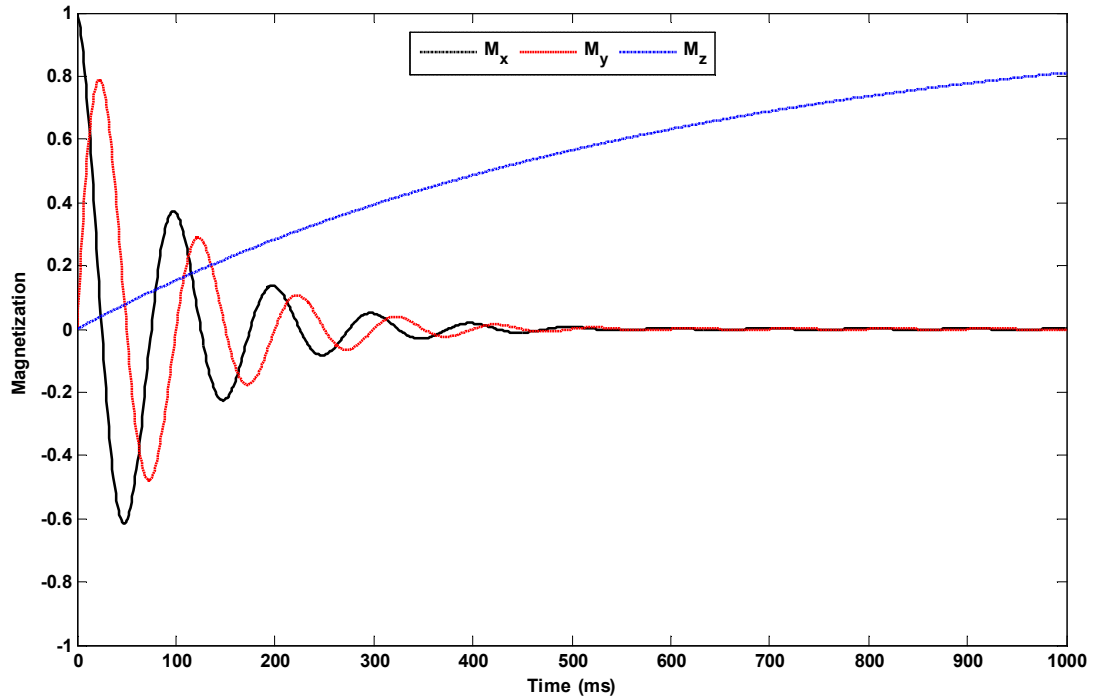
Figure 1.10 *Spiralling decay of the transverse magnetization depending on T_2,* $M_x = cos\omega_0 t e^{-t/T_2}$ *and* $M_y = sin\omega_0 t e^{-t/T_2}$ *; exponential regrowth of longitudinal magnetization depending on T_1, $M_z = M_0(1 - e^{-\frac{t}{T_1}})$.*

1.1.7 Longitudinal T_1 recovery

The rate of longitudinal recovery is described by the T_1 or the spin lattice relaxation time. It corresponds to the exponential regrowth of M_z, and depends on the characteristics of the spin interactions with molecular arrangement and structure of the lattice. It can be derived from the Bloch equation (1.16a),

$$M_z(t) = M_0(1 - \exp(-t/T_1)) \tag{1.17}$$

where M_0 is the equilibrium magnetization and T_1 is the time needed to recover 63% of the M_z shown in Figure 1.11.
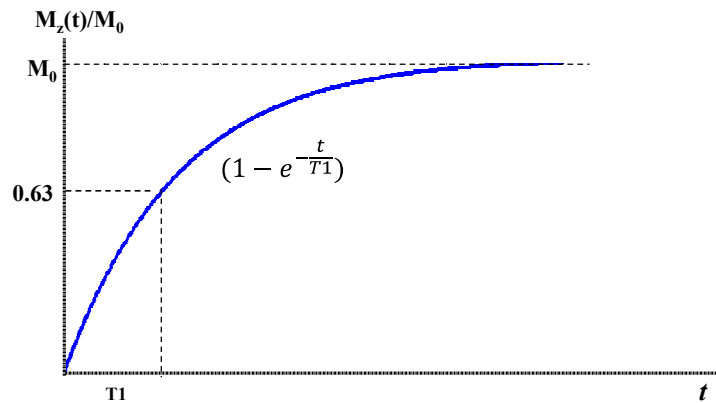
Figure 1.11 *Longitudinal magnetization recovery with T_1*

The longitudinal magnetization recovery is mainly caused by the fluctuating magnetic fields at the Larmor frequency due to the motion of neighbouring molecules also called the dipole-dipole interactions. This is because these molecules also contain magnetic moments from various sources, and hence if they are moving at frequencies close to the Larmor frequency they will give rise to RF magnetic fields. The rate at which the energy is lost indicates how closely the spins are coupled to the lattice. Therefore, the T_1 relates the mobility of interacting molecules and binding with the macromolecules. Molecular motion depends on temperature, therefore T_1 depends on temperature. Also T_1 depends on the magnetic field strength as this determines the Larmor frequency.

__Measurements of T_1 relaxation:__

Saturation recovery:

The saturation recovery sequence depends on the recovery of longitudinal magnetization and is shown in Figure 1.12, where RF pulses are repeated at an interval TR.

Provided no transverse magnetization remains between pulses the signal in this sequence is given by,

$$M_z(t) = M_0(1 - \exp(-\frac{TR}{T_1})) \tag{1.18}$$

If TR is long compared to T_1, the magnetization can relax back to its equilibrium state. In this case, the amplitude of FID acquired after the pulse will only depend on the equilibrium magnetization M_0 and does not show T_1 dependency producing proton density images. However, if TR is comparable to T_1, the M_z will not fully relax after the first excitation, and the following 90^0 pulse will rotate the reduced M_z into the xy plane (Figure 1.12). In this case the spin system will be partially saturated, with the amount of saturation dependent on the T_1 relaxation time. Thus short T_1 tissue has less saturation than a long T_1 tissue, giving greater signal. This creates T_1 weighted images in MRI.
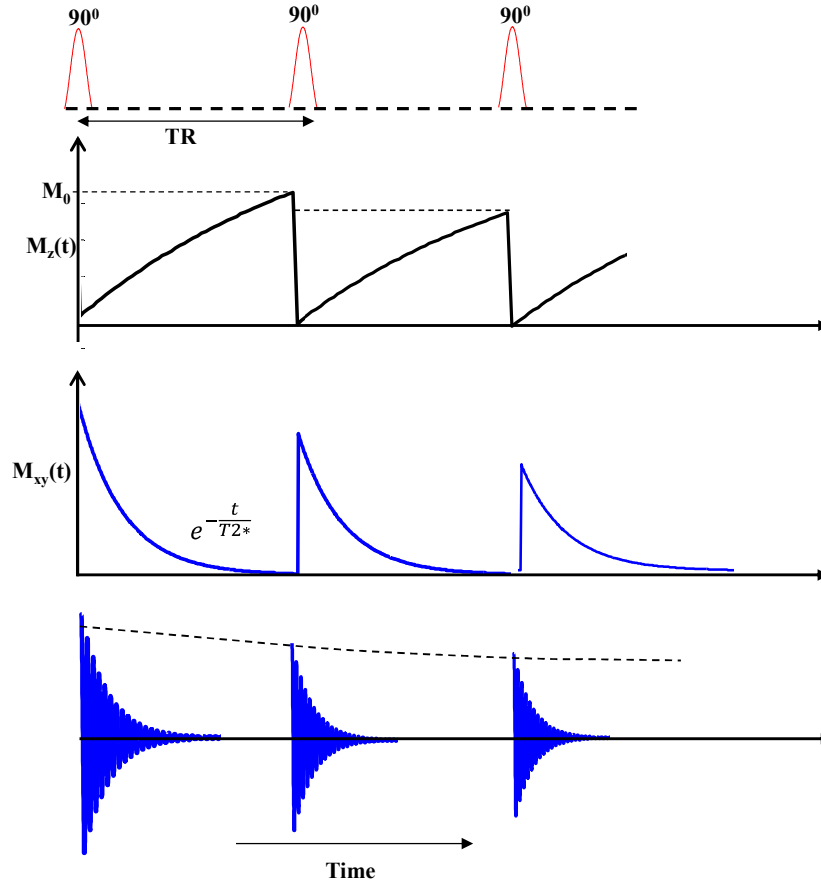
Figure 1.12 *Saturation recovery sequence, showing change of transverse and longitudinal magnetization with time followed by the RF pulses.*

Inversion Recovery:

The inversion recovery (IR) pulse sequence emphasizes the T_1 relaxation time of the spin system. Thus can produce T_1 weighted images. An initial 180^0 RF pulse inverts the longitudinal magnetization M_z to $-M_z$. After a delay of time known as the time of inversion (TI), a 90^0 RF pulse rotates the recovered fraction of M_z into the transverse plane to generate the FID. A second 180^0 pulse at time TE/2 produces an echo signal at TE. TR in this case is the time between 180^0 inversion pulses. The amplitude of the signal depends on TI, TE, TR and M_z. The signal intensity from the IR sequence is given by,

$$S \propto (1 - 2\exp\left(-\frac{TI}{T_1}\right) + \exp\left(-\frac{TR}{T_1}\right)) \qquad (1.19)$$

The factor 2 arises from the recovery, and the final term allows for incomplete recovery during the period TR schematic sequence shown in Figure 1.13.
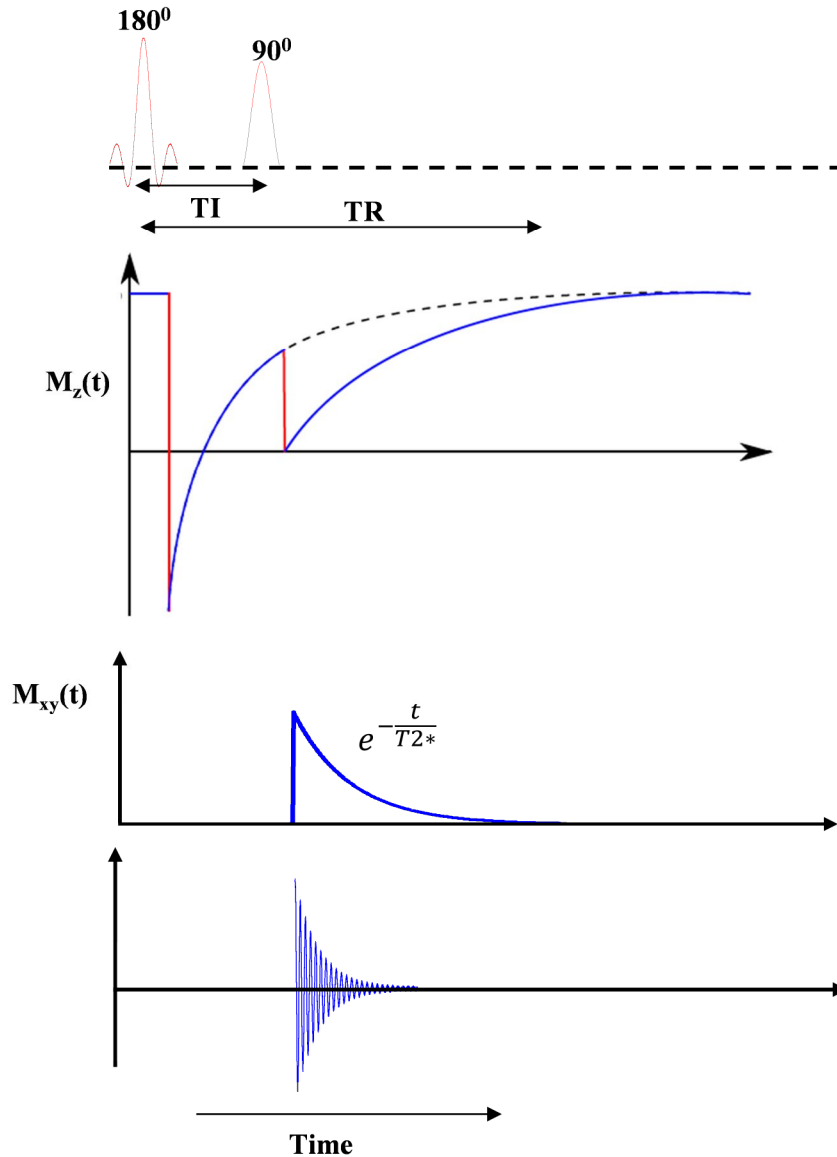
Figure 1.13 *Inversion recovery sequence, showing change of transverse and longitudinal magnetization with time followed by the RF pulses.*

1.1.8 Transverse T_2 decay

The exponential relaxation decay, T_2, represents the characteristic time for loss of the phase coherence acquired during the RF excitation. The decay envelope of the FID is the result of the loss of phase coherence of the spins at a rate of the T_2 time constant that causes the nulling of net magnetization in the $x'y'$ rotating plane. Recovery of Mz will also lead to less of transverse magnetization (hence $T_2 \leq T_1$). From the Bloch equations (1.16b) and (1.16c) the transverse magnetization decay is given by,

$$M_{xy} = M_0 \exp(-t/T_2) \tag{1.20}$$

where M_0 is the transverse magnetization at $t = 0$. The elapsed time between the peak transverse signal and 37% of the peak level ($1/e$) is the T_2 decay constant shown in Figure 1.14.
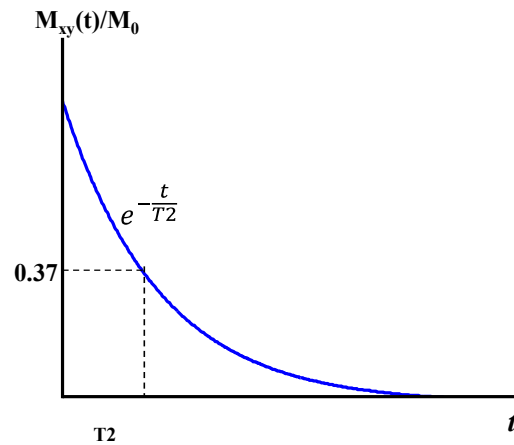
Figure 1.14 *Transverse magnetization decay with T_2*

The T_2 relaxation process involves the loss of phase coherence caused by processes such as: the micromagnetic inhomogeneities intrinsic to the structure of the sample, whereby the individual spins precess at different frequencies due to slight changes in the local magnetic field strength. Some spins moves faster and some slower, resulting in a loss of phase coherence. If the spins move in these fields it will lead to irreversible loss of phase coherence. Dipole-dipole interactions also affect the T_2, due to low frequency components of time varying fields. Thus the mobile molecules in liquids exhibit a long T_2, because rapid and fast molecular motion reduces or cancels the intrinsic magnetic inhomogeneities, whereas, solid and non-moving structures with stationary magnetic inhomogeneities have a very short T_2.

1.1.9 T_2^* decay

Experimentally the MR signal decays faster than predicted by T_2, due to the extrinsic magnetic inhomogeneities. These are anything that gives rise to time invariant differences in the local magnetic fields of the spins, such as an imperfect main magnetic field, B_0, which creates inhomogeneities in the magnetic field across the sample, or differences in the magnetic susceptibility of the sample that causes local field gradients at tissue boundaries. This causes dephasing of the transverse magnetisation more rapidly than from spin-spin interactions. This accelerated decay time is called T_2^* and it is related to T_2 by,

$$\frac{1}{T_2^*} = \frac{1}{T_2} + \frac{1}{T_2'} \tag{1.21}$$

where T_2' accounts for the processes arising from imperfections in the B_0 field, i.e.

$$T_2' \sim \frac{1}{\gamma \Delta B_0}$$
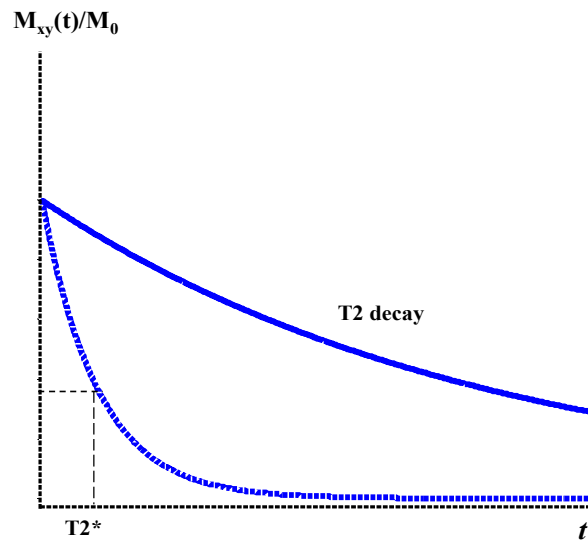
Figure 1.15 T_2^* and T_2 decay after the 90^0 excitation pulse.

__Measurements of transverse relaxation time__:

Spin Echo (SE):

The T_2 relaxation time constant can be measured by forming an echo of magnetization named the spin echo (SE). For that an initial 90^0 pulse along x- direction produces the maximal transverse magnetization, M_{xy} and puts the spins in phase coherence. The spins will start to dephase and signal decays exponentially with T2* due to intrinsic and extrinsic time varying and static magnetic field variations. After a time delay t (=TE/2), an 180^0 RF pulse is applied along x-direction which inverts M_{xy} resulting in rephasing of the spin system. Complete rephasing occurs at a time TE known as the echo time. The echo reforms in the opposite direction from the initial M_{xy} vector. The echo signal will be attenuated compared to the field immediately following the 90^0 pulse because of random thermal motion of the spins which causes irreversible dephasing.

The maximum echo amplitude depends on the T2 constant and not on T2*, since the effects of static magnetic field inhomogeneities are refocused by the 180^0 pulse. The exponential decay of transverse magnetization follows the Equation (1.17). The standard spin echo imaging pulse sequence uses a 90^0 pulse followed by 180^0 pulse repeated after a period known as the time of repetition (TR), which typically ranges

from 300 to 3000msec to allow for longitudinal magnetization recovery. A schematic diagram of a SE acquisition is shown in Figure 1.16.
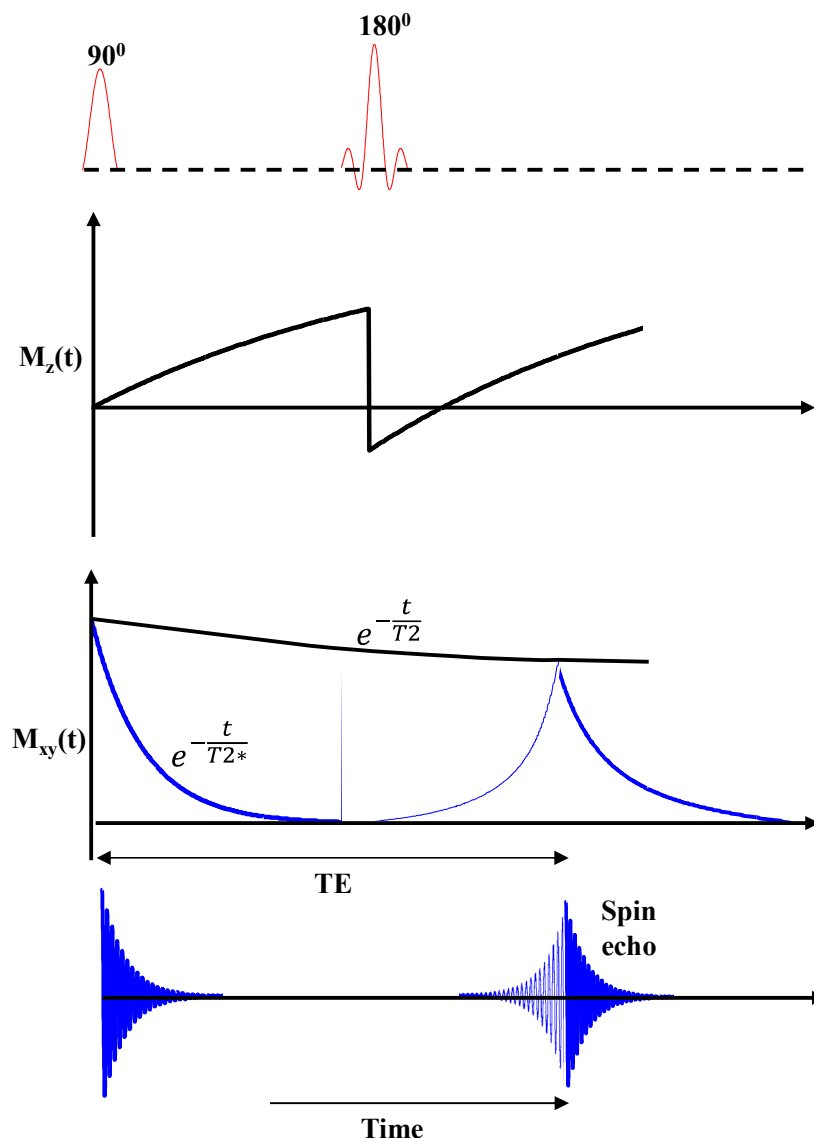

Figure 1.16 *Spin echo sequence, showing changing of transverse and longitudinal magnetization with time followed by the RF pulses.*

1.1.10 Proton density observation

When placed in a strong magnetic field, the spins precess along their polarization axis creating the stable net magnetization M_0 at thermal equilibrium. By manipulating the magnetization correctly, it is possible to measure M_0. This is called the proton density (PD) measurements. Although PD is the primary source of signal, PD changes often correlate with T_1 changes as well.

Comparison of relaxation effects:

Molecular motion, size and interactions influence the T_1 and T_2 relaxation times. Molecules can be roughly categorised into three groups- small, medium and large- with corresponding fast, medium and slow vibrational frequencies. Small molecules exhibit long T_1 and T_2, and intermediate sized molecules have short T_1 and short T_2; however, large, slowly moving or bound molecules have long T_1 and short T_1. Most tissues of interest in MRI consist of intermediate to small-sized molecules, thus the differences in T_1, T_2, T_2^* and proton density variations provides the contrast in MRI. Magnetic field strength influences T_1 due to Larmor frequency dependence. Contrast agents that disrupt the local magnetic field environment, such as gadolinium DTPA can influence the T_2^*.

To summarize, the spin density, T_1 and T_2 are the intrinsic properties of the systems and these properties can be exploited in NMR and MRI. Some general rules are that:

$T_2 \leq T_1$

$T_2 \sim T_1$ in systems in which the molecules are highly mobile (e.g. water)

$T_2 \ll T_1$ in solids

The relaxation mechanism of the spin is related to its surroundings and thus can help to compare between different systems.

Signal from the Diffusion:

Self-diffusion describes the random motion of molecules in a given structure, in the NMR system if the spins are moving randomly through a spatially varying magnetic field, due to diffusion sensitized gradients the mobility and directionality of the diffusing particles will create signal differences and that can be used to quantify the diffusion properties of the microstructures. A detailed analysis will be discussed in Chapters 3 and 4.

Magnetization transfer contrast:

Frequencies of the protons in the large macromolecules are not the same as the Larmor frequency of water due to chemical shifts leading to a broad resonance linewidth. Also these protons have very short T_2 thus are not visible in imaging. The magnetization transfer contrast technique is used to highlight those protons indirectly, based on transfer

of magnetization from saturated bound protons. Applications and use of this technique will be discussed in Chapters 3 and 5.

Chemical shift and MR spectroscopy:

The net magnetic field experienced by the nucleus is the sum of the external field applied to the system and the much smaller fields generated by the electrons surrounding the nucleus. These additional fields alter the precession frequency by a tiny fraction known as Chemical shift. Spins resonating slightly off-resonance can create chemical shift artefacts in MRI. Chemical shift forms the basis of magnetic resonance spectroscopy (MRS). MR spectroscopy uses the MR signals from a variety of chemical species to probe tissue metabolism. Different metabolites containing a given resonant nucleus emit signals at slightly different frequencies. These signals appear as distinct peaks on an MR spectrum. The areas of the peaks are proportional to metabolite concentration.

In the presence of an external magnetic field $\mathbf{B}_0$, the Larmor frequency of a nucleus is determined by the macroscopic main magnetic field ($\mathbf{B}_0$) and microscopic magnetic field ($\Delta\mathbf{B}$) caused by the surrounding electrons of the molecule. Thus the local magnetic field ($\mathbf{B}_{\mathrm{eff}}$) at the position of the nucleus is expressed as,

$$\mathbf{B}_{\mathrm{eff}} = \mathbf{B}_0 + \Delta\mathbf{B} \tag{1.22}$$

As experimental and theoretical investigations have shown, the microscopic field is proportional to the macroscopic field, $\Delta\mathbf{B} = -\sigma\mathbf{B}$, which yields the expression of the resonance frequency of the nucleus considered as,

$$\omega = \gamma\mathbf{B}_{\mathrm{eff}} = \gamma(1-\sigma)\mathbf{B} \tag{1.23}$$

where σ is the dimensionless shielding constant and depends on the electron density around the nucleus. Since the electron density is a function of the bonding structure within the molecule, the magnitude of the frequency shift varies among different types of molecules, and among distinct chemical groups within the same molecule. As the absolute value of the frequency shift cannot easily be measured, it is usually determined relative to the resonance frequency ω_r as a reference for that substance. The difference in frequencies is expressed as a dimensionless parameter, $\delta = \frac{\omega - \omega_r}{\omega_0} \times 10^6 \cong (\sigma_r - \sigma) \times 10^6$, relative to the frequency $\omega_0 = \gamma B_0$ of the MR system in parts per million (ppm).

1.2 Magnetic Resonance Imaging

The importance of magnetic resonance imaging (MRI) in clinical imaging has exceeded even the most optimistic hopes of researchers from the 1980s. An ability to manipulate and adjust tissue contrast with developed and efficient pulse sequences and significant improvement of MR hardware are the basis of this success. This section describes how the MR images are created from the imaging sequences using RF pulses and magnetic field gradients designed based on k-space. Then imaging techniques relevant to this thesis are introduced. An overview of MR equipment requirement and limitations, sources of artefacts arising and biological safety issues are discussed.

1.2.1 Principle of spatial encoding

Spatial localization in MRI requires the imposition of magnetic field non-uniformities. The magnetic gradients superimposed on the homogeneous and much stronger main magnetic field are used to distinguish the spatial encoding of the signal in a three dimensional object (the subject).

Magnetic field gradient:

In practice, the image encoding is achieved almost exclusively by means of magnetic field gradients from one or more coils with a precisely defined geometry. With appropriate design, the gradient coil creates a magnetic field that linearly varies in strength with distance over a predefined field of view (FOV). Virtually all modern MRI scanners use spatially variations in the magnetic field B_0, to make the Larmor frequency spatially dependant. Magnetic field gradients can be formed in any direction ($G_x = \dfrac{dB_z}{dx}, G_y = \dfrac{dB_z}{dy}, G_z = \dfrac{dB_z}{dz}$).

When superimposed with the main magnetic field B_0, positive part of the gradient field adds to $\mathbf{B}_0$ and negative part reduces $\mathbf{B}_0$. It causes the protons to alter their precessional frequency dephasing on their position along the applied gradient. In order to avoid image distortions, the magnitude of the gradients have to be chosen such that the applied field variations are markedly greater than the local inhomogeneities of B_0; typical values are 1 to 50 milli Tesla per meter (mT/m). The slew rate is the time required to achieve the maximum amplitude of the gradient field. Lower slew rate reduces eddy current effects. Eddy currents are electrical currents

induced in a conductor by a changing magnetic field. Eddy currents are generated when the MR gradients turn on and off. Without compensation of eddy currents it may produce image distortions. By precompensating the gradient driving currents or by using shielded gradients the eddy current effects can be minimized.

Localization of protons in the three dimensional volume requires the application of three distinct gradients: slice selection, frequency encode and phase encode gradients. These gradients are applied in a specific manner, depending on the pulse sequence employed.

1.2.2 Slice select gradient

The slice select gradient determines the slice of the body to be imaged in conjunction with the RF excitation pulse. Proton precessional frequencies vary according to the spatial variations in the magnetic field. A narrow bandwidth RF pulse is applied to the whole body, but only those spins along the gradient that have a precessional frequency equal to the frequency centred with the RF pulse will absorb energy due to the resonance. Slice thickness is determined by the bandwidth of the RF pulse and the gradient strength across the FOV, related by the equation $\delta\omega = \gamma G(\delta z)$, where $\delta\omega$ is the RF bandwidth (BW), G is the gradient strength, and δz is the slice thickness, schematically shown in Figure 1.17. Thus, the slice select gradient applied during the RF pulse results in proton excitation in a single plane which localizes the signal in the dimension orthogonal to the gradient.
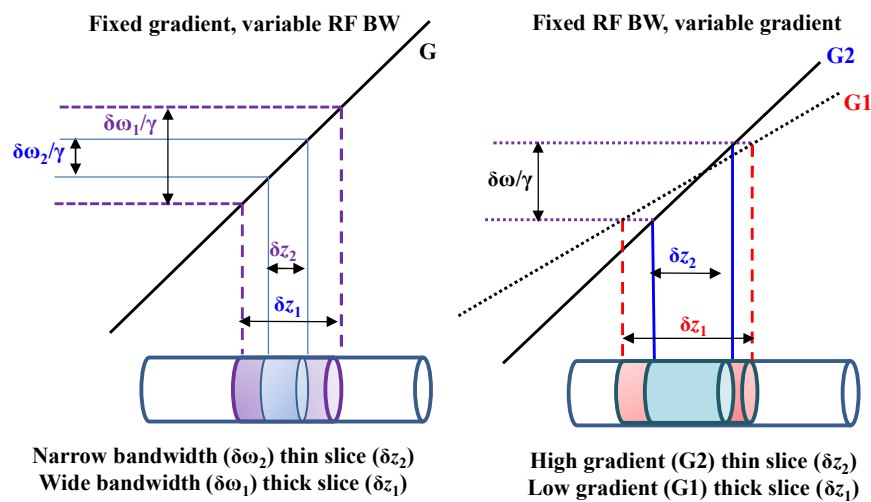
Figure 1.17 *Slice selection gradient, showing dependency of slice thickness (δz) on RF bandwidth (δω) and gradient strength (G).*

Slice select gradients and pulses induce spin dephasing across the slice. To re-establish the original phase of the protons after the slice-select excitation, a gradient of opposite polarity equal to one-half area of the original gradient is applied, known as the rephasing gradient which is schematically shown in Figure 1.18.
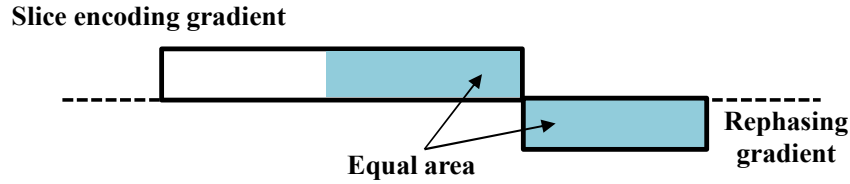
Figure 1.18 *Slice selection gradient leaves dephased spins, rephasing gradient of opposite polarity and one half area of the slice select gradient serves to rewind the spins back to the original phase.*

1.2.3 Frequency encoding

The frequency encoding gradient (also known as the readout gradient) influences those spins that have been excited by the slice selection gradient, schematically shown in Figure 1.19.

Let, a uniform linear magnetic field gradient $G = \frac{\partial B_z}{\partial x}$ be applied along the x-axis, the net magnetic field in the z-direction is given by,

$$B_z = B_0 + Gx$$

Then from the Larmor equation the angular frequency of precession of all the spins which lie at a particular value of x will precess at the same frequency as,

$$\omega_0(x) = \gamma B_z = \gamma (B_0 + Gx)$$

or in a more general three dimensional form as,

$$\omega_0(\boldsymbol{r}) = \gamma (\boldsymbol{B_0} + \boldsymbol{G.r}) \tag{1.24}$$

Thus the transverse magnetisation in different parts of the sample will precess at different frequencies. If a number of spins $n(\omega)$ precess at frequency $\omega_0(x)$, then the frequency spectrum will produce the spatial information about the object under the magnetic field.
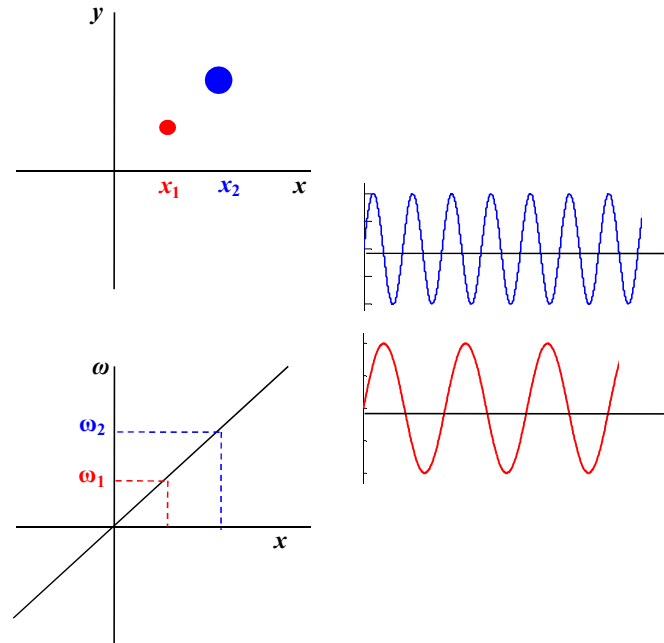
Figure 1.19 *Frequency encoding and spatially dependent variation in the precessional frequencies from the slices (that are slice selection encoded).*

Projection reconstruction imaging: An image of a two dimensional object can be generated using the frequency encoding via projection reconstruction imaging as in X-ray CT methods. The spin density of a given slice is sampled in a multitude of directions (projections) and back projected to obtain a radial density image. However, the image is blurred when reconstructed in a Cartesian grid due to the sampling of measurements, but can be overcome using specific filters or via appropriate interpolation. An alternative approach is spin warp imaging which is widely used in MRI nowadays.

1.2.4 Phase encoding

The position of the spins in the third spatial dimension is determined with a phase encode gradient, applied before the frequency encode gradient and after the slice encode gradient, along the third axis perpendicular to both slice selective and frequency encoding gradients. It employs a short lived pulse of field gradient, resulting in a relative phase shift among the spins. The detected signal, therefore, contains components with different phases, which originate from different positions along the direction of the gradient. To extract the amplitude of each component, the entire process of excitation and signal acquisition must be repeated many times, with phase encoding gradient pulses of incrementally different strengths. The change in the

phase between successive acquisitions uniquely identifies the position of the tissue along the direction of the gradient, schematically shown in Figure 1.20 .
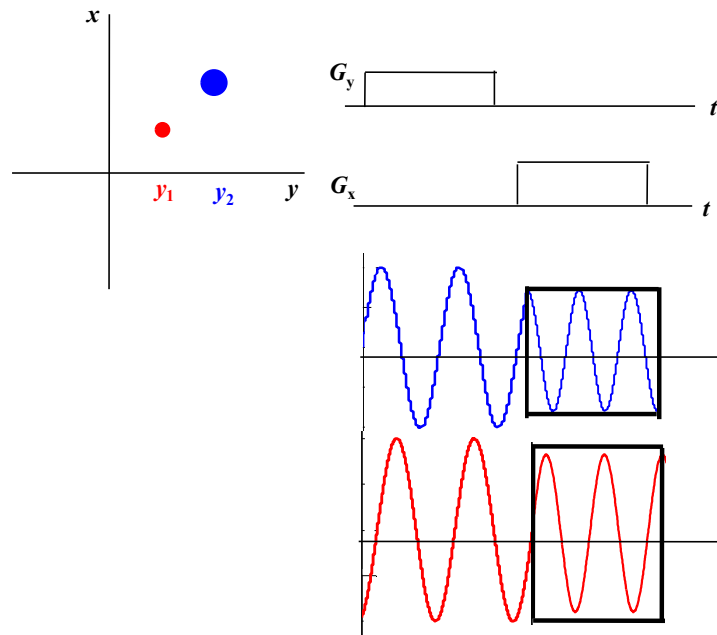
Figure 1.20 *Schematic diagrams for phase encoding and frequency encoding gradients*.

Two dimensional MR images are produced by using both frequency and phase encoding. Conventionally frequency encoding is considered to be in the x direction and phase encoding in the y direction and the slice selection considered in the z direction. These labels are completely arbitrary, and are not connected with the physical axes of the scanner or the gradient coils. In fact, the gradient coils can be used in combination to image the tissue in any oblique plane.

1.2.5 k-space concept and image reconstruction

k-space is introduced as a way of visualization of the trajectories of the spins phase under the influence of field gradients. k-space describes a two dimensional matrix of positive and negative spatial frequency values, encoded as complex numbers. The high spatial frequencies represent the fine detail appearing at the edges of the k-space and low spatial frequencies represent coarse structures appearing close to the origin of the k-space. k-space (k_x, k_y, k_z) can be considered as the Fourier conjugate of Cartesian image space (x,y,z), and the trajectory by which k-space is sampled defines the imaging sequence.

In a general description **k** is a vector defined by,

$$\boldsymbol{k} = \int \gamma \boldsymbol{G}(t)dt \tag{1.26a}$$

where $\boldsymbol{G}(t) = G_x(t)\hat{\boldsymbol{x}} + G_y(t)\hat{\boldsymbol{y}} + G_z(t)\hat{\boldsymbol{z}}$, with $G_\alpha = \frac{dB_z}{d\alpha}$ for α = x, y or z.

By taking the Fourier transform of k-space, proton density can be achieved,

$$FT[S(k)] = \int_{-\infty}^{\infty} S(k)e^{-ikx}dk \propto \rho(x) \tag{1.26b}$$

where ρ is the proton density.

Applying field gradients in the imaging plane encodes the spatial positions of signal as frequencies and phases. When the signal is acquired in the presence of a constant *x*-gradient, it samples k-space along a line in the k_x-direction. During frequency encoding, data points are recorded at regular intervals as k-space is swept, while during phase encoding the location in k-space is altered as instantaneous jumps in the sampled trajectory. Likewise all four quadrants of k-space need to be covered by the gradients, although theoretically only half of the *k*-space is necessary as the other half being the complex conjugate. Figures 1.21 and 1.22 shows a schematic diagram of k-space and k-space acquisitions.
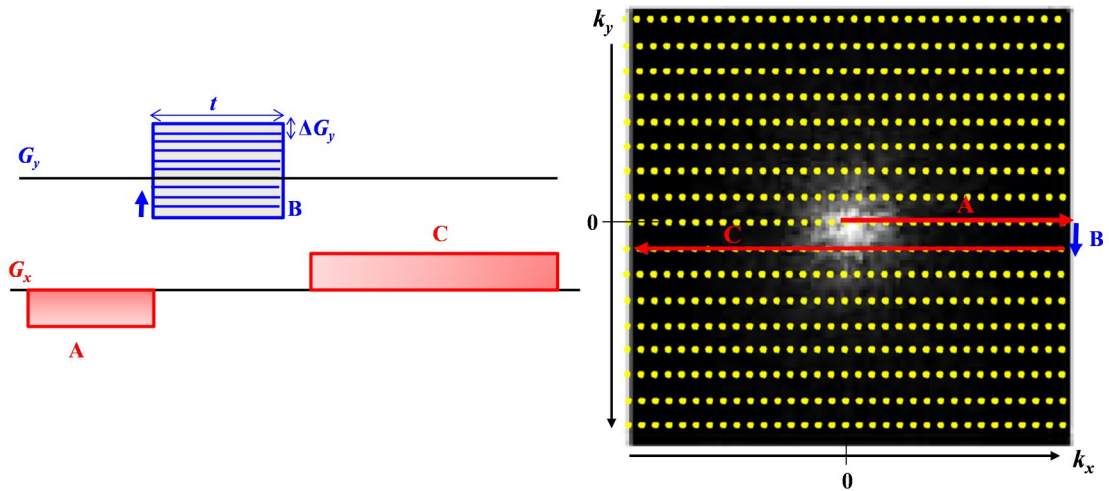
Figure: 1.21 *k-space sampling for frequency and phase encoding gradients, showing filling the k-space.*
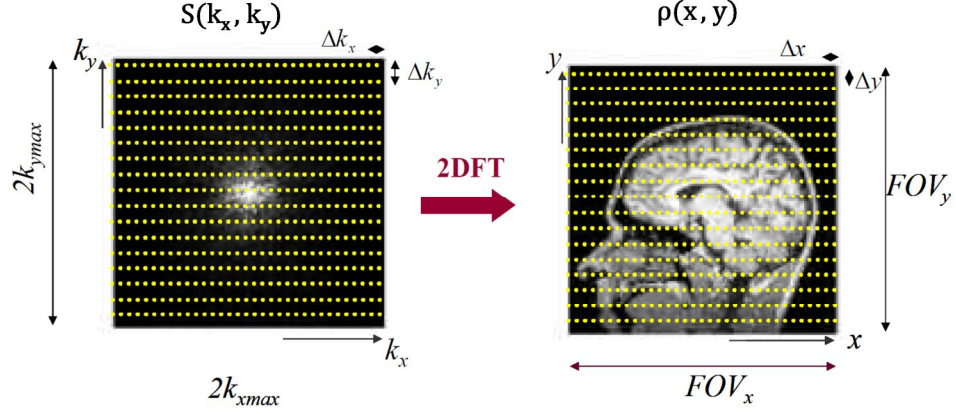
Figure 1.22 *The k-space matrix and image formation.*

From the Figure 1.22 the image FOV and spatial information are related as,

$$FOV_y = \frac{2\pi}{\Delta k_y} = \frac{2\pi}{\gamma \Delta G_y t}; \Delta y = \frac{\pi}{k_{y,max}} = \frac{2\pi}{\gamma \Delta G_y Nt}$$

$$FOV_x = \frac{2\pi}{\Delta k_x} = \frac{2\pi}{\gamma G_x T}; \Delta x = \frac{\pi}{k_{x,max}} = \frac{2\pi}{\gamma G_x T}$$

A large gradient-time product is needed for a higher spatial resolution and a large FOV requires small steps in k-space. The spatial distribution of the signal can be recovered by Fourier transformation of k-space. Thus the proton density of a sample is given by,

$$\rho(x,y) = \iint S(k_x, k_y)e^{-i(k_x x + k_y y)} \, dxdy$$

1.2.6 Parallel Imaging: SENSE

Acceleration of the k-space sampling can be achieved by the parallel imaging technique. It is based on the reconstruction of the images through multi coil arrays which improves the time efficiency of MR image acquisition. It can be obtained by using two adjacent coil elements in an RF receive array with non-overlapping sensitivity profiles, each of which detects the MR signals from only one half of the full FOV, thus providing same spatial information and hence reducing the total scan time. The number of phase encoding steps and thus the acquisition time can be further decreased if receive arrays with more than two coils are used.

In sensitivity encoding (SENSE), the spatial dependence of receiver coil array field B_1 is used to either remove or prevent the aliasing. With the SENSE technique the scan time is reduced by spreading the phase encoded k-space lines by the acceleration factor or SENSE factor. The FOV of the reconstructed image is therefore reduced by the same factor. With SENSE the individual receive coil k-space data sets are

separately Fourier transformed, resulting in aliased images. The aliased images are then combined using weights constructed from the sensitivities to give a single final image with the aliasing artefacts removed. However, SENSE always decreases the SNR because of the scan time reduction and sensitivity of the RF coils.

1.2.7 Image characteristics

For any given type of imaging sequence, there are many different parameters under the user's control, and these provide much of the versatility of MR imaging. The timing parameters and flip angle governs the signal contrast, the spatial parameters determine the resolution, and the number of signal averages affects the overall signal to noise ratio. An MR image is digital and consists of a matrix of pixels or picture elements. A matrix is a two dimensional grid of rows and columns and each element is a pixel which corresponds to a signal intensity. Each pixel of an MR image provides information on a corresponding three dimensional volume element termed a voxel.

Spatial resolution: The spatial resolution depends on the field of view (FOV) pixel size, slice thickness, the gradient field strength and the sampling bandwidth and image matrix. The slice thickness is controlled by the amplitude of the slice select gradient. FOV cannot be reduced arbitrarily to improve the resolution, because the tissue extending outside the FOV will create wraparound artefacts in the phase encoding direction.

Signal to noise ratio: Mathematically in the MR images the signal to noise ratio (SNR) is the quotient of the signal intensity of a region of interest (ROI) and standard deviation of the signal intensity of the region outside the anatomy i.e. region from which no tissue signal is obtained. The SNR of the MR images depends on a number of variables generally expressed as,

$$SNR \propto I \times voxel_{x,y,z} \times \frac{\sqrt{NEX}}{\sqrt{BW}} \times QF \times B_0$$

where *I* is the intrinsic signal intensity based on transverse magnetization created by the pulse sequence; $voxel_{x,y,z}$ is the voxel volume determined by the FOV, image matrix and slice thickness; *NEX* stands for the number of excitations, and repeats of signal acquisition; *BW* is the frequency bandwidth of RF to which the transmitter/receiver is tuned; *QF* is the coil quality factor parameter that indicates RF

coil sensitivity to induced currents in response to signals emanating from the subject; B_0 is the strength of main magnetic field.

Furthermore, there are other factors that can cause noise in MR images, for example, inhomogeneities in the magnetic field; thermal noise from RF coils; nonlinearity of amplifiers; factors associated with image processing; patient related factors such as movement etc. Thus optimization of the MR imaging sequence is required depending on the parameter to be studied.

1.2.8 Image contrast

Contrast in an image is proportional to the difference in signal intensity between adjacent pixels in the image, corresponding to two different voxels in the subject. The tissue parameters to which the MRI signal is sensitive are known as endogenous sources of contrast.

T_1 weighting:

T_1 weighted images produce contrast chiefly based on the T_1 characteristics of tissues by de-emphasizing T_2 contributions. This is generally achieved with the use of a relatively short TR to maximize the differences in longitudinal magnetization during the return to equilibrium, and a short TE to minimize T_2 dependency during the signal acquisition. The amount of transverse magnetization which gives rise to measurable signal after the 90^0 pulse depends on the amount of longitudinal recovery that has occurred in the tissue. Fat with a short T_1, has higher signal because the short T_1 value allows rapid recovery to the equilibrium magnetization. White and grey matter have intermediate T_1 values, and CSF has long T_1 thus corresponding signals are low. A short TE preserves the T_1 signal differences with minimal transverse decay, which reduces T_2 effects.

Proton density weighting:

Image contrast with proton density weighting relies mainly on differences in the number of magnetisable protons per volume of tissue. At thermal equilibrium, tissues with a greater spin density exhibit a larger longitudinal magnetization. Tissues such as lipids and fats have a high proton density compared with proteinaceous soft tissues; aqueous tissues such as CSF also have a relatively high proton density. To minimize the effects of T_1 differences a relatively long TR is required, and to minimize the T_2

influences a short TE is used. In the proton density images signal amplitudes are, CSF > fat > grey matter > white matter.

T$_2$ weighting:

T$_2$ characteristics of a tissue depend on how fast the protons in that tissue dephase, if they dephase rapidly T$_2$ will be short and vice versa. The T$_2$ weighted signal is usually acquired with a long TR and long TE. Compared with T$_1$ weighted image, it greatly shows reverse tissue contrast, where CSF becomes brighter than fat. As TE increases tissues with long T$_2$ maintain transverse magnetization longer than short T$_2$ tissues, and thus result in higher contrast.

Flow:

Flow, like any movement in MRI, is at the origin of spatial encoding perturbations and artifacts. Moving fluid has an appearance in studied MR images that depends on many factors, including flow velocity, vessel orientation, laminar versus turbulent flow, etc. Flow generally leads to enhancement of the MRI signal from the blood. This MRI sensitivity was used to develop vascular imaging using the physical modifications linked to flow named as: time-of-flight angiography (TOF), phase contrast angiography (PCA) and contrast-enhanced angiography.

The TOF angiography using a gradient echo sequence with high flip angle and short TR, the magnetization of the stationary spins is thus saturated, without affecting the signal from fresh spins flowing into the imaging slice. The PCA relies on dephasing the moving spins by bipolar gradient. For a bipolar gradient of a given intensity and time, the moving spins will dephase in proportion to their velocity thus producing signal intesntiy differences, schematically shown in Figure 1.23. The contrast enhanced angiography exploits relaxivity properties of contrast agents to visualize vascular structures.
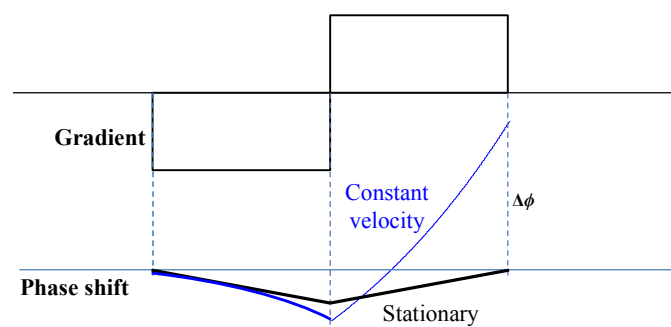
Figure 1.23 *Schematic sequence for flow imaging, showing phase shift Δϕ.*

Diffusion:

Diffusion of spins refers to the random motion of molecules associated with their thermal energy. Diffusion can be mapped using a pulse sequence that incorporates diffusion gradients between (90^0 and 180^0) RF excitations and data acquisition. Changes and directionality of diffusivities within the tissue can be signatures of restriction structures and tracts of water molecules. Figure 1.24 shows a schematic sequence for diffusion imaging.
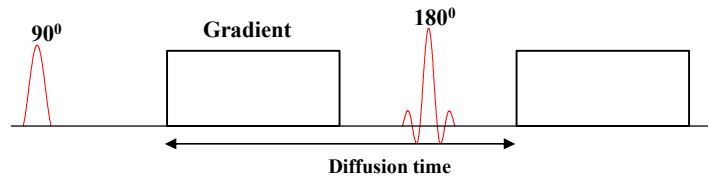
Figure 1.24 *Schematic sequence for diffusion imaging.*

Magnetization transfer:

Magnetization transfer is another endogenous contrast mechanism, it refers to the exchange of longitudinal magnetization between the protons in water and those in macromolecules, such as proteins. Protons in the macromolecules do not contribute directly to the MR signal because their T_2 times are too short. However, they can alter the signal amplitude indirectly via magnetization transfer. One of the ways to observe this effect is by applying strong preparatory off resonance RF pulse, and saturating the macromolecular protons without affecting the water protons. This saturation can be transferred to water molecules to attenuate the water signal. Figure 1.25 shows a schematic diagram of magnetization transfer imaging.
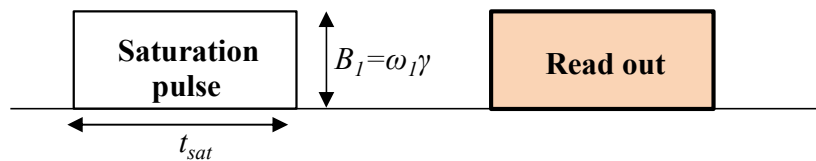
Figure 1.25 *Schematic sequence for magnetization transfer imaging. A rectangular saturation pulse of width t_{sat}, frequency offset $\Delta\omega$ and amplitude B_1 applied to saturate the bound macromolecules longitudinal magnetization and followed by readout of the signal.*

Exogenous contrast agents:

Further scope for modifying signal contrast in MRI is provided by the use of exogenous contrast materials. MR contrast agents do not contribute to the signal directly; rather, they alter the signal of surrounding water protons relaxation rates.

Clinically relevant contrast such as intravascular blood pool agent gadolinium-DTPA modifies the relaxation of protons in the blood.

1.2.9 Imaging pulse sequences

In NMR and MRI experiments, the RF signal is measured by the emf induced in the receiver coil by rotating transverse magnetization. The excitation and preparation of the spin system requires repeated RF pulses co-ordinated with magnetic field gradients. The entire process is known as a pulse sequence. Pulse sequences can be tailored by changing the timing, order, polarity and repetition frequency of RF pulse and gradients, that can help to provide the contrast developed by the spin density, T_1, T_2 leading to exquisite versatility of MR images. To improve shortening of measurement time and tissue contrast a great number of imaging sequences have been developed in recent years, each of which are utilized in research and routine clinical applications. The following paragraphs provide a brief overview of sequences applied in this thesis.

MR imaging sequences are generally based either on a spin echo (SE) or a gradient echo (GE). The SE image contrast depends on the tissue specific transverse relaxation time T_2 (discussed in Section 1.1.9), whereas GE image contrast is a function of the transverse relaxation time T_2^*. Within the SE and GE sequences the contrast can be manipulated by preparing the longitudinal magnetization prior to starting the imaging sequence.

1.2.9.1 Gradient echo (GE)

The gradient echo (GE) pulse sequence uses a magnetic field gradient instead of the 180^0 RF pulse to form an echo. The magnetic field gradient changes the local magnetic field to slightly higher and slightly lower strength across the bore of the magnet and therefore causes the proton frequencies under its influence to precess at slightly higher or lower frequencies along the direction of the applied gradient. Therefore for an FID signal generated under a linear gradient, the transverse magnetization dephases rapidly as the gradient is continually applied. If the gradient polarity is reversed after a predetermined time, the spins will rephase and produce a gradient echo. Figure 1.26 shows a schematic diagram of gradient echo sequence.
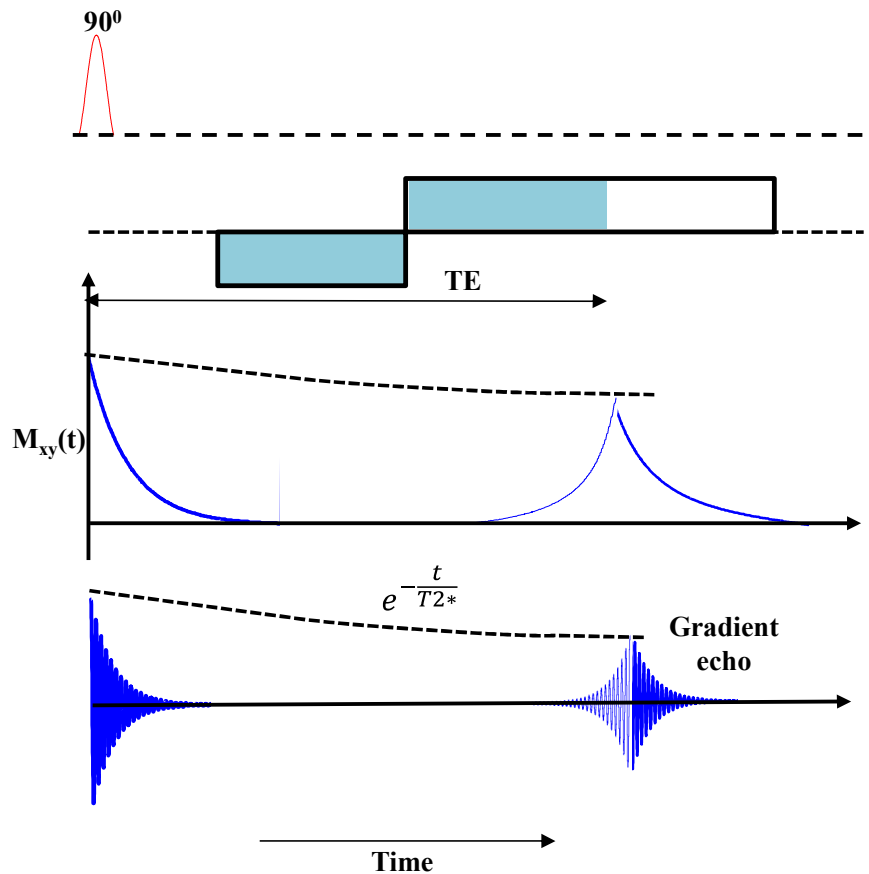
Figure 1.26 *Gradient echo sequence, showing the transverse magnetization and echo formation followed by the RF pulse.*

The peak of gradient echo occurs when the integral under the gradient waveform is zero. Thus the GE provides purposeful dephasing and rephasing of the FID. In a GE sequence the magnetic field inhomogeneities and tissue susceptibilities are emphasized, and the signal depends on T_2^*. The term TE is used in the context of GE sequence to denote the interval between RF excitation and the centre of gradient echo. TE can be controlled either by inserting a time delay between negative and positive gradients or by changing the amplitude of the reversed gradient, thereby changing the time for the rephasing process to occur.

1.2.9.2 Turbo spin echo: Fast spin echo

A turbo spin echo (TSE) sequence also called fast spin echo (FSE), uses multiple phase encode steps in conjunction with multiple 180^0 refocusing pulses per TR interval to produce an echo train. Each echo experiences differing amounts of phase encoding that correspond to different lines in the *k*-space. The number of refocusing pulses applied after the excitation pulse is called the echo train length (ETL), it is also

known as turbo factor by which the total scan time can be reduced compared to a conventional spin echo which allows higher resolution images to be acquired. TSE sequences are mainly used for the acquisition of T2 weighted images. Figure 1.27 shows schematic diagram of TSE sequence.
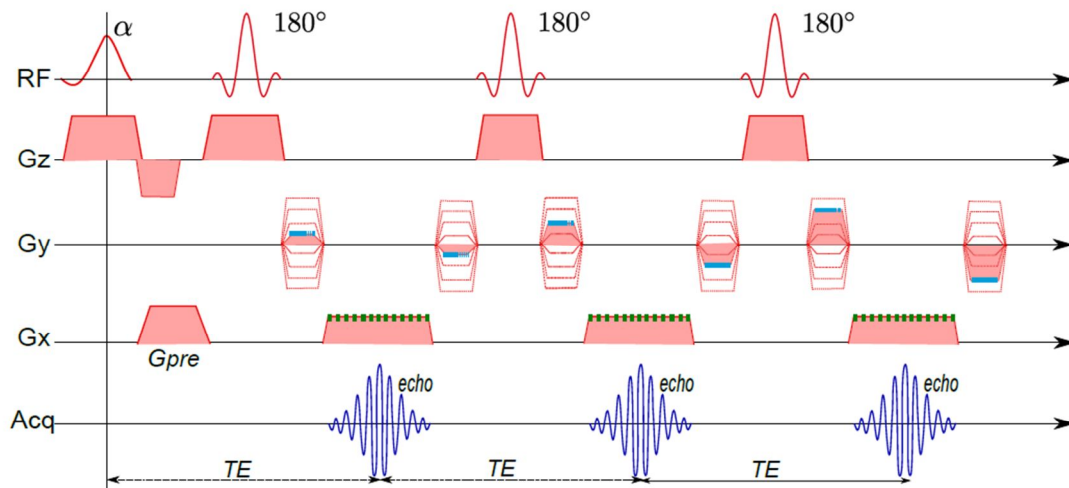
Figure 1.27 *Schematic diagram of the turbo spin echo sequence. The diagram shows the evolution of signal with RF pulses and gradients.*

1.2.10 Echo planar imaging

Echo planar imaging (EPI), proposed by Mansfield in 1977, is a much faster imaging technique, which aims at generating a series of spin or gradient echoes with different phase encoding in the short period of time after a single excitation of the spin system by an RF pulse.

In the EPI sequence, image acquisition typically begins with a standard 90^0 flip, negative lobes of the phase encoding and frequency encoding gradients then cause a phase evolution that moves the spin system to the periphery of the k-space. The frequency encoding gradient or read out gradient is then rapidly switched between maximum positive and negative amplitude, repeatedly refocusing the transverse magnetization to yield a train of gradient echoes while sweeping across k_x in alternate directions. Alternating k-space lines (echoes) are traversed in opposite directions of the readout gradient, therefore every other line has to be time-reversed before Fourier transform is applied to generate an image. The effective echo time TE occurs when the maximum amplitude of the echoes occurs. In the EPI technique acquisition of the data must proceed in a period less than T2* (around 25 to 50ms), a schematic EPI

41

sequence based on gradient echo shown in Figure 1.28. EPI is good for a quantification study is the and most commonly used dynamic sequence.
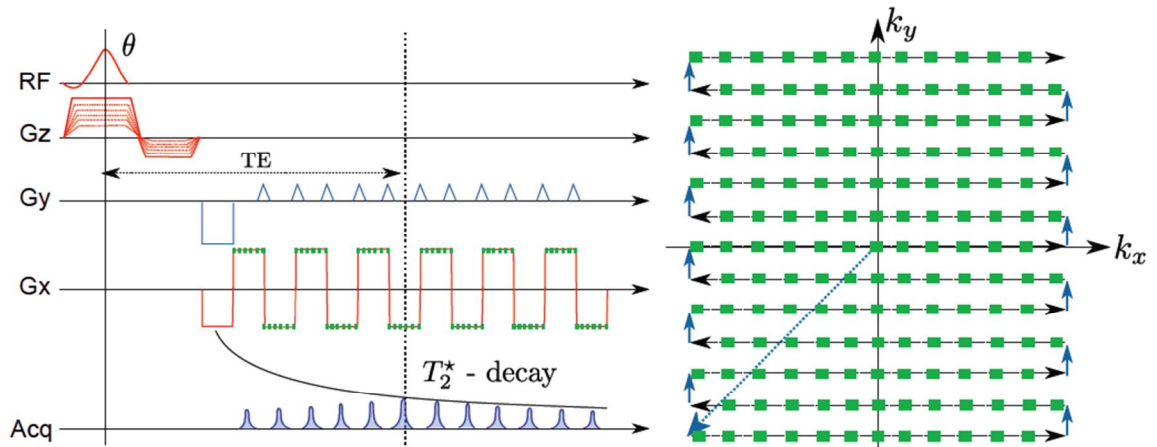
Figure 1.28 *Schematic diagram of the echo planar imaging and k-space trajectory. The repeatedly reversing readout gradients and blipped phase encoding gradients forms a series of echoes.*

The sensitivity of EPI sequence images can be increased with high field strength scanners, however, the implementation of EPI in the high magnetic field gives rise to a number of challenges. In EPI, the acquisition time for a given spatial resolution is proportional to the field of view in the phase encoding direction and thus to the number of k-space lines. Shortening of T2 and T2* poses a limit on the number of k-space lines that can be acquired after excitation, as it is not possible to sample the entire k-space with a long echo train length and retain a good TE. Higher resolution also puts demands on the gradients and due to the use of high slew rates can cause peripheral nerve stimulation (PNS) in the subject.

Inhomogeneities of the $\mathbf{B}_0$ field due to poor shimming and susceptibility effects influence the evolution of the phase during the echo train, affecting EPI severely. Local field inhomogeneities and chemical shifts, results geometric distortions and phase variations that accumulates along the phase encode direction and can cause substantial displacement of the signal during EPI. Imperfections in the gradient coils or eddy currents cause a slight offset between lines collected in the positive and negative directions, leading to a Nyquist ghosting artefact in the reconstructed image.

1.2.11 Artefacts

In MRI, artefacts manifest as positive or negative signal intensities that do not accurately represent the imaged subject. Although some artefacts are relatively

insignificant and easily identified, others can limit the diagnostic potential of the exam by obscuring the images. An overview of MRI artefacts is discussed below.

Motion artefacts:

The most ubiquitous and noticeable artefacts in MRI arise with patient motion, that includes voluntary and involuntary movement and flow (blood, CSF). The long acquisition time of certain MRI sequences increases the probability of motion blurring and contrast resolution losses. Motion artefacts mostly occur along the phase encode direction, since the phase encoding lines are separated by a TR interval that can last for 3 seconds or longer. Thus even very slight motion will cause a change in the recorded phase variation across the FOV throughout the acquisition. The frequency encode direction is less affected especially by periodic motion, since the evolution of the echo signal, frequency encoding, and sampling occur simultaneously over several milliseconds. There are several techniques for motion artefact corrections, such as,

-cardiac and respiratory gating

-signal averaging to reduce artefacts of random motion

-short TE that limits phase evaluation during the readout

-gradient moment nulling by additional gradient pulses for flow compensation

-presaturation pulses applied outside the imaging region to suppress flowing blood

Machine dependent artefacts:

Magnetic field inhomogeneities are either global or local field perturbations that lead to the mismapping of tissues within the image, and can cause more rapid $T2^*$ relaxation. Automatic shimming helps to reduce the magnetic field inhomogeneities.

Water fat shift:

The water-fat shift arises due to the chemical shift of fat with respect to water occurs in measurement direction, and it depends on the frequency bandwidth of the measurement gradient. The higher the bandwidth the smaller the WFS and lowers the SNR. WFS is field strength dependent, larger field strength will result in larger WFS.

Fat suppression: STIR

STIR: The Short tau inversion recovery (STIR) pulse sequence uses a very short TI for magnitude signal acquisition. As the inversion recovery (IR) sequence based on recovery from the transverse magnetization, it is possible to separate specific tissues (such as fat) by varying inversion time (TI). When the signal from the target tissue

passes the null point the 90^0 pulse is applied to create the echo of the whole spin system, while no signal from the target tissue.

Partial volume artefacts:

The finite resolution of the imaging device generally results in a single voxel representing more than one tissue type, this is known as the partial volume effect (PVE). Partial volume artefacts arise from the finite size of the voxel over which the signal is averaged. This results in a loss of detail and spatial resolution. Reduction of partial volume artefacts can be undertaken by using a smaller pixel size and/or a smaller slice thickness.

1.2.12 Instrumentation

The MRI scanner is composed of multitude of components, the main magnet, the gradient coils, the RF system, the console controlling the scanner and different electronics parts. This section provides a brief discussion of the MRI instruments.

Main magnet: The central component of an MR scanner is the main magnet which produces the $\mathbf{B}_0$ field. The high magnetic field is usually produced by an electromagnet made from coils of niobium-titanium (Nb_3Ti) wire, which become superconducting at about 10K (-263^0C). To produce such a low temperature, a bath of liquid helium is used to keep the wires superconducting. Active or passive shielding also surrounds the magnet in order to reduce the fringe of the magnetic field at the edge of the magnet.

Shim coils: Homogeneity of the $\mathbf{B}_0$ field is very important in minimizing the spin dephasing. Susceptibility differences within the sample itself also introduce spatial variations, so that the field needs to be shimmed dynamically at the beginning of each scan session. The MR scanner incorporates shim coils that produce compensatory magnetic fields to correct for spatial variations in the main magnetic field. This is done to ensure that the generated magnetic field is homogeneous enough for imaging purposes.

Gradient coils: An MR scanner contains three orthogonal gradient coils, which produce magnetic fields that vary linearly in strength along each direction. The gradient coils are generally placed inside the shim coils and deliberately alter the magnetic field when energized in order to localize the MR signal. They can be used in combination to produce magnetic field gradients in any direction, and allow images to be acquired in arbitrary planes. For this thesis data acquired from the Philips 3.0T

Achieva scanner, Philips Medical Systems, Best, the Netherlands; the scanner is set up with three fully independent gradient axes for orthogonal, oblique and double-oblique imaging with maximum amplitude 40 mT/m, maximum slew rate 120 mT/m/ms, minimum imaging rise time 0.33 ms, these are non-resonant, actively shielded and 100% duty cycle gradients.

RF coils: The MR scanner includes RF transmitter and related circuitry to produce the B_1 field for excitation. It also incorporates receiver coils and the data acquisition system for signal emitted by the excited protons. RF coils are produced in a variety of geometries and generally classified as volume or surface coils. To maximize SNR, the coil should match the size and shape of the anatomy, otherwise noise from the outside tissue will be included. The coil must also be resonant at the Larmor frequency, which depends on both the field strength and nucleus under study. The Philips 3.0T Achieva scanner RF performances: nominal frequency 127.73MHz, maximu frequency offset 415 kHz, transmitter/ reciver coils.

1.2.13 Safety

Although ionizing radiation is not used with MRI, there are important safety considerations. These include the presence of high magnetic field, RF energy, time varying magnetic gradient fields, cryogenic liquids, a confined imaging space (claustrophobia), and noisy operation due to gradient coil activation and deactivation. Patients with implants, prostheses, aneurysm clips, pace makers, heart valve, etc. should be aware of such high magnetic fields which can cause serious adverse effects. Even non-metallic implant materials can lead to heating in RF fields. Ferromagnetic objects can turn into potentially lethal projectiles in the magnetic field of scanner. The long term biologic effects of high magnetic field strengths are not well known. The most common bio-effect of MR system is the tissue heating caused by RF energy deposition and stimulation by rapid switching of high strength gradients. The dosimetric term used to describe the absorption of RF radiation is the specific absorption rate (SAR), a mass normalized rate at which RF power is coupled to biologic tissue and typically indicated in units of watts per kilogram. Special care is necessary with the use of additional hardware positioned close to the subject, as cables presented in the RF field can create skin burn.

Having introduced the basics principles of nuclear magnetic resonance and MR imaging principles in this chapter, the next chapter will briefly discuss the overview of human nervous system, brachial plexus and related neuropathies.

References:

Bernstein, M. A., K. F. King and X. J. Zhou (2004). Handbook of MRI pulse sequences, Elsevier.

Brown, M. A. and R. C. Semelka MRI: basic principles and applications, John Wiley & Sons.

Callaghan, P. T. (1993). Principles of nuclear magnetic resonance microscopy, Oxford University Press.

Haacke, E. M., R. Brown, M. Thompson and R. Venkatesan "Magnetic resonance imaging: physical principles and sequence design. 1999." New York: A John Wiley and Sons.

Haacke, E. M., R. W. Brown, M. R. Thompson and R. Venkatesan (1999). Magnetic resonance imaging, Wiley-Liss New York:.

Hashemi, R. H., W. G. Bradley and C. J. Lisanti MRI: the basics, Lippincott Williams & Wilkins.

McRobbie, D. W. (2007). MRI from Picture to Proton, Cambridge University Press.

Morris, P. G. (1986). "Nuclear magnetic resonance imaging in medicine and biology."

Chapter 2
Overview of Human Nervous system

The human nervous system is the most complex physical system known to mankind; it consists of many billions of interactive units whose constantly changing patterns of activity are reflected in every aspect of human behavior and experience. This chapter describes a brief overview of the human nervous system.

2.1 Basic unit of the nervous system-Neuron

The functional unit of the nervous system is the neuron, a term coined by Waldeyer in 1891. Neurons are the excitable cells of nervous tissue which conduct impulses. A nerve that is commonly understood is in fact a bundle containing tens of thousands of fine nerve fibres or neurons having diameters between 1 and 20 μm (1 μm = 1 millionth of a meter). Neurons can encode information, conduct it and then transmit it to other neurons or to various non-neural cells. The movement of such information within the nervous system depends on the rapid conduction of minute transient electrochemical fluctuations along the neural surface membrane. Neurons exist in huge populations, estimated at more than 10^{12} within the brain; the sum of total synapses (connections) within the nervous system is, therefore, truly astronomical.

Most neurons have a rounded central mass of cytoplasm enclosing the cell's nucleus (the cell body or soma), one or more 'input' fibres called dendrites, and a long transmitting fibre called an axon. The portion of the axon immediately adjacent to the cell body is called the axon hillock. This is the point at which action potentials are usually generated. Certain types of neurons have axons or dendrites coated with a fatty insulating substance called myelin. The myelin sheath is a lipid protein structure (70~80% lipid and 30~20% protein) and the fibre is said to be myelinated. In some cases, the myelin sheath is interrupted at rather regular intervals by the nodes of Ranvier. The myelin sheath helps to speed up the transmission of information along the nerves. Outside the central nervous system, another insulating layer, sometimes called neurilemma, surrounds the myelin sheath. This layer is thinner than the myelin sheath and continuous over the nodes of Ranvier. Figure 2.1 shows a schematic diagram of a neuron cell.

In a nerve, the nerve fibres are surrounded by the endoneurium, which consists of loose connective tissue. Then multiple nerve fibres are enclosed in robust connective tissue, the perineurium, to form a nerve fascicle, and all nerve fascicles are surrounded by the epineurium. Thus, overall, nerves consist of major tissue

components nerve fibres, Schwann cells, myelin layers, and the connective tissues (endoneurium, perineurium, and epineurium) of collagen fibrils shown in figure 2.2 and 2.3.
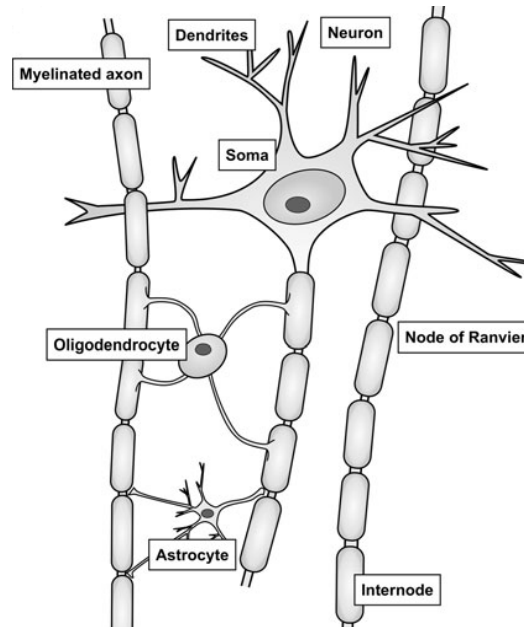
Figure: 2.1 *Schematic diagram of neuron cell.*
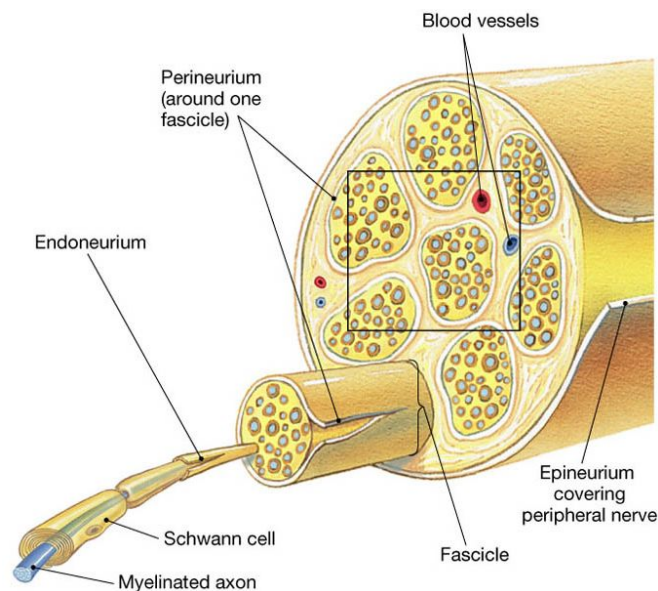
Figure 2.2 *Schematic drawing of nerve anatomy. The fibres surrounded by epineurium, each fascicle enclosed by dense perineurium and contain myelinated and unmyelinated axons supported by endoneurium connective tissues* (Adapted from http://bmc.erin.utoronto.ca/).
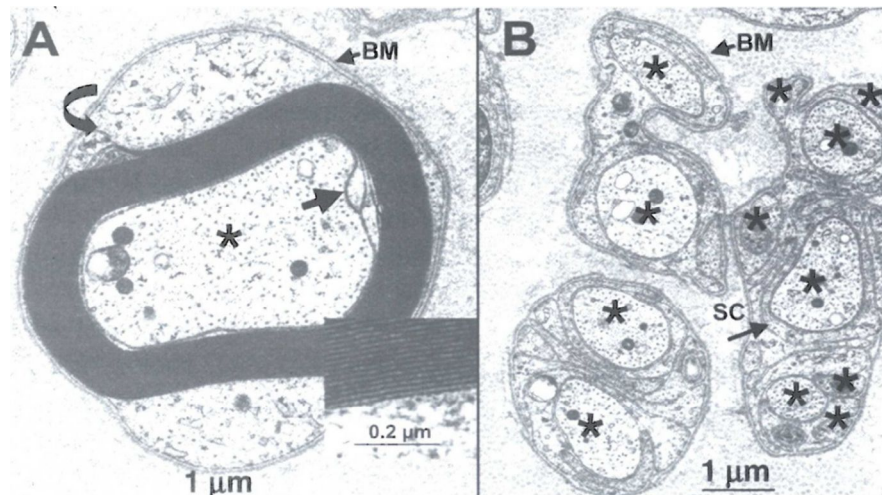
Figure 2.3 *Myelinated and unmyelinated fibres from a nerve. A single axon is surrounded by compact myelin lamellae (A); several axons are surrounded by Schwann cell in unmyeniated fibres (B)(Kimura 2013).*

2.2 Types of neurons

The neurons are classified according to a number of different criteria such as morphology or appearance, anatomical location, whether they are sensory or motor, conduction velocity and fibre diameter, and myelination. According to morphology neurons are classified as monopolar, bipolar and multipolar according to whether the soma has one, two or many extensions respectively, as shown in figure 2.4.

Monopolar neurons have only one prominent dendrite extending from the soma, which then branches into two long processes, one central (directed toward the CNS) and one peripheral (directed away from the CNS). Most neurons of this type are sensory and are exclusively located in the peripheral nervous system. The dorsal root ganglion cells of the spinal nerves are monopolar neurons. They relay information from receptors sensitive to touch, pressure, pain, temperature, and stretch, as well as body position and movement. Bipolar neurons have two prominent dendrites extending from the soma. One conducts impulses toward and one away from the soma. Bipolar neurons are found in the retina, the cochlear and vestibular ganglia, the olfactory epithelium, and in some parts of the central nervous system.

Multipolar neurons are the most common type of neuron. They populate both the central and peripheral nervous systems and are characterized by several short, highly branched processes called dendrites and a single, long process extending out from the

soma. A slight enlargement at the point where the axon leaves the soma, called the axon hillock is often observed.
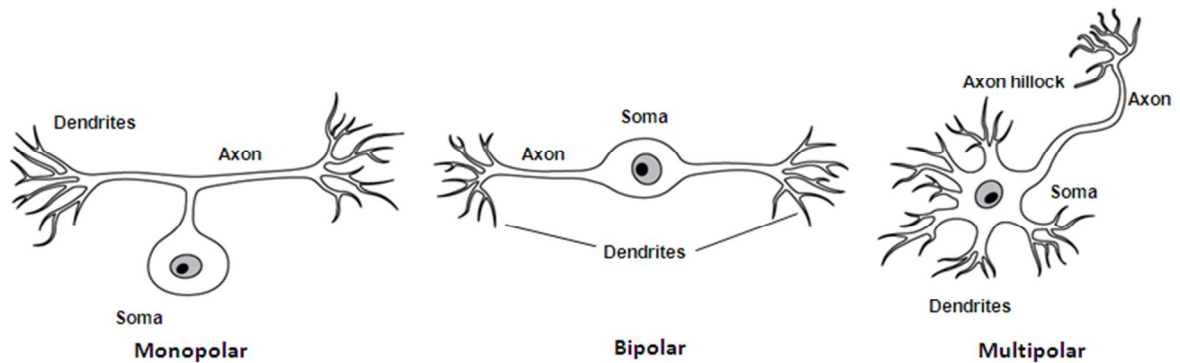
Figure 2.4 *Different types of neurons show the monopolar, bipolar and multipolar neurons.*

According to functional arrangement, a neuron is 'afferent' to a particular site if it conducts impulses towards it and 'efferent' if it conducts the impulses away. For example, a neuron, which conducts impulses from the thalamus to the cerebral cortex, is efferent from the thalamus and afferent to the cerebral cortex. An efferent neuron which directly innervates a muscle or a gland and causes it to respond, is called a 'motor neuron'. An afferent neuron, which responds to changes in the external or internal environment and gives rise to conscious sensation is termed a 'sensory neuron'.

The sensory or afferent neurons are able to detect a wide range of signal forms, such as mechanical, chemical, thermal and electrical. Sensory neurons conduct impulses from a sense organ to the cell body of the neuron and the axon conducts impulses from the cell body to the central nervous system. The motor or efferent neurons send signals from the central nervous system to the effector organs chiefly muscles and glands. The cell body of a motor neuron is embedded in the central nervous system. This collects impulses from other neurons through its dendrites. A long, single axon carries these impulses from the cell body to a muscle fibre or a gland. Figure 2.5 shows a schematic arrangement of sensory and motor nerves.
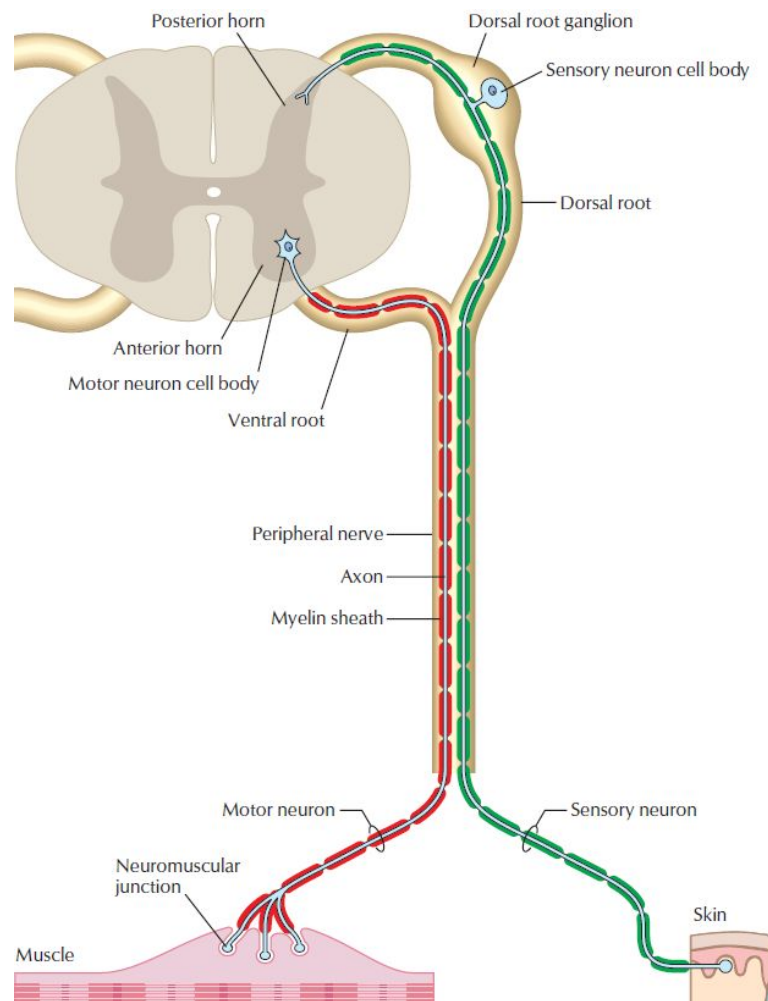
Figure 2.5 *Sensory and motor neurons (Frank 2002).*

The nerve fibre or axon may be myelinated or unmyelinated. The myelinated fibres are wrapped around by Schwann cells membranes, which form the myelin sheath.

From the previous considerations, it is clear that, within the class of either myelinated or unmyelinated fibres, diameter is the major determinant of the distribution of conduction velocity (DCV) of the nerve fibres. This relationship was predicted from theoretical considerations and has been confirmed by experimental observations. For myelinated fibres, conduction velocity has a linear relation with diameter, whereas for unmyelinated fibres the velocity has a square root relation with diameter (Krarup 2006, Levin 2006). Figure 2.6 shows a schematic diagram of relation between fibre diameter and conduction velocities.
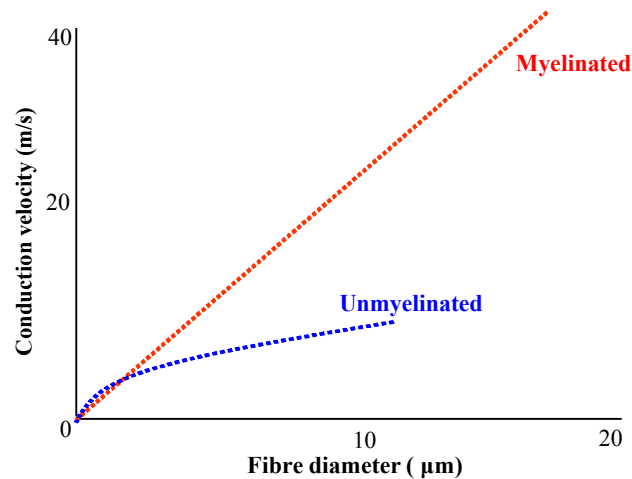
Figure2.6 *Schematic graph shows the conduction velocity changes with fibre diameter of the myelinated and unmyelinated nerves.*

For a normal human subject, the DCV has several peaks. Erlanger & Gasser (1937) in their original study on nerve diameter measurements divided the mammalian nerve fibres into A and C groups, further subdividing the A group into α, β, γ and δ fibres. According to the classifications type A fibres are the typical large and medium-sized myelinated fibres of spinal nerves and type C fibres are the small unmyelinated nerve fibres that conduct impulses at low velocities. The C fibres constitute more than one half of the sensory fibres in most peripheral nerves as well as all the postganglionic autonomic fibres. The initial peak in the DCV is referred to as the A-α and the subsequent peak called A-γ. This designation indicates the preganglionic fibres in nerves. Figure 2.7 shows a schematic diagram of DCV for myelinated nerves where the fibre diameter linearly varies with conduction velocities (CV).
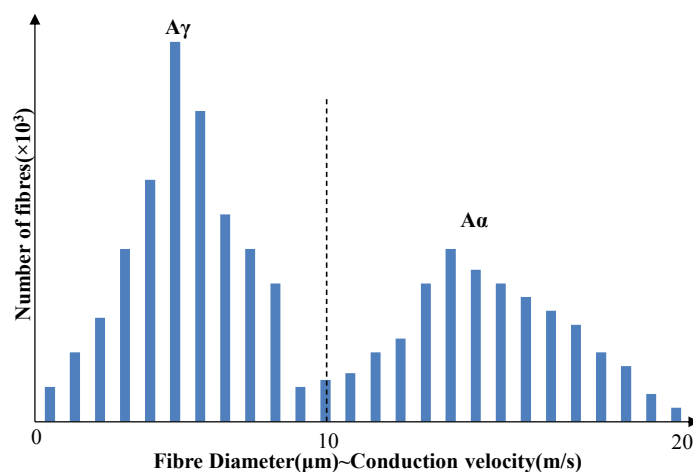
Figure 2.7 *Schematic diagram of distribution of conduction velocity (DCV) for myelinated nerve, where the fibre diameters are linearly proportional to the conduction velocities (CV).*

The sizes, velocities of conduction, and functions of the different nerve fibre types are shown in the Figure 2.8 below.
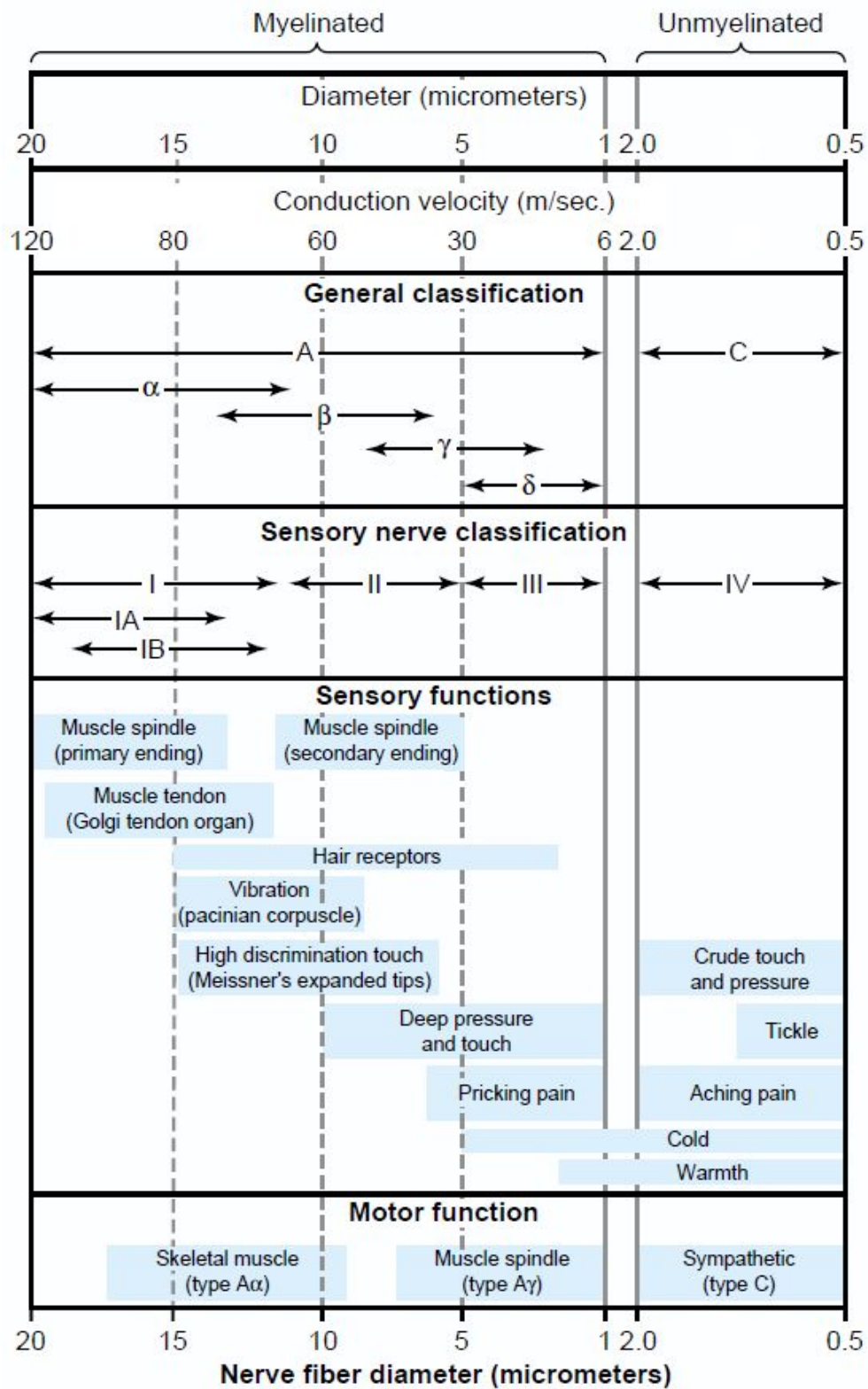
Figure 2.8 *Sensory and motor neuron classification (Guyton et al. 2008).*

2.3 Functionality of neuron

The neurons carry information to and from the brain through specified connections between neurons and muscles. Discussed briefly below:

Synapse: The interconnections between neurons are called synapses. All synapses occur at or near cell bodies. Neurons that synapse do not touch each other but do come into close proximity, so that the axon (output) of one nerve can activate the dendrite or cell body (input) of another by producing a chemical that stimulates the membrane of a dendrite cell body. In some cases, the chemical is produced by one axon, near another axon, to inhibit the second axon from activating a neuron with which it can normally communicate. The transmission across a synapse from axon to dendrite or cell body can take place in one direction only.

Muscle: Muscle cells are also known as *myocytes*. Myocytes differentiate along one of three main pathways to form skeletal, cardiac and smooth muscle. Both skeletal and cardiac muscle may be referred to as striated muscle, because these cells appeared as finely cross-striated. All skeletal muscles are made of numerous fibres ranging between 10 to 80 microns in diameter. Each of these fibres is made up of successively smaller sub units. In most muscles, the fibres extend the entire length of the muscle and except for about two percent of the fibres, each is innervated by only one nerve ending located near the middle of the fibre. Muscles are generally known as effectors. An effector is a structure, which responds directly or indirectly to a stimulus. Muscle nerves are frequently referred to as 'motor nerves', but they contain both motor and sensory components. The major motor component consists of the large myelinated axons that supply the muscle fibres; these α-efferents, or α-motor axons are among the fastest-conducting nerve fibre in the body. In human body, muscles works as effector and are controlled and responds when it receives impulses from efferent (motor) nerves.

Neuromuscular junction: Neuromuscular junction is a specialized synapse formed where the terminal branch of an α-motor axon contacts the muscle fibre, as shown in Figure 2.9. The axon terminal gives off several short, curling branches over an elliptical area, the *motor end plate*. The terminal branches of α-motor axons are normally in a 'one-to-one' relationship with their muscle fibres. When a motor neuron is excited, an action potential is propagated along the axon and its branches to all of the muscle fibres that it supplies. The motor neuron and the muscle fibres that it

innervates can therefore be regarded as a functional unit, the *motor unit*, which accounts for more or less simultaneous contraction of a number of fibres within the muscle.
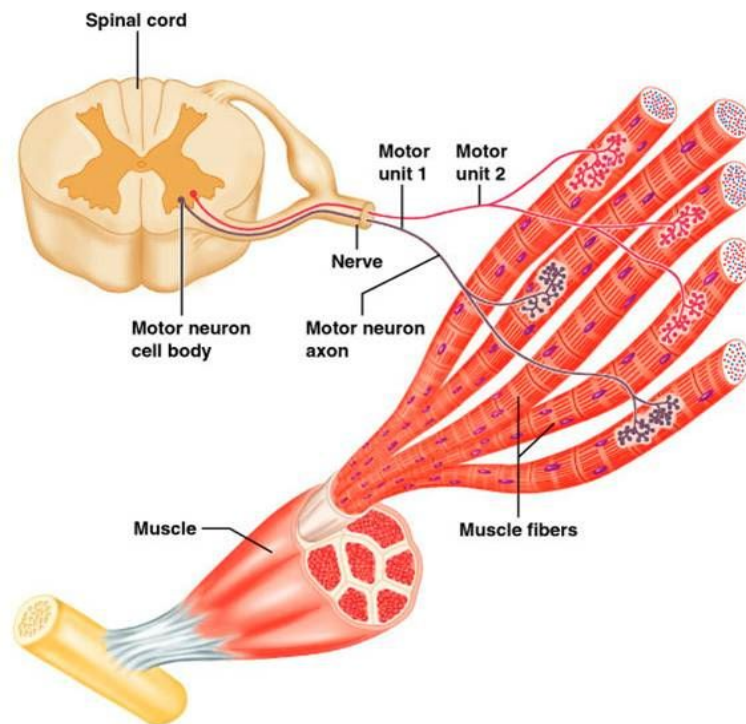
Figure 2.9 *Neuromuscular junction (Frank 2002).*

The arrival of an action potential at the motor end plate causes *acetylcholine* (ACh) to be released from the storage vesicles into the synaptic cleft that separates the nerve ending from the sacrolemma. This generates a local depolarization whose duration is self-limited by voltage limited conformational changes in the membrane. Because of the extended neuromuscular junction, the end plate potential is normally several times larger than is needed to initiate an action potential in the surrounding sacrolemma. This ensures that excitation is passed with high security to the muscle so that, except under conditions of extreme fatigue, a muscle action potential is generated for each nervous impulse.

2.4 Major divisions of the nervous system

The nervous system is divided into two major parts, the central nervous system (CNS), containing the great majority of neuronal cell bodies, and the peripheral nervous system (PNS), composed mainly of the axons of sensory and motor neurons

passing from the central nervous system into all parts of the body schematically shown in Figure 2.10.
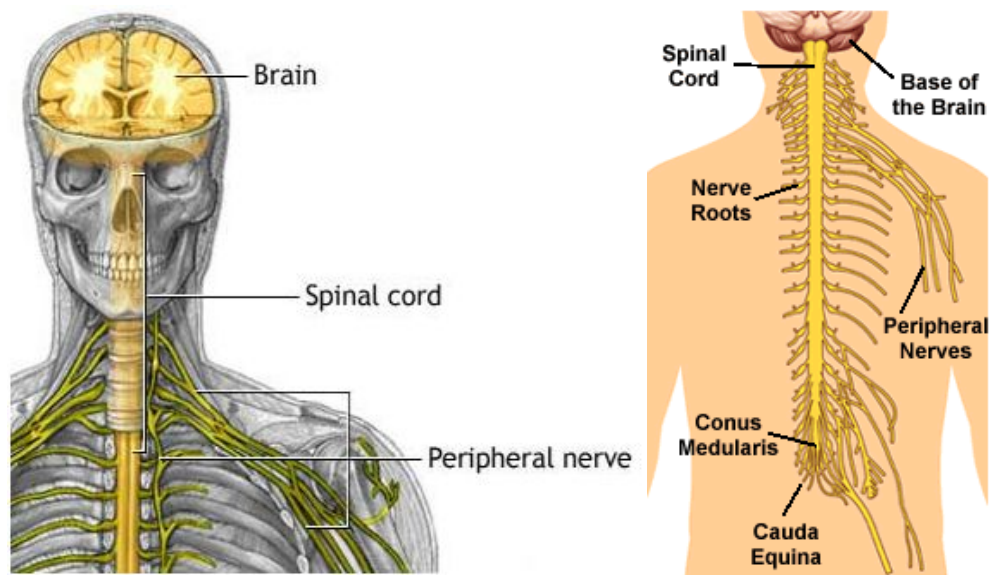
Figure 2.10 *Human central and peripheral nervous system (Greenstein et al. 2000, Standring 2008).*

2.4.1 Central Nervous System (CNS)

The *encephalon* or brain and *medulla spinalis* or spinal cord forms the central nervous system (CNS). The encephalon or brain lying wholly within the cranium is divided, for convenience, into regions, which are of considerable morphological and functional significance. Ascending in order from the spinal cord these are: the *rhombencephalon* or *hindbrain*, *mesencephalon* or *midbrain* and *prosencephalon* or *forebrain*.

The rhombencephalon includes the *myelencephalon* or *medulla oblongata*, *metencephalon* or *pons* and the *cerebellum*. The prosencephalon comprises the *diencephalon* (between brain) and the *telencephalon*. The former is the central connecting part, which includes the *thalamus* and *hypothalamus*; the latter is mainly composed of a left and right cerebral 'hemisphere' or *cerebrum*. The cerebrum occupies a major fraction of the brain's volume. The outer surface of the cerebrum is called the cerebral cortex. The corpus callosum is the interconnection between the left and right hemispheres of the brain. Structurally, the two hemispheres appear to be identical, but they seem to differ functionally in man. Midbrain, pons and medulla oblongata form the brainstem, connecting the forebrain and spinal cord. Behind the brainstem is the cerebellum. The cell bodies of neurons in the CNS are often grouped together in areas termed *nuclei*. Cell bodies and small fibres in fresh brain are grey in

color and are called *grey matter*, whereas the myelin coating of large fibres has a white appearance, so that a collection of these fibres is referred to as *white matter*.

2.4.2 Spinal cord

The spinal cord is elongated, approximately cylindrical in shape, occupying the superior two-thirds of the vertebral canal schematically shown in Figure 2.11. It is arbitrarily continuous with the medulla oblongata just below the foramen magnum. The anatomy of the spinal cord itself consists of millions of nerve fibres, which transmit electrical information to and from the limbs, trunk and organs of the body, back to and from the brain.

The spinal cord plays three important functions of the individual's sensation, autonomic and motor control. From the brain, the spinal cord descends down the middle of the back and is surrounded and protected by the bony vertebral column. The spinal cord is surrounded by a clear fluid called Cerebral Spinal Fluid (CSF), that acts as a cushion to protect the delicate nerve tissues against damage from banging against the inside of the vertebrae.
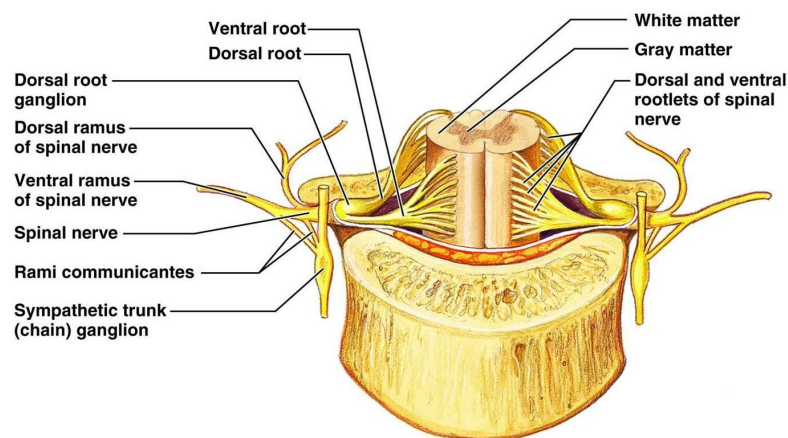
Figure 2.12 *Spinal cord cross section view (Standring 2008).*

The spinal cord grey matter is composed of largely nerve cell bodies, glial cells, and interneurons, with a characteristic butterfly-shape cross section at the centre of the cord and surrounded by the white matter. The spinal cord white matter is composed of millions of ascending and descending fibres. The ascending fibres conduct impulses up the cord while descending fibres conduct impulses downward. Most of these fibres have also been myelinated by oligodendrocytes that give the white matter its characteristic color.

Most of the spinal cord fibres are grouped together in functional units called 'ascending' and 'descending' tracts. Ascending tracts within the spinal cord carry sensory information from the body, upwards to the brain, such as touch, skin temperature, pain and joint position. Descending tracts within the spinal cord carry information from the brain downwards to initiate movement and control body functions.

2.4.3 Peripheral Nervous System (PNS)

The peripheral nervous system comprises the afferent or centripetal nerve fibres connecting receptors to the central nervous system and efferent, centrifugal nerve fibres connecting the central nervous system to the effector apparatus. These are grouped into 12 pairs of cranial nerves from the brain and 31 pairs of spinal nerves. The sympathetic trunks, ganglia and splanchnic nerves are also part of this system. The cell bodies of neurons in the PNS are often grouped together in areas termed *ganglia* (swellings). The ganglia are connected to each other to form a vertical sympathetic chain.

2.4.4 Spinal nerves

The spinal nerve has thirty-one pairs emerging through intervertebral foramina such as 8 cervical nerves "C"; 12 thoracic nerves "T"; 5 lumbar nerves "L"; 5 sacral nerves "S"; and 1 coccygeal schematically show in Figure 2.12. Each is continuous with the spinal cord by the ventral (anterior) roots and dorsal (posterior) roots; later they bear a spinal ganglion. Immediately distal to the spinal ganglia they divide into dorsal and ventral rami. At the central or distal end of the spinal nerves, the epineurium is continuous with the spinal cord dura matter. At the distal or peripheral end the epineurium is reduced in thickness, eventually incorporated into the perineurium.

The spinal ganglia are collections of nerve cells on the posterior roots of the spinal nerves. Just after exiting from the foramen the dorsal rami of spinal nerves divide into medial and lateral branches to supply the muscle and skin of the posterior regions of the neck and trunk. The ventral rami of the spinal nerves supply the limbs and the anterolateral aspects of the trunk. The cervical, lumber and sacral ventral rami connect

near their origin to form as Brachial plexus, Lumbar plexus and Sacral plexus respectively.
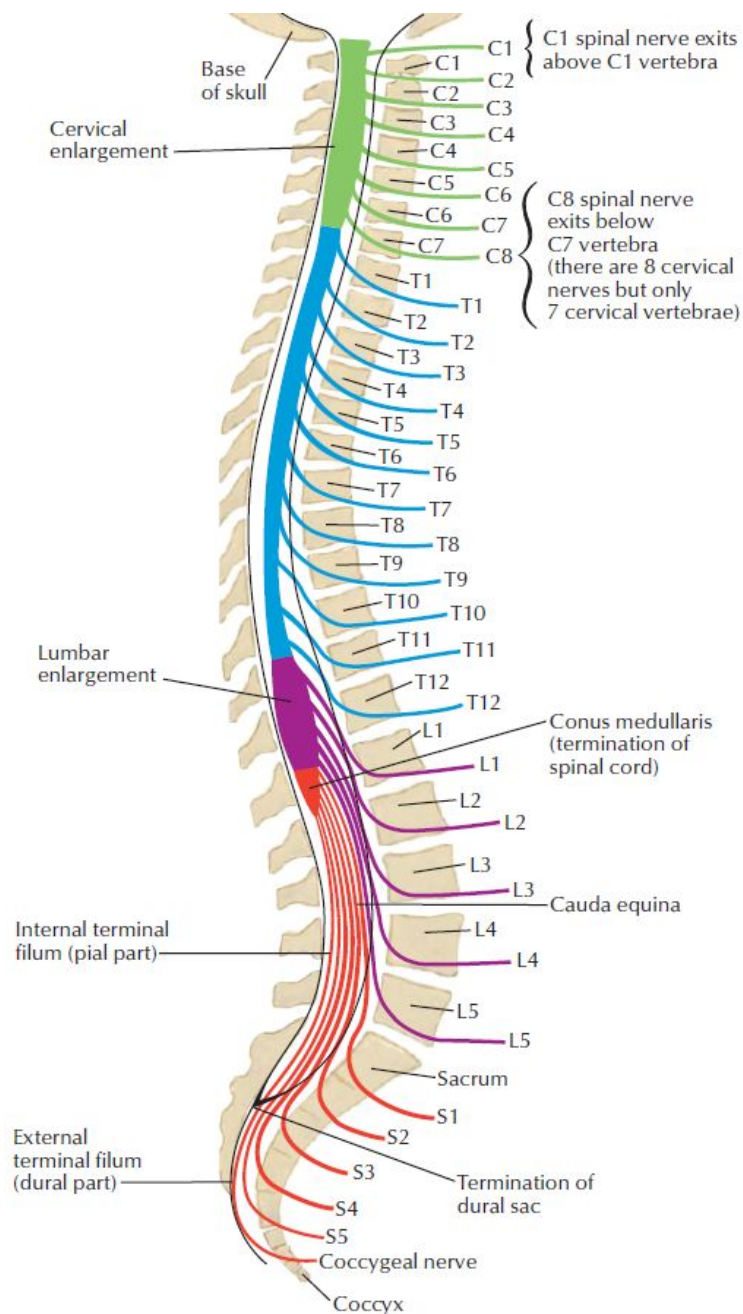
Figure 2.12 *Spinal nerves at different vertebral levels (Frank 2002).*

Median nerve

The median nerve arises from the roots C5, C6, C7, C8 and T1. In the hand, the median nerve supplies motor innervation to the 1st and 2nd lumbrical muscles. It also supplies the muscles of the thenar eminence by a recurrent thenar branch. The median

nerve innervates the skin of the palmar side of the thumb, the index and middle finger, half the ring finger, and the nail bed of these fingers. The lateral part of the palm is supplied by the palmar cutaneous branch of the median nerve, which leaves the nerve proximal to the wrist creases. This palmar cutaneous branch travels in a separate fascial groove adjacent to the flexor carpi radialis and then superficial to the flexor retinaculum.

Ulnar nerve

The ulnar nerve arises from the roots C8, T1 but it often receives fibres from the ventral ramus of C7. It is the major motor nerve to the intrinsic muscles of the hand and gives sensory innervates to the hand. The ulnar nerve provides cutaneous sensory innervation to the back of the little finger and adjacent half of the ring finger.

Radial nerve

The radial nerve arises from the roots C5, 6, 7, 8, T1. It is the largest branch of the brachial plexus. In the upper arm and above the elbow, the radial nerve innervates the muscles. The radial nerve and its branches provide motor innervation to the dorsal arm muscles (the triceps brachii and the anconeus) and the extrinsic extensors of the wrists and hands; it also provides cutaneous sensory innervation to most of the back of the hand.
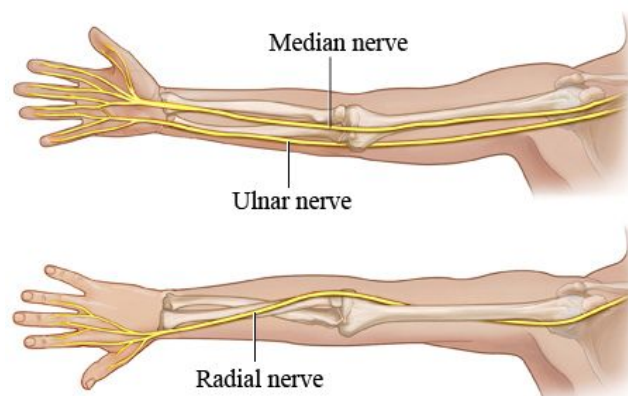
Figure2.13 *Nerves in the arm exits from brachial plexus (Frank 2002, Smith 2006).*

In this thesis, we focused on brachial plexus for combined EMG and MRI study of the upper extremity and thus will discuss an overview of the brachial plexus and related neuropathies in the following sections.

2.5 Brachial plexus

The anatomy of the brachial plexus provides motor and sensory innervations to the upper extremities formed by intercommunications between the ventral rami of the lower four cervical nerves C5, C6, C7, C8 and first thoracic nerve T1. Anatomically the brachial plexus is divided into five segments: roots; trunks; divisions; cords; and terminal branches. After exiting the neural foramen of the cervical spine the roots of the brachial plexus combine to form three trunks: upper trunk formed from the union of the C5 and C6 roots, middle trunk formed solely from the C7 root and lower trunk formed from the union of C8 and T1. Each trunk divides to form an anterior and posterior division. The anterior and posterior divisions of the trunks are approximately posterior to the clavicle and they combine to form three cords at the level of the lateral margin of the first rib in the axilla. The three cords are named after their position relative to the axillary artery: lateral, posterior and medial. As the cords exit the axilla, they recombine to form terminal branches. The main branches of the lateral cord are the musculocutaneous nerve and the lateral root of the median nerve. The branches of the medial cord are the ulnar nerve and the medial root of the median nerve, and those of the posterior cord are the radial nerve and the axillary nerve, shown schematically in figure 2.14.
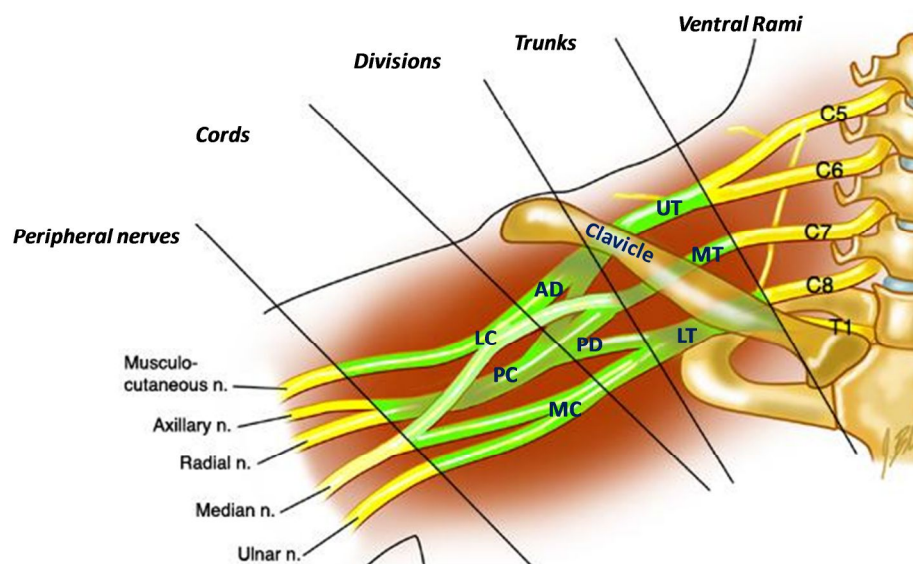
Figure 2.14 *Schematic representations of brachial plexus. The C5 to T1 ventral rami are called as roots. These form three trunks upper trunk (UT), middle trunk (MT) and lower trunk (LT) near the clavicle. Trunks divide into anterior division (AD) and posterior division (PD) laterally and join to form the lateral cord (LC), posterior cord (PC) and medial cord (MC). Each cord ends into peripheral nerve branches (Frank 2002, Standring 2008).*

In the brachial plexus each upper extremity nerve is attached to the medulla spinalis or spinal cord by two roots, an anterior, ventral or motor root, and a posterior, dorsal or sensory root. The dorsal root is also characterized by the presence of spinal ganglion called the dorsal root ganglion (DRG). The ventral root emerges from the anterior surface of the spinal cord from the anterior horn cell and exits from the cord ventrally. The dorsal root is attached with the dorsal horn and dorsolateral white matter, coalesces into two bundles, and is linked at dorsal root ganglion. The DRG contains bipolar cells. Each ganglion is oval in shape, reddish in color, and its size bears a proportion to that of the nerve root on which it is situated; it is bifid medially where it is joined by the two bundles of the posterior nerve root. The ganglia are usually placed in the intervertebral foramina. Immediately distal to the dorsal root ganglion, the motor and sensory roots come together to form the spinal nerve. Each spinal nerve quickly divides into a dorsal and ventral ramus. Each ramus contains both motor and sensory fibres. Figure 2.15 shows a schematic axial view of brachial plexus.
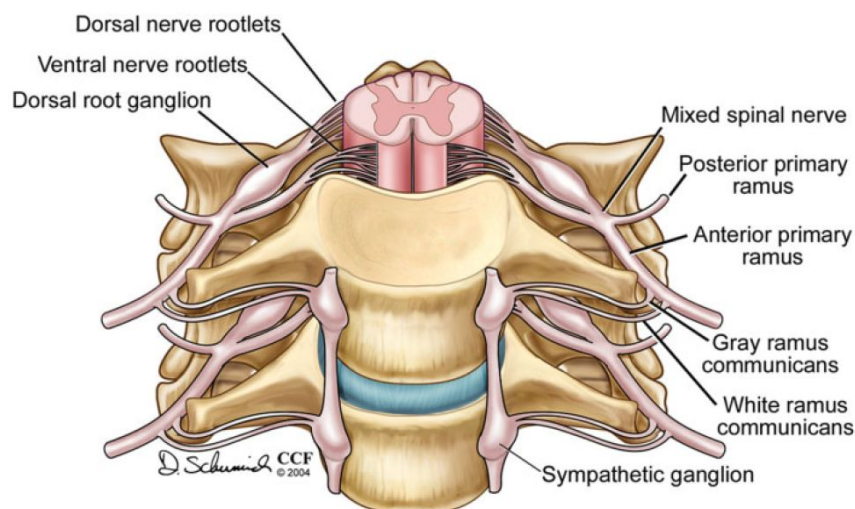
Figure 2.15 *Spinal cord and nerve roots. The motor root, originating from anterior horn cells, leaves the cord ventrally, whereas the sensory root enters on the dorsal side. Immediately distal to the dorsal root ganglion, the motor and sensory roots come together to form the spinal nerve (Frank 2002, Standring 2008).*

The brachial plexus roots have an oblique angle to a vertical axis in the frontal plane that decreases from upper to lower portion of the spinal cord (Bonnel 1984). The average size of the roots of the spinal nerves, as they exit the intervertebral foramen are in the range of mm (Hovelacque 1927). The nerve root lengths exiting from the

intervertebral foramen to the point of origin of the trunk were measured by Sunderland (1978) in the brachial plexus. Measured values are shown in the Table 2.1.

Table 2.1 Brachial plexus nerve root measurement

Root	Average angle with vertical axis	Size of the root (mm)	Length of the root (mm)
C5	138^0	3~4	15
C6	123^0	4~6	15
C7	114^0	4~4.5	15
C8	100^0	3~4.5	17
T1	85^0	3~4	25

The cervical spine has a slightly lordotic curvature in the sagital plane, and the vertebral discs become broader and gradually increase in size from C3 to C7. The cervical spinal cord is nearly elliptical in cross section. The spinal cord is small 1~1.5 cm in diameter at the cervical level and its component white-matter columns are on the order of several millimetres. Spinal cord structure and anatomy is discussed in section (2.1) (Pandey *et al.* 2007, Aggarwal *et al.* 2010, Johnson *et al.* 2010).

2.6 Brachial plexus disorders

Damage to the brachial plexus i.e. cervical spine and nerves may be caused by a wide range of pathologies that result in profound functional disability in the arm and shoulder. Trauma is the most common cause of those injuries. Depending on its pathogenesis, the peripheral neuropathy involves degradation of peripheral nerves, due to metabolic disorder and infection. Such disorders affect sensory and motor axons and causing demyelination.

Cervical spondylotic myelopathy and radiculopathy are the common degenerative conditions most likely caused by the changes in the intervertebral discs in the brachial plexus. Cervical spondylotic myelopathy results from the compression of the spinal cord due to bulging discs, and cervical spondylotic radiculopathy results from compression of the nerve roots exiting from vertebra due to osteophytes or herniated discs, schematic diagram shown in Figure 2.16 (Mukherji *et al.* 1996, Sureka *et al.* 2009).
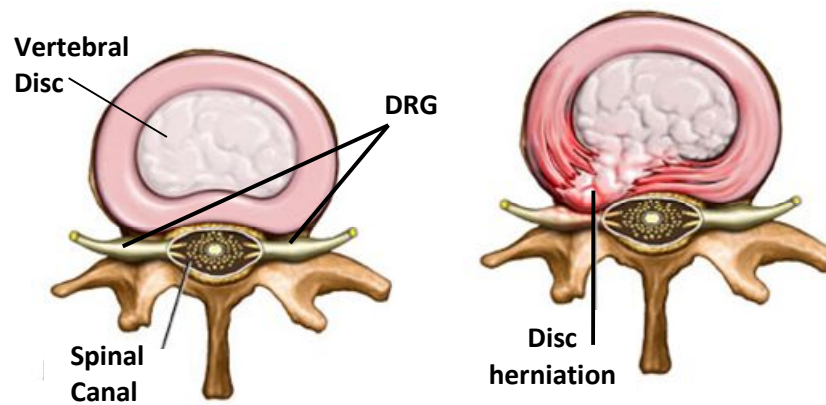
Figure 2.16 *Pictorial views at the C4–C5 cervical spine space shows changes due to disc herniation causing cervical radiculopathy (http://www.necksolutions.com/cervical-spondylosis.html).*

Clinically, several syndromes are seen for the disorders: neck and shoulder pain, suboccipital pain and headache. Surgery may be needed in more severe cases; most people can find relief of symptoms through non-surgical means such as traction or physical therapy techniques. MRI of the cervical spine is the procedure of choice during the initial screening process of patients with suspected cervical spondylosis on MRI images and link with the nerve root pathology (Levine *et al.* 1996, Wainner *et al.* 2000, Eubanks 2010) shown in Figure 2.17a.

EMG and nerve conduction studies are widely used to localize the lesions and types of observed lesions to assess severity. Although, EMG is a cheap and handy technique for such evaluation, it cannot display the anatomic detail needed for precise localization and treatment planning and also to apply this technique a detailed knowledge of the anatomy of the nerve roots, paths of the nerves and distribution of the peripheral nerves are necessary (Aminoff 2006, Date *et al.* 2006, Oh 2006, Trojaborg *et al.* 2006, Wilbourn 2006, Alam *et al.* 2010, Preston *et al.* 2012, Kimura 2013). Figure 2.17b shows an example of EMG based diagnosis of cervical spondylosis disorder.

(a)   **(b)**
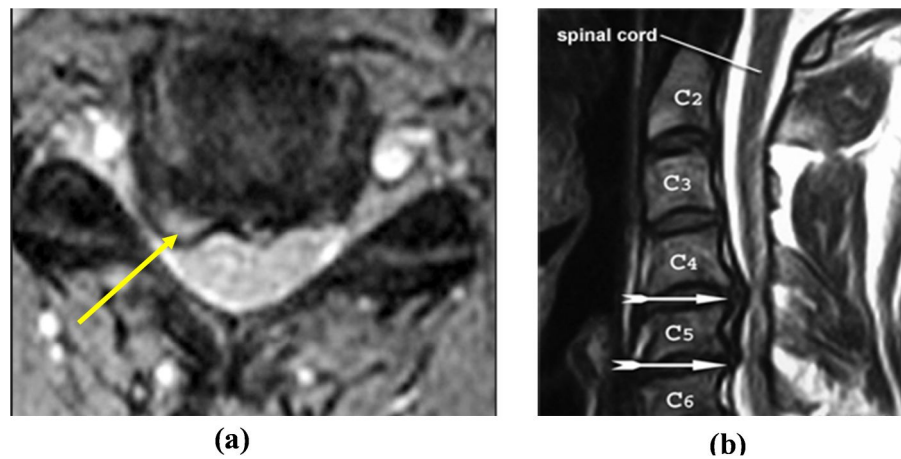
Figure 2.17a (a) *Axial T2W MRI at the C4–C5 space white arrow shows narrowing of the nerve root due to osteophyte caused cervical radiculopathy. (b) T2W sagittal MRI showing cord compression from cervical spondylosis, which caused central spondylotic myelopathy. Note the signal changes in the cord at C4-C5, the ventral osteophytosis, buckling of the ligamentumflavum at C3-C4, and the prominent loss of disk height between C2 and C5 (Cook et al. 2008).*
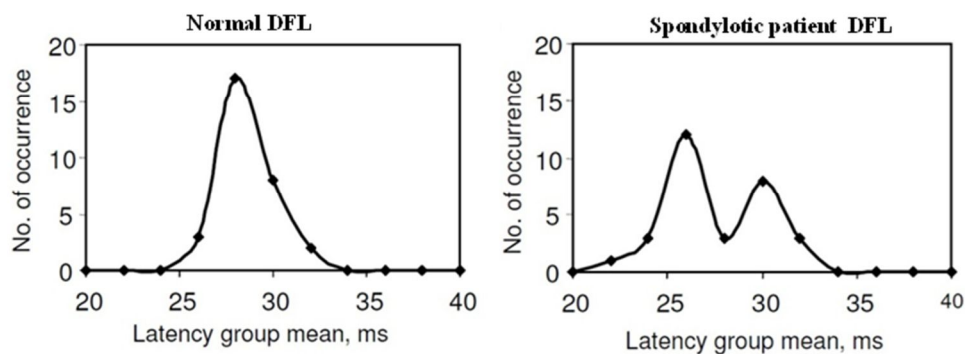
Figure 2.17b *EMG study in the form of DFL for normal and spondylotic patient, showing changes in the shape of DFL (Alam et al. 2010).*

So far we have discussed about anatomical and physiological overview of nervous system, brachial plexus and brachial plexopathis, the next chapter will describe the MRI and EMG measurement techniques for the brachial plexus.

References:

Aggarwal, A., N. Puri, A. K. Aggarwal, K. Harjeet and D. Sahni (2010). "Anatomical variation in formation of brachial plexus and its branching." Surgical and Radiologic Anatomy 32(9): 891-894.

Alam, M. and K. Rabbani (2010). "Possible detection of cervical spondylotic neuropathy using Distribution of F-latency (DFL), a new neurophysiological parameter." BMC Research Notes 3(1): 112.

Aminoff, M. J. (2006). Chapter 30 Lumbosacral radiculopathies. Handbook of Clinical Neurophysiology. K. Jun, Elsevier. Volume 7: 621-630.

Bonnel, F. (1984). "Microscopic anatomy of the adult human brachial plexus: an anatomical and histological basis for microsurgery." Microsurgery 5(3): 107-117.

Cook, C., A. Braga-Baiak, R. Pietrobon, A. Shah, A. C. Neto and N. de Barros (2008). "Observer agreement of spine stenosis on magnetic resonance imaging analysis of patients with cervical spine myelopathy." Journal of Manipulative and Physiological Therapeutics 31(4): 271-276.

Date, E. S. and B. J. Kim (2006). Chapter 28 Cervical and thoracic radiculopathies. Handbook of Clinical Neurophysiology. K. Jun, Elsevier. Volume 7: 601-611.

Erlanger, J. and H. S. Gasser (1937). "Electrical signs of nervous activity."

Eubanks, J. D. (2010). "Cervical Radiculopathy: Nonoperative Management of Neck Pain and Radicular Symptoms." American Family Physician 81(1): 33-40.

Frank, H. N. (2002). "Atlas of Neuroanatomy and Neurophysiology-Selections from the Netter Collection of Medical Illustrations."

Greenstein, B. and A. Greenstein (2000). Color atlas of neuroscience: Neuroanatomy and neurophysiology, Thieme.

Guyton, A. C. and J. Hall (2008). "Textbook of medical physiology. 1996." WB Saunders, Philadelphia: 549-551.

Hovelacque, A. (1927). Anatomie des nerfs craniens et rachidiens et du système grand sympathique chez l'homme: avec 89 figures dans le texte et CXXI planches hors texte, o. Doin.

Johnson, E., M. Vekris, T. Demesticha and P. Soucacos (2010). "Neuroanatomy of the brachial plexus: normal and variant anatomy of its formation." Surgical and Radiologic Anatomy 32(3): 291-297.

Kimura, J. (2013). Electrodiagnosis in diseases of nerve and muscle: principles and practice, Oxford university press.

Krarup, C. (2006). Chapter 2 Physiology and function. Handbook of Clinical Neurophysiology. K. Jun, Elsevier. Volume 7: 23-61.

Levin, K. H. (2006). Chapter 6 Motor nerve conduction studies. Handbook of Clinical Neurophysiology. K. Jun, Elsevier. Volume 7: 139-154.

Levine, M., T. Albert and M. Smith (1996). "Cervical Radiculopathy: Diagnosis and Nonoperative Management." Journal of the American Academy of Orthopaedic Surgeons 4(6): 305-316.

Mukherji, S. K., M. Castillo and A. G. Wagle (1996). "The brachial plexus." Seminars in Ultrasound, CT, and MRI 17(6): 519-538.

Oh, S. J. (2006). Chapter 41 Diseases of the nerves in the pelvic girdle and lower limbs. Handbook of Clinical Neurophysiology. K. Jun, Elsevier. Volume 7: 859-892.

Pandey, S. K. and V. K. Shukla (2007). "Anatomical variations of the cords of brachial plexus and the median nerve." Clinical Anatomy 20(2): 150-156.

Preston, D. C. and B. E. Shapiro (2012). Electromyography and Neuromuscular Disorders: Clinical-Electrophysiologic Correlations (Expert Consult-Online), Elsevier Health Sciences.

Smith, B. E. (2006). Chapter 1 Anatomy and histology of peripheral nerve. Handbook of
        Clinical Neurophysiology. K. Jun, Elsevier. Volume 7: 3-22.

Standring, S. (2008). "Gray's anatomy." The anatomical basis of clinical practice 3.

Sunderland, S. S. (1978). "Nerves and nerve injuries." 854-869.

Sureka, J., R. A. Cherian, M. Alexander and B. P. Thomas (2009). "MRI of brachial
        plexopathies." Clinical Radiology 64(2): 208-218.

Trojaborg, W. and J. Payan (2006). Chapter 29 Brachial plexopathies. Handbook of Clinical
        Neurophysiology. K. Jun, Elsevier. Volume 7: 613-620.

Wainner, R. S. and H. Gill (2000). "Diagnosis and nonoperative management of cervical
        radiculopathy." Journal of Orthopaedic & Sports Physical Therapy 30(12): 728-744.

Wilbourn, A. J. (2006). Chapter 31 Lumbosacral plexopathies. Handbook of Clinical
        Neurophysiology. K. Jun, Elsevier. Volume 7: 631-645.

Chapter 3
Monitoring the Brachial plexus using MRI and EMG

Introduction

The ability to measure the brachial plexus peripheral nerve structure in vivo has far reaching consequences for our understanding of the normal anatomy, development of the peripheral nervous system, as well as characterization of a wide variety of neurological disorders. In 1987 Blair first described the anatomic details of the brachial plexus using MRI. Other studies followed and described the excellent capabilities of MRI in delineating the anatomy and pathology of the brachial plexus (Blair *et al.* 1987, de Verdier *et al.* 1993, Bilbey *et al.* 1994, van Es *et al.* 1997, Du *et al.* 2010, van Es *et al.* 2010, Adachi *et al.* 2011, Chalian *et al.* 2011, Chhabra *et al.* 2011). EMG and nerve conduction studies provide important information of the peripheral nerve through temporal behaviour of action potentials and has significant applications in clinical studies of brachial plexus neuropathies (Denno *et al.* 1991, Montgomery *et al.* 1992, Bono *et al.* 2011, Preston *et al.* 2012) . So far no attempt to link MRI and EMG measurements in the form of nerve conduction studies has been made for the brachial plexus. This thesis aims to study quantitative measures of the peripheral axons related to microstructure using quantitative MRI and physical measurements using EMG and then relate those observations. In Chapter 2 an outline of anatomical and physiological overview for nervous system and brachial plexus has been discussed. As a background of the MRI and EMG applications in brachial plexus, this chapter will describe the basics of anatomical MRI, quantitative MRI and electrophysiology of nerve conduction studies. For that the current chapter is divided into following sections:

A. Anatomical MRI
B. Diffusion weighted MRI
C. Magnetization transfer MRI
D. T2 relaxation
E. EMG studies of brachial plexus

3.1 Anatomical MRI in the form of MR neurography of brachial plexus

Magnetic resonance imaging is the imaging method of first choice for brachial plexus anatomical and neuropathy studies. The brachial plexus structures and its peripheral nerves are well visualized with MRI, termed MR neurography (Filler *et al.* 1993, Aralasmak *et al.* 2010, Adachi *et al.* 2011, Mallouhi *et al.* 2012, Subhawong *et al.* 2012). MR neurography comprises a group of scanning protocols applicable to clinical scanners. MR neurography can be further categorized according to the type of MR technique used to acquire the images: conventional MR neurography and Diffusion Weighted MR neurography. Both techniques can be used to visualize the nerve locations and its branches with the use of surface coils (e.g. torso coil, spine coil etc.). This section describes a general overview of conventional MR neurography and the following section 3.2 will introduce diffusion MRI and diffusion weighted MR neurography.

MR neurography, introduced by Filler *et al.* (1993), produces fat suppressed T2 weighted images with higher intensity structures of peripheral nerves. This technique produces images with intermediate-to-high contrast where the nerves appear considerably hyperintense within a hypointense fat saturated background (Le Bihan *et al.* 2006, Jones *et al.* 2010). T1 weighted (T1W) images are used to define the bony structures and tissue planes surrounding the nerves, and fat suppressed T2 weighted (T2W) images are used to better characterize the nerve structure and pathology (Chhabra *et al.* 2011, Chhabra *et al.* 2011). Other standard protocols such as axial proton density weighted (PDW), sagittal T1W images are also used for visualization and anatomical localization of peripheral nerves and corresponding disorders useful for treatment planning (van Es *et al.* 1997, van Es *et al.* 2010, Vargas *et al.* 2010). Typically MR neurography of the brachial plexus is performed in different anatomical planes e.g. coronal, axial and sagittal. The coronal plane helps left to right comparisons of root ganglion, roots, trunks, divisions, and cords in one plane. However, it is usually not possible to observe all the five ventral rami in one single plane because of the cervical lordosis. The axial plane is useful for delineating the ve roots as they exit the foramina. The sagittal plane demonstrates nerves and roots in

cross sections. Combination of these views can be used according to the location of neuropathy.

Figures 3.1.1, 3.1.2 and 3.1.3 show MR neurography images of a healthy subject brachial plexus acquired from Philips 3 T Achieva scanner using the Torso coil.

Sequence Figure	Resolution/mm FOV(mm) Acquisition time	Sequence parameters	Features observed in the image (key to abbreviation)
PDW SPIR, 3.1.1(a)	2.4 pixels, 160×149×49, 3:52min	TSE factor15, TE=30ms, TR=3137ms, Flip angle 90^0	C7 level, Disc, Articular process, nerve roots exiting from spinal cord, vertebral artery (VA) and CSF, ventral root (VR), dorsal root (DR), spinal ganglion, spinous process
T1W FFE, 3.1.1(b)	2.2pixels, 160×253×36, 3:33min	Flip angle 80^0, TE=4.6ms,TR=140 ms	C5 level, spinous process, Disc, spinal cord, two exiting nerve roots, the ventral root (VR), dorsal root (DR) close to ventral artery (VA).
STIR TSE, 3.1.1(c)	1.1pixels, 250×250×43, 4:09min	TSE factor 17, TE=80ms, TI=250ms, TR=5172ms, SENSE =2	C7 level, spinous process, Disc, spinal cord, two clear exiting nerve roots, the ventral root (VR), dorsal root (DR), Articular process
Balance FFE, 3.1.1(d)	1.1pixels, 150×150×48, 1:00min	TFE factor 256, Partial echo TE=3ms, TR=7ms, flip angle=45^0	C6 level demonstrating normal preganglionic segment ventral and dorsal rootlets on both sides (yellow arrows), spinal cord, vertebral artery (VA), high signal intensity CSF, bony structures and the nerve roots have very low intensity.

Figure 3.1.1 *Transverse view of brachial plexus.*
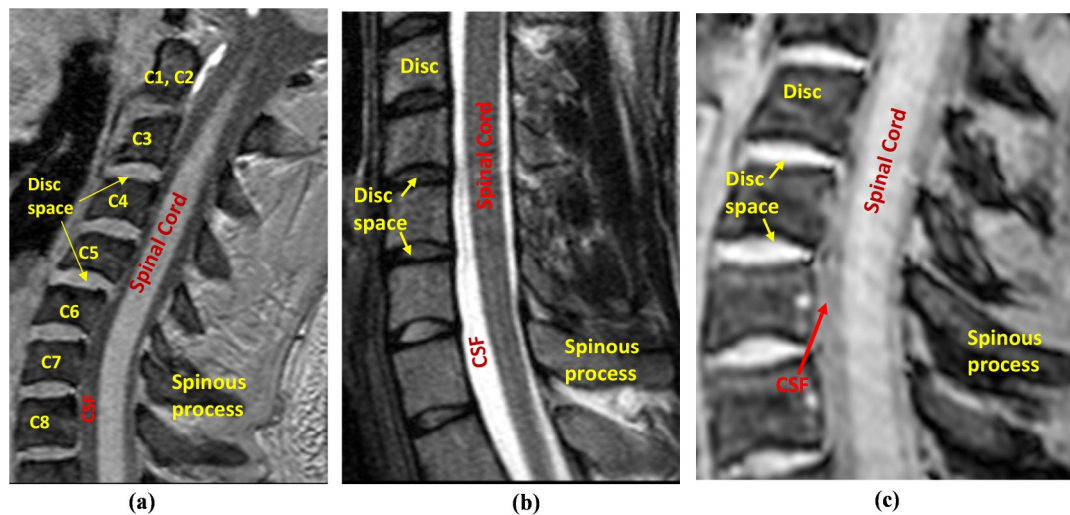
Sequence Figure	Resolution/mm FOV(mm) Acquisition time	Sequence parameters	Features observed in the image (key to abbreviation)
T1W FFE, 3.1.2(a)	2.2pixels/mm, 160×253×36, 3:33min	Flip angle 80^0, TE=4.6ms,TR=140ms	Clear vertebral levels, spinous process, spinal cord, intervertebral disc space, CSF
T2W TSE, 3.1.2(b)	2.2pixels/mm, 160×251×43, 2:42min	TSE factor24, Flip angle 90^0, TE=100ms, TR=3557ms	Clear vertebral levels, bright CSF, dark spinal cord, disc space and intervertebral discs, contrast between WM and GM, vertebral disc and cord
T2W FFE, 3.1.2(c)	2pixels/mm, 250×200×36, 2:58min	Flip angle 25^0, TE=5.8ms,TR=132ms	Clear vertebral levels, spinous process, disc space, CSF and spinal cord, contrast between GM and WM, vertebral disc and cord

Figure 3.1.2 *Sagittal view of brachial plexus*.
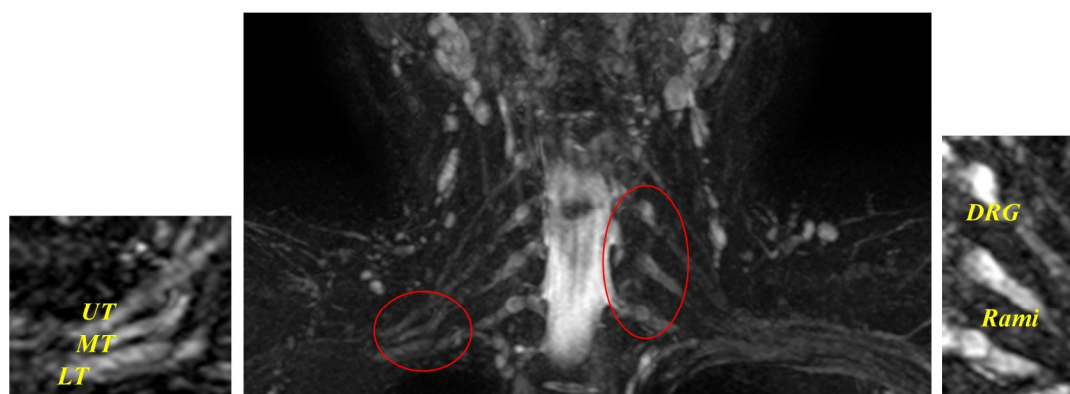
Figure 3.1.3 *Coronal MIP view of brachial plexus from STIR TSE sequence. The trunks are marked as a smaller red circle and zoomed view of upper trunk (UT), middle trunk (MT) and lower trunk (LT) shown in the left inset; the DRG and Rami are marked as bigger red circle and zoomed view shown in the right inset (corresponding anatomical Figure 2.15).*

The T1W, T2W and PDW images provide excellent resolution for the postganglionic and preganglionic region of the brachial plexus showing the nerve roots exiting from the spinal cord. The white matter, grey matter and CSF have clear contrast and vertebral discs, intervertebral disc space have great conspicuity surrounding the spinal cord. Fat suppression provides higher intensity images of the nerve roots and path of the exiting nerves. However, it is rather difficult to distinguish the nerves from the surrounding vascular structures such as veins and arteries that certainly have similar signal intensity with peripheral nerves on both T1 and T2 weighted images. Also it is difficult to depict three dimensional trajectories of the nerves from anatomical MRI. On the other hand, diffusion weighted MRI neurography is able to depict the peripheral nerves by nicely suppressing the surrounding soft tissues. Thus DW neurography can be applied as an efficient way to identify the brachial plexus nerve and cord ROI objectively. The basics of diffusion MRI and its applications to brachial plexus will be discussed in the next section.

3.2 DW-MR neurography

Diffusion weighted MRI (DWI) is an effective way to visualize the peripheral nerves as it suppresses signal from structures with relatively free diffusion, such as CSF or blood vessels, and highlights structures with relatively impeded or restricted diffusion, such as nerve axons. Application of DW neurography for brachial plexus using body signal suppression (DWIBS) has successfully been used to observe the root ganglions, the nerve roots, and the nerve paths from both sides of the body with better SNR than conventional neurography (Takahara *et al.* 2004, Kwee *et al.* 2008). Proper imaging of the peripheral nerves can explore the microstructure and nature of diffusion of the water molecules within the axons using restricted diffusion MRI models (Horsfield *et al.* 1994, Sen 2004, Alexander 2008), which is challenging for brachial plexus imaging studies. The aim of this thesis is to develop a DWIBS sequence for the brachial plexus and to study the nature of diffusion of water molecules using restricted diffusion MRI models. On this context, this section aims to discuss an overview of diffusion MRI, its acquisition and optimization techniques; applications of diffusion MRI in brachial plexus imaging; and then finally restricted diffusion and its applications to peripheral nerve structure studies.

3.2.1 Diffusion MRI-physical background

Diffusion weighted MRI is based on the Brownian molecular motion of the spins. Molecular motion within the fluid is related to thermal kinetic energy of the particles which can be expressed as, $E_k = \frac{3}{2} k_B T$, where k_B is the Boltzmann's constant and T is the temperature. Diffusion is a non-equilibrium thermodynamic process causing transport of particles from high concentration to low concentration. The diffusion of molecules in a liquid or in a gas is completely stochastic and quantitatively described by the diffusion coefficient D [mm^2/s]. The diffusion coefficient D which describes the mean displacement, x of particles within a diffusion time Δ, can be expressed from Einstein's diffusion equation for n-dimension, $x = \sqrt{2nD\Delta}$ (3.2.1)

In the context of MRI (Hahn 1950) it has been shown that diffusion in a magnetic field contributes to decay of the transverse magnetization in the system.

The diffusion decay is derived from the Bloch-Torrey equation (Torrey 1956, Slichter 1990),

$$\frac{dM_{xy}}{dt} = -i\gamma\left(\vec{G}.\vec{r}\right)M_{xy} - \frac{M_{xy}}{T_2} + D\frac{d^2M_{xy}}{d^2x} \qquad (3.2.2)$$

where D is the self-diffusion coefficient, G is the time dependent linear magnetic field gradient, and the last term describes the dynamics of magnetization due to self-diffusion of particles. It is clear that M_{xy} is a function of both space and time, and Equation (3.2.2) can be solved by making substitution with the attenuated transverse magnetization expression,

$$M_{xy} = S(t)\exp(-D\gamma^2 \int_0^t [\vec{G}(t')dt']^2 dt)\exp(-t/T2) \qquad (3.2.3)$$

To calculate the diffusion coefficient Stejskal and Tanner (1965) introduced the approach of incorporating two additional gradient pulses symmetrically with respect to the 180^0 pulse. Because of the presence of an 180^0 pulse, the transverse magnetization refocuses at time TE after excitation. However, diffusion of the spins (protons) in the direction of the applied gradients causes irreversible phase dispersion, which leads to additional signal attenuation, schematically shown in Figure 3.2.1.
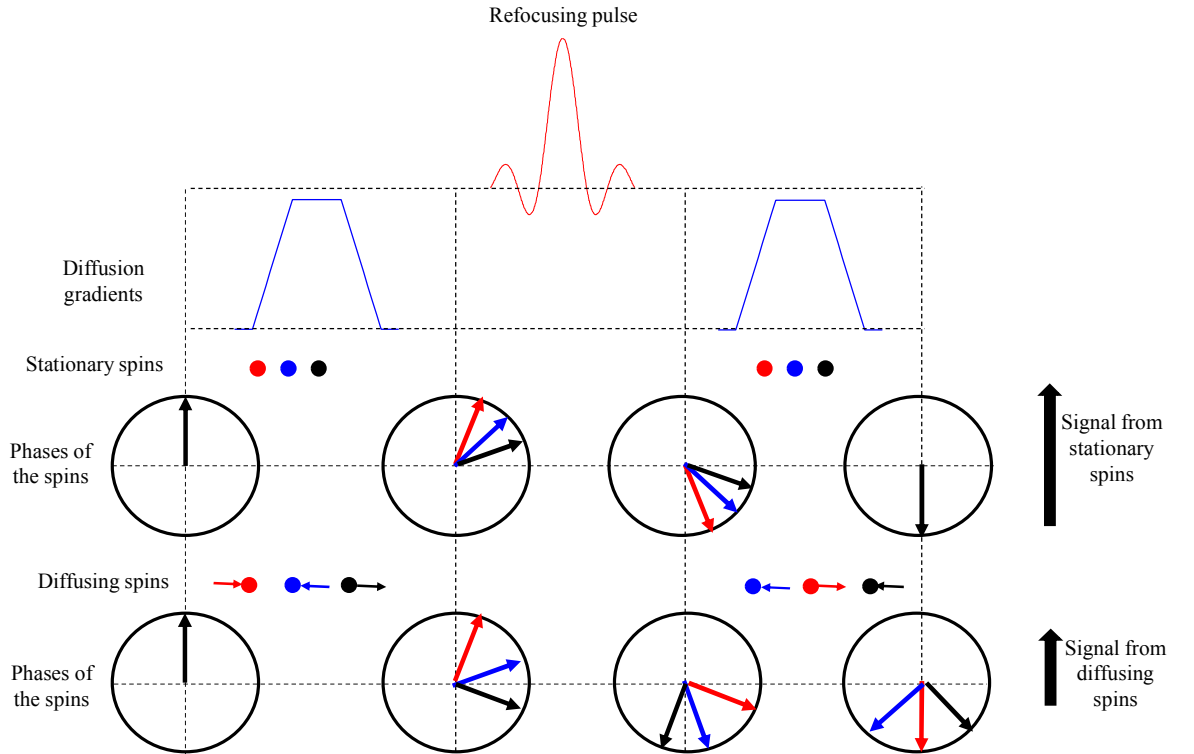
Figure 3.2.1 *Schematic diffusion MRI shows the dephasing of spins due to diffusion gradients on stationary and diffusing spins and changes in signal.*

Under the assumption that the diffusion gradients are much higher than the intrinsic magnetic field gradients present in the sample, the effective attenuation of the spin echo signal can be derived by substituting Equation (3.2.3) to (3.2.2) and then integrating the result and expressing the signal,

$$S = S_o e^{(-\frac{TE}{T_2})} e^{(-bD)} \tag{3.2.4}$$

Equation (3.2.4) is the well-known Stejskal-Tanner equation, where S_0 is the original signal without diffusion gradients, and b is a scalar quantity called diffusion sensitizing factor or b-value, $b = \gamma^2 \int_0^{TE} (\int_0^t G(t')dt')^2 dt$ $\qquad$ (3.2.5)

For a spin echo sequence with rectangular diffusion encoding gradients the b-value becomes: $b = \gamma^2 G^2 \delta^2 (\Delta - \frac{\delta}{3})$ $\qquad$ (3.2.6)

where G is the amplitude of the diffusion gradient, δ is the duration of the gradient, Δ is the interval between the two gradients and γ is the gyromagnetic ratio. The b-value (in the units of s/mm^2) represents the level of diffusion weighting observed in the MR images due to diffusion of molecules. In biological tissues, diffusion of water molecules is influenced by many biophysical factors such as, the cell membranes, cell organelles, or large macromolecules, and experimental set up which can restrict and hinder the molecular motion. At body temperature 37^0 for instance the diffusion coefficient of pure water is about $3.1 \times 10^{-3} mm^2/s$, whereas the diffusion coefficient of water measured in vivo is in the range of 0.3 to $3.0 \times 10^{-3} mm^2/s$. Thus diffusivity of water molecules obtained is not an actual diffusion coefficient, but only an apparent diffusion coefficient or, ADC. By using the diffusion signal equation (3.2.4) at long TE, the ADC can be calculated as:

$$ADC = -\frac{1}{b_1 - b_0} \ln(\frac{S}{S_0}) \tag{3.2.7}$$

Highly cellular areas have low ADC values due to restricted diffusion; less cellular areas have higher ADC values. Thus restricted areas for diffusion will appear as higher in signal intensity on DW MRI, but appear as low signal intensity on the ADC map. A schematic comparison of different tissue diffusivities is shown in figure 3.2.2.
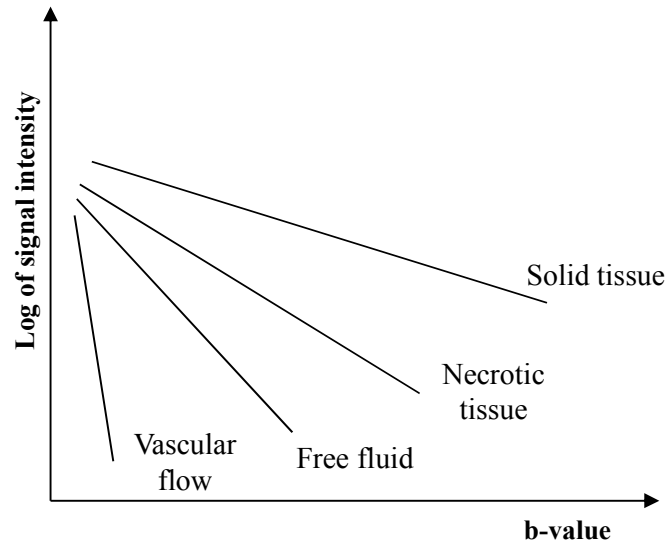
Figure 3.2.2 *Simplified schematic diagram showing the signal attenuation of different tissues with increasing b-values. Signal from vascular flow rapidly attenuated in the small b-value range. However, solid cellular tissue shows less attenuation at higher b-values compared to the free fluid or necrotic tissues.*

DWI is typically performed with at least two b-values to enable meaningful interpretation. It is important to mention that the Stejskal-Tanner equation is valid for free or unbounded motion of water molecules in an unrestricted and homogeneous medium, and in the limit of $\Delta \gg \delta$. The basic pulse sequences and necessary optimization for DWI will be discussed in the following subsections.

3.2.2 Pulse sequences for DWI

Pulsed gradient spin echo (PGSE)

Most MR methods for measuring molecular diffusion rely on the pulsed gradient spin echo (PGSE) sequence introduced by Stejskal-Tanner. The standard PGSE diffusion MRI sequence is schematically shown in Figure 3.2.3 can be explained as follows:

I.   the first gradient pulse with a duration δ labels the initial phase of the spins of the water molecules according to their positions,

II.   after the 180^0 radio frequency pulse which inverts the spin phases, a second gradient pulse at a time delay Δ labels the final positions of the nuclei through their signal phase

III.   the receiver coil receives the signal at the echo time TE and three situations are possible at this point: either the water molecules were not in motion, so that spin labels cancel out each other; the spin moves coherently and all

have the same phase, or water molecules move stochastically during the diffusion time lapse which leads to each spin having a different phase and a signal loss, which is thus a measure of molecular diffusion.
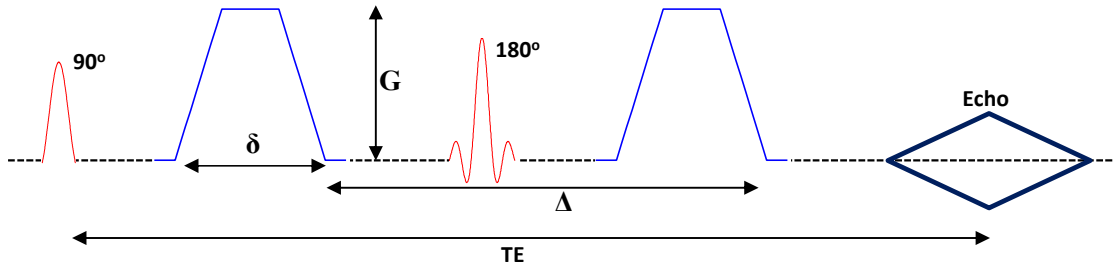
Figure 3.2.3 *Pulsed gradient spin echo sequence. Diffusion gradients applied both sides of the 180^0 RF pulse to sensitize the molecular diffusion.*

PGSE sequence based DWI suffers from T2 relaxation effects, so that long diffusion encoding time reduces SNR. However, as a basis of DWIBS techniques the PGSE sequence is used in this thesis.

Stimulated echo encoding (STEAM)

For DWI, the stimulated echo encoding (STEAM) technique is also used, it allows increment of diffusion time without T2 relaxation effects. A stimulated echo is generated by introducing three 90^0 RF pulses, placing one diffusion gradient between the first and second pulse and another one after the third pulse of a stimulated echo sequence to generate images (illustrated in Figure 3.2.4).
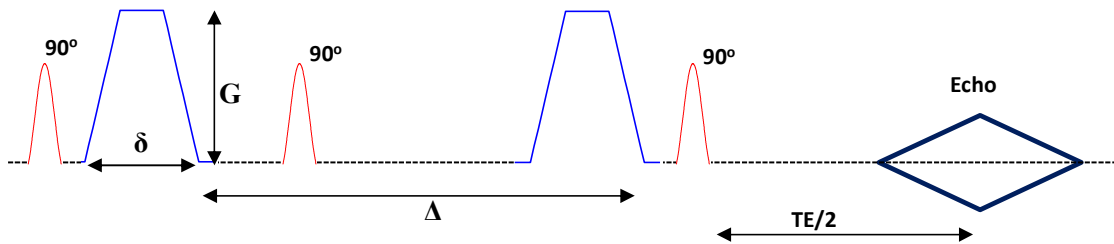
Figure 3.2.4 *Stimulated echo acquisition mode (STEAM) sequence. The echo signal generated from three 90^0 RF pulses. Corresponding diffusion time Δ can be longer without TE penalty.*

STEAM imaging allows high b-values and much longer diffusion time without T2 decay effects (magnetization is affected only by T1 in the period between 2nd and 3rd 90^0 pulses). However, the STEAM technique provides less intensity (one-half) signals compared to the spin echo signal (Tanner 1970, Frahm *et al.* 1985, Merboldt *et al.* 1985, Merboldt *et al.* 1992, Franconi *et al.* 1994, Rangwala *et al.* 2013).

Oscillating gradient spin echo (OGSE)

For observing restricted diffusion in the short diffusion time regime, oscillating gradient spin echo encoding (OGSE) is a suitable sequence. This technique uses a train of oscillating gradients for diffusion encoding. In this sequence the b-value expressed as, $b = \frac{\gamma^2 G^2 \delta^3}{4\pi^2 f^2}$, where the effective diffusion time is inversely proportional to the frequency of the oscillating gradient, $\Delta_{eff} \sim 1/f$, illustrated in Figure 3.2.5.
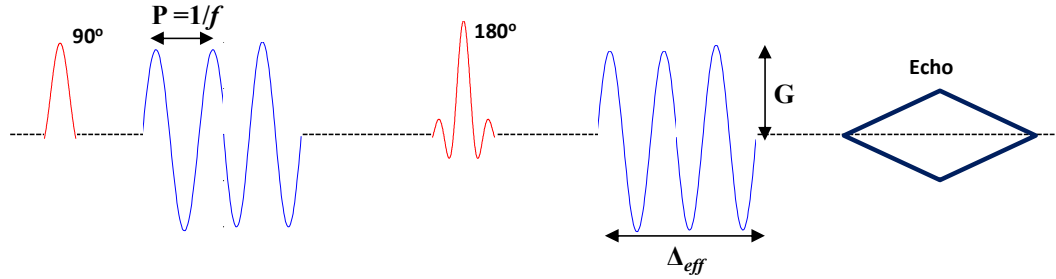
Figure 3.2.5 *Oscillating gradient spin echo sequence. Gradients applied both sides of the 180^0 RF pulse with frequency f and duration T, corresponding diffusion time $\Delta \sim 1/\pi f$.*

Thus the effective diffusion time depends on oscillation period only, no longer related to the time between the gradient pulses. By using OGSE qualitative and quantitative information from in-vivo brain and spinal cord WM have been studied. However, this approach requires powerful gradients and is generally only suitable for animal MRI scanners (Gross *et al.* 1969, Stepišnik 1981, Callaghan *et al.* 1996, Schachter *et al.* 2000, Parsons *et al.* 2006, Colvin *et al.* 2008, Xu *et al.* 2009, Drobnjak *et al.* 2010, Gore *et al.* 2010, Aggarwal *et al.* 2012).

3.2.3 Optimizing DWI

As DWI depends on signal loss, the main acquisition difficulty is linked to signal to noise ratio (SNR) which is usually quite low. To get higher diffusion weighting, a higher b value is required by increasing either the diffusion time which inevitably leads to a rather long TE, this in turn reduces the SNR; or by shortening the diffusion gradient lobe or by increasing the gradient amplitude, these are challenging for human MRI scanners. On the other hand at low b values (0 to 100 s/mm^2), DW signals are sensitive to capillary tissue perfusion. Hence, the choice of the optimum b value must always be considered in order to maintain the sufficient SNR and maximize diffusion effect. Another general problem of DWI is the very high motion sensitivity. As DWI

involves sensitizing MRI to microscopic motion, acquisitions are sensitive to molecular motion and more generally to macroscopic motion (patient motion) as well. The most important source of such motions are CSF pulsation, pulsatile blood flow, cardiac or respiratory motion, and peristaltic bowel motion. To reduce such motion artifacts, images must be acquired fast. The fastest and most frequently used pulse sequence for DWI in general is the single-shot spin-echo echo-planar-imaging (EPI) sequence. This sequence is relatively insensitive to influences from macroscopic patient motion because of the very fast readout of the complete image data, within about 100ms after a single excitation pulse. However, the maximum attainable spatial resolution can be markedly limited by the $T2^{*}$-decay during the long period of data acquisition. Also, EPI has only a very small bandwidth per pixel along the phase encoding direction. Consequently, EPI is very susceptible to main field (B_0) inhomogeneities, susceptibility variations, and chemical shift, which all may lead to severe image degradation. To reduce the artifacts, relatively recently introduced parallel imaging techniques, such as sensitivity encoding (SENSE), can be combined with DW EPI, which in turn can increase the bandwidth per pixel in the phase encoding direction and shorten the EPI train, thus significantly decrease the image distortion (Jones *et al.* 2010, Jones 2011).

DW images are inherently acquired with the same T2 weighted contrast, due to long probing time of the magnetic field gradients. Consequently, an area with a very long T2 relaxation time may have high signal at DWI and be mistaken for restricted diffusion. To separate confounding T2 relaxation and diffusion related changes of the signal, it is therefore helpful to calculate an ADC map using the equation 3.2.7. It should be noted that long transverse relaxation does not necessarily hinder image interpretation, but, in fact, often even increases conspicuity of lesions, since many lesions have both a prolonged T2 and an impeded diffusion (Jones *et al.* 2010).

An overview of DWI for body imaging is described in the next section.

3.2.4 DWI for body imaging-DWIBS

In 2004, Takahara (2004) proposed DW imaging of the body under free breathing known as diffusion weighted whole-body imaging with background body signal suppression (DWIBS), which overcame the problems inherent to breath holding or respiratory triggering DWI outside the brain (Jones *et al.* 2010, Jones 2011). DWIBS

employs single shot EPI, so that phase shift of the water molecules due to respiratory motion in the diffusion gradients is equal in each phase encoding step and, therefore, will not affect the image formation. Also the long TE in this sequence will work for background suppression. Besides a free breathing approach DWIBS is combined with either a short inversion time inversion recovery (STIR) pre-pulse or frequency selective (chemical shift selective, CHESS) pre-pulse for fat suppression, in order to optimize background body signal suppression and improve lesion conspicuity. The choice of diffusion weighting and the method of fat suppression depend on the organ/body region under examination. Furthermore, this method also enables volumetric image processing like Maximum Intensity Projections (MIPs), volume rendering, etc. created in any plane.

3.2.5 DWIBS in brachial plexus

The DWIBS sequence allows acquisition of thin section datasets that make it possible to highlight peripheral nerves from its surrounding tissues. In the brachial plexus DWIBS provides improved conspicuity of the peripheral nerves from the surrounding vascular structures. It helps visualization of the spinal cord white matter and grey matter, dorsal root ganglia, postganglionic nerve roots, divisions, trunks and peripheral nerves (Takahara *et al.* 2004, Kwee *et al.* 2008, Kwee *et al.* 2010, Lin *et al.* 2010), Figure 3.2.6 shows brachial plexus images using DWIBS collected from a normal subject using the 3T Philips Achieva scanner.
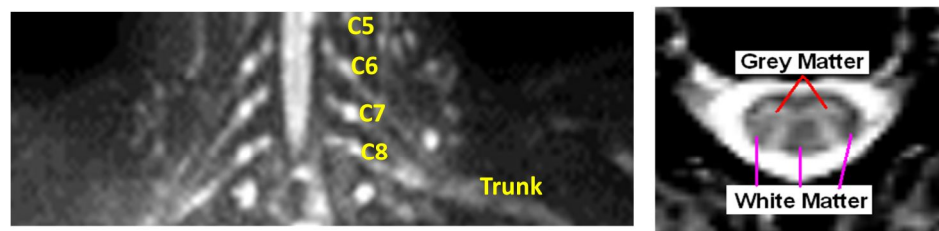
Figure 3.2.6 *DWIBS-MR neurography of brachial plexus, coronal and transverse view images. Obtained with STIR, b=200s/mm^2, TE=75ms, Δ=25ms, δ=10ms. Coronal view shows the nerve roots and trunks; transverse view shows the grey matter and white matter within the spinal cord.*

Compared to diffusion tensor imaging (DTI), DWIBS does not require multiple directional gradients; typically, diffusion gradients are applied in one of three orthogonal directions which are sufficient for peripheral nerve visualization or even better by one direction (Koh *et al.* 2010, Zhao *et al.* 2013). Also DWIBS does not attempt to follow the directionality of water diffusion inside the nerve i.e. neural

tractography, rather only aims to study high-quality nerve images for 3D evaluation and image display (Koh *et al.* 2010, Chhabra *et al.* 2011). Compared to conventional MR neurography (section 3.1), the DWIBS neurography has improved contrast to noise ratio (CNR). Furthermore, as shown in section 3.1 the vascular structures such as veins, arteries and peripheral nerves have similar signal on both T1 and T2 weighted imaging, thus it can be difficult to distinguish neural elements using conventional MR neurography. However, structures such as lymph nodes and tonsils are often present in the DWIBS images and must be removed by post processing of the images. Also, the pre-ganglion part of the nerve roots is usually not visible because of its smaller size and CSF flow, infraclavicular portions of the C8, T1 nerves are not well seen and discrimination of the nerve divisions after the nerve trunks are difficult from DWIBS images. Furthermore, DWIBS imaging demands an appropriate combination of suitable hardware and selective diffusion sequence parameters to cover the entire region of the brachial plexus.

DWIBS has been widely used for qualitative and quantitative studies in oncology and diagnosis of peripheral nerve disorders (Andreisek *et al.* 2006, Chhabra *et al.* 2011, Guggenberger *et al.* 2012, Gasparotti *et al.* 2013, Zhao *et al.* 2013, Chhabra *et al.* 2014).

However, restricted diffusion study from the DWIBS brachial plexus images and combined DWIBS, EMG studies for brachial plexus are completely new fields to be explored, which are important bases of this thesis. The following sub sections discuss the basics of restricted diffusion MRI and applications to microstructure study in biological tissues.

3.2.6 Restricted diffusion and biological tissue structure

From the perspective of molecular motion, generally there are three possible diffusion processes in biological tissues such as: free, hindered, and restricted diffusion. For example, intravascular molecular motion corresponds to free diffusion, intracellular space molecular motion corresponds to hindered diffusion and extracellular molecular motion corresponds to restricted diffusion. The degree of restriction to diffusion in biological tissue is inversely correlated to the tissue cellularity and integrity of cell membranes. The motion of water molecules is more restricted in tissues with a high cellular density. By contrast, that motion is less restricted in areas of low cellularity.

For example, peripheral nerves consist of many neuronal fibres across which motion of water molecules is more restricted compared to motion within blood vessels or cerebrospinal fluid.

At very short diffusion times most molecules will not move far enough to interact with the barriers, thus D measured in the short time regime is the free diffusion coefficient values. At longer diffusion times the molecule's motion begins to be restricted by the boundaries and the measured D reduces. Thus the time characterizing the transition between the degrees of restriction can be used as an indicator of compartment sizes in the fluid containing medium. From Einstein's diffusion equation (3.2.1) free and hindered diffusion will show linearity and partially restricted (or highly hindered) and restricted diffusion will show non-linearity between mean displacement of the molecules with diffusion time. Figures 3.2.7a, 3.2.7b and 3.2.7c show schematic diagrams of the water molecular motion in biological tissue and different types of diffusions respectively.
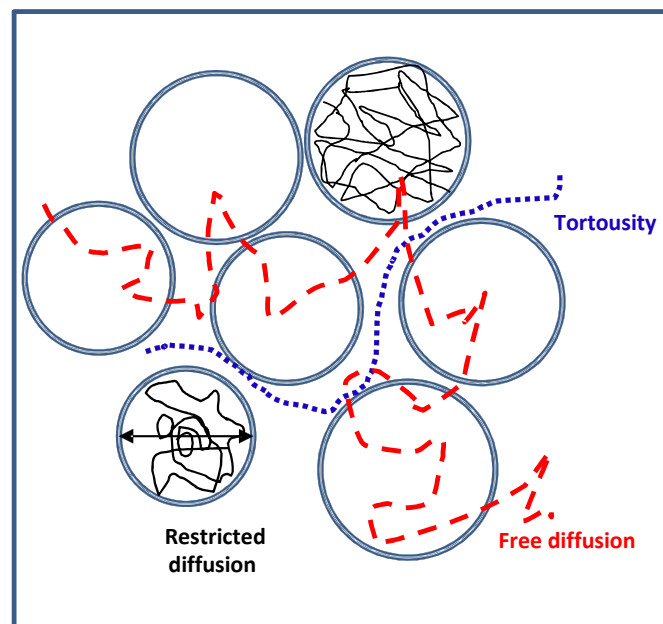
Figure 3.2.7a *Schematic diagram of molecular movements in biological tissues. Freely diffusing molecules (red line) crossing through the space; restricted diffusion molecules inside each cell (black line) and hindered diffusion molecules (blue line) creates tortousity in extracellular space.*

Free Diffusion   **Restricted Diffusion**
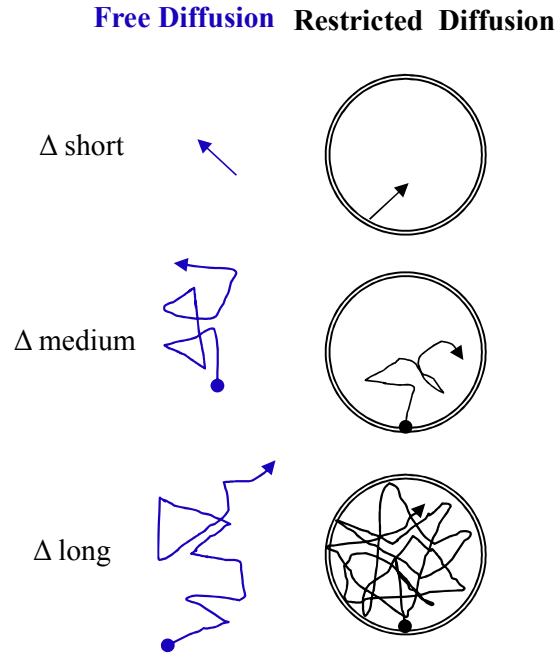
Figure 3.2.7b *Schematic diagram of comparison of free diffusion and restricted diffusion with diffusion time. Left displacement of the free water molecules with Δ and Right restricted water molecules. At short Δ the particles does not displaced enough thus both diffusion coefficients are similar; at medium Δ there are differences in displacement thus difference in diffusion coefficients expected; at long Δ significant differences in displacements thus large difference in diffusion coefficients is expected.*
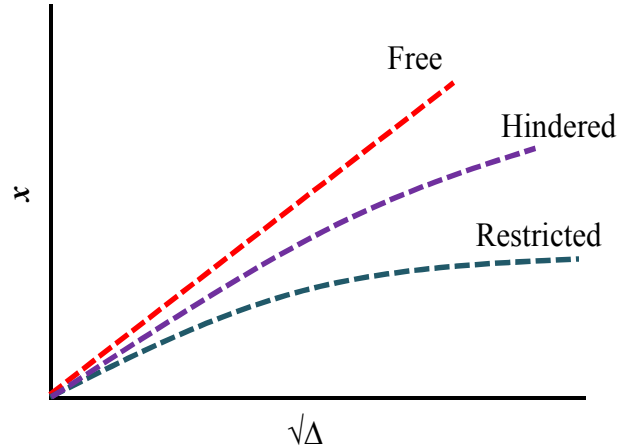
Figure 3.2.7c *Diffusion processes occurring in biological tissues, as relation between mean displacement and squared diffusion time. Free diffusion showing linearity, partially restricted and restricted diffusions showing non-linearity.*

Thus by observing the diffusivities with diffusion time it is possible to study the microstructural organizations of the biological tissues. Thus in MRI applications by varying the diffusion pulse sequence parameters i.e., variations of diffusion gradient (G) and diffusion timings (Δ and δ), the type of hindrances or restrictions and shape of

the restricting volumes can be studied. It is possible to vary these parameters with PGSE, STEAM and OGSE pulse sequences already discussed in section 3.2.2.

The following subsections will discuss an overview of different approaches of restricted diffusion MRI.

3.2.6.1 q-space analysis

The methods of microstructure measurements based on MRI was facilitated by the development of the q-space concept; introduced by Callaghan and Cory (Callaghan *et al.* 1991, Callaghan 1995, 1996) using the reciprocal spatial vector,

$$q = (2\pi)^{-1}\gamma G\delta \tag{3.2.8}$$

where γ is the gyromagnetic ratio. q-space analysis was developed under the short gradient pulse approximation, $\delta \rightarrow 0$ and $\delta \ll \Delta$ and higher diffusion gradients G. This analysis describes a Fourier relationship between the echo signal and probabilistic function that express the probability of molecules to diffuse a certain distance at a given diffusion time.

$$E_\Delta(\boldsymbol{q}) = \int \overline{P_S}(\boldsymbol{R}, \Delta)\exp(i2\pi\boldsymbol{q}.\boldsymbol{R})d\boldsymbol{R} \tag{3.2.9}$$

where E_Δ is the echo signal decay as a function of q, P_S is the displacement probability; **R** is the net displacement vector.

Performing a Fourier transform of E_Δ with respect to q gives the displacement probability profile of the molecules. Figure 3.2.8 shows schematic diagrams of particle displacement probability at different diffusion times. For free diffusion water molecules displacement broadens with long diffusion time; but for restricted diffusion the displacement remains the same with different diffusion times. Thus q-space analysis provides sensitivity and extent of restricted diffusion, by indicating the displacement distributions with diffusion time.
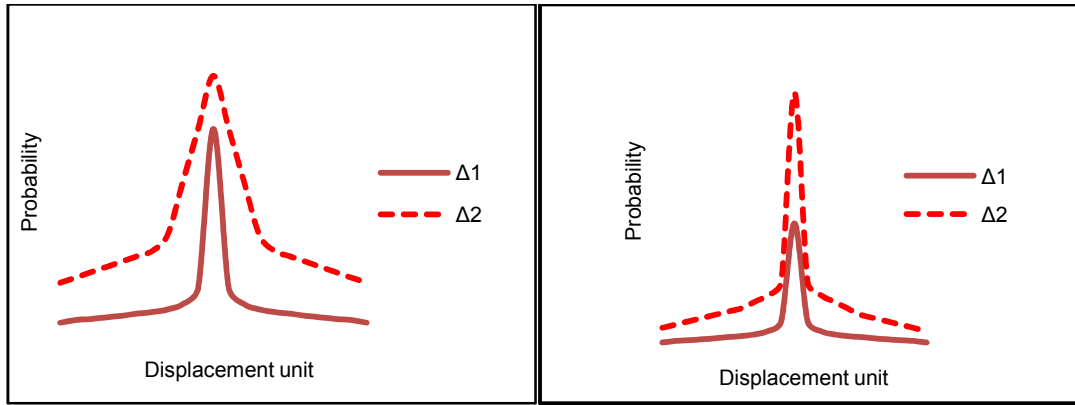
Figure 3.2.8 *q-space probability distribution of molecular displacement at different diffusion times (Δ1< Δ2). Left figure shows for free diffusion showing broadening and higher probability peak with long diffusion time; right figure shows for restricted diffusion same width but higher probability peak with long diffusion time.*

Different models of the diffusion q-space signal decay have also been implemented to enable extraction of specific information on various compartments of biological tissues. For example the Composite Hindered And Restricted Model of Diffusion (CHARMED) (Assaf *et al.* 2005, Alexander 2007) assumes that the corresponding signal decay contributed by the (i) *hindered diffusion* from extra and intra cellular spaces modeled by diffusion tensor and (ii) *restricted diffusion* from the intra axonal volume modeled by spin echo diffusion within impermeable cylinders, schematically shown in Figure 3.2.9.

$$E(\boldsymbol{q}, \Delta) = \underbrace{f_h E_h(\boldsymbol{q}, \Delta)}_{Hindered} + \underbrace{f_r E_r(\boldsymbol{q}, \Delta)}_{Restricted}$$
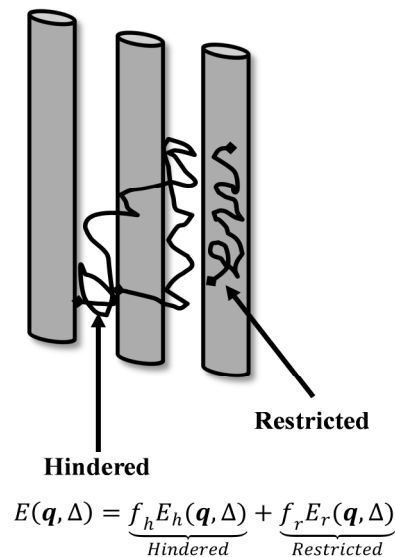
Figure 3.2.9 *CHARMED model for restricted and hindered diffusion in cylindrical volume (Assaf et al. 2005).*

In order to model the diffusion process, the CHARMED model uses an experimental framework that measures the diffusion in shells of multiple *b*-values. In this way the

space is covered homogeneously in the low *b*-value range to deal with the hindered part; as well as in the high *b*-value range to deal with the restricted part. The maximum *b* value in these experiments was approximately 44000 s/mm^2 and the maximal *q* value was 89.4 mm^{-1}. Total experimental time was about 18 hours. The CHARMED model allows estimation of diffusivities of the different compartments or components and their relative weightings. The Ax-caliber method produces images of axonal density and estimates the axon diameter distribution using the CHARMED model (Figure 3.2.10). It simplifies the experiment by assuming restricted diffusion occurs in parallel cylinders and that the corresponding diameter distribution follows a gamma function with different diffusion directions, several b-values and different diffusion times.
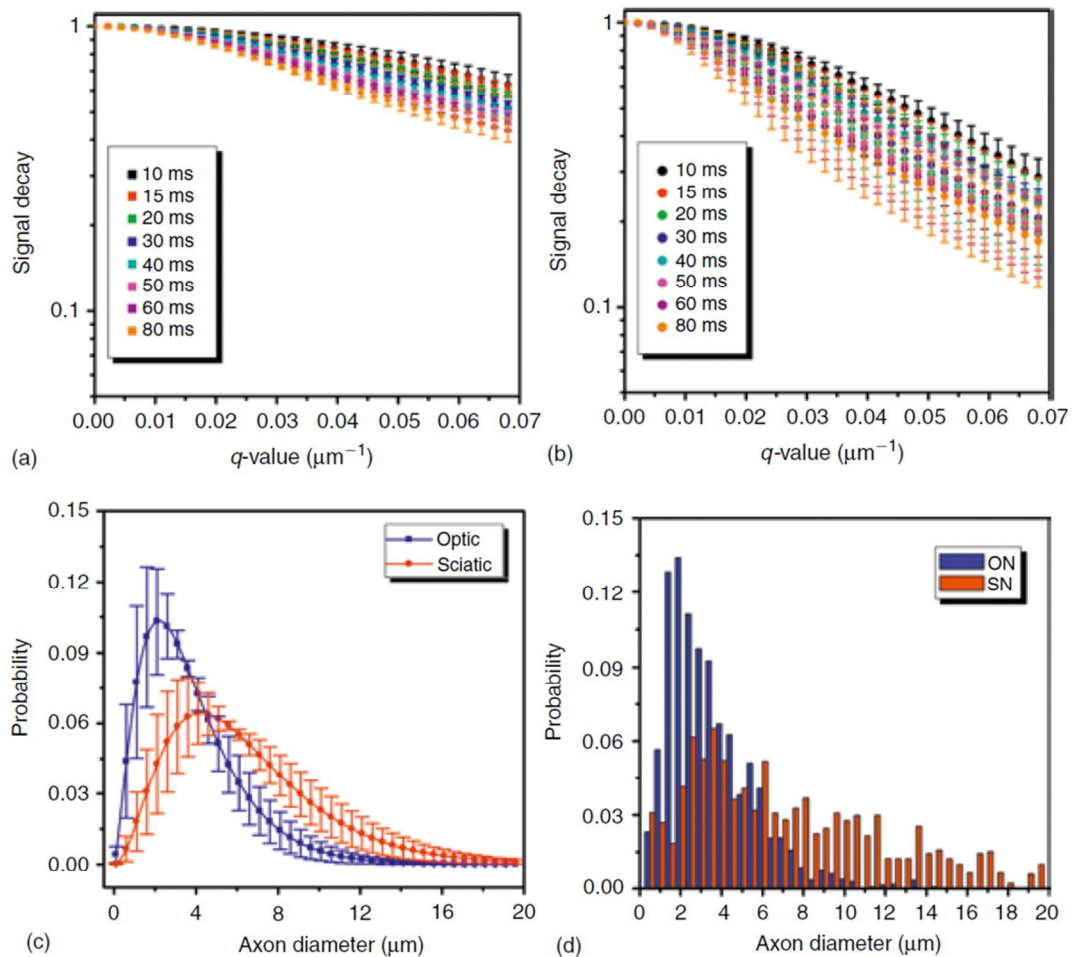
Figure 3.2.10 *Ax-caliber of optic nerve and sciatic nerves. (a) Multi diffusion time diffusion decay optic nerve;(b) Multi diffusion time diffusion decay sciatic nerve; (c) Fibre diameter distribution using Ax-caliber; (d) Fibre diameter distribution from electron microscopy observations (Assaf et al. 2008).*

However, these models demand much longer acquisition times that possible for a human in vivo study; and also require acquisition parameters (short gradient pulse with high amplitude) that are difficult to achieve on conventional clinical scanners. The images also have poor SNR, and these techniques demand appropriate models of the structures (Assaf *et al.* 2004, Assaf *et al.* 2005, Assaf *et al.* 2008, Le Bihan 2013).

3.2.6.2 Porous –media model of restricted diffusion

NMR diffusion techniques have been developed for solid-boundary porous media based on short-time and long-time behavior of the self-diffusion coefficient which enables one to determine pore surface area to volume ratio, tortousity, permeability, connection between different pores, bulk self-diffusion coefficient of the pore fluid (Mitra *et al.* 1992, Mitra *et al.* 1993, Latour *et al.* 1995, Loskutov *et al.* 2013, Song 2013). Applications of the porous media theory have also been approached for biological tissue structures and in-vivo systems from MRI to calculate different restricted diffusion dependent parameters (Horsfield *et al.* 1994, Latour *et al.* 1994, Nicholson 2001, Kim *et al.* 2005, Novikov *et al.* 2010, Sigmund 2011, Le Bihan *et al.* 2012). This sub-section will discuss a brief outline of porous media theory for diffusion coefficient behaviors with diffusion time. In the porous medium the time dependence of the diffusion coefficient is divided into two regimes:

(i) **Short diffusion time limit**, where the mean square displacements of the molecules are much shorter than the restricting space, thus the boundary restricts only those molecules which are next to it initially. It modifies the diffusion coefficient compared to the free molecule's diffusion coefficient D_0.

Let S be the total area of the boundary exposed to the molecules and V is the volume of the fluid, from Einstein's diffusion equation,

Diffusion length $= (D_0 \Delta)^{\frac{1}{2}}$ where Δ is the diffusion time.

Volume of the molecules reaches the boundary $= S\sqrt{D\Delta}$

Volume fraction of those molecules $= \dfrac{S\sqrt{D\Delta}}{V}$

Then the remaining fraction of the free molecules not reaching the boundary

$= 1 - \dfrac{S\sqrt{D\Delta}}{V}$.

By analytical estimation of the mean value of the free molecules and molecules at the boundaries the time dependence of the diffusion coefficient is expressed as,

$$D(t) = D_0(1 - \frac{4}{9\sqrt{\pi}} \frac{S\sqrt{D\Delta}}{V}) \qquad\qquad (3.2.10)$$

Therefore, in the short diffusion time regime the diffusion coefficient $D(t)$ reflects the surface to volume ratio or volume fraction of the medium (Mitra *et al.* 1992, Mitra *et al.* 1993, Sen 2004).

(ii) **Long diffusion time limit**, where the diffusing molecules can travel distances larger than the restricting boundaries and may encounter many obstacles. In this regime $D(t)$ approaches a limiting, diffusion time independent, asymptotic non-zero finite value D_0, by a geometrical factor, known as the tortousity α. The long diffusion time diffusion coefficient relation can be expressed as,

$$D(t \rightarrow \infty) \rightarrow \frac{D_0}{\alpha}. \qquad\qquad (3.2.11)$$

The tortousity α is a dimensionless number and always greater than one, it is a property of the medium. Its relation to the geometry of the restricting space generally links with the connectivity between different restricting spaces, for example movement of the extracellular fluid molecules and correlation between different cells. However, definite tortousity cannot be calculated unless the diffusion time limit is very long, which is bounded by hardware limitations of current human scanners.

Where the diffusion time limits are known, Latour (1994) derived an equation using Páde approximation to interpolate between diffusion coefficient short time and long diffusion time asymptotic behaviours,

$$D(t) = Do\left\{1 - \left(1 - \frac{1}{\alpha}\right)\left(\frac{c\sqrt{\Delta}+\frac{\left(1-\frac{1}{\alpha}\right)\Delta}{\theta}}{\left(1-\frac{1}{\alpha}\right)+c\sqrt{\Delta}+\frac{\left(1-\frac{1}{\alpha}\right)\Delta}{\theta}}\right)\right\} \qquad\qquad (3.2.12)$$

where $c = \frac{4}{9\sqrt{\pi}}(\frac{S}{V})\sqrt{Do}$ and θ=0.02 sec is the approximation parameter used as time scaling factor.

Figure 3.2.11 shows a time dependence of the self-diffusion coefficient as a function of diffusion length for a porous media.
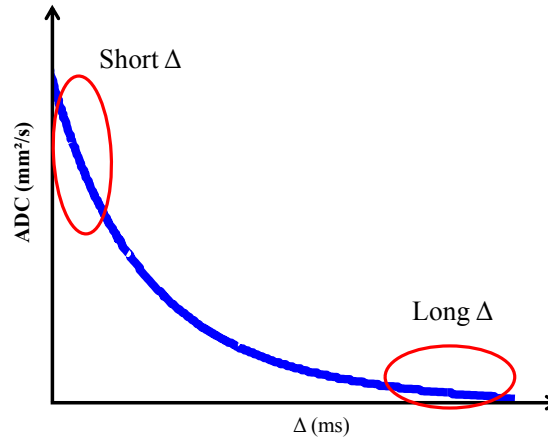
Figure 3.2.11 *Diffusion coefficient study of a porous media (using stimulated echo sequence), showing rapid decay at short diffusion time and asymptotic behaviour with long diffusion time (t→∞) (Loskutov et al. 2013).*

To our knowledge, the application of the porous media diffusion model has not been used for brachial plexus so far. In this thesis, the porous media model with Latour Equation (3.2.12) is used as a simple and practical way of characterizing diffusion time dependence of ADC from DWIBS acquired brachial plexus nerves and cord images.

3.2.7 Diffusion tensor imaging (DTI)

Non-uniform directional diffusion or anisotropic diffusion in biological tissues is studied by diffusion tensor imaging (DTI). DTI provides unique quantitative information of micro-structural and directional features of biological tissues, tracking of the neural fibres called 'DTI fibre tractography', etc. The effective diffusion tensor, D, is estimated from a series of diffusion weighted images (DWI). It describes the directional mobility and correlation of diffusing particles. The diffusion tensor is a 3×3 matrix that fully characterizes the molecular diffusion in 3D space. In the [x,y,z] reference frame the DTI signal can be expressed as:

$$S = \exp(-\sum_{i=x,y,z}\sum_{j=x,y,z} \boldsymbol{b}_{ij}\boldsymbol{D}_{ij}) \hspace{3cm} (3.2.13)$$

The mathematical properties of the diffusion tensor make it possible to extract several useful measures from diffusion tensor images. For example, the mean diffusivity (MD) is computed by averaging the diagonal elements of the matrix and the fractional anisotropy (FA) calculated from the eigenvalues of the matrix, etc. (Basser 1998,

Westin *et al.* 1999, Le Bihan *et al.* 2001, Basser *et al.* 2002, Melhem *et al.* 2002, Westin *et al.* 2002, Masutani *et al.* 2003, Hagmann *et al.* 2006)

The diffusion tensor model performs well in regions where there is only one fibre population, where it gives the fibre orientation clearly. However, it fails in regions with several fibre populations aligned along intersecting axes because it cannot be used to map several diffusion maxima at the same time. In such areas, the multi shell high angular resolution diffusion imaging (HARDI) sequence make it is possible to estimate the in-vivo brain WM fibre size, orientation and directions accurately (Zhang *et al.* 2011, Zhang *et al.* 2012, Dyrby *et al.* 2013, Le Bihan 2013, McNab *et al.* 2013, Tournier *et al.* 2013).

The next section discussed the basics of T2 relaxation and related quantitative measurements.

3.3 T2 relaxation measurement

T2 relaxation is one of the basic features of MRI. And T2 weighted images play a key role in clinical MRI of the spinal cord, showing sensitive changes with pathological conditions. The physical principles and basics of transverse relaxation, T2 and T2 weighted images have been discussed in Chapter 1. This section aims to discuss a brief overview of T2 relaxation measurements and its applications in peripheral nerves.

Studies of the intrinsic MR property of T2 relaxation of nerves and spinal cord of the brachial plexus are important, because the T2 value has the potential to characterize the mobility of water molecules and its exchange with the other molecules in the tissues. The T2 weighted images are often used for qualitative diagnostic information only. However, in principle it is straightforward to extend the principle of T2 weighting to produce quantitative measurements and gain further utility. This can be done by generating images with different values for TE. With long TR>>TE and constant spin density the signal intensities from the spin echo images decreases exponentially with TE. A series of images is generated so that,

$$S(t) = S_0 \exp\left(-\frac{TE_i}{T2}\right) \tag{3.3.1}$$

where the subscript i is used to denote the ith image with echo time TE_i and S_0 is proportional to the mobile proton density. Fitting the data to equation 3.3.1 with least square minimization, a value of T2 can be calculated over a region of interest on a voxel-by-voxel basis.

Often more than one relaxing transverse component is present in one ROI that can result in a multiexponential decay curves with different T2 values that likely represent the presence of separate compartments. A continuous distribution of relaxation times can be represented as the characteristics of T2 relaxation within that tissue,

$$S(t) = \int A(T2) \exp\left(-\frac{t}{T2}\right) dT2 \tag{3.3.2}$$

where A(T2) is the amplitude of the relaxing component at transverse relaxation time T2 (Larsson *et al.* 1998, Fenrich *et al.* 2001). For example, the transverse decay of the water proton magnetization in heterogeneous tissue such as nerve, white matter, or spinal cord be described by multi exponential components, both in vitro and in vivo. The individual T2 components have been interpreted in terms of different water

compartments, such as inter-axonal, axonal, and myelin domains, within the heterogeneous tissue. The T2 component features and changes in their proportions that are quantifiable in vivo provide identification and measure of neurological disorders, examples include compartmental degradation in white matter with multiple sclerosis and in the nerve wallerian degeneration (Does *et al.* 1994, Does *et al.* 1996, Whittall *et al.* 1997, Beaulieu *et al.* 1998, Does *et al.* 2002, Laule *et al.* 2007, Zheng *et al.* 2010). As an important quantitative MRI parameter, T2 relaxation measurements for brachial plexus nerves and spinal cord will be used in this thesis, in order to combine and relate with diffusivity, MTR and EMG parameters.

The next section discusses the basics of magnetization transfer (MT), z-spectra and related quantitative measurements.

3.4 Magnetization Transfer and the z-spectra study

Magnetizations transfer (MT) (Wolff *et al.* 1989, Balaban *et al.* 1992) generates contrast based on exchange of magnetization between bound protons of macromolecules and free protons of water, therefore can aid in the assessment of microstructure studies in MRI. MT imaging has been used in analyses of pathologies in CNS and PNS. The MT measurements and corresponding z-spectra analyses on the peripheral nerves can explore different possible transfer processes between nerves and surrounding tissues, which is a new approach for brachial plexus imaging studies. One of the aims of this thesis is to study the MT and z-spectra characteristics for brachial plexus nerves and spinal cord. On this perspective this section aimed to discuss basics of MT and z-spectra, z-spectra characteristics, a MT biophysical model, pulse sequences and optimization for MT imaging and finally applications of MT imaging.

3.4.1 Basics of Magnetization transfer and z-spectra

MT refers to the transfer of longitudinal magnetization from free water protons to bound macromolecular protons. In biological systems, the MT process describes changes in water proton spin states due to the interaction with the macromolecules and other proton containing molecules. In the context of MRI, the magnetization transfer experiment allows indirect observation of bound macromolecular protons (which have a very short T2~μs), by selective alterations in the magnetization of the bound protons with appropriate off-resonance RF pulses. This causes saturation of the bound protons that exchange with the bulk water (which has a long T2), which results in a loss of longitudinal magnetization and hence decrease the signal from the bulk water. Thus the magnitude of signal detected by this technique depends on the amount and the states of macromolecules in the biological tissues (Wolff *et al.* 1989, Balaban *et al.* 1992, Henkelman *et al.* 1993, Henkelman *et al.* 2001), Figure 3.4.1 shows a schematic diagram of the MT process.
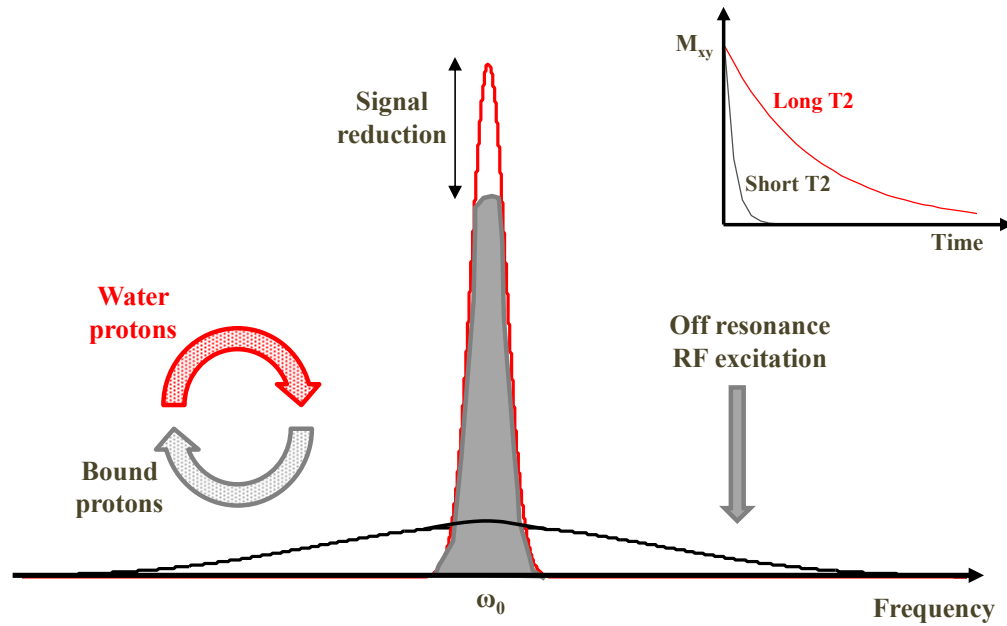
Figure 3.4.1 *The MT mechanism shows an off-resonance RF excitation saturates the bound protons (black) and then leads to a decrease in the free water (red) signal due to magnetization transfer process. The T2 relaxation processes for bound and free protons compared inset*.

MT effects in tissues are usually quantified using the magnetization transfer ratio:

$$MTR = 1 - M_{sat}/M_0 \qquad\qquad (3.4.1)$$

where M_{sat} is saturated magnetization, and M_0 is the non-saturated magnetization at a given irradiation frequency. The MTR is a semi-quantitative parameter, as its value depends on the type of MRI sequence and also the sequence parameters such as MT pulse off-resonance frequency, amplitude, repetition time and others. It is difficult to achieve high resolution and high sensitivity MTR images, due to high RF power deposition at high field or poor contrast to noise ratio at low field (Henkelman *et al.* 1993). However, by altering the irradiating frequencies, variations in the transfer processes can be explored and quantified. The MT effects can be represented by the z-spectrum. The z-spectrum shows the variations of MTR with offset frequencies. Figure 3.4.2 shows a schematic z-spectrum from brachial plexus.
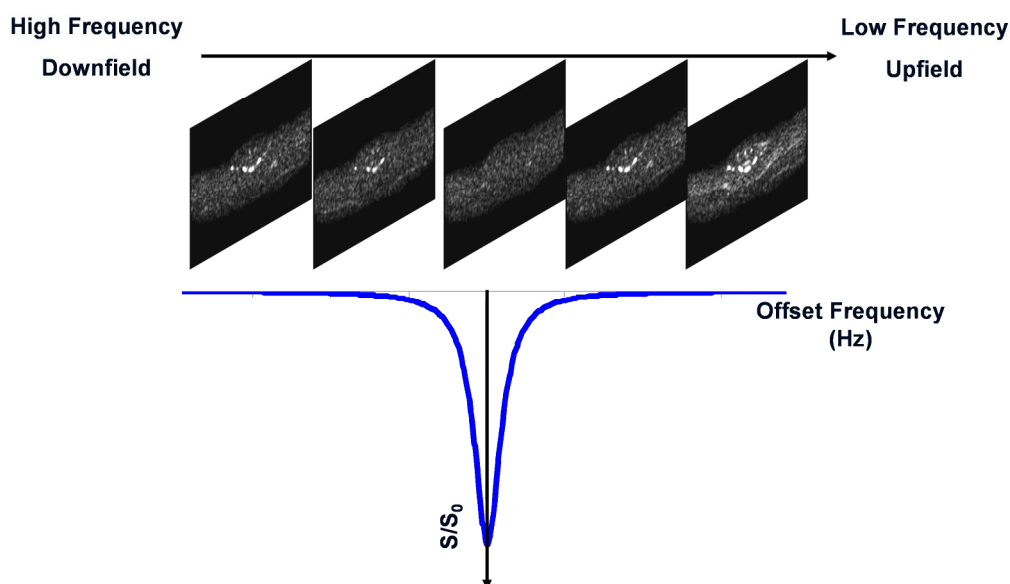
Figure 3.4.2 *MT imaging of brachial plexus at different offset frequencies and corresponding z-spectrum.*

Conventionally in the continuous wave (CW) method of measuring NMR spectra, the magnetic field was scanned from left to right, from low to high values. Thus with respect to the central water peak the right side has considered as upfield or shielded and left side considered as downfield or deshielded. Although later spectrometers gained the capability of scanning frequency, the NMR spectra sign convention has been kept in the z-spectra. In the z-spectra, the water peak is considered as centred at the zero frequency, negative frequency considered in the right and positive frequency on the left. Also it is important to mention that the frequency axis in z-spectra is shifted by 4.7 ppm to the right of water relative to the scale employed in conventional proton spectroscopy. The MT spectra scaling is schematically shown in figure 3.4.3.
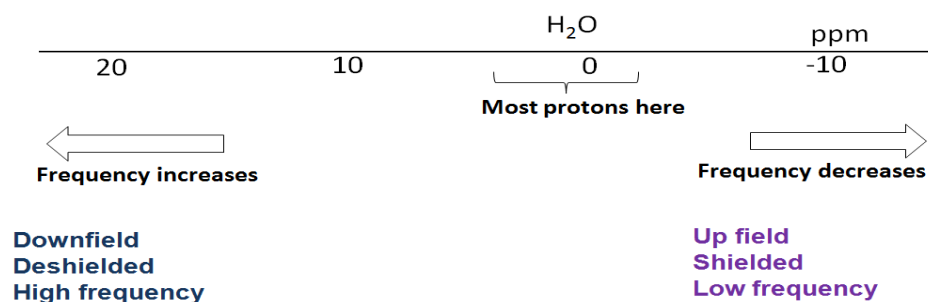
Figure 3.4.3 *The MT z-spectrum scale where the water peak is considered at zero frequency, negative frequencies in the right which are upfield and shielded and positive frequencies on the left which are downfield or deshielded. Effects of the other components are considered with respect to the position of the water frequency.*

The processes that taking place during magnetization transfer are schematically shown in Figure 3.4.4
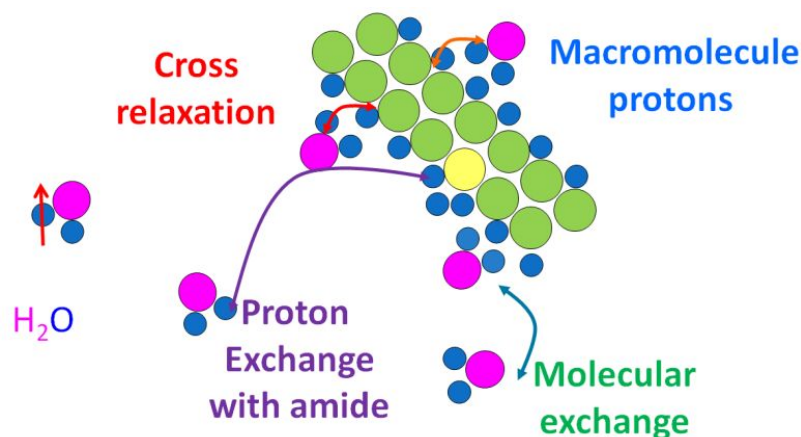
Figure 3.4.4 *Schematic illustration of possible transfer pathways in biological tissues. Transfer between mobile water protons and macromolecules with protein containing chain, cross relaxation between hydrogen in the free water molecule and hydrogen in the macromolecular chains; molecular exchange-between free water molecules and bound macromolecules; proton exchange-between water proton and proton in the amides. All these effects contribute different features in the z-spectrum.*

In general the z-spectra comprises

    I.   the direct water saturation (Mulkern *et al.* 1993, Smith *et al.* 2009)

    II.   magnetization transfer between macromolecular protons with short T2 and water making a broad hump in the z-spectrum. (Balaban *et al.* 1992, Henkelman *et al.* 1993, Henkelman *et al.* 2001, Filippi *et al.* 2007)

    III.   peaks at positive frequency offsets due to chemical exchange (chemical exchange saturation transfer: CEST) in particular amide proton transfer (APT) mediated by various water-exchangeable protons of macromolecules (van Zijl *et al.* 2011, Vinogradov *et al.* 2013, Zaiss *et al.* 2013).

    IV.   a peak at negative frequency offsets due to cross relaxation processes such as nuclear overhauser enhancement (NOE) due to dipolar coupling between the protons, mediated by aliphatic protons of lipids, proteins and various metabolites (Liepinsh *et al.* 1996, Mougin *et al.* 2010, Liu *et al.* 2013, Mougin *et al.* 2013).

These interfering effects strongly depend on the static magnetic field strength (B_0), the RF irradiation amplitude (B_1) and other experimental parameters (Henkelman *et al.* 1993, Henkelman *et al.* 2001, Vinogradov *et al.* 2013, Zaiss *et al.* 2013). The MT

effect for semi-solid macromolecules has resonance linewidth of several kHz in the z-spectrum. It results from the saturation transfer of surface macromolecular bound protons to the protons in water molecules linked with the macromolecular matrix. Macromolecular MT is governed by the proton transfer rate ($\sim 40s^{-1}$) and the concentration of the restricted protons pool. MT imaging has been frequently used for background suppression in MRI angiography and in the studies of demyelination in multiple sclerosis (Wolff *et al.* 1989, Henkelman *et al.* 1993, Henkelman *et al.* 2001, Stanisz *et al.* 2005).

The CEST effects are observed in the z-spectrum in the range of positive ppm values, on the left side of the water peak. CEST are caused by deshielding effects of 'labile' protons of functional groups producing corresponding z-spectrum peak at about +3.5ppm. In general the involved functional groups are amide (-NH), amine(-NH$_2$) and hydroxyl(-OH). CEST is mainly governed by the exchange rate, the concentration of the metabolite protons compared to the water protons, temperature and pH. The exchange rate varies in the range of s^{-1} (-NH) to $10^4 s^{-1}$ (-OH) depending on the type of molecule involved in the reactions. (Terreno *et al.* 2009, van Zijl *et al.* 2011, Zaiß *et al.* 2011, Desmond *et al.* 2012, Yadav *et al.* 2012, Vinogradov *et al.* 2013).

In the right or negative frequency side of the z-spectrum the nuclear overhauser enhancement (NOE) effects are observed. The NOE provides information about the magnetization transfer between water protons and protons in semisolid macromolecules (aliphatic protons situated in proteins, peptides and lipids) with short T2. Although NOE has long been observed in NMR, it has only recently been investigated with MR imaging. NOE is a phenomenon that occurs through space by dipolar coupling between water and aliphatic protons in close proximity. NOE generally resonate at 0~ -10ppm upfield of water, particularly at low saturation power; for example in the brain, NOE produces a peak at about -3.5ppm. The inter-atomic distances derived from the observed NOE can often help to confirm a precise molecular conformation, i.e. the three-dimensional structure of a molecule (Bloch 1946, Jones *et al.* 2013, Liu *et al.* 2013, Mougin *et al.* 2013, Zaiss *et al.* 2013). Figure 3.4.5 shows a MT z-spectrum from brain WM following the conventional frequency axes as protons with low field resonances from water have positive ppm and protons with upfield resonances have negative ppm showing the direct water saturation peak, CEST, APT effects. The next section describes the biophysical model of the MT process.
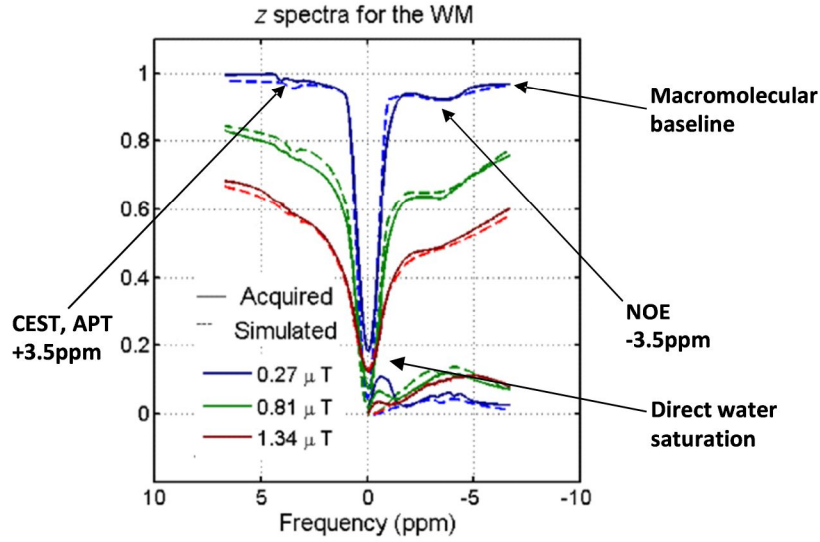
Figure 3.4.5 *In vivo z spectrum of WM, normalized magnetization of water protons as a function of saturation frequencies. The broad macromolecular MT determines the baseline. Direct water saturation governs the spectrum around central point 0 ppm. The CEST and APT effects are resolved around +3.5 ppm and NOE contributions around -3.5 ppm. The apparent effects depend on the saturation frequency powers (Mougin et al. 2013).*

3.4.2 Biophysical model of MT

The biophysical model of magnetization transfer assumes that the tissue is composed of two homogeneous compartments: protons associated with the free water molecules and protons bound to macromolecules. Considering that the longitudinal magnetization of the free and bound compartments are M^f and M^b respectively, the pool magnetization relaxes from initial magnetization M_0^f and M_0^b with relaxation parameters $R^f (= 1/T_1^f), R^b (= 1/T_1^b), T_2^f, T_2^b$ and exchange rate between the two pools R_x. The system longitudinal magnetization can be expressed as coupled differential equations using the modified Bloch equations expressed below,

$$\frac{dM_z^f(t)}{dt} = R^f \left(M_0^f - M_z^f(t) \right) - R_x \left(M_0^b M_z^f(t) \right) + R_x \left(M_0^f M_z^b(t) \right) +$$

$$\omega_1^x(t) M_y^f(t) \tag{3.4.2a}$$

$$\frac{dM_z^b(t)}{dt} = R^b \left(M_0^b - M_z^b(t) \right) - R_x \left(M_0^f M_z^b(t) \right) + R_x \left(M_0^b M_z^f(t) \right) -$$

$$W M_z^b(t) \tag{3.4.2b}$$

where x,y,z denote the Cartesian components of the magnetization vector, ω_1 is the term describing the shape and amplitudes of the pulses and W is the time dependent transition rate for the saturation of the bound protons expressed as,

$$W = \pi\omega_1^2 G(2\pi\Delta) \tag{3.4.3}$$

where $G(2\pi\Delta)$ is the lineshape function of the bound pool. It has previously been shown that a Lorentzian lineshape can be used to approximate the resonating behavior of macromolecular bound pool protons in the small spectral range for short T2 values of bound pools. Due to extremely short transverse relaxation time (~10μs) of the bound proton pool, the transverse magnetization of the bound proton pool is neglected. By solving the equations for different conditions of sequences, the relaxation properties and exchange properties of the two pools can be determined. The next section describes a brief overview of MT pulse sequences and necessary optimization.

3.4.3 Pulse sequences for MT

The straightforward MT saturation scheme uses a long rectangular pulse which is called continuous wave (CW) saturation, as shown in Figure 3.4.6a. However, a CW irradiation sequence is limited by SAR for human MRI systems, thus the saturation is performed by trains of RF pulses, controlling the pulse widths and heights to keep SAR within recommended limits. Thus to measure the whole z spectrum at different powers the applied sequence should be fast, low SAR with high spatial resolution and low distortions. The basic experiment for measuring saturation transfer effects consists of a pre saturation pulse with duration T_{sat} and irradiation field with amplitude B1 tuned to a frequency offset from the water proton resonance. This sequence is followed by excitation, spatial encoding and image acquisition. The saturation and readout can be sequential or interleaved depending on the different applications.

The sequences used for MT experiments can be divided into steady state and non-steady state (inversion recovery) techniques. The steady state sequences typically employ off-resonance RF irradiation to drive the bound-free proton pool system into a steady state from which the saturation transfer is measured, as shown in Figure 3.4.6b. In the inversion recovery non steady state sequence the magnetization is saturated and then an image is read (Figure 3.4.6c) (Henkelman *et al.* 2001, Zaiss *et al.* 2013).
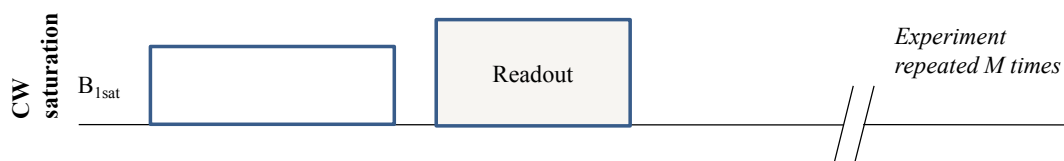
Figure 3.4.6a *CW saturation technique consists of a rectangular pulse of amplitude B1 and read out.*
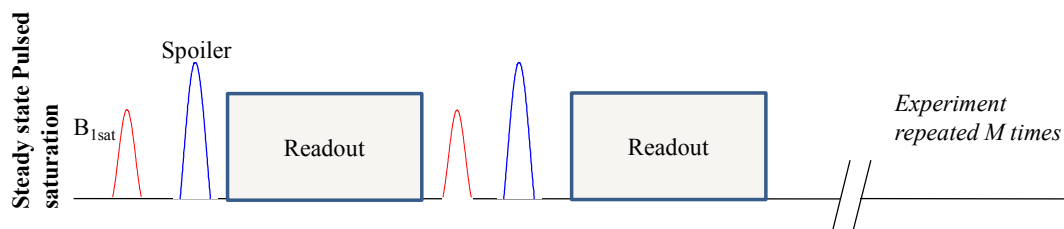
Figure 3.4.6b *Steady state pulsed saturation technique consists of saturation followed by the spoiler gradient and read out. In the pulsed SAT technique the pulse shape, flip angle, duty cycle provides further experimental parameters.*
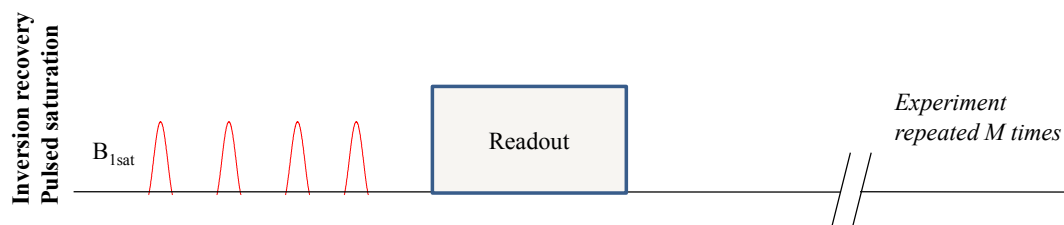
Figure 3.4.6c *Inversion recovery or non-steady state pulsed saturation technique consists of pulses and read out. In the pulsed SAT technique the pulse shape, flip angle, duty cycle provides further experimental parameters (Mougin 2013).*

3.4.4 Optimization of MT imaging

All the z-spectrum parameters MT, CEST, APT and NOE are strongly dependent on the concentrations and relaxation times of the molecules involved, as well as pulse sequence design. Therefore optimal design of MT acquisition is necessary for understanding the z-spectrum characteristics.

All the MT experiments are expected to benefit from increased field strength considering higher SNR and the longer T1 of water that can increase MT effects and pronounce the CEST, NOE peaks. However, for safety reasons power deposition of the saturating RF pulses is restricted. Trains of short pulses and appropriate interpulse delays can help to keep the SAR values within the recommended limit.

The MT sequences are sensitive to $\mathbf{B}_0$ and $\mathbf{B}_1$ field inhomogeneities, which can be a problem at higher field, in particular when asymmetry evaluations within the z-spectra

are required. It is possible to reduce the error via multiple frequency measurements. Also field inhomogeneities can be corrected by post processing by performing the measurements using several offset frequencies and B1 amplitudes, for example by using the water saturation shift referencing (WASSR) technique. In the WASSR technique an additional z-spectrum is collected at very low power where no CEST or NOE effects are present, then locate the water resonance for each voxel to correct the z-spectra, then interpolate every z-spectrum to find minimum (Kim *et al.* 2009, Zaiss *et al.* 2013).

3.4.5 Applications of MT imaging

MT imaging provides contrast within certain tissues (e.g. brain, liver, and muscle) or between different tissues (e.g. flowing blood and brain tissue). Tissues like blood and CSF are hardly affected by MT because of the low macromolecule concentration, and for this reason MT is used for background suppression in angiography. Similarly there is little MT effect in fat because the tissue is relatively homogeneous and the water in fat is not interacting with the fat. MT imaging has also applications in brain imaging and disorders such as studies of myelination changes during the development of white matter (WM) and grey matter (GM) demyelination in multiple sclerosis (Cercignani *et al.* 2001, Schmierer *et al.* 2007, Schmierer *et al.* 2008). In the MT imaging of the peripheral nerves, collagen tissue, myelin, and the proteins contained in the nerve fibres can be viewed as ''bound pool'', and these different elements possibly contribute to the MT spectra observed. Thus the MT study is of interest in peripheral nerves (such as spinal cord) research and its disorders (Kuntz *et al.* 1996, Filippi *et al.* 2007, Gambarota *et al.* 2007, Gambarota 2009, Gambarota *et al.* 2009, Smith *et al.* 2009, Dula *et al.* 2010, Karampinos *et al.* 2012).

As a new approach MTR values and z-spectra asymmetry for brachial plexus nerves and spinal cord will be studied in this thesis, and these observations related with other quantitative parameters such as, diffusivity, T2 and EMG measurements.

3.5 EMG in the form of Nerve Conduction Study

MRI can produce higher resolution and clear images of soft tissues and forms the gold standard for neurological imaging studies, and has significant important applications in neurophysiology. However, MRI is not widely available and expensive on maintenance. Electromyogram (EMG) is a method of studying nerve conduction characteristics which is potentially cost effective and easy to setup. Also EMG provides better temporal information compared to MRI. The aim of this thesis is to combine EMG and MRI for peripheral nerves in the brachial plexus. On this perspective, this section aims to discuss the basics of EMG, nerve conduction study, the responses observed in nerve conduction studies, such as the M-response and F-response, and applications of these observations.

3.5.1 Basics of EMG

EMG and nerve conduction velocity studies (NCS) form the core of the electrophysiological studies. For EMG, needle electrodes with very small exposed tips are used to get localized responses from muscle fibres. Usually expert physicians perform the measurements and identify patterns which have been related to certain disorders of muscles and nerves (Aminoff 1978, Weiss *et al.* 2004). In the NCS, a motor nerve trunk is stimulated artificially over the surface at any suitable point using an electrical pulse of sufficient strength which produces action potentials simultaneously in all the nerve fibres in the nerve trunk. Propagating to the muscle group served by this nerve trunk it gives rise to a distinctive reproducible pattern of combined action potential related to the characteristics of the nerve and muscle (Kimura 2013). Both EMG and NCS studies provide differential diagnosis to localize neuromuscular disorders and also assess their severity. These techniques are often used to diagnose disorders affecting the primary motor neurons (anterior horn cells), sensory neurons (dorsal root ganglia), nerve roots, brachial and lumbosacral plexuses, neuromuscular junctions, peripheral nerves, and muscles (Aminoff 1978, Binnie *et al.* 1995, Preston *et al.* 2012, Kimura 2013).

In routine EMG and NCS studies, electrical signals of the muscle movement as compound muscle action potentials (CMAPs) are measured. The CMAPs result due to voluntary or motor stimulation of nerves, are recorded from the body by placing

needle or surface electrodes over the muscle. The purpose of recording CMAPs is primarily to evaluate conduction in various proximal nerves and assess neural conduction time across the nerve path, and measure the intrinsic electrical activity of the muscle (Aminoff 1978, Binnie *et al.* 1995).

The NCS are performed to measure CMAPs for motor nerves, sensory nerve action potentials (SNAP) for sensory nerves, compound nerve action potentials (CNAPs) for mixed (sensory and motor) nerves and late responses such as F-responses and H-reflexes.

3.5.2 Physiology of nerve conduction

Nerves conduct responses (sensory or motor) as a travelling wave of depolarization along their axons. The basic structure of nerve and axons are discussed in Chapter 1. At rest, the axonal membrane is negatively polarized inside compared to the outside. The resting potential results from the concentration of Na^+ and Cl^- being higher in the extracellular space, and concentration of K^+ and larger anions being greater inside the axon. When an axon is conducting an impulse, voltage-dependent channels open and allow an influx of sodium (Na+) ions. This influx of positive ions depolarizes the axon, changes the resting potential further down the axon, causing those channels to open and thus creates a wave of depolarization (Krarup 2006) shown in Figure 3.5.1.

The myelin acts as an excellent insulator and creates fast propagation of the depolarization through the axon. This occurs due to the depolarization that takes place only at the inter-nodal regions of the axon. That nodal difference creates a type of 'jumping' propagation of the action potential called the saltatory conduction shown in Figure 3.5.2. The saltatory conduction technique increase the conduction velocity by 10-fold. Thus velocities of the myelinated axons are much higher (40 to 70 m/sec), compared to the unmyelinated axons (1−5 m/sec).
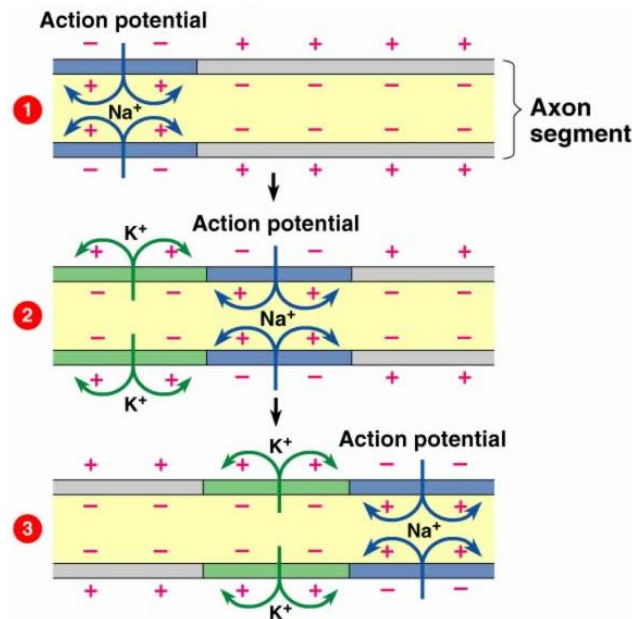
Figure 3.5.1 *Schematic single axon action potential creation and propagation from left to right through the steps 1, 2, 3, etc. (Preston et al. 2012).*
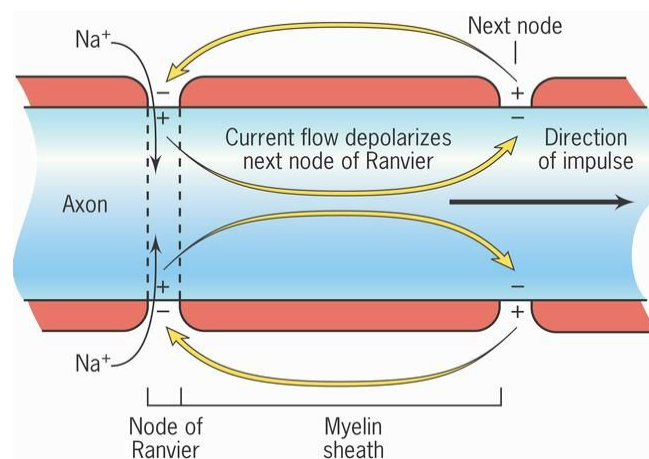
Figure 3.5.2 *Saltatory conduction of action potential through the myelinated axon (Preston et al. 2012).*

3.5.3 Nerve conduction velocity measurements

When a nerve is electrically stimulated anywhere along its course, waves of depolarization will travel in both directions from that point; from the spine towards the motor nerves, called orthodromic conduction, and towards the spine from the sensory nerves, called antidromic conduction. Motor and sensory nerve action potentials can be measured through skin electrodes if the nerve is sufficiently superficial. The conduction velocities of the nerves measured from the latency as travelling time and travelled distance. The onset latency represents the arrival time of the fastest-conducting nerve fibres.

In the sensory nerves, latency is solely dependent on the speed of conduction of the fastest fibres and the distance the wave of depolarization travels. Therefore, conduction velocity can be calculated directly by measuring the time it takes for the propagated action potential to travel the measured distance (Bertorini 2006). However, motor nerves conduct across a myoneural junction, thus the conduction velocity cannot be measured directly. Thus for motor nerve conduction velocity measurements, two sites are stimulated over the nerve as proximal stimulation and distal stimulation and recorded from the connected muscle. The difference in distance from the two stimulation sites is then divided by the difference in latencies of the two action potentials (Levin 2006), schematically shown in Figure 3.5.3. Therefore, motor nerve conduction velocity (MNCV) $= \frac{Difference\ in\ distance}{Difference\ in\ time}$
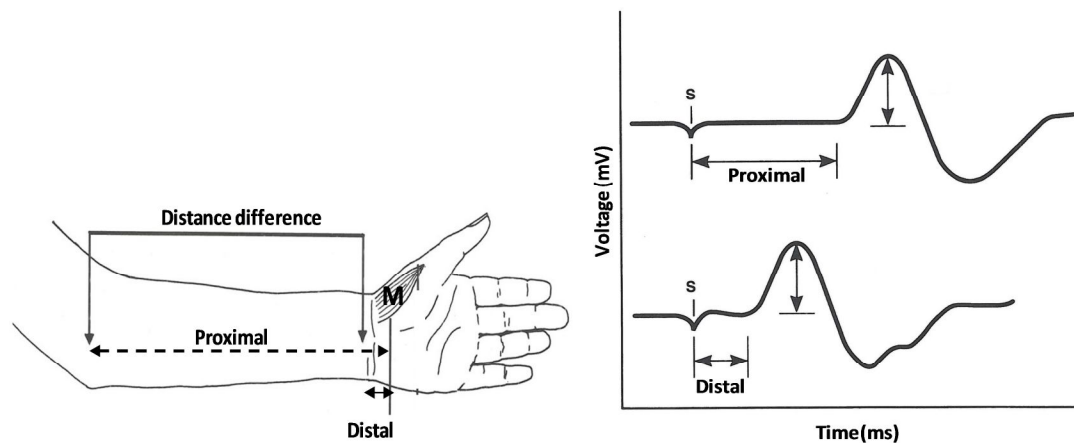
Figure 3.5.3 *Schematic diagram of MNCV measurements. Left side M is the recording electrode, arrows shows the proximal and distal stimulation sites over the median nerve. Right side the CMAP recorded after distal and proximal stimulations. MNCV can be measured from the difference between stimulation sites and corresponding latencies.*

The nerve stimulators are normally two metal electrodes placed 1.5 to 3cm apart on the surface of the skin. In order to accurately stimulate a nerve, it is necessary to find the location of the nerve by recalling the nerve's anatomy. When stimulating, in most cases the cathode electrode is placed towards the direction in which the nerve is to be stimulated. To study the responses the strength of the stimulation should be sufficient to ensure all nerve fibres are stimulated. Supramaximal levels at 10~20% more than the maximal response are required to avoid the submaximal stimulation due to movement of the electrode. However, care should be taken not to 'over stimulate' (Yasunami *et al.* 2005, Nodera *et al.* 2006, Hakimi *et al.* 2013). Three electrodes are

used to record a potential in nerve conduction studies and electromyography. They are the active, reference and ground electrodes.

Active electrode: The active electrode (named E1 or G1) should be placed over the muscle preferably over the motor point, where the nerve enters the muscle for motor conduction studies. During sensory conduction studies, the active electrode should be placed directly over the nerve where the nerve is most superficial.

Reference electrode: The reference electrode (named E2 or G2) should be placed on a nearby tendon or bone away from the muscle when attempting to record a CMAP.

Ground electrode: The ground electrode should be placed between the stimulating electrode and the recording electrode. Usually the ground is larger than the recording electrodes and provides a large surface area in contact with the patient. Grounding is important for obtaining a response that is free of too much artifact.

Conduction gel should be used for all electrodes to ensure good electrical contact with minimum impedance. However, the conventional NCV measures the onset of the responses, which corresponds to the fastest nerve fibres only; it does not give any information of the slower axons in a nerve trunk.

3.5.4 Late responses

Late muscle responses occur over a variable period of time after the direct or orthodromic M-responses when a peripheral nerve is stimulated. The late responses include the H-reflex and the F-response at comparable delays after the M-response (Kimura 1997, Oberthuer *et al.* 2001, Preston *et al.* 2012).

3.5.4.1 H-reflex

The H-reflex is a monosynaptic or oligosynaptic spinal reflex involving both motor and sensory fibres evolved after the M-response. The H-reflex primarily assesses afferent and efferent S1 fibres. The H-reflex plays an important role in distinguishing between S1 from L5 radiculopathies. Clinically, L5 and S1radiculopathies may appear similar on EMG due to the overlap of myotomes.
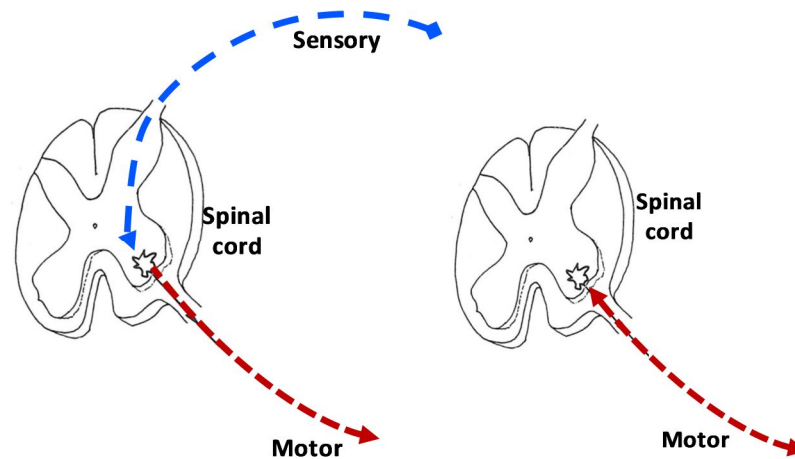
Figure 3.5.4 *H-reflex showing sensory and motor response conduction path (left); F-response backfiring from spinal cord motor path (right).*

3.5.4.2 F-response

The F-response is a motor late response, named so because they were first detected from the peroneal innervated foot muscle by Magladery and Mcdougal (1950). The F-response is not a reflex but pure motor response, because (i) the F-responses present in deafferented nerves, (ii) the motor units in the F-response are present only if the same units are present in the direct motor response, and (iii) single fibre EMG analysis indicates that an F-response requires direct activation of motor axons. F-responses provide an opportunity of examining transmission between stimulation sites in the arm and the leg nerves such as Median, Ulnar, Peroneal, Tibial nerves and the related motor neurons in the cervical and lumbosacral cord (Kimura 2006, Pastore-Olmedo *et al.* 2009).

Under identical conditions of stimulation and recording F-responses vary in shape, amplitude and latency on repeated stimulation; sometimes there will be none (Preston *et al.* 1998, Katirji 2007). This occurs because F-responses depend on the limited number of individual motor neurons as about a fraction of 1~2% of the motor neuron pools, those motor units are activated infrequently with antidromic stimulation. Thus, due to the inherent randomness, meaningful analysis of F-responses requires evaluating several responses following a series of stimuli in a systematic manner (Oberthuer *et al.* 2001, Guiloff 2006). Figure 3.5.5 shows few F-responses after supramaximal stimulations.
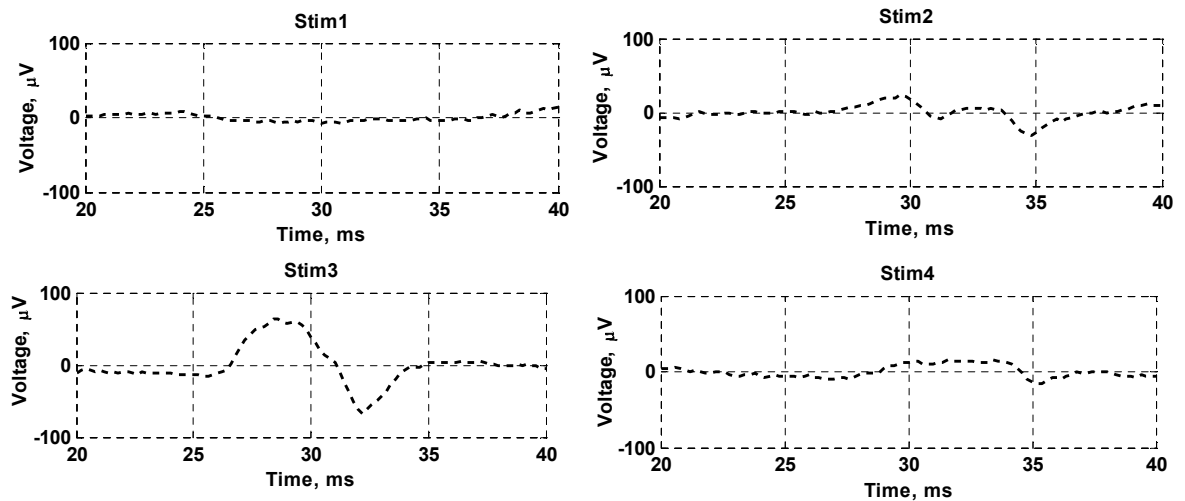
Figure 3.5.5 *F-response and changing behavior with different consecutive stimulations at Median nerve. Second, third and fourth stimulation creates F-response at amplitude ranges 20μV or above.*

3.5.4.3 Measuring parameters from F-response

There are several parameters associated with F-responses; a brief description is given below.

F-latencies are the most frequently reported parameter of F-response analysis, measured from the stimulus artefact to the beginning of the evoked potential either positive or negative with minimum amplitude 20 μV. F latencies are the latencies of the fastest fibres contributing to any F-response. These latencies are directly related to the height, limb length, and age (Fisher 1982, 2007).

F-choronodispersion is defined as the scatter or dispersion of the relative latencies between the maximum and minimum latency values and provides an estimation of the range of conduction properties of the activated motor fibres. These values are not correlated with age, sex or height (Fisher 2007) .

F-response persistence is the number of definable F-responses divided by the number of stimuli. F-persistence is not correlated with height or age. Persistence relates to the state of excitability in the neuronal pool examined (Pastore-Olmedo *et al.* 2009).

Distribution of F-latencies (DFL) is recently proposed on the basis of randomness of F-responses as a statistical frequency distribution of the F-latencies, called the Distribution of F-latency or DFL (Rabbani *et al.* 2007).

Parameters like *F-response amplitude, F-conduction velocity, F-response duration, F/M ratio*, etc. are also commonly derived from F-responses (Guiloff 2006). F-responses have a recognized role in the electrodiagnostic evaluation of peripheral

nerve dysfunction. In polyneuropathies, F-responses can prove the presence as well as diagnose the nature of disorders. Current evidence supports that F-response having a role in electrophysiological evaluation of radiculopathies (Krishnamachari *et al.* 2007, Pinheiro *et al.* 2008). EMG in the form of DFL for brachial plexus is a new non-invasive technique that has the potential to identify the neurological disorders and it can also propose the motor fibre distribution within the nerve. Thus DFL measurements and quantitative MRI will be studied in this thesis.

Discussions

This chapter has described different types of methods of studying the brachial plexus that have great importance and clinical applications over the globe. In the anatomical MRI section several sequences were observed, producing clear and high resolution images of the brachial plexus from the 3T Philips Achieva scanner. Such sequences can be used for qualitative assessment of disorders.

The DWIBS applications, with surrounding tissue signal suppression and highlighting of the nerves has potential for peripheral nerve imaging of brachial plexus. This sequence has versatility to combine with other quantitative MRI sequences to highlight the soft tissues. Other sophisticated and dedicated diffusion MRI methods such as ax-caliber, CHARMED, DTI can exploit microstructure, nature of diffusion and directionality of the axons.

T2 relaxation measurements have the potential to study the intracellular and extracellular space microstructures and myelin of the peripheral nerves. Magnetization Transfer imaging and z-spectra measurements have the potential to study the myelin content, remyelination, and demyelination of peripheral nerves. The EMG study has the potential to diagnose the clinical conditions in the nerve path and roots as well.

The goal of this thesis is to establish robust techniques of brachial plexus study using MRI and EMG in the form of DFL. Since quantitative studies of MRI and EMG to study the brachial plexus is still a new field, further studies are expected to give useful solutions for its clinical applications, and are expected to research breakthroughs. This chapter described the background of MRI and EMG for brachial plexus. The practical implementations of these techniques will be focused in the remaining chapters of this thesis.

References:

Adachi, Y., N. Sato, T. Okamoto, M. Sasaki, H. Komaki, F. Yamashita, J. Kida, T. Takahashi and H. Matsuda (2011). "Brachial and lumbar plexuses in chronic inflammatory demyelinating polyradiculoneuropathy: MRI assessment including apparent diffusion coefficient." Neuroradiology 53(1): 3-11.

Aggarwal, M., M. V. Jones, P. A. Calabresi, S. Mori and J. Zhang (2012). "Probing mouse brain microstructure using oscillating gradient diffusion MRI." Magnetic Resonance in Medicine 67(1): 98-109.

Alexander, D. C. (2007). Axon radius measurements in vivo from diffusion MRI: a feasibility study. Computer Vision, 2007. ICCV 2007. IEEE 11th International Conference on.

Alexander, D. C. (2008). "A general framework for experiment design in diffusion MRI and its application in measuring direct tissue-microstructure features." Magnetic Resonance in Medicine 60(2): 439-448.

Aminoff, M. J. (1978). Electromyography in clinical practice, Addison-Wesley Publishing Company, Medical/Nursing Division.

Andreisek, G., D. W. Crook, D. Burg, B. Marincek and D. Weishaupt (2006). "Peripheral Neuropathies of the Median, Radial, and Ulnar Nerves: MR Imaging Features." RadioGraphics 26(5): 1267-1287.

Aralasmak, A., K. Karaali, C. Cevikol, H. Uysal and U. Senol (2010). "MR Imaging Findings in Brachial Plexopathy with Thoracic Outlet Syndrome." American Journal of Neuroradiology 31(3): 410-417.

Assaf, Y. and P. J. Basser (2005). "Composite hindered and restricted model of diffusion (CHARMED) MR imaging of the human brain." NeuroImage 27(1): 48-58.

Assaf, Y., T. Blumenfeld-Katzir, Y. Yovel and P. J. Basser (2008). "AxCaliber: A method for measuring axon diameter distribution from diffusion MRI." Magnetic Resonance in Medicine 59(6): 1347-1354.

Assaf, Y., R. Z. Freidlin, G. K. Rohde and P. J. Basser (2004). "New modeling and experimental framework to characterize hindered and restricted water diffusion in brain white matter." Magnetic Resonance in Medicine 52(5): 965-978.

Balaban, R. S. and T. L. Ceckler (1992). "Magnetization transfer contrast in magnetic resonance imaging." Magnetic resonance quarterly 8(2): 116-137.

Basser, P. J. (1998). Fibre-tractography via diffusion tensor MRI (DT-MRI). Proceedings of the 6th Annual Meeting ISMRM, Sydney, Australia.

Basser, P. J. and D. K. Jones (2002). "Diffusion-tensor MRI: theory, experimental design and data analysis – a technical review." NMR in Biomedicine 15(7-8): 456-467.

Beaulieu, C., F. R. Fenrich and P. S. Allen (1998). "Multicomponent water proton transverse relaxation and T-2-discriminated water diffusion in myelinated and nonmyelinated nerve." Magnetic Resonance Imaging 16(10): 1201-1210.

Bertorini, T. E. (2006). Chapter 7 Sensory nerve conduction studies. Handbook of Clinical Neurophysiology. K. Jun, Elsevier. Volume 7: 155-176.

Bilbey, J. H., R. G. Lamond and R. F. Mattrey (1994). "MR imaging of disorders of the brachial plexus." Journal of Magnetic Resonance Imaging 4(1): 13-18.

Binnie, C. D. and J. W. Osselton (1995). Clinical neurophysiology: EMG, nerve conduction and evoked potentials, Butterworth-Heinemann.

Blair, D., S. Rapoport, H. Sostman and O. Blair (1987). "Normal brachial plexus: MR imaging." Radiology 165(3): 763-767.

Bloch, F. (1946). "NUCLEAR INDUCTION." Physical Review 70(7-8): 460-474.

Bono, C. M., G. Ghiselli, T. J. Gilbert, D. S. Kreiner, C. Reitman, J. T. Summers, J. L. Baisden, J. Easa, R. Fernand, T. Lamer, P. G. Matz, D. J. Mazanec, D. K. Resnick, W. O. Shaffer, A. K. Sharma, R. B. Timmons and J. F. Toton (2011). "An evidence-based clinical guideline for the diagnosis and treatment of cervical radiculopathy from degenerative disorders." Spine Journal 11(1): 64-72.

Callaghan, P. T. (1995). "Pulsed-Gradient Spin-Echo NMR for Planar, Cylindrical, and Spherical Pores under Conditions of Wall Relaxation." Journal of Magnetic Resonance, Series A 113(1): 53-59.

Callaghan, P. T. (1996). "NMR imaging, NMR diffraction and applications of pulsed gradient spin echoes in porous media." Magnetic Resonance Imaging 14(7–8): 701-709.

Callaghan, P. T., A. Coy, D. Macgowan, K. J. Packer and F. O. Zelaya (1991). "DIFFRACTION-LIKE EFFECTS IN NMR DIFFUSION STUDIES OF FLUIDS IN POROUS SOLIDS." Nature 351(6326): 467-469.

Callaghan, P. T. and J. Stepišnik (1996). "Generalized analysis of motion using magnetic field gradients." Advances in Magnetic and Optical Resonance 19: 325-388.

Cercignani, M., M. Bozzali, G. Iannucci, G. Comi and M. Filippi (2001). "Magnetisation transfer ratio and mean diffusivity of normal appearing white and grey matter from patients with multiple sclerosis." Journal of Neurology, Neurosurgery & Psychiatry 70(3): 311-317.

Chalian, M., N. Faridian-Aragh, T. Soldatos, K. Batra, A. J. Belzberg, E. H. Williams, J. A. Carrino and A. Chhabra (2011). "High-resolution 3T MR Neurography of Suprascapular Neuropathy." Academic Radiology 18(8): 1049-1059.

Chhabra, A., G. Andreisek, T. Soldatos, K. C. Wang, A. J. Flammang, A. J. Belzberg and J. A. Carrino (2011). "MR Neurography: Past, Present, and Future." American Journal of Roentgenology 197(3): 583-591.

Chhabra, A., A. Flammang, A. Padua, J. A. Carrino and G. Andreisek (2014). "Magnetic Resonance Neurography Technical Considerations." Neuroimaging Clinics of North America 24(1): 67-+.

Chhabra, A., P. P. Lee, C. Bizzell and T. Soldatos (2011). "3 Tesla MR neurography—technique, interpretation, and pitfalls." Skeletal Radiology 40(10): 1249-1260.

Colvin, D. C., T. E. Yankeelov, M. D. Does, Z. Yue, C. Quarles and J. C. Gore (2008). "New Insights into Tumor Microstructure Using Temporal Diffusion Spectroscopy." Cancer Research 68(14): 5941-5947.

de Verdier, H. J., P. M. Colletti and M. R. Terk (1993). "MRI of the brachial plexus: A review of 51 cases." Computerized Medical Imaging and Graphics 17(1): 45-50.

Denno, J. J. and G. R. Meadows (1991). "EARLY DIAGNOSIS OF CERVICAL SPONDYLOTIC MYELOPATHY - A USEFUL CLINICAL SIGN." Spine 16(12): 1353-1355.

Desmond, K. L. and G. J. Stanisz (2012). "Understanding Quantitative Pulsed CEST in the Presence of MT." Magnetic Resonance in Medicine 67(4): 979-990.

Does, M. and R. Snyder (1994). "T2 relaxation of peripheral nerve measured in vivo." Magnetic Resonance Imaging 13(4): 575-580.

Does, M. D. and J. C. Gore (2002). "Compartmental study of T1 and T2 in rat brain and trigeminal nerve in vivo." Magnetic Resonance in Medicine 47(2): 274-283.

Does, M. D. and R. E. Snyder (1996). "Multiexponential T2 relaxation in degenerating peripheral nerve." Magnetic Resonance in Medicine 35(2): 207-213.

Drobnjak, I., B. Siow and D. C. Alexander (2010). "Optimizing gradient waveforms for microstructure sensitivity in diffusion-weighted MR." Journal of Magnetic Resonance 206(1): 41-51.

Du, R., K. I. Auguste, C. T. Chin, J. W. Engstrom and P. R. Weinstein (2010). "Magnetic resonance neurography for the evaluation of peripheral nerve, brachial plexus, and nerve root disorders." Journal of neurosurgery 112(2): 362-371.

Dula, A. N., D. F. Gochberg, H. L. Valentine, W. M. Valentine and M. D. Does (2010). "Multiexponential T2, magnetization transfer, and quantitative histology in white matter tracts of rat spinal cord." Magnetic Resonance in Medicine 63(4): 902-909.

Dyrby, T. B., L. V. Sogaard, M. G. Hall, M. Ptito and D. C. Alexander (2013). "Contrast and stability of the axon diameter index from microstructure imaging with diffusion MRI." Magnetic Resonance in Medicine 70(3): 711-721.

Fenrich, F., C. Beaulieu and P. Allen (2001). "Relaxation times and microstructures." NMR in Biomedicine 14(2): 133-139.

Filippi, M. and M. A. Rocca (2007). "Magnetization Transfer Magnetic Resonance Imaging of the Brain, Spinal Cord, and Optic Nerve." Neurotherapeutics 4(3): 401-413.

Filler, A., M. Kliot, H. Winn, J. Tsuruda, C. Hayes, F. Howe, J. Griffiths, A. Filler, B. Bell and A. Filler (1993). "Magnetic resonance neurography." The Lancet 341(8846): 659-661.

Fisher, M. A. (1982). "F-RESPONSE LATENCY DETERMINATION." Muscle & Nerve 5(9): 730-734.

Fisher, M. A. (2007). "F-waves - Physiology and clinical uses." Thescientificworldjournal 7: 144-160.

Frahm, J., K. D. Merboldt, W. Hanicke and A. Haase (1985). "STIMULATED ECHO IMAGING." Journal of Magnetic Resonance 64(1): 81-93.

Franconi, F., C. B. Sonier, F. Seguin, A. Le Pape and S. Akoka (1994). "Acquisition of spin echo and stimulated echo by a single sequence: Application to MRI of diffusion." Magnetic Resonance Imaging 12(4): 605-611.

Gambarota, G. (2009). "T2 Relaxometry of Human Median Nerve." Semin Musculoskelet Radiol 13(01): 024-028.

Gambarota, G., R. Mekle, V. Mlynarik and G. Krueger (2009). "NMR properties of human median nerve at 3 T: proton density, T1, T2, and magnetization transfer." Journal of Magnetic Resonance Imaging 29(4): 982-986.

Gambarota, G., A. Veltien, D. Klomp, N. Van Alfen, R. V. Mulkern and A. Heerschap (2007). "Magnetic resonance imaging and T2 relaxometry of human median nerve at 7 Tesla." Muscle & Nerve 36(3): 368-373.

Gasparotti, R., G. Lodoli, A. Meoded, F. Carletti, D. Garozzo and S. Ferraresi (2013). "Feasibility of Diffusion Tensor Tractography of Brachial Plexus Injuries at 1.5 T." Investigative Radiology 48(2): 104-112.

Gore, J. C., J. Xu, D. C. Colvin, T. E. Yankeelov, E. C. Parsons and M. D. Does (2010). "Characterization of tissue structure at varying length scales using temporal diffusion spectroscopy." NMR in Biomedicine 23(7): 745-756.

Gross, B. and R. Kosfeld (1969). "Anwendung der spin-echo-methode der messung der selbstdiffusion." Messtechnik 77: 171-177.

Guggenberger, R., D. Markovic, P. Eppenberger, A. Chhabra, A. Schiller, D. Nanz, K. Prüssmann and G. Andreisek (2012). "Assessment of Median Nerve with MR Neurography by Using Diffusion-Tensor Imaging: Normative and Pathologic Diffusion Values." Radiology 265(1): 194-203.

Guiloff, R. J. (2006). Chapter 9 Late responses (F- and A-waves): methodology and techniques. Handbook of Clinical Neurophysiology. K. Jun, Elsevier. Volume 7: 189-235.

Hagmann, P., L. Jonasson, P. Maeder, J.-P. Thiran, V. J. Wedeen and R. Meuli (2006). "Understanding Diffusion MR Imaging Techniques: From Scalar Diffusion-weighted Imaging to Diffusion Tensor Imaging and Beyond1." Radiographics 26(suppl 1): S205-S223.

Hahn, E. L. (1950). "Spin echoes." Physical review 80(4): 580.

Hakimi, K. and D. Spanier (2013). "Electrodiagnosis of Cervical Radiculopathy." Physical Medicine and Rehabilitation Clinics of North America 24(1): 1-12.

Henkelman, R. M., X. Huang, Q.-S. Xiang, G. J. Stanisz, S. D. Swanson and M. J. Bronskill (1993). "Quantitative interpretation of magnetization transfer." Magnetic Resonance in Medicine 29(6): 759-766.

Henkelman, R. M., X. M. Huang, Q. S. Xiang, G. J. Stanisz, S. D. Swanson and M. J. Bronskill (1993). "QUANTITATIVE INTERPRETATION OF MAGNETIZATION-TRANSFER." Magnetic Resonance in Medicine 29(6): 759-766.

Henkelman, R. M., G. J. Stanisz and S. J. Graham (2001). "Magnetization transfer in MRI: a review." NMR in Biomedicine 14(2): 57-64.

Horsfield, M. A., G. J. Barker and W. I. McDonald (1994). "Self-diffusion in CNS tissue by volume-selective proton NMR." Magnetic Resonance in Medicine 31(6): 637-644.

Jones, C. K., A. Huang, J. Xu, R. A. E. Edden, M. Schaer, J. Hua, N. Oskolkov, D. Zaca, J. Zhou, M. T. McMahon, J. J. Pillai and P. C. M. van Zijl (2013). "Nuclear Overhauser enhancement (NOE) imaging in the human brain at 7 T." Neuroimage 77: 114-124.

Jones, D. K. (2011). "Diffusion MRI: Theory, Methods, and Applications."

Jones, D. K. and M. Cercignani (2010). "Twenty-five pitfalls in the analysis of diffusion MRI data." NMR in Biomedicine 23(7): 803-820.

Karampinos, D. C., G. Melkus, T. M. Shepherd, S. Banerjee, E. U. Saritas, A. Shankaranarayanan, C. P. Hess, T. M. Link, W. P. Dillon and S. Majumdar (2012). "Diffusion tensor imaging and T2 relaxometry of bilateral lumbar nerve roots: feasibility of in-plane imaging." NMR in Biomedicine: n/a-n/a.

Katirji, B. (2007). Electromyography in clinical practice: a case study approach, Mosby Elsevier.

Kim, M., J. Gillen, B. A. Landman, J. Zhou and P. C. M. van Zijl (2009). "Water Saturation Shift Referencing (WASSR) for Chemical Exchange Saturation Transfer (CEST) Experiments." Magnetic Resonance in Medicine 61(6): 1441-1450.

Kim, S., G. Chi-Fishman, A. S. Barnett and C. Pierpaoli (2005). "Dependence on diffusion time of apparent diffusion tensor of ex vivo calf tongue and heart." Magnetic Resonance in Medicine 54(6): 1387-1396.

Kimura, J. (1997). "Facts, fallacies, and fancies of nerve conduction studies: Twenty-first annual Edward H. Lambert lecture." Muscle & nerve 20(7): 777-787.

Kimura, J. (2006). Peripheral nerve diseases, Elsevier.

Kimura, J. (2013). Electrodiagnosis in diseases of nerve and muscle: principles and practice, Oxford university press.

Koh, D. M., H. C. Thoeny, Y. C. O. N. Amoozadeh, M. C. O. N. Blackledge and D. J. C. O. N. Collins (2010). Diffusion-Weighted MR Imaging: Applications in the Body, Springer.

Krarup, C. (2006). Chapter 2 Physiology and function. Handbook of Clinical Neurophysiology. K. Jun, Elsevier. Volume 7: 23-61.

Krishnamachari, S., B. H. Tracey and D. Iyer (2007). Detection and Classification of Motor Nerve Late-wave Activity. Engineering in Medicine and Biology Society, 2007. EMBS 2007. 29th Annual International Conference of the IEEE.

Kuntz, C., L. Blake, G. Britz, A. Filler, C. E. Hayes, R. Goodkin, J. Tsuruda, K. Maravilla and M. Kliot (1996). "Magnetic Resonance Neurography of Peripheral Nerve Lesions in the Lower Extremity." Neurosurgery 39(4): 750-757.

Kwee, T., T. Takahara, R. Ochiai, R. Nievelstein and P. Luijten (2008). "Diffusion-weighted whole-body imaging with background body signal suppression (DWIBS): features and potential applications in oncology." European Radiology 18(9): 1937-1952.

Kwee, T. C., T. Takahara, P. R. Luijten and R. A. J. Nievelstein (2010). "ADC measurements of lymph nodes: Inter- and intra-observer reproducibility study and an overview of the literature." European Journal of Radiology 75(2): 215-220.

Larsson, H., G. Barker and A. MacKay (1998). "Nuclear magnetic resonance relaxation in multiple sclerosis." Journal of neurology, neurosurgery, and psychiatry 64: S70-76.

Latour, L. L., R. L. Kleinberg, P. P. Mitra and C. H. Sotak (1995). "Pore-Size Distributions and Tortuosity in Heterogeneous Porous Media." Journal of Magnetic Resonance, Series A 112(1): 83-91.

Latour, L. L., K. Svoboda, P. P. Mitra and C. H. Sotak (1994). "Time-dependent diffusion of water in a biological model system." Proceedings of the National Academy of Sciences 91(4): 1229-1233.

Laule, C., I. M. Vavasour, S. H. Kolind, D. K. B. Li, T. L. Traboulsee, G. R. W. Moore and A. L. MacKay (2007). "Magnetic Resonance Imaging of Myelin." Neurotherapeutics 4(3): 460-484.

Le Bihan, D. (2013). "Apparent Diffusion Coefficient and Beyond: What Diffusion MR Imaging Can Tell Us about Tissue Structure." Radiology 268(2): 318-322.

Le Bihan, D. and H. Johansen-Berg (2012). "Diffusion MRI at 25: Exploring brain tissue structure and function." Neuroimage 61(2): 324-341.

Le Bihan, D., J. F. Mangin, C. Poupon, C. A. Clark, S. Pappata, N. Molko and H. Chabriat (2001). "Diffusion tensor imaging: concepts and applications." Journal of magnetic resonance imaging 13(4): 534-546.

Le Bihan, D., C. Poupon, A. Amadon and F. Lethimonnier (2006). "Artifacts and pitfalls in diffusion MRI." Journal of Magnetic Resonance Imaging 24(3): 478-488.

Levin, K. H. (2006). Chapter 6 Motor nerve conduction studies. Handbook of Clinical Neurophysiology. K. Jun, Elsevier. Volume 7: 139-154.

Liepinsh, E. and G. Otting (1996). "Proton exchange rates from amino acid side chains— implications for image contrast." Magnetic Resonance in Medicine 35(1): 30-42.

Lin, C., A. Luciani, E. Itti, T. El-Gnaoui, A. Vignaud, P. Beaussart, S.-j. Lin, K. Belhadj, P. Brugières, E. Evangelista, C. Haioun, M. Meignan and A. Rahmouni (2010). "Whole-body diffusion-weighted magnetic resonance imaging with apparent diffusion coefficient mapping for staging patients with diffuse large B-cell lymphoma." European Radiology 20(8): 2027-2038.

Liu, D., J. Zhou, R. Xue, Z. Zuo, J. An and D. J. J. Wang (2013). "Quantitative Characterization of Nuclear Overhauser Enhancement and Amide Proton Transfer Effects in the Human Brain at 7 Tesla." Magnetic Resonance in Medicine 70(4): 1070-1081.

Loskutov, V. V. and V. A. Sevriugin (2013). "A novel approach to interpretation of the time-dependent self-diffusion coefficient as a probe of porous media geometry." Journal of Magnetic Resonance 230(0): 1-9.

Mallouhi, A., W. Marik, D. Prayer, F. Kainberger, G. Bodner and G. Kasprian (2012). "3T MR tomography of the brachial plexus: Structural and microstructural evaluation." European Journal of Radiology 81(9): 2231-2245.

Masutani, Y., S. Aoki, O. Abe, N. Hayashi and K. Otomo (2003). "MR diffusion tensor imaging: recent advance and new techniques for diffusion tensor visualization." European Journal of Radiology 46(1): 53-66.

McNab, J. A., B. L. Edlow, T. Witzel, S. Y. Huang, H. Bhat, K. Heberlein, T. Feiweier, K. Liu, B. Keil, J. Cohen-Adad, M. D. Tisdall, R. D. Folkerth, H. C. Kinney and L. L. Wald (2013). "The Human Connectome Project and beyond: Initial applications of 300 mT/m gradients." NeuroImage 80(0): 234-245.

Melhem, E. R., S. Mori, G. Mukundan, M. A. Kraut, M. G. Pomper and P. C. M. van Zijl (2002). "Diffusion Tensor MR Imaging of the Brain and White Matter Tractography." American Journal of Roentgenology 178(1): 3-16.

Merboldt, K. D., W. Hänicke, H. Bruhn, M. L. Gyngell and J. Frahm (1992). "Diffusion imaging of the human brain in vivo using high-speed STEAM MRI." Magnetic resonance in medicine 23(1): 179-192.

Merboldt, K. D., W. Hanicke and J. Frahm (1985). "SELF-DIFFUSION NMR IMAGING USING STIMULATED ECHOES." Journal of Magnetic Resonance 64(3): 479-486.

Mitra, P. P. and P. N. Sen (1992). "Effects of microgeometry and surface relaxation on NMR pulsed-field-gradient experiments: Simple pore geometries." Physical Review B 45(1): 143.

Mitra, P. P., P. N. Sen and L. M. Schwartz (1993). "Short-time behavior of the diffusion coefficient as a geometrical probe of porous media." Physical Review B 47(14): 8565.

Montgomery, D. M. and R. S. Brower (1992). "CERVICAL SPONDYLOTIC MYELOPATHY - CLINICAL SYNDROME AND NATURAL-HISTORY." Orthopedic Clinics of North America 23(3): 487-493.

Mougin, O., M. Clemence, A. Peters, A. Pitiot and P. Gowland (2013). "High-resolution imaging of magnetisation transfer and nuclear Overhauser effect in the human visual cortex at 7 T." NMR in Biomedicine 26(11): 1508-1517.

Mougin, O. E., R. C. Coxon, A. Pitiot and P. A. Gowland (2010). "Magnetization transfer phenomenon in the human brain at 7 T." Neuroimage 49(1): 272-281.

Mulkern, R. V. and M. L. Williams (1993). "THE GENERAL-SOLUTION TO THE BLOCH EQUATION WITH CONSTANT RF AND RELAXATION TERMS - APPLICATION TO SATURATION AND SLICE SELECTION." Medical Physics 20(1): 5-13.

Nicholson, C. (2001). "Diffusion and related transport mechanisms in brain tissue." Reports on progress in Physics 64(7): 815.

Nodera, H. and R. Kaji (2006). "Principles of stimulation and recording." Handbook of Clinical Neurophysiology 7: 123-138.

Novikov, D. S. and V. G. Kiselev (2010). "Effective medium theory of a diffusion-weighted signal." Nmr in Biomedicine 23(7): 682-697.

Oberthuer, A., P. Sagave, M. Dueck, C. Wedekind and C. Diefenbach (2001). "F-Wave recording:monitoring residual neuromuscular blockade." European Journal of Anaesthesiology (EJA) 18: 26.

Parsons, E. C., M. D. Does and J. C. Gore (2006). "Temporal diffusion spectroscopy: Theory and implementation in restricted systems using oscillating gradients." Magnetic Resonance in Medicine 55(1): 75-84.

Pastore-Olmedo, C., O. González and E. Geijo-Barrientos (2009). "A study of F-waves in patients with unilateral lumbosacral radiculopathy." European Journal of Neurology 16(11): 1233-1239.

Pinheiro, D. S., G. M. Manzano and J. A. M. Nóbrega (2008). "Reproducibility in nerve conduction studies and F-wave analysis." Clinical Neurophysiology 119(9): 2070-2073.

Preston, D. C. and B. E. Shapiro (1998). Electromyography and neuromuscular disorders: clinical-electrophysiologic correlations, Butterworth-Heinemann.

Preston, D. C. and B. E. Shapiro (2012). Electromyography and Neuromuscular Disorders: Clinical-Electrophysiologic Correlations (Expert Consult-Online), Elsevier Health Sciences.

Rabbani, K. S., M. J. Alam and M. A. Salam (2007). "Frequency distribution of F-latencies (DFL) has physiological significance and gives distribution of conduction velocity (DCV) of motor nerve fibres with implications for diagnosis." Journal of Biological Physics 33(4): 291-303.

Rangwala, N. A., D. B. Hackney, W. Dai and D. C. Alsop (2013). "Diffusion restriction in the human spinal cord characterized in vivo with high b-value STEAM diffusion imaging." NeuroImage 82(0): 416-425.

Schachter, M., M. D. Does, A. W. Anderson and J. C. Gore (2000). "Measurements of restricted diffusion using an oscillating gradient spin-echo sequence." Journal of Magnetic Resonance 147(2): 232-237.

Schmierer, K., D. J. Tozer, F. Scaravilli, D. R. Altmann, G. J. Barker, P. S. Tofts and D. H. Miller (2007). "Quantitative magnetization transfer imaging in postmortem multiple sclerosis brain." Journal of Magnetic Resonance Imaging 26(1): 41-51.

Schmierer, K., C. A. M. Wheeler-Kingshott, D. J. Tozer, P. A. Boulby, H. G. Parkes, T. A. Yousry, F. Scaravilli, G. J. Barker, P. S. Tofts and D. H. Miller (2008). "Quantitative magnetic resonance of postmortem multiple sclerosis brain before and after fixation." Magnetic Resonance in Medicine 59(2): 268-277.

Sen, P. N. (2004). "Diffusion and tissue microstructure." Journal of Physics: Condensed Matter 16(44): S5213.

Sen, P. N. (2004). "Time-dependent diffusion coefficient as a probe of geometry." Concepts in Magnetic Resonance Part A 23(1): 1-21.

Sigmund, E. E. (2011). "Perspectives on Porous Media MR in Clinical MRI." AIP Conference Proceedings 1330(1): 13-16.

Slichter, C. P. (1990). Principles of magnetic resonance, Springer.

Smith, S. A., J. W. M. Bulte and P. C. M. van Zijl (2009). "Direct Saturation MRI: Theory and Application to Imaging Brain Iron." Magnetic Resonance in Medicine 62(2): 384-393.

Smith, S. A., X. Golay, A. Fatemi, A. Mahmood, G. V. Raymond, H. W. Moser, P. C. M. van Zijl and G. J. Stanisz (2009). "Quantitative magnetization transfer characteristics of the human cervical spinal cord in vivo: Application to Adrenomyeloneuropathy." Magnetic Resonance in Medicine 61(1): 22-27.

Song, Y.-Q. (2013). "Magnetic Resonance of Porous Media (MRPM): A perspective." Journal of Magnetic Resonance 229(0): 12-24.

Stanisz, G. J., E. E. Odrobina, J. Pun, M. Escaravage, S. J. Graham, M. J. Bronskill and R. M. Henkelman (2005). "T1, T2 relaxation and magnetization transfer in tissue at 3T." Magnetic Resonance in Medicine 54(3): 507-512.

Stejskal, E. O. and J. E. Tanner (1965). "Spin Diffusion Measurements: Spin Echoes in the Presence of a Time-Dependent Field Gradient." The journal of chemical physics 42(1): 288-292.

Stepišnik, J. (1981). "Analysis of NMR self-diffusion measurements by a density matrix calculation." Physica B+ C 104(3): 350-364.

Subhawong, T., K. Wang, S. Thawait, E. Williams, S. Hashemi, A. Machado, J. Carrino and A. Chhabra (2012). "High resolution imaging of tunnels by magnetic resonance neurography." Skeletal Radiology 41(1): 15-31.

Takahara, T., Y. Imai, T. Yamashita, S. Yasuda, S. Nasu and M. Van Cauteren (2004). "Diffusion weighted whole body imaging with background body signal suppression (DWIBS): technical improvement using free breathing, STIR and high resolution 3D display." Radiation medicine 22(4): 275-282.

Tanner, J. (1970). "Use of the stimulated echo in NMR diffusion studies." The Journal of Chemical Physics 52: 2523.

Terreno, E., J. Stancanello, D. Longo, D. D. Castelli, L. Milone, H. M. H. F. Sanders, M. B. Kok, F. Uggeri and S. Aime (2009). "Methods for an improved detection of the MRI-CEST effect." Contrast Media & Molecular Imaging 4(5): 237-247.

Torrey, H. C. (1956). "Bloch Equations with Diffusion Terms." Physical review 104(3): 563-565.

Tournier, J. D., F. Calamante and A. Connelly (2013). "Determination of the appropriate b value and number of gradient directions for high-angular-resolution diffusion-weighted imaging." NMR in Biomedicine 26(12): 1775-1786.

van Es, H. W., T. L. Bollen and H. P. M. van Heesewijk (2010). "MRI of the brachial plexus: A pictorial review." European Journal of Radiology 74(2): 391-402.

van Es, H. W., A. M. Engelen, T. D. Witkamp, L. M. P. Ramos and M. A. M. Feldberg (1997). "Radiation-induced brachial plexopathy: MR imaging." Skeletal Radiology 26(5): 284-288.

van Zijl, P. C. M. and N. N. Yadav (2011). "Chemical exchange saturation transfer (CEST): What is in a name and what isn't?" Magnetic Resonance in Medicine 65(4): 927-948.

Vargas, M. I., M. Viallon, D. Nguyen, J. Y. Beaulieu, J. Delavelle and M. Becker (2010). "New approaches in imaging of the brachial plexus." European Journal of Radiology 74(2): 403-410.

Vinogradov, E., A. D. Sherry and R. E. Lenkinski (2013). "CEST: From basic principles to applications, challenges and opportunities." Journal of Magnetic Resonance 229: 155-172.

Weiss, L., J. K. Silver and J. Weiss (2004). Easy EMG: a guide to performing nerve conduction studies and electromyography, Butterworth-Heinemann Medical.

Westin, C.-F., S. E. Maier, H. Mamata, A. Nabavi, F. A. Jolesz and R. Kikinis (2002). "Processing and visualization for diffusion tensor MRI." Medical image analysis 6(2): 93-108.

Westin, C. F., S. E. Maier, B. Khidhir, P. Everett, F. A. Jolesz and R. Kikinis (1999). Image Processing for Diffusion Tensor Magnetic Resonance Imaging. Medical Image Computing and Computer-Assisted Intervention – MICCAI'99. C. Taylor and A. Colchester, Springer Berlin Heidelberg. 1679: 441-452.

Whittall, K. P., A. L. Mackay, D. A. Graeb, R. A. Nugent, D. K. B. Li and D. W. Paty (1997). "In vivo measurement of T2 distributions and water contents in normal human brain." Magnetic Resonance in Medicine 37(1): 34-43.

Wolff, S. D. and R. S. Balaban (1989). "Magnetization transfer contrast (MTC) and tissue water proton relaxation in vivo." Magnetic Resonance in Medicine 10(1): 135-144.

Xu, J., M. D. Does and J. C. Gore (2009). "Quantitative characterization of tissue microstructure with temporal diffusion spectroscopy." Journal of Magnetic Resonance 200(2): 189-197.

Yadav, N. N., C. K. Jones, J. Xu, A. Bar-Shir, A. A. Gilad, M. T. McMahon and P. C. M. van Zijl (2012). "Detection of rapidly exchanging compounds using on-resonance frequency-labeled exchange (FLEX) transfer." Magnetic Resonance in Medicine 68(4): 1048-1055.

Yasunami, T., Y. Miyawaki, K. Kitano and H. Okuno (2005). "Shortening of distal motor latency in anode distal stimulation." Clinical Neurophysiology 116(6): 1355-1361.

Zaiss, M. and P. Bachert (2013). "Chemical exchange saturation transfer (CEST) and MR Z-spectroscopy in vivo: a review of theoretical approaches and methods." Physics in Medicine and Biology 58(22): R221-R269.

Zaiss, M., P. Kunz, S. Goerke, A. Radbruch and P. Bachert (2013). "MR imaging of protein folding in vitro employing Nuclear-Overhauser-mediated saturation transfer." NMR in Biomedicine 26(12): 1815-1822.

Zaiß, M., B. Schmitt and P. Bachert (2011). "Quantitative separation of CEST effect from magnetization transfer and spillover effects by Lorentzian-line-fit analysis of z-spectra." Journal of Magnetic Resonance 211(2): 149-155.

Zhang, H., P. L. Hubbard, G. J. Parker and D. C. Alexander (2011). "Axon diameter mapping in the presence of orientation dispersion with diffusion MRI." NeuroImage 56(3): 1301-1315.

Zhang, H., T. Schneider, C. A. Wheeler-Kingshott and D. C. Alexander (2012). "NODDI: Practical in vivo neurite orientation dispersion and density imaging of the human brain." NeuroImage 61(4): 1000-1016.

Zhao, L., G. Wang, L. Yang, L. Wu, X. Lin and A. Chhabra (2013). "Diffusion-Weighted MR Neurography of Extremity Nerves With Unidirectional Motion-Probing Gradients at 3 T: Feasibility Study." <u>American Journal of Roentgenology</u> 200(5): 1106-1114.

Zheng, S. and Y. Xia (2010). "On the measurement of multi-component T2 relaxation in cartilage by MR spectroscopy and imaging." <u>Magnetic Resonance Imaging</u> 28(4): 537-545.

Chapter 4
Diffusion MRI study of the Brachial Plexus

Introduction

As discussed in previous chapters, MRI allows depiction of the anatomy, recognition of particular anatomical landmarks and hence characterization of some pathological conditions of the brachial plexus. The aim of this chapter is to extend these morphological studies to quantitative characterization of tissue properties. Specifically this chapter will study the variability of apparent diffusion coefficient (ADC) with Δ as a potential method of studying the microstructure of peripheral nerves of the brachial plexus.

The DWIBS sequence using a single shot EPI readout with free breathing (discussed in Chapter 3), made it possible to obtain images of the nerve root, root ganglion, nerve paths in brachial plexus region, and the DWIBS sequence. This has been applied in a novel manner for a quantitative study of restricted diffusion in nerves and spinal cord in the brachial plexus. This chapter is divided in two sections:

4.1: The Development of DWIBS imaging protocol for quantitative diffusion imaging of the brachial plexus

This section describes the optimization of the DWIBS acquisition protocol for detecting quantitative imaging.

4.2: A study of diffusion time dependent ADC of the brachial plexus

Optimization of the sequence for diffusion time measurements, a novel way of characterizing restricted diffusion MRI and set-up for the initial in-vivo experiments are described in this section.

4.1 The development of DWIBS imaging protocol for quantitative diffusion imaging of the brachial plexus

4.1.1 Introduction

In 2004 Takahara *et al.* (2008) proposed DW imaging of the body under free breathing known as diffusion weighted whole-body imaging with background body signal suppression (DWIBS). DWIBS uses the Stejskal-Tanner pulsed gradient single-shot spin echo EPI sequence with background tissue suppression achieved by diffusion weighting and T1-weighted fat suppression.
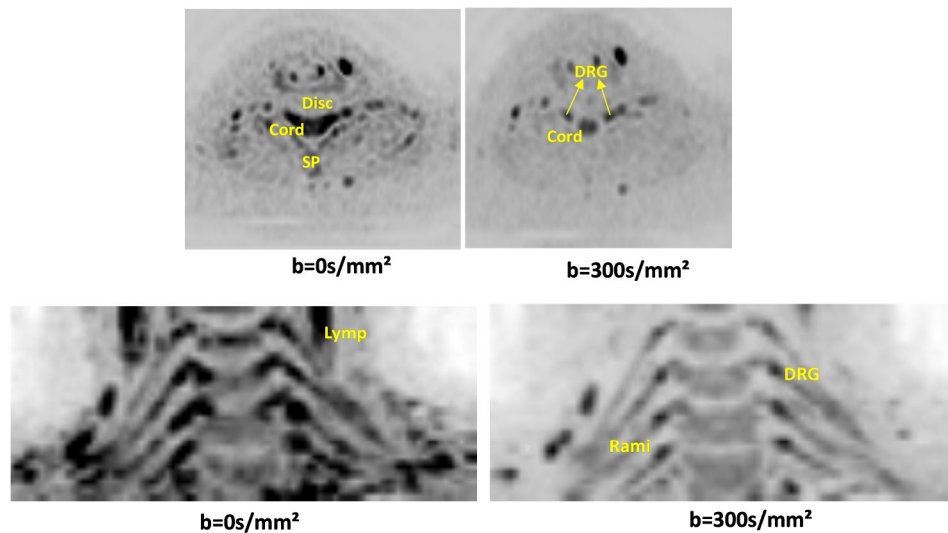

Figure 4.1.1 Application of DWIBS to Brachial plexus (inverted grey scale) with b=0 and b=300s/mm^2 respectively showing attenuation of nerve surrounding tissues at higher b value. In the figure: SP=spinous process, D=Disk, DR=dorsal root, DRG= dorsal root ganglion, Lymp=lymp node.

DWIBS was chosen as the basic imaging scheme for quantitative measures of the brachial plexus as it provides a method of isolating the signal from the nerve separately from the other tissues of the neck. The partial volume effect (PVE) produces blurring and potentially misleading images, and will also cause quantitative image data of a given tissue type to be contaminated by other tissues. The PVE can be minimized by using thin slices and high in-plane spatial resolution. However, this will not be sufficient in quantitative imaging of the brachial plexus where the nerves are small with respect to the achievable spatial resolution so that all voxels are likely to contain a mixture of signal from nerve tissue and surrounding tissues. Instead DWIBS

scanning uses inversion recovery fat suppression, T2 weighting (TE) and same diffusion weighting to suppress surrounding tissues so that each voxel only contains signal from the nerves, grey matter and white matter of the cord, as shown in Figure 4.1.1.

DWIBS produces thin-section three-dimensional datasets, which are frequently reconstructed as grey scale inverted, maximum intensity projection (MIP) images, reconstructed at different orientations around the volume to show the relative spatial positions of the nerve roots and nerve paths particularly when played as a movie (Figure 4.1.2). DWIBS has not previously been used for quantitative diffusion measurements in the brachial plexus, and there are number of practical challenges to using DWIBS in such a way. In standard DWIBS imaging, high image contrast to noise ratio will be the primary requirement for detection of pathology, but quantitative diffusion imaging has different trade-offs. The key factors that affect image quality have been investigated in this section.
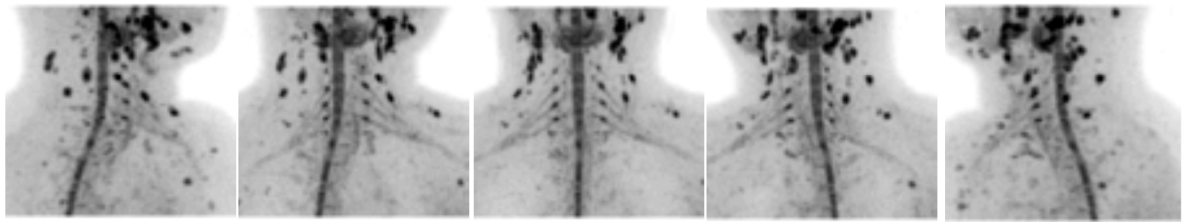

Figure 4.1.2 MIPS from a set of DWIBS data at $b=200s/mm^2$, for 30^0 rotations. (ideally this data set would be observed as a movie) Nerves and lymph nodes can be seen on these images.

Increasing the magnetic field leads to linear increase in the magnetization of the sample, which can be used to improve the SNR and resolution and shorten the acquisition time. However, the expected gain in SNR may not be realised because of the intrinsic long TE of most diffusion imaging sequences, combined with the decrease in apparent T2 at high field due to the effects of diffusion in inhomogeneous B_0 fields. In addition, increased B_0 and B_1 field inhomogeneities at high field will cause distortions and signal drop out. DWIBS images were initially acquired at both 1.5T and 3T scanners to determine whether adequate image quality and SNR could be achieved at both field strengths.

Obtaining good fat suppression is difficult in the soft tissues in the neck and the bottom of the skull due to sharp angles in the anatomy and the presence of tissues with very different susceptibilities within the area which can cause large variations in

the magnetic field. DWIBS uses an inversion recovery sequence to preferentially null fat signals independent of frequency offset. The null time will depend on field strength and also B1 field errors, and so the TI was optimized for these studies. In conventional DWIBS a long TE is recommended to increase suppression of background tissue (Takahara *et al.* 2004, Koh *et al.* 2010, Lin *et al.* 2010) but this reduces the signal due to T2 decay which might compromise quantitative measurements. Thus the variation in contrast to noise ratios of nerves and cord regions with TE were assessed.

Eddy currents can result from the rapidly switched diffusion gradient, causing geometric distortions and misaligned images with the appearance of 'shearing', 'translational' and 'scaling' artefacts (Le Bihan *et al.* 2006, Jones *et al.* 2010). The possible presence of image eddy current distortions in the DWIBS images of brachial plexus was investigated.

A major confounding issue in diffusion MRI is that of the movement of blood (perfusion) or other fluids (CSF) in the tissue. For instance in the biological tissues, in addition to diffusion, the water molecules micro-circulate in the pseudo-random capillary segments mimicking a random walk. Such mixed effects of microscopic translational motions of water molecules cause intravoxel incoherent motion (IVIM) in each image voxel in MRI (Le Bihan *et al.* 1987). This movement does not necessarily have to be in randomly orientated capillary networks, provided that the flow is incoherent across the voxel (Moore *et al.* 2000, Koh *et al.* 2011, Harkins *et al.* 2012). In the context of diffusion MRI, the mixed incoherent motion occurring in biological tissues is generally represented by the IVIM equation which describes bi-exponential diffusion decay with increasing b values:

$$S(b) = S_0[(1-f)e^{-bD} + fe^{-bD^*}]$$
(4.1.1)

In the Equation (4.1.1), D is the apparent molecular diffusion coefficient of water in tissues, D^* is the pseudo diffusion coefficient related to the tissue perfusion or other incoherent motion, and f is the volume fraction of that second component. This assumes a two component system, which is generally found to be sufficient empirically.
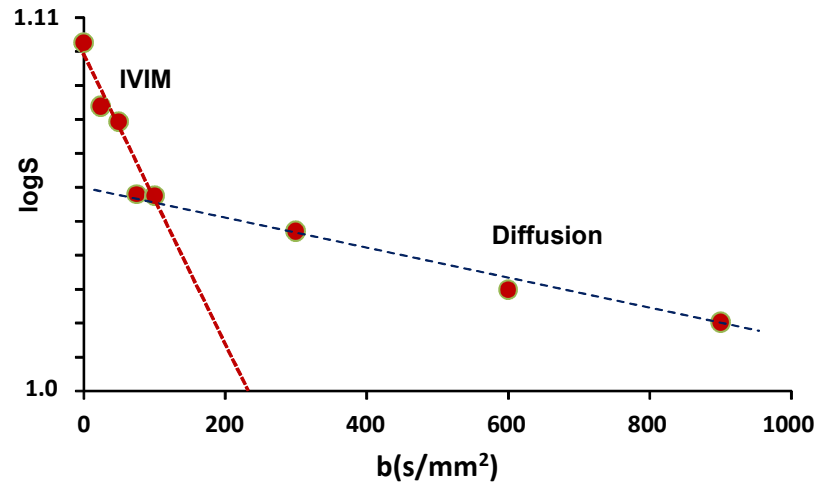
Figure 4.1.3 *Typical IVIM graph logS vs b plot. Pure diffusion effects are found in the part of the attenuation curve seen for large b values (blue dashed line). The deviation from straight line observable for small b values has generally been ascribed to intravoxel incoherent microcirculation effects. The slope of this initial part (red dashed line) of the curve gives the pseudodiffusion coefficient D*. The ratio of the intercepts gives an estimation of the vascular volume fraction. Based on the IVIM graph the relative values for D* are an order of magnitude higher than D.*

The IVIM effect due to blood flow and any CSF movement would confound the measurement of water diffusion in nerve tissues. It is clear from Figure 4.1.3 that IVIM contributions can be eliminated by not using small b values to measure diffusion. Signal attenuation from large vessels, with rapid fluid flow occurs at very low b values ($<50s/mm^2$); whereas signal attenuations from smaller vessels, with slower fluid flow sensitive to higher b values (Moore *et al.* 2000, Vestergaard-Poulsen *et al.* 2007, Koh *et al.* 2011, Lasic *et al.* 2011, Harkins *et al.* 2012). Initial work was carried out to determine an appropriate b value threshold to eliminate IVIM effects from diffusion measurements of the brachial plexus.

Objective of this section is to design the basic DWIBS sequence for quantitative imaging of the brachial plexus nerves and spinal cord.

4.1.2 Methods

4.1.2.1 Subjects for the study

The subjects used throughout this thesis are described in this section for clarification. For all the human MRI and EMG experiments described in this thesis, ethics approval was obtained from the Faculty of Medicine and Health Sciences, Medical School Research Ethics Committee, University of Nottingham under the B/03/2011 ethics code. The experiment was explained to the subjects verbally and in writing and they gave written consent to participate. A total of 46 normal healthy subjects were recruited to several subgroups as shown in Table 4.1 for the studies. Some subjects were included in more than one study. All subjects were examined with a 3.0T MRI scanner (Philips Achieva, Philips Medical Systems, Best, the Netherlands), with using torso 16 channel phased-array surface coil. This multi-application coil consisted of four elements with flexible anterior and posterior sections, thus it provides high quality images with adequate anatomical coverage. Soft, thin foam designed contours attached with the coil for quick set-up and comfortable exams for the patients. The maximum gradient strength of the scanner 40 mT/m, and the slew rate 120 mT/m/s (discussed in Chapter 1 page 45).

Table 4.1 Groups of normal healthy subjects used in this thesis:

Experiment	Chapter	Cohort	Number	Male	Female	Age range (years)	Mean Age (years)
Development of DWIBS	**4.1**	A	7	3	4	22~55	31
Restricted Diffusion study	**4.2**	B	8	4	4	22~55	33
T2 relaxation	**5**	C	10	4	6	24~55	28
Magnetization Transfer	**6**	D	15	6	9	23~38	29
Combined EMG and MRI	7	E	6	4	2	24~55	31

4.1.2.2 Pulse sequence

A schematic pulsed gradient spin echo DWIBS sequence with STIR fat suppression is shown in Figure 4.1.4. This sequence was implemented in a patch to the standard

Philips sequence code written by Dr. Andrew Peters. The different gradients and variable timing parameters of the sequence are briefly discussed below.
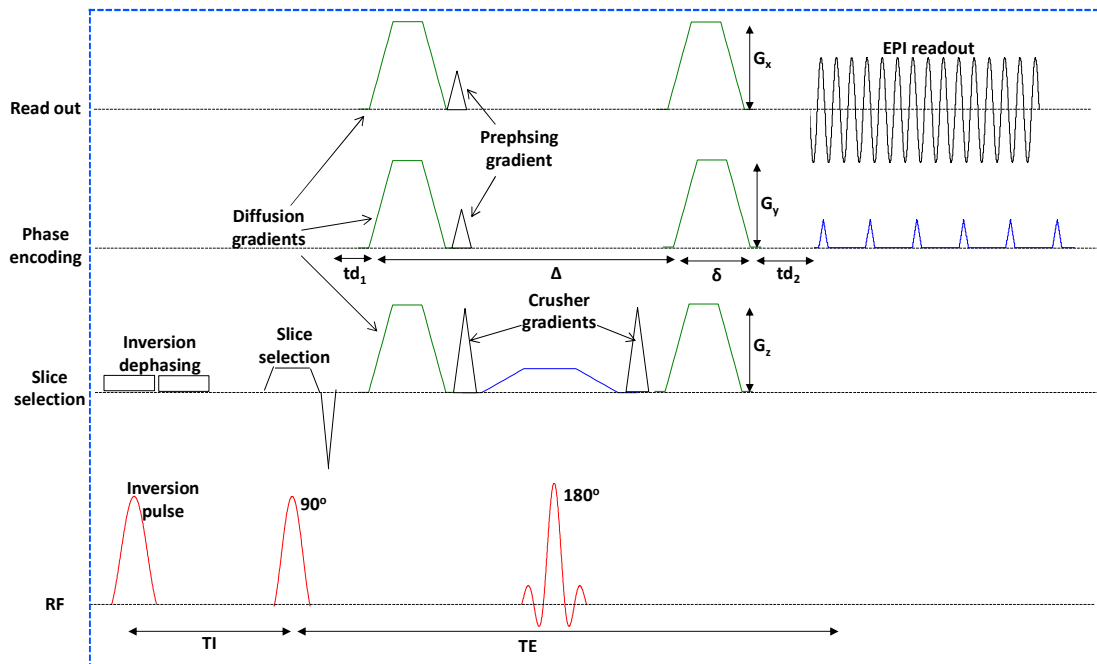

Figure 4.1.4 *Pulsed gradient spin echo (PGSE) DWIBS sequence. The figure indicates relevant pulse sequence timings.*

This sequence employs a 90^0 excitation and a single 180^0 refocusing pulse to form one spin echo per slice per TR interval. The 180^0 pulse is shorter in time (at zero crossing) to provide a wider bandwidth than the 90^0 pulse and hence better refocusing. It is surrounded by crusher gradients in the z-direction to eliminate unwanted signals from the refocusing pulse, whilst maintaining the spin echo (this crusher is superfluous for b>0). To minimize the echo time of the sequence, the crusher gradient lobes are fused with the slice selection gradient. The prephasing gradient of the EPI switch gradient is also shifted to be before the 180^0 pulse to minimize TE.

Spatially selective adiabatic inversion recovery (IR) was used for lipid and fat suppression in the short tau inversion recovery (STIR) technique. The level of fat suppression was controlled by changing the inversion time (TI). The inversion pulse was followed by another de-phasing gradient to crush any transverse magnetization created by the pulse.

The diffusion gradient pulses are placed on each side of the 180^0 RF pulse. In the standard software the amplitude of the gradients is automatically set to the maximum allowed by the system, with independent control of diffusion gradient duration δ and

TE, thus coupling diffusion time Δ and TE. Therefore the standard Philips sequence was edited ('patched') to allow independent control of TE, b value, diffusion gradient duration δ and diffusion time Δ. Trapezoidal shape diffusion gradients were used to allow for the finite rise time necessary due to the non-negligible coil inductance. t_{d2} is the delay time between the diffusion gradient and EPI read-out on the right side of the 180^0 RF pulse; and t_{d1} is the delay time between the diffusion gradient and excitation pulse on the left side of the 180^0 RF pulse. Both the delay times are used to change the diffusion time for constant δ. A short dead time (ξ) between the imaging and diffusion gradient pulses is always maintained to avoid eddy currents spilling over into the readout and to limit the gradient hardware duty cycle.

The aim of this work was to measure the diffusion coefficient, not to perform tractography, therefore given the orientation dependence of nerve diffusion, the problems in defining the exact direction of the nerve at the time of scanning, and the need for high sensitivity to diffusion gradients it was decided to apply the three orthogonal gradients simultaneously for maximum net gradient amplitude along the oblique direction. The images were always acquired close to transverse direction, the relative amplitudes of three gradients (X : Y : Z=0.42 : 0.42 : 0.21) gave a net gradient at 45^0 to the x-axis and 70^0 to the z axis. Figure 4.1.5 shows a schematic diagram of orthogonal diffusion gradients and net resulting gradient that crosses the brachial plexus nerves.
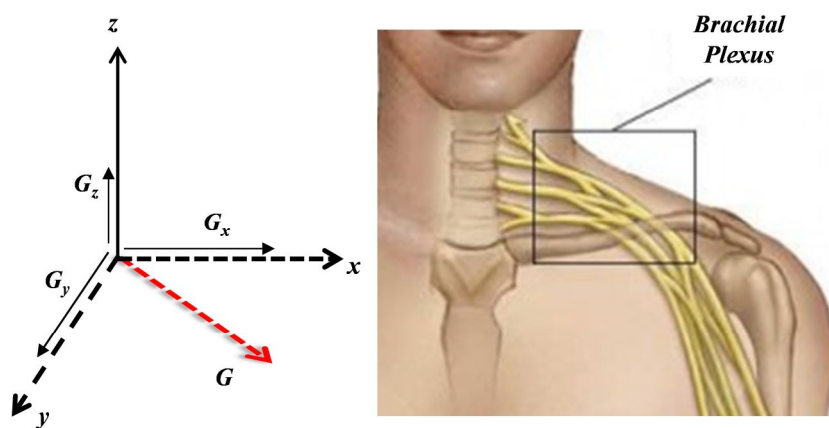

Figure 4.1.5 *Orthogonal diffusion gradients and the net diffusion gradient (red dotted arrow) and coronal view of brachial plexus.*

4.1.2.3 Initial set up

For this development study various MR images in the brachial plexus were acquired from **cohort A** (page 126) subjects who were positioned head first supine in the MR scanner.

Data were acquired using the torso XL 16 channel array coil, positioned so that the subject's nose was just at the top edge of the coil and appropriate padding was used to space the coil just above the subject's face, shown in Figure 4.1.6. Upper portion of the coil has been used for better sensitivity. This ensured good signal to noise ratio across the brachial plexus compared to the spine coil (Receiver) and whole body coil (Transmitter/Receiver), and also allowed imaging of the entire brachial plexus in different head positions (for comparison with EMG measurements in Chapter 6).
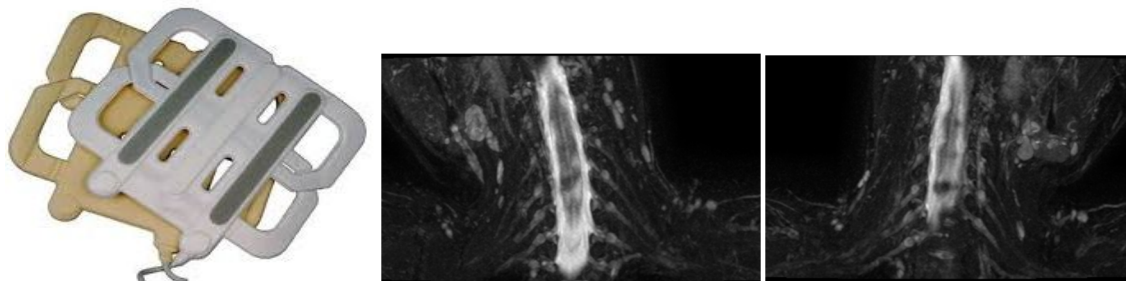

Figure 4.1.6 *Torso XL coil and coronal view of brachial plexus at different postures of the head. Those positions would not be possible on a standard spine coil, though positioning of the torso coil over the face (up to nose) of the subject needs extra padding over both shoulders; otherwise it becomes little bit uncomfortable.*

T1 weighted Philips survey images were used to assess the anatomical locations of C5 to T1 nerves in cervical spine, then axial/oblique single shot EPI DWIBS scans were acquired centred between C5/C6 vertebrae (Figure 4.1.6) to obtain adequate coverage of the brachial plexus nerves and spinal cord, from C1 to T1, shown in Figure 4.1.7. The EPI readout had FOV 192×54×300 mm, 3 mm isotropic voxels, 18 slices with no gap to cover the region, water/fat shift 4.64 pixels, SENSE factor = 2 to reduce the acquisition time and hence signal distortions drop out, fold over direction Anterior-Posterior (AP), with whole volume shimming preparation step. For the STIR fat suppression inversion time initially set to 150 ms were employed.
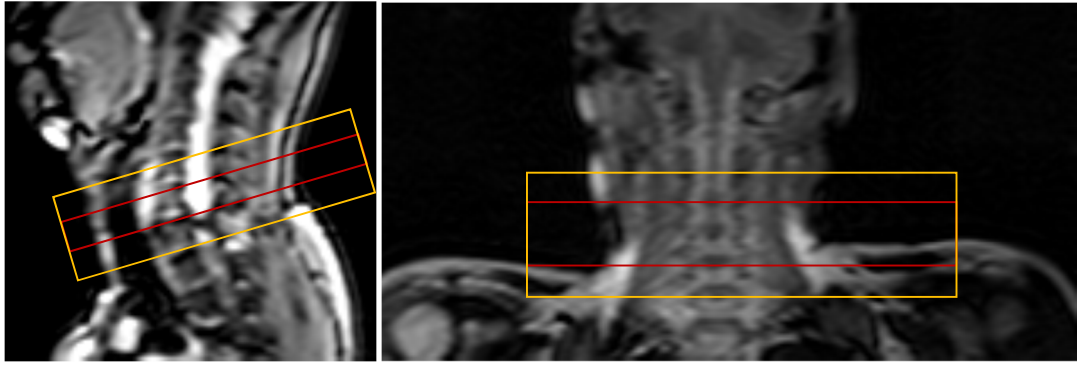
Figure 4.1.7 *Survey images of the brachial plexus and positioning at C5/C6 vertebral disc.*

4.1.2.4 Experiments

Initially coronal and transverse MIP views of brachial plexus were acquired from 3T and 1.5 T scanners for comparison of signal to background ratio defined as,

SBR $= \frac{Nerve\ or\ cord\ signal}{Background}$ where the background ROI was drawn in a region of suppressed tissue and fluid and captures both genuine noise and errors in suppression, but all subsequent data were acquired at 3 T.

To find the best available fat suppression sequence images were acquired from two subjects from ***cohort A*** with TI = 155, 180, 190, 210, 230, 250 ms; b = 500 s/mm^2; TE = 48 ms; and TI =155, 180, 190, 210, 230, 250 ms, b = 500 s/mm^2, TE =70 ms, TR = 8813 ms. The SBR was measured for each TI. To check the effect of the diffusion gradient on image distortions, data were acquired from the same two subjects with b = 0, 100, 300, 600, 900 s/mm^2. The position and sizes of the nerves in these images were monitored using software described below. To find the threshold b value required to eliminate IVIM contamination, DWIBS images were acquired from five subjects of ***cohort A***, with b = 0, 25, 50, 75, 100, 300, 500, 700, 900 s/mm^2, TE = 60 ms, Δ = 28.3 ms, δ = 10 ms. An agar phantom was placed above the shoulder as a pure diffusion reference standard. The difference between nerve and cord IVIM parameters was compared.

4.1.2.5 Image analysis

For image analysis all software was written in Matlab. In the DWIBS images due to small sizes of the nerves beyond the dorsal root ganglion (DRG) and rami, the data were too noisy to reliably identify individual nerve paths. However, the DRG and adjacent nerve roots (as ramus) are high intensity regions and easy to locate. Thus

DRG and ramus are considered and named as 'nerves' in the remaining experiments. In the transverse view the cord is shown as a bright intensity region in the DWIBS images, representing the white matter (WM) and grey matter (GM) surrounded by CSF.

Maximum intensity projection (MIP) images are useful for verifying the images of nerves, although MIPs could be produced on the scanner; they were also reconstructed off line, from 2D coronal views reconstructed from the axially acquired images. To exclude other surrounding bright structures, the volume was masked to include only the local region of interest. Figure 4.1.8 shows the coronal slides viewing nerves and cord and resulting MIP.
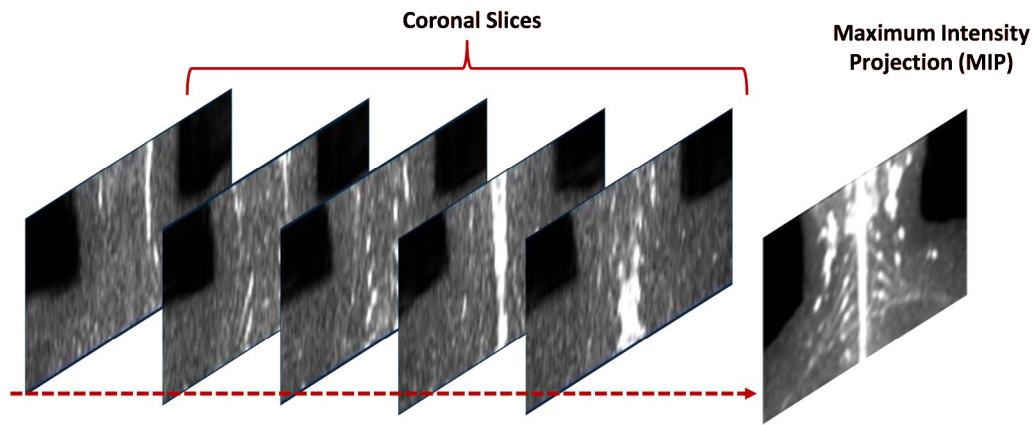

Figure 4.1.8 *Coronal view of different slices which used to form the MIP view of Brachial plexus showing spinal cord, nerve roots and path of the nerves. With b=300 s/mm^2, TE =100 ms.*

(i) Nerve region of interest (ROI) selection process:

Semi-automated methods of selecting ROIs on the raw data were developed to make the results more objective. To reduce residual PVE for the C5/C6/C7/C8 nerve root ROIs, it was first necessary to define a sagittal plane which the nerve cut through orthogonally. This was selected by initially studying the coronal MIPS. The resulting images are shown in Figure 4.1.8. To objectively estimate the amplitude of the signal from these nerves and the position of these nerves, the resulting images were fitted to a 2-D multiple (N) Gaussian equation,

$$f(x,y) = \sum_i^N A_i \, exp\{-(\frac{(x-x_{0i})^2}{2\sigma_{xi}^2} + \frac{(y-y_{0i})^2}{2\sigma_{yi}^2})\} \tag{4.1.2}$$

where A_i is the amplitude constant, x_{0i} and y_{0i} are the positions of the peak corresponding to the nerve in the image and σ_{xi} and σ_{yi} are the spread of the peaks in x and y directions, and N is the number of nerves visible in the image.

131

This assumes that the nerve has an approximately Gaussian signal profile. The resulting fit is shown in Figure 4.1.9 for two different b values. When the signal is low the background could contain noise peaks that might be wrongly interpreted as nerves and furthermore low signals would also skew the diffusion fitting (Henkelman 1985, Macovski 1996). Therefore any peak less than 2 times standard deviation of background of whole image was neglected. When two or more b values were used the ROI was first defined from the low b value data and then applied to the high b value data.
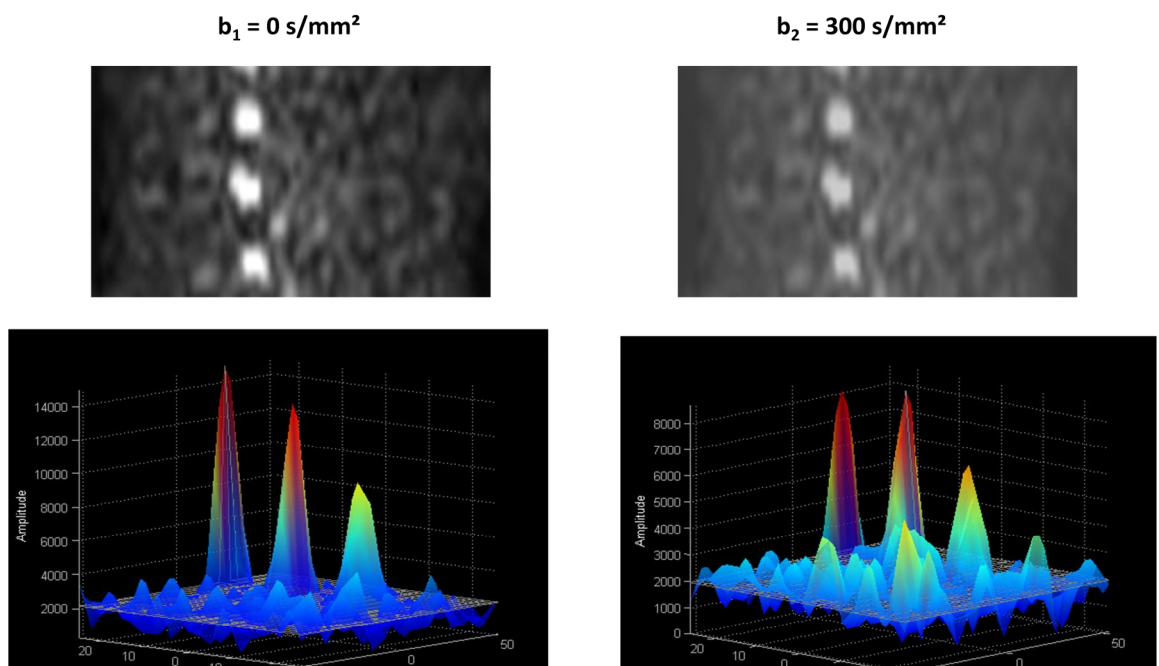

Figure 4.1.9 *Sagittal view of brachial plexus showing locations of C6/C7/C8 nerve roots at b_1 and at $b_2 > b_1$; corresponding 2D Gaussian fitting showing peak for each nerve (using equation 4.1.2).*

(ii) Cord ROI selection process:

In the transverse images, the spinal cord appeared as a bright broad region of grey and white matter surrounded by CSF. To select a cord ROI transverse slices were selected, then 2D Gaussian fitting applied over those slices resulting in a single broad higher intensity peak (Figure 4.1.10), since the cord signal profile only approximates to a Gaussian shape. Four maximum voxel values were selected and averaged as the cord intensity value (including both grey and white matter). Background noise was excluded as for the nerve.
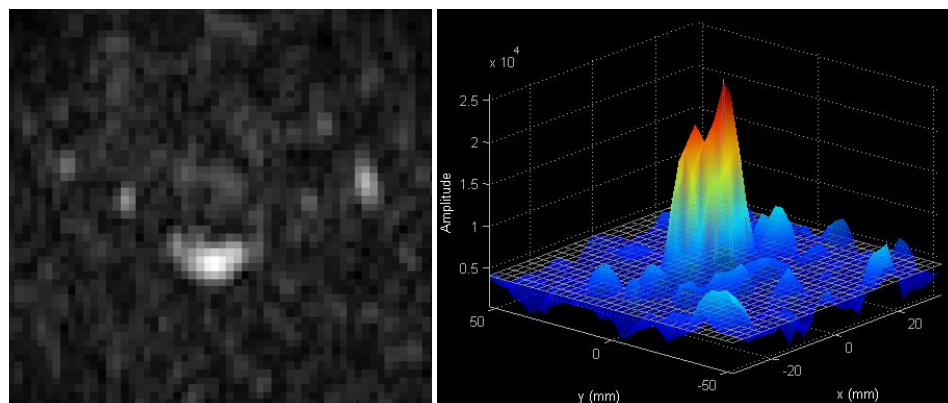
Figure 4.1.10 *Transverse view of spinal cord and 2D Gaussian fitting, the broad peak shows the cord (using equation 4.1.2).*

4.1.3 Results

Figures 4.1.11a and 4.1.11b show brachial plexus images obtained at 1.5 and 3 T for two different subjects. Qualitatively the brachial plexus nerves and cord images were more visible and have had higher SBR at 3T compared to 1.5T, but the images acquired at 1.5 T showed the nerve paths more medially on both sides of the spinal cord.
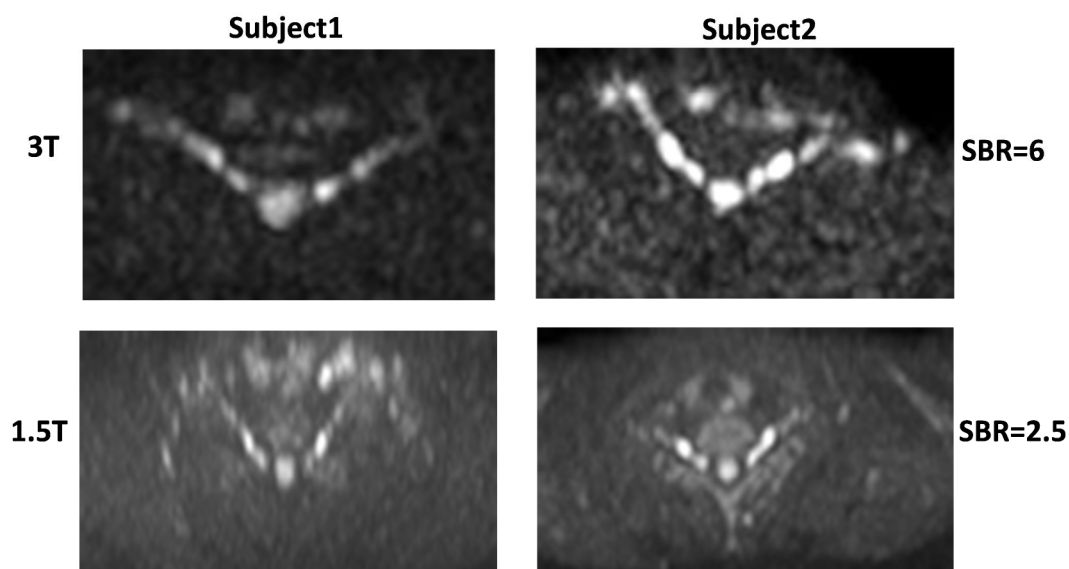

Figure 4.1.11a *Transverse view of Brachial plexus from 2 subjects, obtained from 3T and 1.5T using DWIBS with b=250s/mm².*
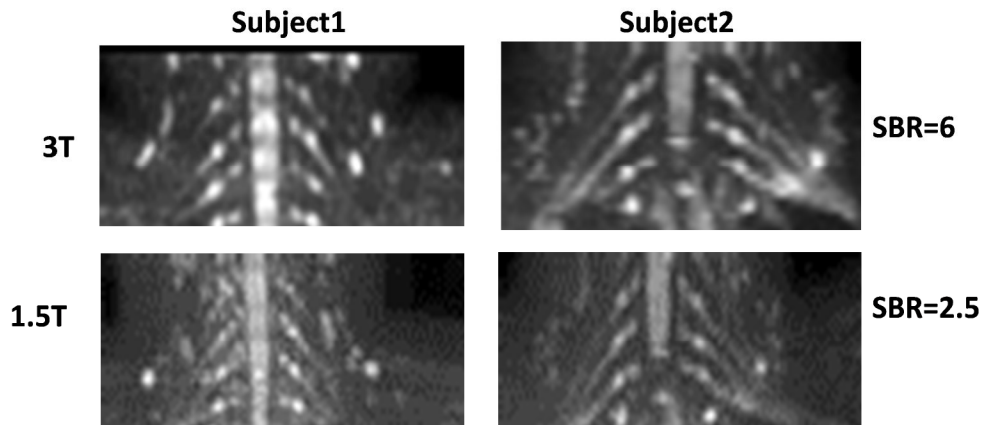
Figure 4.1.11b *Coronal view MIP of brachial plexus from 2 subjects, obtained from 3T and 1.5T using DWIBS with b=250s/mm².*

Figure 4.1.12 shows the effects of changing the TI on brachial plexus images and Figure 4.1.13 shows maximum SBR ratios from nerves and cord were achieved for an inversion time of 220 ms, corresponding to optimal nulling of signal from surrounding fat.
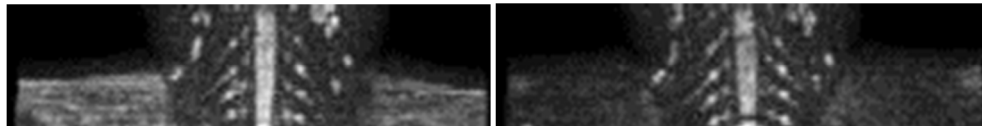
Figure 4.1.12 *Coronal MIP of Brachial Plexus with b=500 s/mm^2, TE=70ms, TI=155ms and TI=220ms; higher TI showing more fat suppression.*
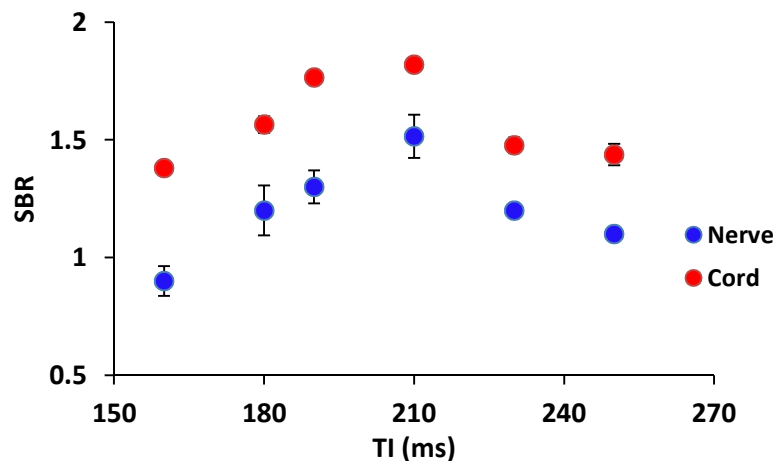

Figure 4.1.13 *Signal to background ratio (SBR) study for TI at nerves and cord with standard error bar of measurements from two subjects.*

Figure 4.1.14 shows the position and size of the nerves with increasing b values to observe the eddy current effects.
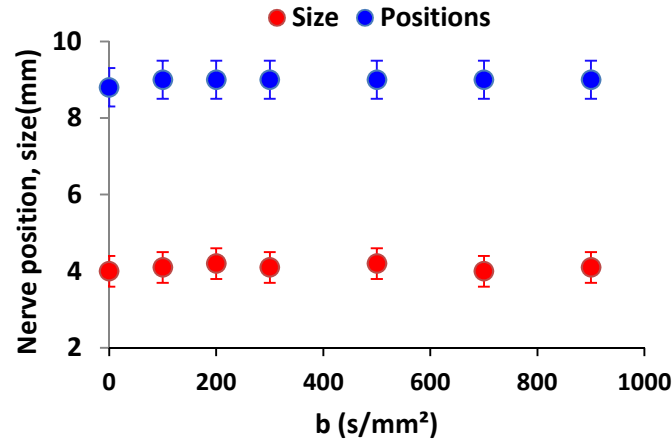
Figure 4.1.14 *Mean position and size variations of nerves with b values obtained from one subject nerve images. There was no systematic shift in the position or size of the nerves with increasing b value, indicating no significant variations in image distortion due to eddy currents.*

Figure 4.1.15 shows example logS vs b plots for nerve, cord and agar gel from one subject. Figure 4.1.16 shows the IVIM plots from nerves and cord from five subjects. From these figures it is clear that for b values lower than 300s/mm^2 data is contaminated with IVIM effects. Table 4.1.2 summarizes the IVIM parameters fitted from these data sets.
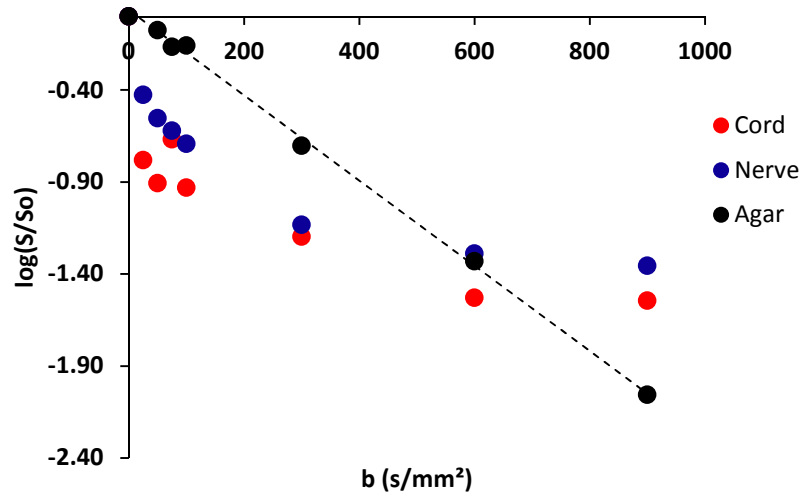
Figures 4.1.15 *Example IVIM plots for nerves, cord and agar phantom. Agar phantom shows linear changing with b values as there is no IVIM effect. However, nerve and cord signals show clear IVIM effects.*
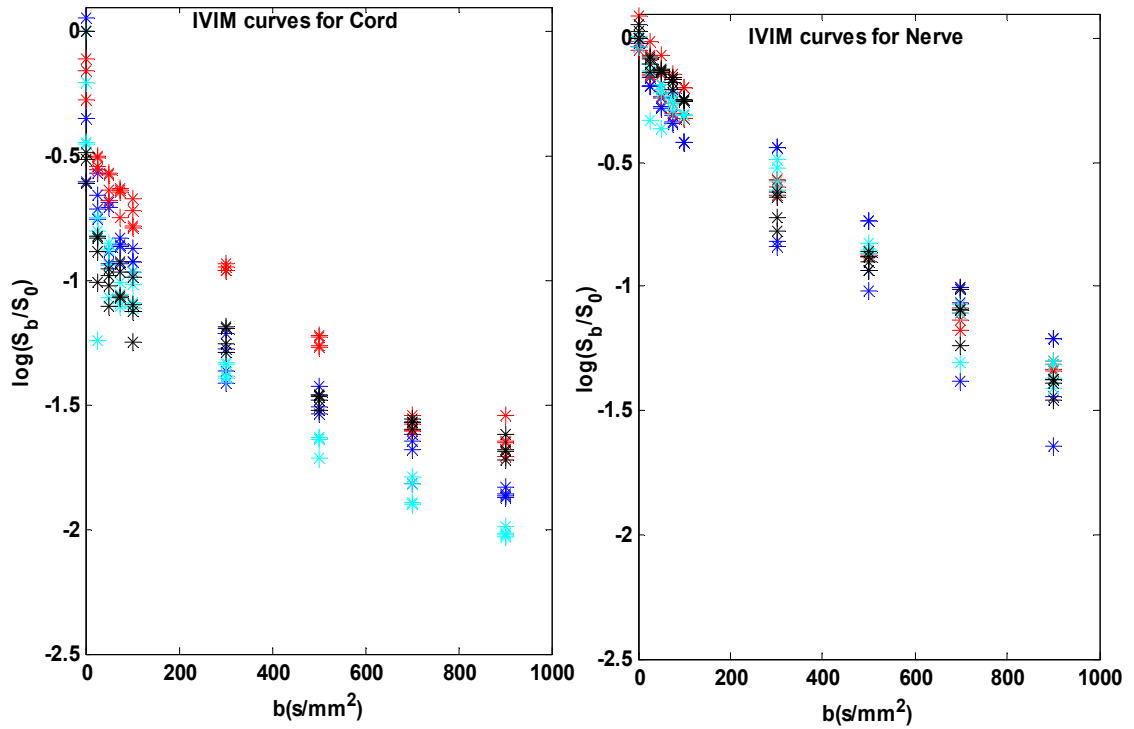
Figure 4.1.16 *IVIM plots for Brachial plexus nerves and cord, each colour presents individual subject.*

Table 4.1.2: IVIM parameters calculated from five subjects with individual subject

measurement variances

Subject	Nerve			Cord		
	$D \times 10^{-3}$ mm²/s	$D^* \times 10^{-3}$ mm²/s	f	$D \times 10^{-3}$ mm²/s	$D^* \times 10^{-3}$ mm²/s	f
Sub1	1.4±0.04	7.0±0.4	0.20±0.04	1.0±0.04	70±4	0.50±0.04
Sub2	0.9±0.02	5.0±0.6	0.20±0.02	0.9±0.02	60±3	0.46±0.01
Sub3	1.0±0.03	6.0±0.8	0.30±0.01	1.0±0.04	90±6	0.48±0.00
Sub4	1.3±0.05	7.0±1.0	0.15±0.01	0.8±0.01	70±7	0.46±0.02
Sub5	1.1±0.05	8.0±1.4	0.33±0.02	0.9±0.00	60±5	0.50±0.03
Mean±S.E.	1.1±0.02	7.0±1.0	0.24±0.01	0.9±0.011	70±7	0.48±0.02

There was a significant difference between nerve and cord measured parameters for D^* (t =-20.6, p =0.00003) and f (t =-12.7, p =0.0005), but not for D (t =0.2, p =0.85).

4.1.4 Discussion

A quantitative imaging and analysis procedure of the brachial plexus has been developed using DWIBS sequence. Such semi-automated method will help further quantitative measurements from MR images. From these preliminary measurements a basic sequence set up was decided. Subsequent scanning was performed at 3 T for maximum SNR, although it should be noted that in future work 1.5 T might give better images of the nerves more medially, probably due to the effects of field inhomogeneities caused by the lungs. Subsequent work used TI = 220 ms for optimal fat suppression. Also the results showed that there were no significant eddy current distortions in these data sets.

From Figure 4.1.16 it is clear that ADCs measured between 0 and 300s/mm^2 region are not representing pure diffusion, whereas at higher b values the measured signal is dominated by pure diffusion effects. Thus for later measurements of ADC for nerve and cord in brachial plexus the minimum b-value used was $b_1 = 300$ s/mm² to avoid the IVIM effects with other b value as $b_2 > 300$ s/mm². The volume fraction parameter f for cord is almost double that of the nerve, also D^* for cord is higher by an order of magnitude than the nerve, this implies that cord has higher fluid mobility due to movement of CSF and blood flow through the subarachnoid Virchow Robin spaces. There was a weak (insignificant) trend for $D_{cord} < D_{nerve}$ which might reflect the fact that axons in the peripheral nerves have a larger diameter (5 -20 µm) than axons in cord (2-6 µm). This will be investigated further in the next section.

4.2 A study of diffusion time dependent ADC of the brachial plexus

4.2.1 Introduction

In biological tissues, the diffusive displacement will deviate from its expected linear relationship with the diffusion time Δ, as predicted by Einstein's diffusion equation, already discussed in Chapter 3. It will plateau at a level determined by the size of the restricting volume as shown in schematic diagram in Figure 4.2.1. An experimental determination of the degree of restriction can, therefore, be obtained by examining the diffusion time dependence of the diffusion coefficient.
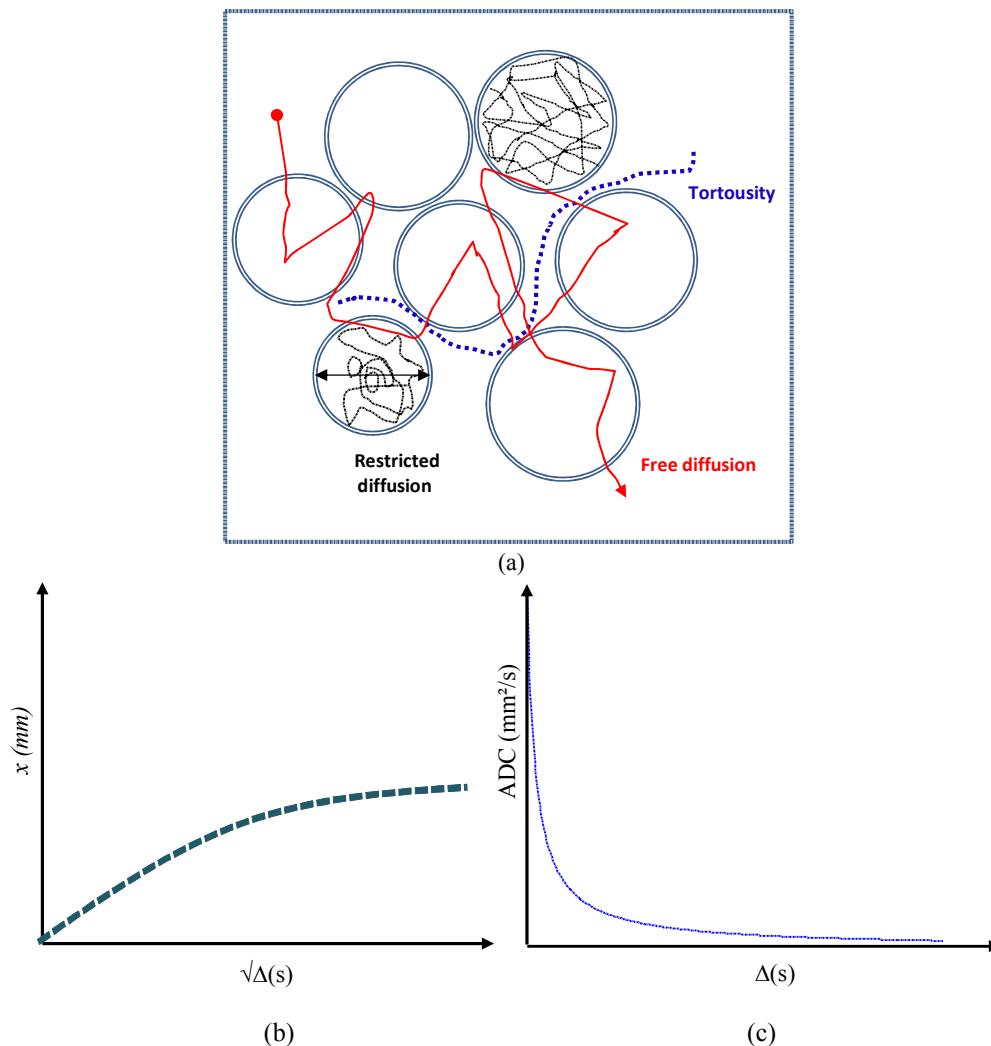

Figure 4.2.1 *(a) Illustrating possible diffusion processes in biological tissues; (b) mean displacement of molecules with square root of diffusion time and (c) variations of apparent diffusion coefficient and diffusion time in the case of restricted diffusion.*

The reduction in ADC with diffusion time in vivo has been explained by several factors, such as combination of high viscosity, macromolecular crowding, and restriction (Hazlewood *et al.* 1991), and tortousity in the extracellular space (Nicholson *et al.* 1981, Chen *et al.* 2000, Nicholson 2001). These potential factors have been characterized by the intraaxonal restricted and extra axonal hindered diffusion model (CHARMED) (Assaf *et al.* 2005, Assaf *et al.* 2008); porous media model (Latour *et al.* 1994, Sigmund 2011); the cell membranes hindering (Le Bihan *et al.* 2006, Le Bihan 2011); and cell membrane permeability and density effects (Novikov *et al.* 2011). This section aims to measure the ADC values from brachial plexus nerves and cord and study the change in ADC within the scanner accessible diffusion time as a marker of restricted diffusion. As a simple approach, and to parameterize the diffusion time dependence of ADC of the brachial plexus, the porous media restricted diffusion model has been used in this section.

Unfortunately for a constant b value and TE only a limited range of diffusion times are achievable on the clinical MRI scanner used for in vivo scanning. Thus first of all the range of accessible diffusion times for different b values had to be assessed. Furthermore statistical noise is an inherent characteristic in all MR images, and this noise will propagate into ADC estimates, and so it is important to design experiments that are sensitive to the effects of restricted diffusion. Thus the sequence has been optimized for high sensitivity to ADC differences and low sensitivity to noise, using analytical methods and Monte Carlo simulations.

The porous media restricted diffusion model assumes that the long diffusion time is greater than the time needed for the water molecules to encounter the restriction boundaries, and the short diffusion time is such that the corresponding diffusion length is less than the dimension of the restriction. The dimensions of the spinal cord WM and GM fibres are ~2 μm and ~6 μm respectively and of the DRG and rami nerve fibres are 5~15 μm (Mukherji *et al.* 1996). Considering the free water diffusion coefficient D~0.002 mm^2/s at body temperature, root mean square molecular displacement would be greater than the size of the WM fibres after t~1 ms, for GM fibres after t~9 ms and for the peripheral nerve fibres after t~6 to 56ms.

Therefore this model was used in an attempt to parameterize the in vivo ADC data from the brachial plexus nerves and cord, by fitting the data to the porous media restricted diffusion model expressed by Latour *et al*, discussed in section (3.2.6.2). To

determine the robustness of fitting the brachial plexus data to this model, the sensitivity of the model to its parameters was investigated by simulation.

Objectives: Optimize the scanner parameters for DWIBS sequence and verify with Monte Carlo restricted simulation; measure the ADC from brachial plexus nerves and cord over a range of accessible diffusion time in a human scanner; finally study of ADC vs Δ with the Latour equations and derive the tortousity and S/V parameters.

4.2.2 Methods

4.2.2.1 Accessible values of the pulse sequence

To study restricted diffusion it is necessary to vary diffusion times for fixed b values over a range that is appropriate for the biologically interesting range of restrictions. However, this imposes practical limitations, since the maximum value of Δ is limited by TE and hence SNR. The minimum value of Δ is limited by the gradient area required to achieve the required b value. Thus achievable combinations of Δ, δ, TE and b were determined for the patched code on the Philips 3T Acheiva scanner. In the patched code delay times td_1 and td_2 can be varied to produce a range of diffusion times (Δ_{min} to Δ_{max}) at fixed δ, TE and b if G is varied. Figure 4.2.2 shows the schematic PGSE diffusion sequence with timing parameters.

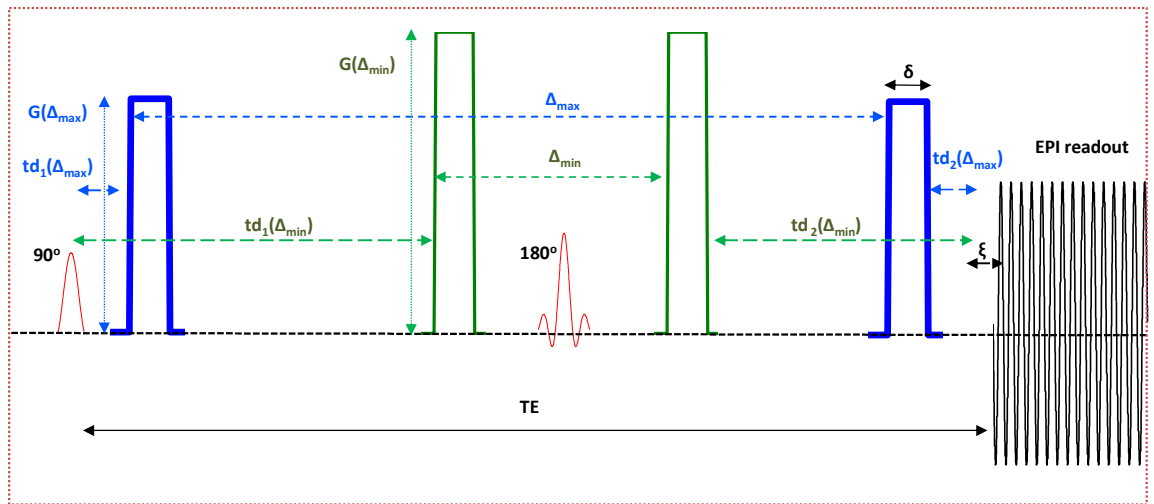Figure 4.2.2 *PGSE diffusion sequence with time parameter relation as* $TE=\Delta+td_1+td_2+\delta+\xi$, *where ξ is the minimum time between the end of the second gradient lobe and the centre of k space.*

The patched code did not properly report b values for given values of Δ, TE and δ. Thus b values achievable for an accessible range of Δ, delay times td_1 and td_2 and

maximum G amplitudes were calculated using b-value expression (already discussed in section 3.5.2) in MAPLE®15 software to allow diffusion gradient ramps and other gradients in the sequence. Thus using $b = \gamma^2 \int_0^{TE} (\int_0^t G(t')dt')^2 dt$, with TE=Δ+td$_1$+td$_2$+δ+ξ, where ξ (=19.7 ms) is the minimum time between the end of the second gradient lobe and the centre of k space, that limits the range of Δ_{max} and Δ_{min}.

4.2.2.2 Numerical optimization

Let *K* be a parameter used for describing the changes in diffusion coefficient with diffusion time. If D$_1$ is the ADC on short diffusion time (Δ_1) and D$_2$ is the ADC at long diffusion time (Δ_2), then define the diffusivity difference,

$$K = D(\Delta_1)-D(\Delta_2) \tag{4.2.1}$$

The aim of the optimization is to determine how the error in the value of *K* varies with sequence parameters. It is important to note that *K* is not a physical parameter but instead a measure of the potential sensitivity of an MR sequence to restricted diffusion. For this optimization the standard propagation of error formula has been used:

$$\sigma^2[f(x,y,z)] = \sigma_x^2 \left(\frac{\partial f}{\partial x}\right)^2 + \sigma_y^2 \left(\frac{\partial f}{\partial y}\right)^2 + \sigma_z^2 \left(\frac{\partial f}{\partial z}\right)^2 \tag{4.2.2}$$

where σ_x, σ_y, σ_z are the variances for different parameters. From Section 3.2 the diffusion signal can be expressed as

$$S = S_o e^{-bD} e^{-TE/T2} \tag{4.2.3}$$

where D is the apparent diffusion coefficient.

Generally D can be calculated by weighted linear least square fit of diffusion signal at different b values assuming monoexponential decay. Now as a first step the error in *D* will be estimated. Let the noise in the raw images be expressed as variance in the signal = $(\sigma_s^2)^{1/2}$ (4.2.4)

Using the Equations (4.2.2) and (4.2.3) noise in the diffusion signal can be expressed as,

$$\sigma_{lnS} = \frac{\partial lnS}{\partial S}\sigma_S = \frac{1}{S}\sigma_S = \frac{1}{S_o e^{-b_i D} e^{-TE/T2}}\sigma_S \tag{4.2.5}$$

By the method of maximum likelihood in weighted least square fitting (Bevington 1994), error in the slope of *logS* vs *b* where the signal S is acquired at multiple (*N*) b values can be expressed as,

$$\sigma_D = \sqrt{\frac{1}{N\Delta}\sum\frac{1}{\sigma_i^2}} \tag{4.2.6}$$

where $\Delta = \sum\frac{1}{\sigma_i^2}\sum\frac{x_i^2}{\sigma_i^2} - \left(\sum\frac{x_i}{\sigma_i^2}\right)^2$, $x_i = b_i$ and σ_i is the variance in logS, that can be

expressed as, $\sigma_i = \frac{1}{S_0 e^{-b_i D} e^{-TE/T2}}$.

Now from Equations (4.2.5) and (4.2.6),

$$\sigma_D = \frac{1}{S_0 e^{-\frac{TE}{T2}}}\left(\frac{1}{N}\sum e^{-2b_i D}\right)^{1/2}\left\{\sum e^{-2b_i D}\sum b_i^2 e^{-2b_i D} - \left(\sum b_i e^{-2b_i D}\right)^2\right\}^{-1/2} \tag{4.2.7}$$

Thus for different values of b the approximate errors in D, σ_D can be calculated using Equation (4.2.7), by taking account of effect of Δ on TE. However it has previously been shown that in the case of monoexpoential decay with b value, D can be optimally measured by using appropriately selected two values of b (Bito *et al.* 1995; Xing *et al.* 1997; Conturo *et al.* 2005). Thus for the noise estimation in D two point acquisition strategy allows simpler model and time efficient method that was formulated.

Considering the diffusion data acquired at two b values (b1 and b2),

$$S_1 = S_0 e^{-b_1 D} e^{-TE/T2}, \quad S_2 = S_0 e^{-b_2 D} e^{-TE/T2} \tag{4.2.8}$$

Using Equation (4.2.7) and (4.2.8) the variance in D can be expressed as,

$$\sigma_D = \frac{1}{\sqrt{2}S_0 e^{-\frac{TE}{T2}}}(e^{-2b_1 D}+e^{-2b_2 D})^{1/2}\{(e^{-2b_1 D} + e^{-2b_2 D})(b_1^2 e^{-2b_1 D} +$$

$$b_2^2 e^{-2b_2 D}) - (b_1 e^{-2b_1 D} + b_2 e^{-2b_2 D})^2\}^{-1/2}$$

By simplification and squaring,

$$\sigma_D^2 = \frac{\sigma_S^2}{(b_2-b_1)^2}\frac{1}{\left(S_0 e^{-\frac{TE}{T2}}\right)^2}(e^{2b_1 D} + e^{2b_2 D}) \tag{4.2.9}$$

Thus the error in D has been estimated and it can be used to find the error in the diffusion time dependent diffusivity difference, *K* for restricted diffusion study.

Now the variance in diffusivity difference, *K* (Equation 4.2.1), can be expressed as

$$\sigma_k = (\sigma_{D_1}^2 + \sigma_{D_2}^2)^{1/2} \tag{4.2.10}$$

Using Equations (4.2.9) & (4.2.10)

$$\sigma_k = \left[\frac{\sigma_S^2}{(b_2-b_1)^2 S_0^2 e^{-\frac{2TE}{T2}}}(e^{2b_1 D_1} + e^{2b_2 D_1} + e^{2b_1 D_2} + e^{2b_2 D_2})\right]^{1/2} \tag{4.2.11}$$

Assuming the optimum value of $b_1=0$ for maximum SNR Equation (4.2.11) reduces to

$$\sigma_k = \frac{\sigma_S}{b_2 S_0 e^{-\frac{TE}{T2}}}(2 + e^{2b_2 D_2} + e^{2b_2 D_1})^{1/2} \tag{4.2.12}$$

(If in reality $b_1 \neq 0$ due to IVIM effects, then b_2 will be difference in two b values used). However we are not only interested in minimizing the variance in K, we want to maximize the contrast to noise in K, so we define the term sensitivity in combined ADC measurement as,

$$\Gamma_K = \frac{K}{\sigma_k} = \frac{D_1 - D_2}{\sigma_k} \tag{4.2.13}$$

Thus the study of ADC variations with diffusion time requires that Γ_K should be maximum, to sensitize the sequence with difference in diffusivity with diffusion time as a marker of restricted diffusion with minimum sensitivity to noise.

A Monte Carlo (MC) simulation of restricted diffusion with impermeable restriction boundaries (described in **Appendix-I**) was used to determine the reasonable range of values of D within scanner accessible diffusion times, and hence this optimization used to estimate the variation in K with scanner parameters Δ, δ, and TE, T2 and restriction sizes.

For the initial optimization the error in ADC (σ_D) was studied analytically from Equation (4.2.7) using two different b-value sets, and corresponding Δ values, at T2 = 50 ms and 80 ms. Then, the K values and its variance, σ_k from Equations (4.2.1) and (4.2.12); and the corresponding sensitivities, Γ_K from Equation (4.2.13) were studied from the MC simulated restricted diffusion. For these calculations the b-values 0,100 s/mm²; 0,200 s/mm²; 0,300 s/mm²; 0,400 s/mm² and 0,500 s/mm² are used with variations

(i) TE and range of Δ values: using Δ_1 = 18.3 ms to Δ_2 = 91.3 ms and TE_1 = 110 ms; Δ_1 = 18.3 ms to Δ_2 = 81.3 ms and TE_2 = 100 ms; and Δ_1 = 18.3 ms to Δ_2 = 66.3 ms and TE_3 = 85 ms, with δ = 10 ms, T2 = 100 ms.

(ii) δ values: where gradient G changes with δ to keep b-values fixed, 5, 10, 20, 40 ms with restriction sizes 8, 20 and 45 μm; Δ_1 = 18.3 ms and Δ_2 = 81.3 ms, TE = 100 ms, T2 = 100 ms.

(iii) T2 values: 60 ms and 120 ms with a fixed restriction size 45 μm; Δ_1 = 18.3 ms and Δ_2 = 81.3 ms, TE = 100 ms and δ = 10 ms.

(iv) the restriction sizes: R = 5, 20, 30, 45 and 55 μm using Δ_1 = 18.3 ms and Δ_2 = 81.3 ms, TE = 100 ms, T2 = 100 ms. The variance σ_k also studied with bD_{av} where $D_{av} = (D_1 + D_2)/2$.

4.2.2.3 Sensitivity of Latour equation to fitted parameters

As discussed earlier the Latour equation for porous media restricted diffusion model is expressed as,

$$D(t) = Do\left\{1 - \left(1 - \frac{1}{\alpha}\right)\left(\frac{c\sqrt{\Delta} + \frac{\left(1-\frac{1}{\alpha}\right)\Delta}{\theta}}{\left(1-\frac{1}{\alpha}\right) + c\sqrt{\Delta} + \frac{\left(1-\frac{1}{\alpha}\right)\Delta}{\theta}}\right)\right\}$$ (4.2.14)

where, $c = \frac{4}{9\sqrt{\pi}}\left(\frac{S}{V}\right)\sqrt{Do}$ and $\theta = 0.02$ sec is the scaling factor which depends on the restriction size, α is the tortousity limit, and S/V is the surface to volume ratio.

Initially the sensitivity of the Latour equation to its fitted parameters was investigated using biological cell red blood cells (RBC), tumour cells etc. experimental observations (Latour *et al.* 1994, Latour *et al.* 1995, Loskutov *et al.* 2013). To illustrate this, the sum of squared difference was found between values of ADC calculated from the Latour equation for $\alpha = 1.1$ to 3.5 and S/V = 100 to 250 mm^{-1} and ADC calculated for $\alpha = 1.2$ and S/V = 200 mm^{-1}, assuming $D_0 = 0.002$ mm^2/s (as water molecular diffusion coefficients in body temperature) and $\theta = 0.01$ s (as time scaling factor) and for scanner accessible diffusion times ($\Delta_1 = 18.3$ ms to $\Delta_2 = 81.3$ ms). These sums of squared differences were displayed as a contour plot.

To more formally test the sensitivity of the fit to the Latour equation, ADC values were simulated from the Latour equation within the scanner accessible diffusion time, random noise was added, and then the data were fitted with Latour equation for α and S/V. This was repeated for 50 realisations of the random noise and for the same values of α and S/V as above. Results were displayed using five contour plots: (1) the % error in α_{fit} as a function of simulated α and S/V; (2) similarly % error in S/V$_{fit}$ as a function of simulated α and S/V; (3) standard deviation of error in α_{fit} as a function of simulated α and S/V; (4) standard deviation of error of S/V$_{fit}$ as a function of simulated α and S/V; (5) chi square values ($\chi^2 = \sum\frac{(x-\mu)^2}{\sigma^2}$) between the simulated and fitted parameters as a function of α and S/V.

4.2.2.4 Experimental investigations of restricted diffusion

Next ADC values were measured from brachial plexus nerves and cord. Images were acquired from *cohort B* (page 126) using the DWIBS sequence and methods discussed in Section 4.1.1. To eliminate IVIM effects (discussed in Section 4.1.2), the low b value used was $b_1 = 300$ s/mm^2. From the optimization the higher b value was

selected to be double the lower one i.e. $b_2 = 600$ s/mm^2. Using TR = 8813 ms, TE = 100 ms, δ =10 ms, with maximum range of diffusion time as Δ = 18.3, 25.3, 33.3, 41.3, 49.3, 57.3, 65.3, 73.3, 81.3 ms. ROIs were selected using 2D Gaussian fitting with one pixel for each nerve in sagittal view and four pixels for cord in transverse view (discussed in section-4.1). ADC values were calculated using the equation $D = \frac{lnS_1 - lnS_2}{b_2 - b_1}$. To compare the possible statistical difference between ADC values of nerves and cord the Wilcoxon rank sum test used to test the null hypothesis, H$_0$: ADC$_{cord}$ = ADC$_{nerve}$.

To compare restricted diffusion and free diffusion ADCs were also calculated from two phantoms with agar gel and distilled water using the same procedure followed for in vivo observations. Finally the measured variations of ADCs for nerves and cord with the diffusion times were non-linearly fitted with Latour Equations (4.2.14) for both α and *S/V* and then for α only. The ADC values are regenerated by statistical bootstrapping technique. 50 resamples of the ADC dataset created, each of which is obtained by random sampling based on the differences between data and fitting equation respectively.

The method proceeds as follows.

    (i)   Fit the ADC values (D_i) with model and retain the fitted values $D*_i$ and the residuals $\varepsilon_i = D_i - D*_i$, (i =1,2,..,9)

    (ii)   For each D_i value add a randomly resampled residual, ε_i to the response variable D_i.

    (iii)   Refit the model using the fictitious new variable $D*_j$.

Repeated steps for 50 times.

4.2.3 Results

4.2.3.1 Accessible values of the pulse sequence

Figure 4.2.3 shows the accessible range of Δ and TE at different b values from the Philips 3 T scanner and Table 4.2 shows the numerical values; the ranges of Δ for a given TE decrease with higher b values as expected.
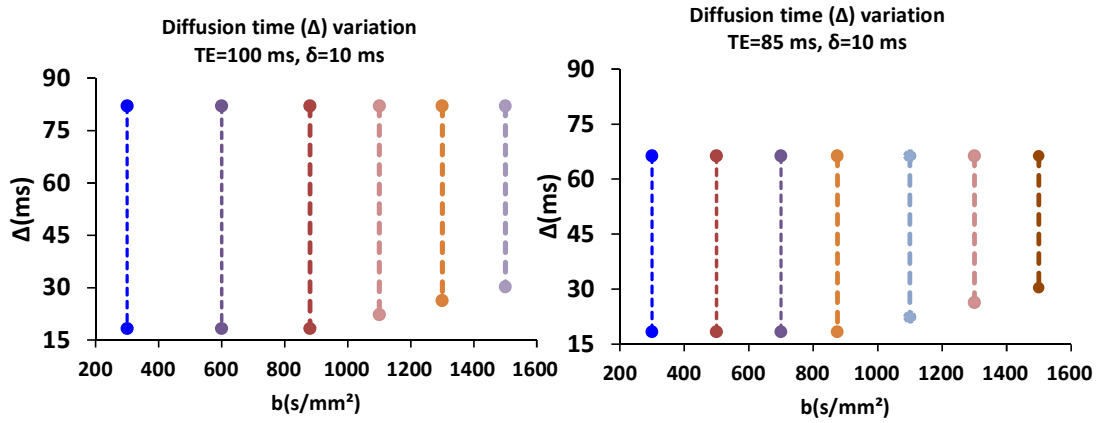

Figure 4.2.3 *Variations of the ranges of diffusion time Δ with b values at TE=100 and 85ms observed from 3T scanner.*

Table 4.2.1 Diffusion time limit

TE (ms)	Δ_{min} (ms)	Δ_{max} (ms)	b_{max} (s/mm²)
100	18.3	81.3	920
85	18.3	66.3	880

4.2.3.2 Numerical optimization

The following sections shows the results of optimization of parameters of restricted diffusion by minimization of error in diffusivity σ_D, variance in diffusivity difference, σ_k, and maximizing ADC difference K and sensitivity in diffusivity difference, Γ_K using Equations 4.2.7, 4.2.9 and 4.2.10 respectively.

Figures 4.2.4 shows the initial results from numerical optimization of measurements of ADC using Equation 4.2.7, this takes account of how Δ interacts with b values with maximum gradient amplitude (G_{max}) in the measurement of restricted diffusion considering diffusivity D = 0.001 mm²/s comparable with nerve ADC values, TE = 100 ms and δ = 10 ms. It also shows σ_D variations with bD at two T2 values as well.
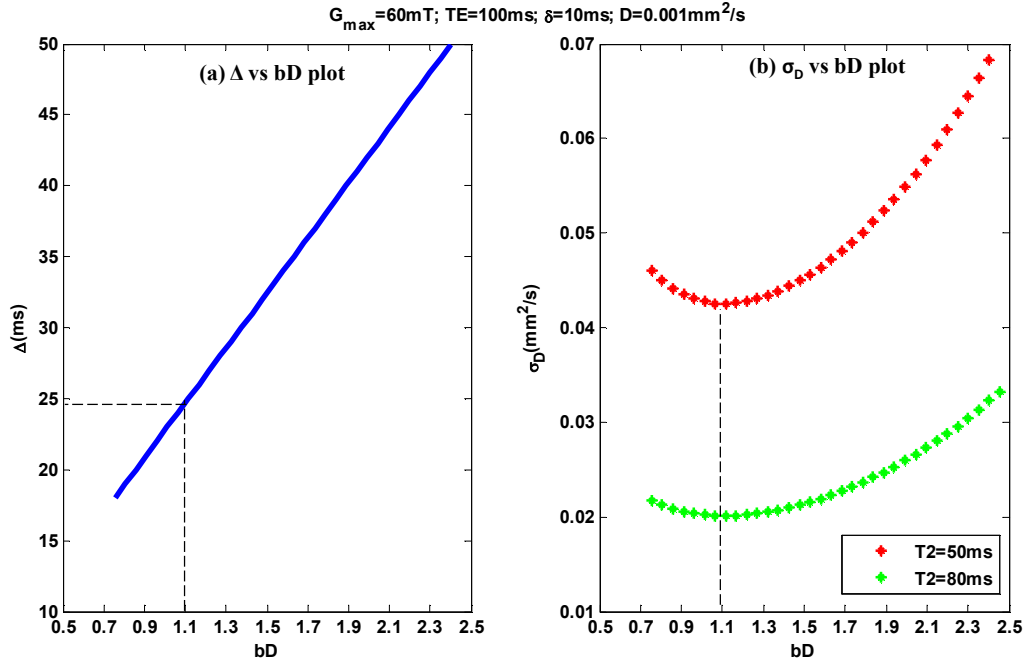
Figure 4.2.4 *(a) Δ variations with bD values at scanner maximum gradient amplitude G_{max} showing Δ=24.8ms when bD=1.1; (b) $σ_D$ variations with bD with G_{max} at T2=50ms and 80ms, showing the minima occurs when bD=1.1.*

From the curves error minima occurs when, *bD* = 1.1 and corresponding Δ = 24.8 ms for both T2 values when corresponding diffusion gradient amplitude is maximum. Thus the required diffusion time, Δ is in the accessible range in the Philips 3T scanner.

Effects of scanner parameters on sensitivity to restricted diffusion

These sections show the results of optimization using Monte Carlo simulation of restricted diffusion. It shows the difference in diffusion coefficients measured in two different experiments, *K* dependency, on experimental parameters and physical parameters in assessing restricted diffusion.

Figure 4.2.5 shows variations of $σ_k$ and $Γ_K$ with b-value for different ranges of Δ corresponding to different TE for a fixed restriction size of 20 μm.
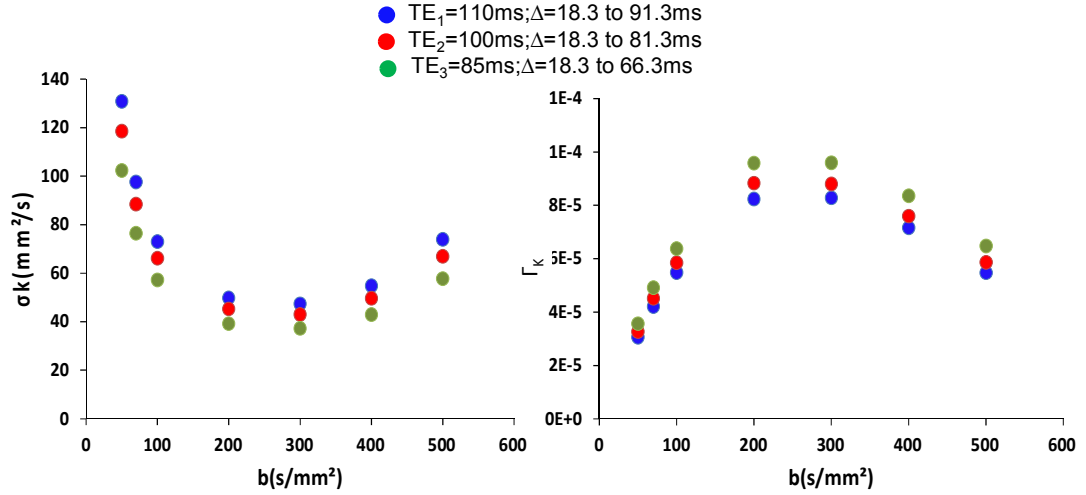
Figure 4.2.5 *Variation of σ_k and Γ_K with b-values at different TE and range of Δ at fixed $\delta=10ms$. σ_k decreases for short TE and Γ_K increases with short TE. It also shows minima of σ_k and maxima of Γ_K at b=250s/mm^2.*

It shows the variance K, σ_k has a minima at b = 250 s/mm² and decreases with shorter TE as expected the increased SNR despite the smaller accessible range of Δ. Similarly the sensitivity in diffusivity difference, Γ_K shows maxima at same b-value, and reduces with increasing TE. It is not possible to achieve an adequate value of a TE< 80ms for a suitable b value.

Figure 4.2.6 shows the ADC differences K with δ (while changing the gradients for a fixed b-value) at restriction boundaries 20 μm and 8 μm for given diffusion times (Δ_1 = 18.3 ms, Δ_2 = 81.3 ms), TE = 100 ms and at different b-values.

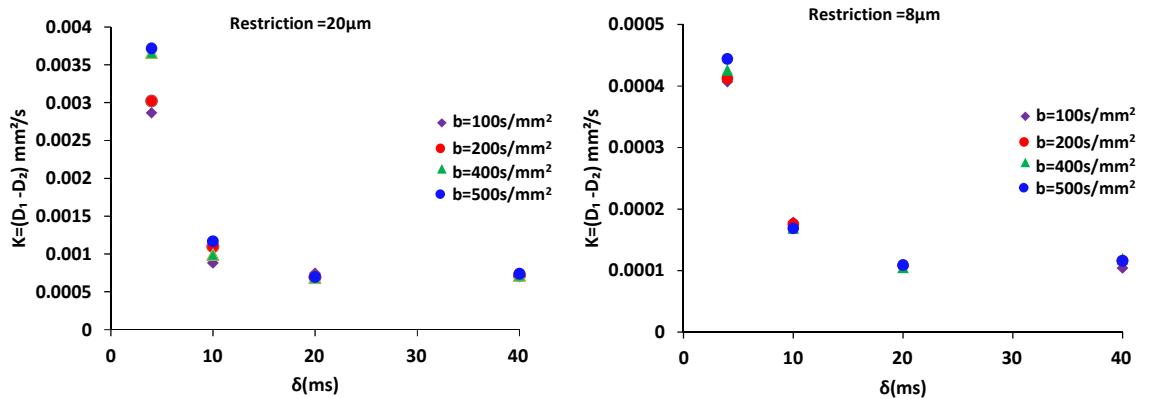Figure 4.2.6 *Variations of K with δ and b-values at restriction boundary 20 μm and 8 μm at fixed range of Δ(18.3 ms to 81.3 ms) and TE =100 ms. Shows K increases with shorter δ.*

148

It shows that the ADC differences increase for shorter δ. It also shows that the diffusivity difference is higher for large b-values as expected due to more diffusion weighting as long as TE is constant.

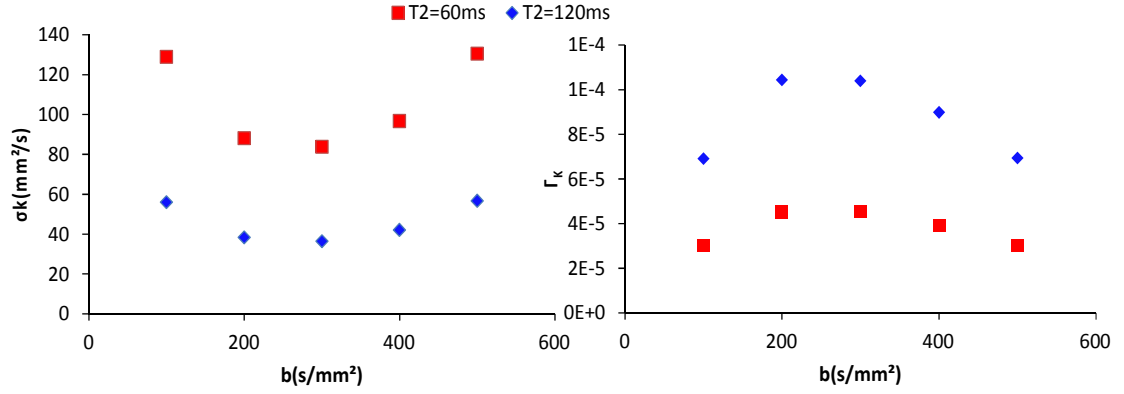Figure 4.2.7 shows how σ_k and Γ_K vary with b-values for different T2.

Figure 4.2.7 *Variation of σ_k and Γ_K with b-values at different T2 with fixed range of Δ(18.3 ms to 81.3 ms) and TE = 100 ms. Shows minima of σ_k and maxima of Γ_K at b = 250 s/mm².*

The σ_k becomes smaller with increasing T2 as expected due to increased SNR. Similarly Γ_K is greater for long T2. The minima of σ_k and maxima of Γ_K at the same b-value as observed before.

Figure 4.2.8 show the variations of K, σ_k and Γ_K with b values and σ_k variations with bD_{av}, where $D_{av}=(D1+D2)/2$ for different restriction sizes.
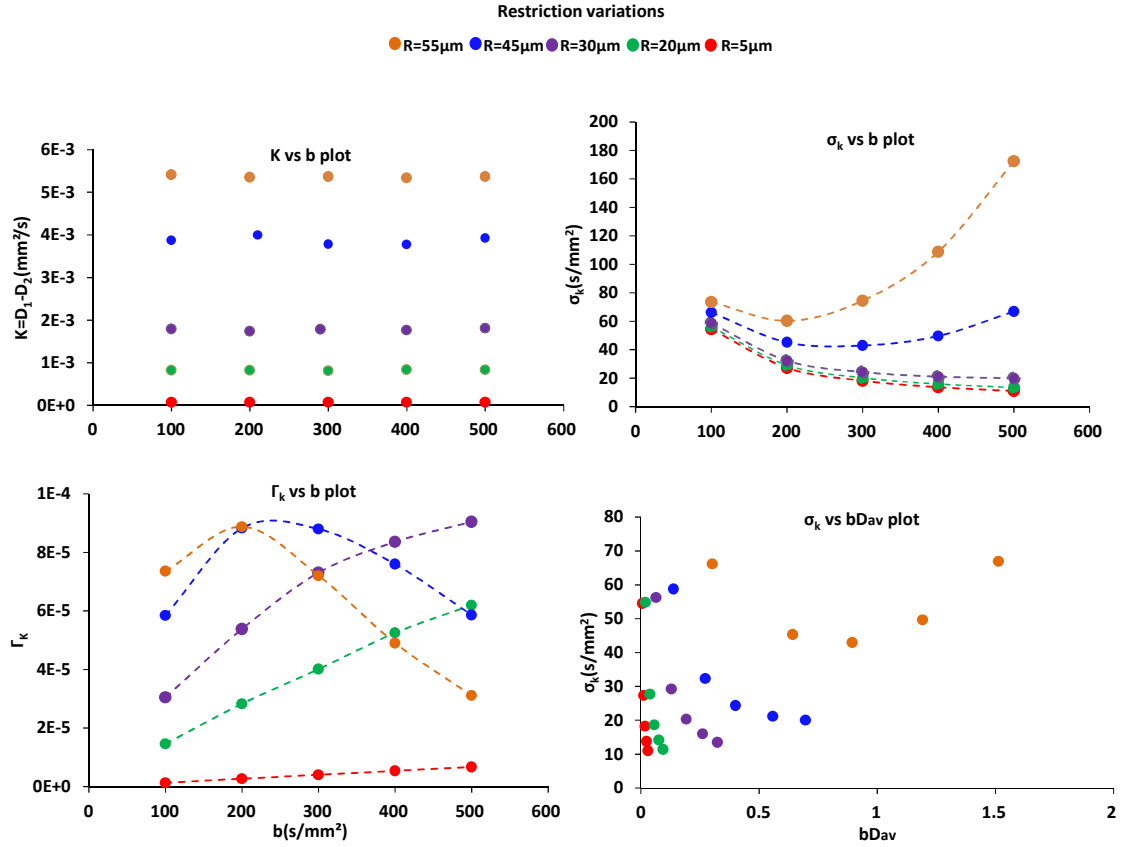
Figure 4.2.8 Restriction variations with fixed δ = 10 ms, Δ = 18.3 ms to 81.3 ms and TE=100ms. ADC difference K increase with higher restriction boundary sizes but no change with b-values as expected; σ$_k$ decreases with smaller restriction sizes and there are minima at b = 250 s/mm^2 when R>30 μm; Γ$_K$ decreases with smaller restriction sizes at low b-values; the variance in K, σ$_k$ shows minima for higher restriction sizes at bD$_{av}$~1.0 which decreases for smaller restriction sizes.

The diffusivity differences *K* increases with higher restriction sizes and variance in *K* (σ$_k$) reduces with decreasing restriction sizes within the range examined as expected. For restriction sizes *R* > 30 μm there is an optimal value of b = 250 s/mm^2. The sensitivity of diffusivity differences decreases with smaller restriction sizes and shows maxima for higher restriction sizes. The variance in *K* shows minima at bD$_{av}$~1 for higher restriction size, however, that decreases with smaller restriction sizes. It shows that higher b-values required for smaller restricted diffusion sensitization.

4.2.3.3 Sensitivity of Latour equation to fitted parameters

Figure 4.2.9 illustrates ADC variations with Δ and dependencies on tortousity (α) and S/V values according to the Latour equations.
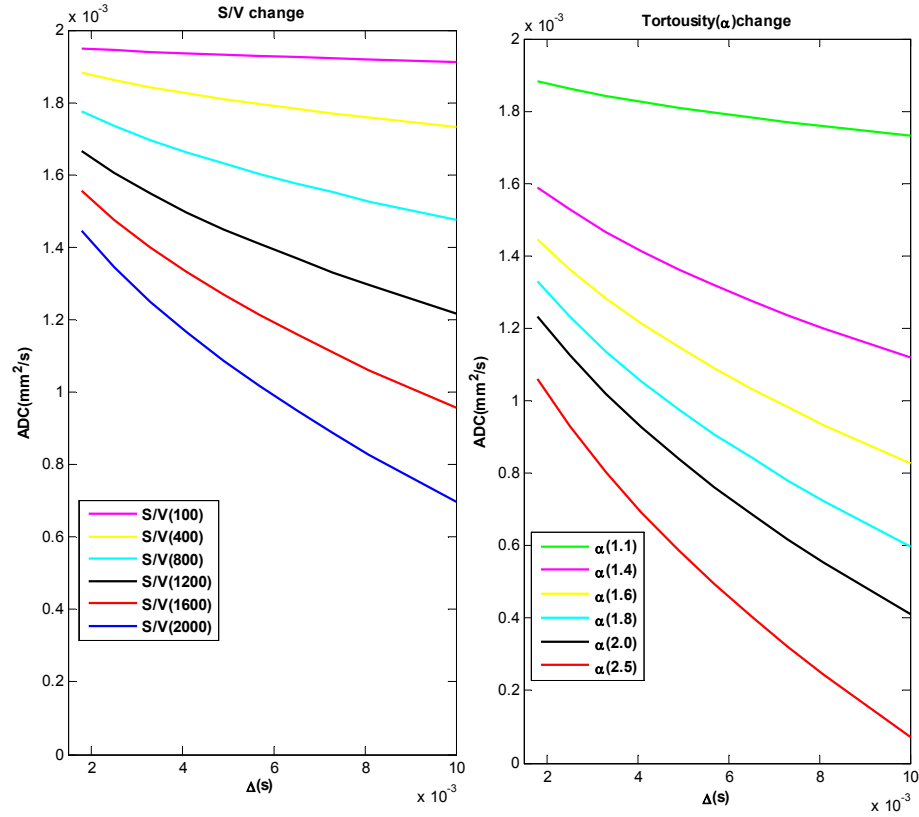

Figure 4.2.9 *Variations of ADC with diffusion time (Δ) from Latour equation with S/V and α variation.*

Figure 4.2.10 shows contour plot of residual sum square between ADC for $\alpha = 1.2$ and S/V = 200 mm^{-1} and ADC for other parameter values $\alpha = 1.1$ to 3.5 and S/V = 30 to 250 mm^{-1}; while using $D_0 = 0.002$ mm^2/s and $\theta = 0.01$ s. Figure 4.2.11 shows contour plots with percent error in α_{fit} as a function of α and S/V; percent error in S/V$_{fit}$ as a function of α and S/V; standard deviation of error in S/V as a function of α and S/V; standard deviation of error in α as a function of α and S/V and χ^2 plot between fitted and simulated α and S/V.
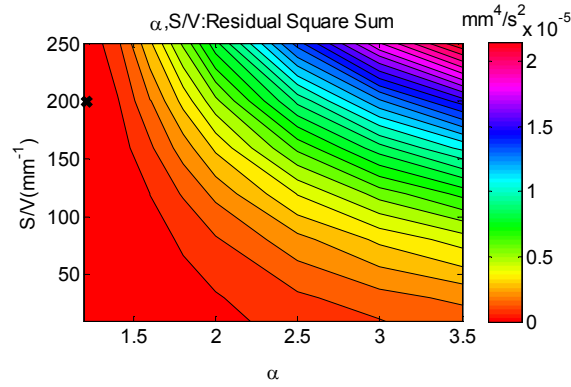
Figure 4.2.10 *Contour plot of residual sum square between ADC calculated from the Latour equation at α= 1.2 and S/V = 200 mm^{-1} (black cross marker) and difference with other values of α = 1.1 to 3.5 and S/V=30 to 250 mm^{-1}.*

Figure 4.2.11 *Contour plot of % error in α$_{fit}$ (a) and S/V$_{fit}$ (b) as function of simulated α and S/V; % Error standard deviation in α$_{fit}$ (c) and S/V$_{fit}$ (d) as a function of α and S/V; (e) χ²values for fitted and simulated parameters as a function of α and S/V.*

4.2.3.4 Experimental investigations of restricted diffusion

ADC versus Δ from phantoms and in-vivo and scanning are shown in the Figures 4.2.12 and 4.2.13.
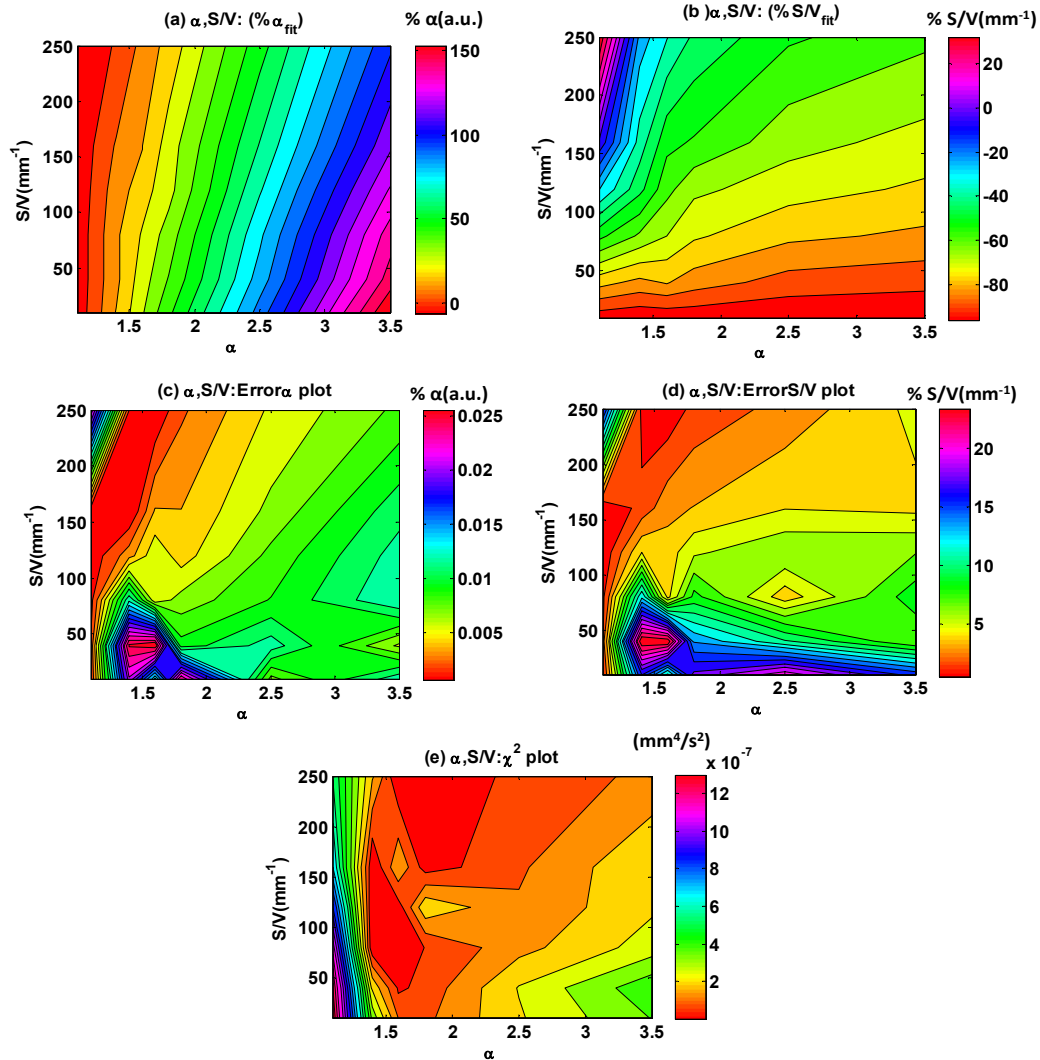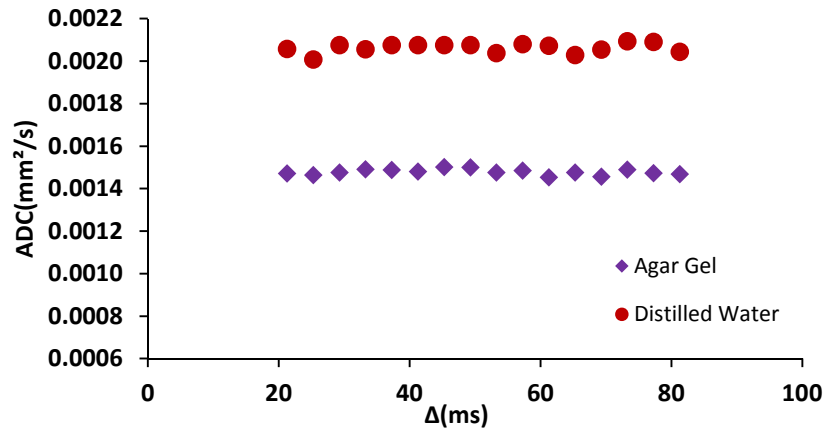

Figure 4.2.12 *ADC vs Δ plots for agar gel and water phantoms.*
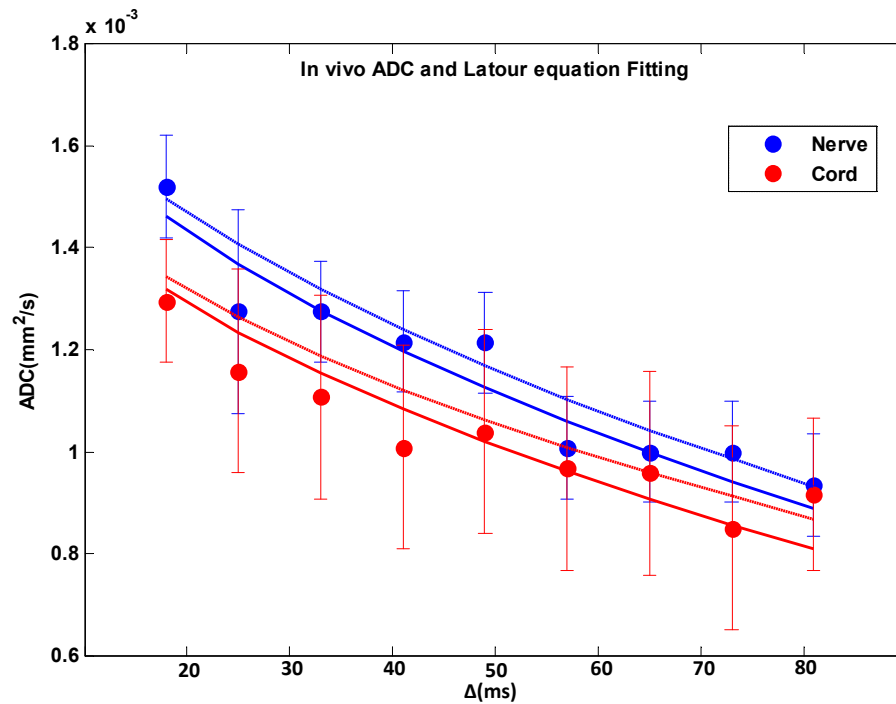
Figure 4.2.13 *Measured values of ADC vs Δ for nerves (blue) and cord (red) averaged over 8 subjects. These also indicate fit to Latour equation. The solid lines fitted for α and S/V and dotted lines fitted for α only. Error bars indicate standard deviations of 8 subject's measurements.*

In vivo ADC vs Δ values were fitted to Latour equation (4.2.14) for α and S/V parameters and for α parameter. From the Wilcoxon rank sum test between the ADC of nerves and cord, p= 0.1972 and H = 0 indicate that there is not enough evidence to

reject the null hypothesis ($ADC_{cord} = ADC_{nerve}$). Table 4.2.3 and 4.2.4 presents the Latour fitting parameters with in vivo ADC measurements.

Table 4.2.3 Parameters associated with in vivo ADC vs Δ data fitting to the Latour equation for α and S/V, assuming D_0 =0.002 mm^2/s and θ=0.08 s; error values from standard deviation of 50 bootstrapping repetitions

Region	α	S/V (mm^{-1})
Nerve	1.25±0.005	234±6
Cord	1.30±0.006	229±6

Table 4.2.4 Parameters associated with in vivo ADC vs Δ data fitting to the Latour equation for α; assuming S/V = 200 mm^{-1}, D_0 = 0.002 mm^2/s, θ = 0.08 s; error values from standard deviation of 50 bootstrapping repetitions

Region	α
Nerve	1.30±0.008
Cord	1.28±0.006

4.2.4 Discussion

This study has shown that it is possible to detect restricted diffusion in the human brachial plexus and spinal cord and to fit this data to Latour equation. In the 3 T Philips scanner for b~300,600 s/mm^2, δ = 10 ms and TE = 100ms the longest accessible diffusion time, Δ = 81.3 ms and the shortest diffusion time, Δ = 18.3ms. TE = 100 ms was used as the longest possible echo time to achieve a reasonable SNR.

The longest accessible diffusion time (= 81.3 ms) corresponds to restricted diffusion lengths corresponding to the size of the fibres in the brachial plexus and WM and GM fibres in the cord (discussed in section 4.2.1). However, the short diffusion time (=18.3 ms) corresponding molecular displacement is about~8 μm, which is not smaller than the dimensions of all observed fibres, but covers middle range of the fibres (Barker *et al.* 1979, Cummins *et al.* 1979, Cummins *et al.* 1979).

From ADC error estimation it is clear that minimum error (σ_D) occurs when bD=1.1, and the Δ values within the accessible range of this scanner, these observations agree

154

with the previous studies for optimization of diffusion b values (Bito *et al.* 1995, Xing *et al.* 1997, Conturo *et al.* 2005, Heidi Johansen-Berg 2009, Jones 2011, D. M. Koh 2012).

From the Monte Carlo (MC) simulated restricted diffusion, variance in diffusivity differences (σ_k) decreased with

> -short TE due to increased SNR despite resulting decrease in range of Δ;
>
> - long T2 due to high SNR;
>
> - smaller restriction structures due to more restricted diffusion.

For all of these conditions σ_k has minima when $b_2 \sim 250$ s/mm^2. Conversely sensitivity to diffusivity differences (Γ_K) increased for short TE and Δ, long T2, and higher restricted structures, and the maxima of Γ_K occurs at the same b2-value.

Diffusivity difference *K* results with δ shows that short values ($\delta < 5$ ms) are really required being able to achieve good sensitivity to diffusion restriction. However, on the scanner at maximum gradient amplitude, the minimum achievable δ is 10 ms at maximum gradient amplitude for $b = 920$ s/mm^2.

Restriction size results showed the expected minima in variance σ_k occurs with averaged diffusivity and showing the optimal b-value relation, $bD_{av} \sim 1$ for higher restriction sizes. However, for smaller restriction sizes high b-values would be required for restricted diffusion sensitizing.

Simulated restricted diffusion was studied using b values as $b_1 = 0$ and $b_2 > b_1$, however, b values can be shifted to match with the scanner applied values. The results of the above simulation shows that the minima of σ_k and maxima of Γ_K occurs when low b-value, $b_1 = 0$ and higher b-value, $b_2 \sim 250$ s/mm². Now for in-vivo brachial plexus imaging the b-values used as $b_1 = 300$ s/mm² to eliminate IVIM effects and $b_2 = 600$ s/mm² as the higher b-value. Thus experimentally applied b-values would suitably match with the simulated b-value ranges with 8% variations to fulfil the minima and maxima conditions of σ_k and Γ_K respectively.

From the in vivo experiments there was clear reduction in the ADC with increasing diffusion time for the brachial plexus nerves and cord. The phantom data from the same sequences shows no change with diffusion time. This confirms that these

changes are due to physical structures in tissues and not due to artefacts from the scanner, confirming the presence of restricted diffusion in brachial plexus. From the Wilcoxon test there was no significant difference between cord and nerve diffusivities with the current experimental observation, as expected since the dimensions of axon fibres in nerves are comparable with the cord axons.

Figure 4.2.14 shows comparison between the in vivo ADC values (from the brachial plexus nerve and cord) and MC restricted simulation ADC values at the same diffusion times (Appendix I). It shows that both the nerve and cord ADCs are apparently in the same range of MC simulated ADC values, and that they decrease with diffusion times.
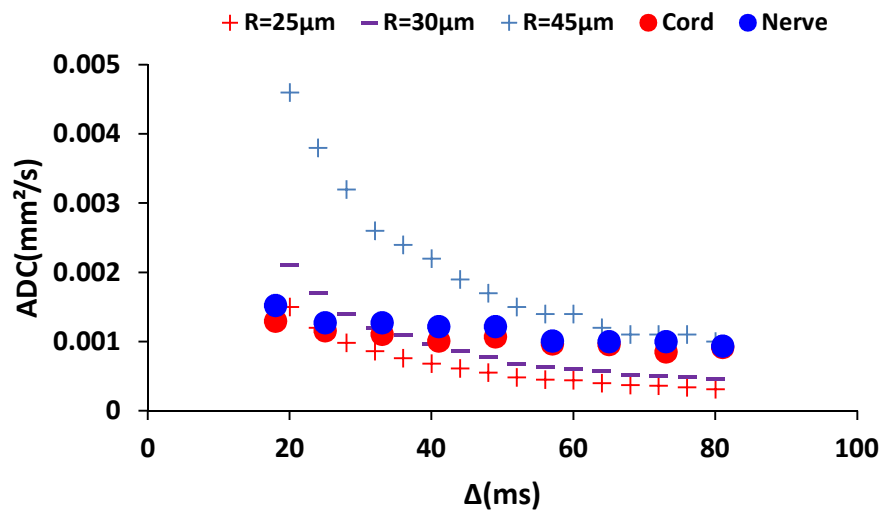

Figure 4.2.14 *Comparing simulated and measured diffusivity variations with diffusion time. In vivo ADCs of nerves and cord shown as solid markers and simulated ADCs at different restrictions (R) as open markers.*

From Figure 4.2.14 the in-vivo ADCs are in the range of the expected values of R~30μm. However, the data does not follow the curve for a single value of R presumably indicating that there are multicompartments of restriction in the nerves and cord axons. However, the data does fit to the Latour equations probably since this is able to characterize the porosity. By introducing compartments and varying the permeability of the restriction boundaries in Monte Carlo simulations, in vivo ADC data can be further explained.

From the Tables 4.2.3 and 4.2.4 fits for tortousity (α) of the nerve and cord fibres are similar whether or not S/V is indicated in the fit. Both fitted parameters are in the

same range and comparable with values observed in the other biological samples like red blood cell (RBC), tumour cells, etc. microscopic values (Latour *et al.* 1994, Helmer *et al.* 1995). The behaviour of diffusivities may be due to extra-axonal hindered diffusion and intra-axonal restricted diffusion at membrane boundaries. However, ADC does not decrease as asymptotic for long Δ. One possible reason is that the restricting barriers of the fibres are not impermeable, but it could also reflect the studied range.

Conclusion

The DWIBS sequence has been optimized for brachial plexus imaging for 3T Philips Achieva scanner. The method developed helps to highlight the nerve and spinal cord by using background soft tissue and fat suppression and can allow indirect study of the microstructure of the neurons. As DWIBS can produce clear images of the brachial plexus it can be applied to a more detailed study of each nerve root and paths for detecting and distinguishing neurological disorders. It could also be applied to the lumbosacral plexus. DWIBS might also be used in other regions such as lymph node, tonsils and fat to characterize the metabolic changes with time. DWIBS would be used with more directional gradients to study the nerve paths and directionality.

The presence of restricted diffusion in brachial plexus nerves and cord has been confirmed from this study. The porous media time dependent diffusion model adopted for brachial plexus nerves and spinal cord microstructure provided a novel approach for characterizing restricted diffusion in the brachial plexus. Resulting estimates of the surface to volume ratio and tortousity are comparable with values obtained previously on biological cells and can give information about the intraaxonal and extraaxonal spaces. Applying other restricted diffusion models and modifying the simulation to take account of membrane permeability and cell structure will provide more information from in vivo data.

References:

Assaf, Y. and P. J. Basser (2005). "Composite hindered and restricted model of diffusion (CHARMED) MR imaging of the human brain." NeuroImage 27(1): 48-58.

Assaf, Y., T. Blumenfeld-Katzir, Y. Yovel and P. J. Basser (2008). "AxCaliber: A method for measuring axon diameter distribution from diffusion MRI." Magnetic Resonance in Medicine 59(6): 1347-1354.

Barker, A. T., B. H. Brown and I. L. Freeston (1979). "DETERMINATION OF THE DISTRIBUTION OF CONDUCTION VELOCITIES IN HUMAN NERVE TRUNKS." Ieee Transactions on Biomedical Engineering 26(2): 76-81.

Bevington, P. R. (1994). "Data reduction and error analysis for the physical sciences."

Bito, Y., S. Hirata and E. Yamamoto (1995). Optimum gradient factors for apparent diffusion coefficient measurements. Proceedings of the 3rd Annual Meeting of Society of Magnetic Resonance, Nice.

Chen, K. C. and C. Nicholson (2000). "Changes in brain cell shape create residual extracellular space volume and explain tortuosity behavior during osmotic challenge." Proceedings of the National Academy of Sciences 97(15): 8306-8311.

Conturo, T. E., R. C. McKinstry, J. A. Aronovitz and J. J. Neil (2005). "Diffusion MRI: precision, accuracy and flow effects." NMR in Biomedicine 8(7): 307-332.

Cummins, K. L., L. J. Dorfman and D. H. Perkel (1979). "Nerve fibre conduction-velocity distributions. II. Estimation based on two compound action potentials." Electroencephalography and Clinical Neurophysiology 46(6): 647-658.

Cummins, K. L., D. H. Perkel and L. J. Dorfman (1979). "Nerve fibre conduction-velocity distributions. I. Estimation based on the single-fibre and compound action potentials." Electroencephalography and Clinical Neurophysiology 46(6): 634-646.

D. M. Koh, H. C. T. (2012). "Diffusion Weighted MR Imaging Applications in the Body."

Harkins, K. D., A. N. Dula and M. D. Does (2012). "Effect of intercompartmental water exchange on the apparent myelin water fraction in multiexponential T2 measurements of rat spinal cord." Magnetic Resonance in Medicine 67(3): 793-800.

Hazlewood, C. F., H. E. Rorschach and C. Lin (1991). "Diffusion of water in tissues and MRI." Magnetic Resonance in Medicine 19(2): 214-216.

Heidi Johansen-Berg, T. E. J. B. (2009). "Diffusion MRI from quantitative measurement to in vivo neuroanatomy."

Helmer, K. G., B. J. Dardzinski and C. H. Sotak (1995). "The application of porous-media theory to the investigation of time-dependent diffusion in in vivo systems." NMR in Biomedicine 8(7): 297-306.

Henkelman, R. M. (1985). "Measurement of signal intensities in the presence of noise in MR images." Medical Physics 12(2): 232-233.

Jones, D. K. (2011). Diffusion MRI: theory, methods, and applications, Oxford University Press

Jones, D. K. and M. Cercignani (2010). "Twenty-five pitfalls in the analysis of diffusion MRI data." NMR in Biomedicine 23(7): 803-820.

Koh, D. M., D. J. Collins and M. R. Orton (2011). "Intravoxel Incoherent Motion in Body Diffusion-Weighted MRI: Reality and Challenges." American Journal of Roentgenology 196(6): 1351-1361.

Koh, D. M., H. C. Thoeny, Y. C. O. N. Amoozadeh, M. C. O. N. Blackledge and D. J. C. O. N. Collins (2010). Diffusion-Weighted MR Imaging: Applications in the Body, Springer.

Lasic, S., M. Nilsson, J. Latt, F. Stahlberg and D. Topgaard (2011). "Apparent Exchange Rate Mapping with Diffusion MRI." Magnetic Resonance in Medicine 66(2): 356-365.

Latour, L. L., R. L. Kleinberg, P. P. Mitra and C. H. Sotak (1995). "Pore-Size Distributions and Tortuosity in Heterogeneous Porous Media." Journal of Magnetic Resonance, Series A 112(1): 83-91.

Latour, L. L., K. Svoboda, P. P. Mitra and C. H. Sotak (1994). "Time-dependent diffusion of water in a biological model system." Proceedings of the National Academy of Sciences 91(4): 1229-1233.

Le Bihan, D. (2011). WATER AND THE MIND: ROLE OF WATER, CELL MEMBRANES, AND DIFFUSION IN BRAIN FUNCTION IMAGING. Singapore, Pan Stanford Publishing Pte Ltd.

Le Bihan, D., E. Breton, M. L. Aubin, D. Lallemand and J. Vignaud (1987). "STUDY OF CEREBROSPINAL FLUID DYNAMICS BY MRI OF INTRAVOXEL INCOHERENT MOTIONS IVIM." Journal of Neuroradiology 14(4): 388-395.

Le Bihan, D., C. Poupon, A. Amadon and F. Lethimonnier (2006). "Artifacts and pitfalls in diffusion MRI." Journal of Magnetic Resonance Imaging 24(3): 478-488.

Le Bihan, D., S.-i. Urayama, T. Aso, T. Hanakawa and H. Fukuyama (2006). "Direct and fast detection of neuronal activation in the human brain with diffusion MRI." Proceedings of the National Academy of Sciences 103(21): 8263-8268.

Lin, C., A. Luciani, E. Itti, T. El-Gnaoui, A. Vignaud, P. Beaussart, S.-j. Lin, K. Belhadj, P. Brugières, E. Evangelista, C. Haioun, M. Meignan and A. Rahmouni (2010). "Whole-body diffusion-weighted magnetic resonance imaging with apparent diffusion coefficient mapping for staging patients with diffuse large B-cell lymphoma." European Radiology 20(8): 2027-2038.

Loskutov, V. V. and V. A. Sevriugin (2013). "A novel approach to interpretation of the time-dependent self-diffusion coefficient as a probe of porous media geometry." Journal of Magnetic Resonance 230(0): 1-9.

Macovski, A. (1996). "Noise in MRI." Magnetic Resonance in Medicine 36(3): 494-497.

Moore, R. J., B. Issa, P. Tokarczuk, K. R. Duncan, P. Boulby, P. N. Baker, R. W. Bowtell, B. S. Worthington, I. R. Johnson and P. A. Gowland (2000). "In vivo intravoxel incoherent motion measurements in the human placenta using echo-planar imaging at 0.5 T." Magnetic Resonance in Medicine 43(2): 295-302.

Mukherji, S. K., M. Castillo and A. G. Wagle (1996). "The brachial plexus." Seminars in Ultrasound, CT, and MRI 17(6): 519-538.

Nicholson, C. (2001). "Diffusion and related transport mechanisms in brain tissue." Reports on progress in Physics 64(7): 815.

Nicholson, C. and J. M. Phillips (1981). "Ion diffusion modified by tortuosity and volume fraction in the extracellular microenvironment of the rat cerebellum." Journal of Physiology Vol. 321: 225-257.

Novikov, D. S., E. Fieremans, J. H. Jensen and J. A. Helpern (2011). "Random walks with barriers." Nature physics 7(6): 508-514.

Sigmund, E. E. (2011). "Perspectives on Porous Media MR in Clinical MRI." AIP Conference Proceedings 1330(1): 13-16.

Takahara, T., J. Hendrikse, T. Yamashita, W. P. T. M. Mali, T. C. Kwee, Y. Imai and P. R. Luijten (2008). "Diffusion-weighted MR Neurography of the Brachial Plexus: Feasibility Study1." Radiology 249(2): 653-660.

Takahara, T., Y. Imai, T. Yamashita, S. Yasuda, S. Nasu and M. Van Cauteren (2004). "Diffusion weighted whole body imaging with background body signal suppression (DWIBS): technical improvement using free breathing, STIR and high resolution 3D display." Radiation medicine 22(4): 275-282.

Vestergaard-Poulsen, P., B. Hansen, L. Ostergaard and R. Jakobsen (2007). "Microstructural changes in ischemic cortical gray matter predicted by a model of diffusion-weighted MRI." Journal of Magnetic Resonance Imaging 26(3): 529-540.

Xing, D., N. G. Papadakis, C. L. H. Huang, V. M. Lee, T. Adrian Carpenter and L. D. Hall (1997). "Optimised diffusion-weighting for measurement of apparent diffusion coefficient (ADC) in human brain." Magnetic Resonance Imaging 15(7): 771-784.

Chapter 5
T2 Measurements of the Brachial plexus

To further quantify the MR study of brachial plexus this chapter aimed to study the T2 relaxation time of nerves and cord and also observe possible correlation between molecular diffusion phenomena and their T2 relaxation properties.

5.1 Introduction

T2 relaxation, the transverse relaxation time, describes the irreversible decay of the MR signal in the transverse plane. Immediately following the excitation pulse (90^0 pulse), the MR signal is maximum because all of the spins are aligned with each other. However, the signal decays at a rate determined by the magnetic field distribution or chemical shift distribution of the spins. By following the excitation pulse with a refocusing (180^0) pulse, the signal dephasing caused by the inhomogeneous magnetic field and/or chemical shift dispersion can be refocused to produce an echo. The amplitude of this spin echo is determined by the irreversible process; it decreases exponentially with time from the excitation pulse with the time constant T2 (discussed in section 1.1.8).

T2 weighted imaging plays a key role in spinal cord clinical MRI, showing sensitive changes with the pathological conditions. The T2 relaxation time carries specific information about myelin content as well as about the water environments in the intra- and extra-cellular compartments. These measurements have yielded new insights into brain development and also provide a biomarker for central nervous system pathologies (Vasilescu *et al.* 1978, Does *et al.* 1994, Whittall *et al.* 1997, Does *et al.* 1998, Does *et al.* 2002, Zheng *et al.* 2010). Measurements of T2 relaxation times in brachial plexus nerves and spinal cord can also produce information about the microenvironment in the peripheral nerves, adjacent structures and related neuropathies (discussed in Chapter 3). However, delineating the peripheral nerves in the brachial plexus is challenging due to shape of the neck and similar signal from nerve surrounding vascular tissues. This can be overcome by using DWIBS to suppress signals from surrounding tissues. Figure 5.1 shows a standard T2W image and DWIBS image for the same subject at the same cervical spine level, which demonstrates the usefulness of DWIBS for highlighting the peripheral nerves.
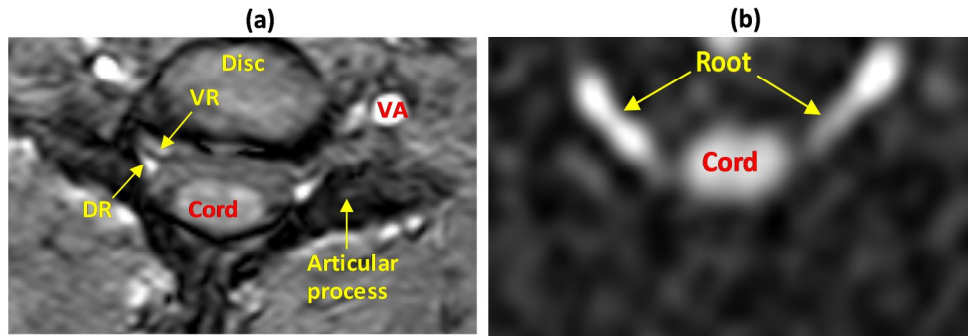
Figure 5.1 *(a) T2W image of normal brachial plexus axial view at C6 level highlighting spinal cord, dorsal root (DR) and ventral root (VR) of the spinal nerves, ventral artery (VA), vertebral disc and aritcular process. Obtained with STIR TSE sequence, TE = 60 ms, TR = 2250 ms (discussed in section 3.); (b) Diffusion weighted image of brachial plexus axial view at C6 level highlighting only the spinal cord and nerve roots. Obtained with b = 300 s/mm², TE = 60 ms.*

Water diffusion is a suitable MR parameter for studying the compartments in biological tissues because of its sensitivity to spatial boundaries (Peled *et al.* 1999). The existence of multiexponential transverse relaxation decay curves in biological tissues is often assumed to be an indicator of compartmentation (Whittall *et al.* 1997, Webb *et al.* 2003, Zheng *et al.* 2010). Thus, the relation between T2 relaxation times and diffusivities of nerve tissues might provide additional information about the properties of different compartments in nerve axons (Beaulieu *et al.* 1998, Peled *et al.* 1999, Tan *et al.* 2013, Stroman *et al.* 2014). For that, as an initial approach, the T2 variations with different levels of diffusion weighting (b value) and the variations in apparent diffusion coefficient (ADC) with TE have been studied in brachial plexus.

The aims of this Chapter are (1) to measure the T2 values of spinal cord and nerves in brachial plexus using DWIBS technique (2) to determine how the measured T2 depends on the degree of diffusion weighting, and how the measured diffusion coefficient depends on TE.

5.2 Methods

For the T2 time measurement study, images were acquired from **cohort C** (page 126) subjects using the same DWIBS sequence used in Chapter 4, a schematic pulse sequence is shown in figure 5.2.
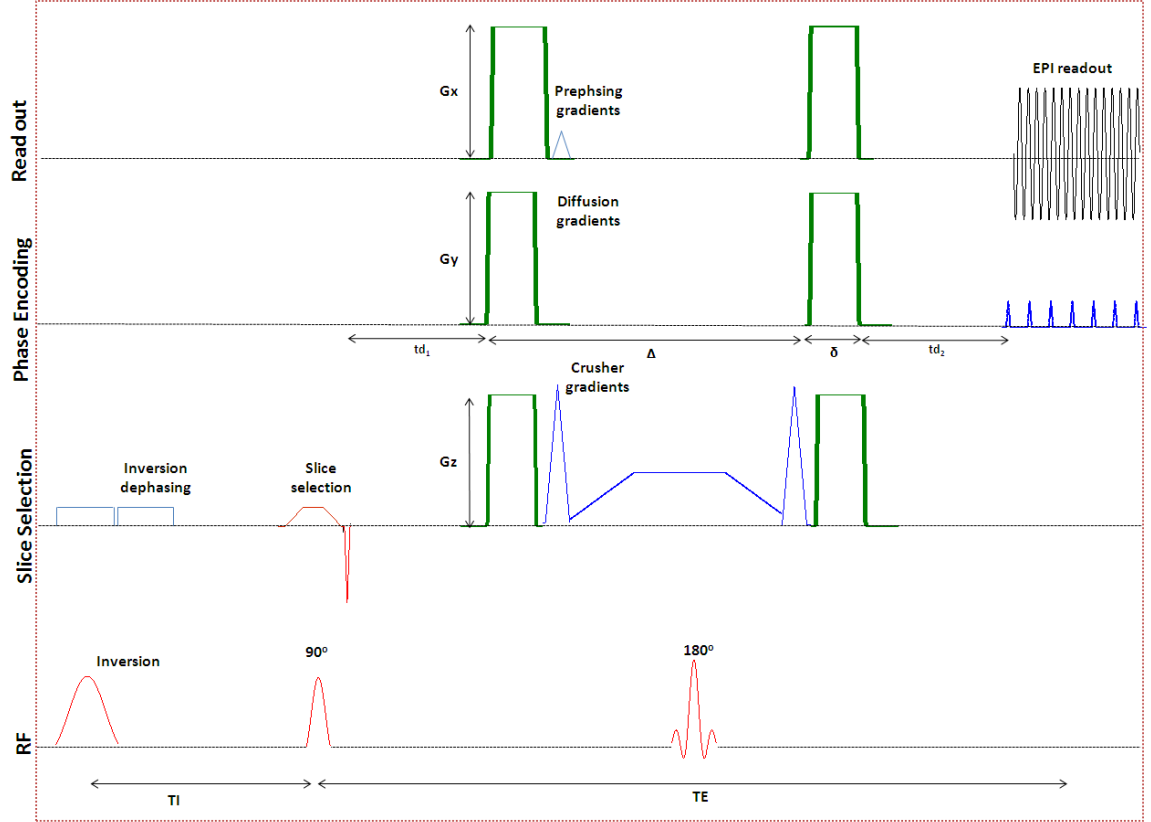

Figure 5.2 *Schematic DWIBS pulse sequence used to achieve background suppression and fluid suppression for T2 measurements. The figure indicates relevant pulse sequence timings.*

Brachial plexus images were acquired following the same procedure discussed in section 4.1.1. Then ROIs for nerves and cord were selected using 2D Gaussian fitting with one pixel for each nerve in the sagittal view and four pixels for cord in the transverse view (discussed in section 4.1.2).

To calculate the T2 values, images were acquired with TE = 55, 60, 65, 70, 75, 80 ms; TR = 6000 ms, using a diffusion factor b = 300 s/mm^2 to eliminate IVIM effects and supress background signal (discussed in section 4.1.2), Δ = 28.3 ms and δ = 10 ms.

The T2 values are calculated using the weighted linear square fit to the spin echo expression,

$$S(TE) = S_o e^{(-\frac{TE}{T_2})} \tag{5.2.1}$$

Since the data are noisy it is likely to produce some scattered points in the logS vs TE plot, which can be defined as outliers. In statistics, Cook's distance or Cook's D is a commonly used estimate of the influence of a data point when performing least squares regression analysis (Cook *et al.* 1982), in this method points further than three or more standard deviations from the mean are considered as "outliers". Cook's distance 'outlier rejection' technique was applied before fitting the data for T2 calculations.

As an initial approach to compartmental studies in brachial plexus nerves and cord, the T2 values were calculated at different b values with fixed Δ and δ; and the ADC values were calculated at different TE values with the same fixed Δ and δ. The images of brachial plexus were acquired from two of out of ten subjects of ***cohort C*** (page 126).

For T2 vs b study, the T2 values were calculated using TE = 55, 60, 65, 70, 75, 80 ms at   b = 300, 400, 500, 600, 800 s/mm^2 and Δ = 28.3 ms, δ = 10 ms and TR = 6000 ms. For ADC dependence on TE study, ADC values were calculated using b = 400, 800 s/mm^2 with fixed Δ = 28.3 ms, δ = 10 ms at TE = 55, 60, 65, 70, 75, 80ms and TR = 6000 ms.

5.3 Results

Figure 5.3 shows the logS vs TE plot from brachial plexus nerves with outlier rejection technique indicated. Using the outlier rejection technique the subject averaged T2 values with standard deviation for Nerve 80±5 ms and for cord 100±6 ms using b = 300 s/mm^2.

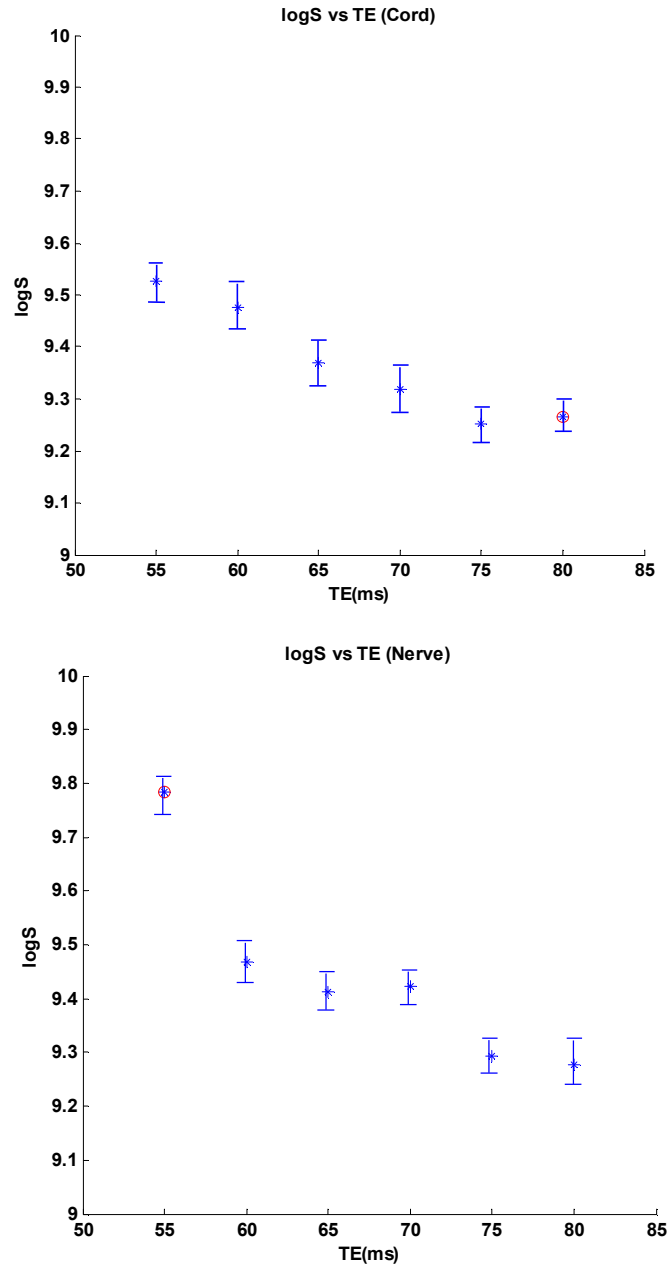Figure 5.3 *T2 decay plot for nerve and cord from single subject using DWIBS sequence with b=300s/mm². The red circled point rejected as outlier.*

Figure 5.4 shows the T2 vs b plot from brachial plexus nerves and cord from two subjects. Figure 5.5 shows the ADC vs TE plot from the same two subjects.
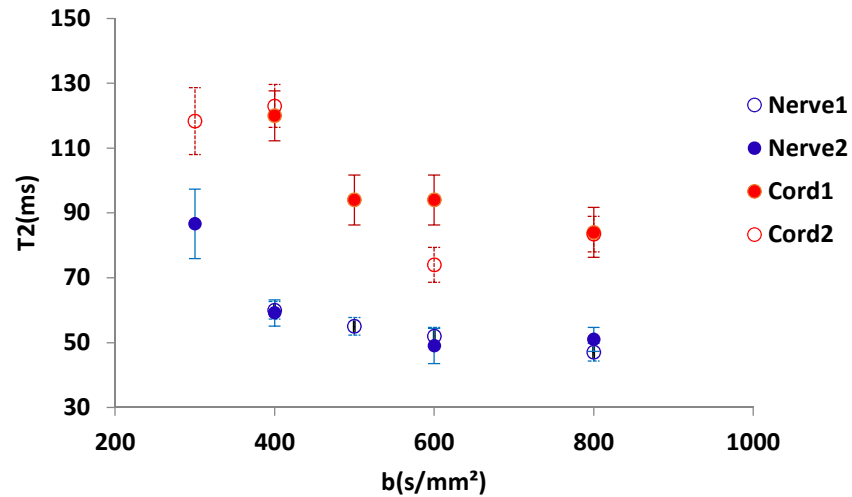
Figure 5.4 *T2 vs b plot averaged from two subjects, showing clear decrease of T2 at higher b values and that T2 are higher for cord compared to nerves. Error bars for standard error of measurements.*
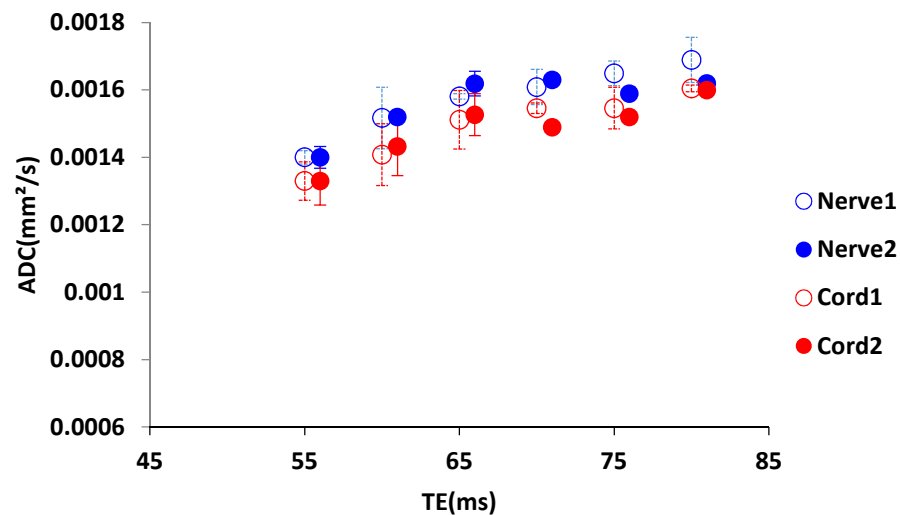

Figure 5.5 *ADC variations with TE. ADC of nerve and cord are increasing with higher TE. ADC values for nerves slightly higher than cord similar showed in restricted diffusion ADC vs Δ study. Error bars represents standard error of the measurements.*

5.4 Discussion

Using a DWIBS sequence for T2 measurements of the brachial plexus helps to suppress background signal and surrounding fluids which have a long T2. The outlier rejection technique helped to calculate T2 values with more accuracy. T2 values are comparable with similar in vivo compartmental studies of the nerve, with short T2 (10~50 ms) assigned to myelin water and long T2 (70~130 ms) assigned to intra and extracellular water. (Whittall *et al.* 1997, Wansapura *et al.* 1999, Laule *et al.* 2007, Minty *et al.* 2009, Zheng *et al.* 2010, MacMillan *et al.* 2011, Tan *et al.* 2013). Thus T2 values of nerves and cord are related to the intra and extracellular water. Also the cord T2 values are longer compared to nerves possibly due to the presence and slow movement of CSF, which may explain the slightly higher intra-subject variations.

Studies of the transversal relaxation time T2 with diffusion weighting b-values in nerves and cord showed longer T2 with lower b values and shorter T2 with higher b values. The b-values are higher than 300 s/mm^2 which eliminates the IVIM contribution on nerve and cord signals. Thus the T2 dependence on b-values could suggest the signal from different diffusivity compartments in brachial plexus, such as, higher b values correspond to more diffusion weighting thus the signal could arise from tissues with bound macromolecular tissues which are characterized by short T2; lower b-values could relate with less bound molecules which are characterized by long T2.

The ADC measurements at different TE showed ADC increases with long TE both for nerves and cord. Possibly for long TE the images were weighted to long T2 compartments which may include fluids (CSF) that likely have higher ADCs. This experiment also suggests that the ADC of nerves is slightly higher than that of cord, as also observed in previous chapter on restricted diffusion study. From Figures 5.5 and 5.4 longer T2 and low ADC are found in the cord which contains smaller diameter axons and more intra cellular fluid, on the other hand shorter T2 and high ADC are found in the nerves which has slightly higher diameter axons and extra cellular fluid. Thus these results can help to characterize nerve and cord axons.

5.5 Conclusion

A DWIBS based T2 measurement has been developed for brachial plexus nerves and cord. Calculated T2 values are in the same range with other studies of peripheral nerves (Does *et al.* 1994, MacMillan *et al.* 2011). Preliminary data on the diffusion weighting dependence on T2, and the echo time dependence of diffusion coefficients suggests that these might provide a signature of compartments within the nerves and cord axons. The combination of quantitative MR parameters measured in this chapter can be used in a combined EMG and MRI study.

References

Beaulieu, C., F. R. Fenrich and P. S. Allen (1998). "Multicomponent water proton transverse relaxation and T-2-discriminated water diffusion in myelinated and nonmyelinated nerve." Magnetic Resonance Imaging 16(10): 1201-1210.

Cook, R. D. and S. Weisberg (1982). "Residuals and influence in regression."

Does, M. and R. Snyder (1994). "T2 relaxation of peripheral nerve measured in vivo." Magnetic Resonance Imaging 13(4): 575-580.

Does, M. D., C. Beaulieu, P. S. Allen and R. E. Snyder (1998). "Multi-component T1 relaxation and magnetisation transfer in peripheral nerve." Magnetic Resonance Imaging 16(9): 1033-1041.

Does, M. D. and J. C. Gore (2002). "Compartmental study of T1 and T2 in rat brain and trigeminal nerve in vivo." Magnetic Resonance in Medicine 47(2): 274-283.

Laule, C., I. M. Vavasour, S. H. Kolind, D. K. B. Li, T. L. Traboulsee, G. R. W. Moore and A. L. MacKay (2007). "Magnetic Resonance Imaging of Myelin." Neurotherapeutics 4(3): 460-484.

MacMillan, E. L., B. Mädler, N. Fichtner, M. F. Dvorak, D. K. B. Li, A. Curt and A. L. MacKay (2011). "Myelin water and T2 relaxation measurements in the healthy cervical spinal cord at 3.0T: Repeatability and changes with age." NeuroImage 54(2): 1083-1090.

Minty, E. P., T. A. Bjarnason, C. Laule and A. L. MacKay (2009). "Myelin Water Measurement in the Spinal Cord." Magnetic Resonance in Medicine 61(4): 883-892.

Peled, S., D. G. Cory, S. A. Raymond, D. A. Kirschner and F. A. Jolesz (1999). "Water diffusion, T2, and compartmentation in frog sciatic nerve." Magnetic resonance in medicine: official journal of the Society of Magnetic Resonance in Medicine/Society of Magnetic Resonance in Medicine 42(5): 911.

Stroman, P. W., C. Wheeler-Kingshott, M. Bacon, J. M. Schwab, R. Bosma, J. Brooks, D. Cadotte, T. Carlstedt, O. Ciccarelli, J. Cohen-Adad, A. Curt, N. Evangelou, M. G. Fehlings, M. Filippi, B. J. Kelley, S. Kollias, A. Mackay, C. A. Porro, S. Smith, S. M. Strittmatter, P. Summers and I. Tracey (2014). "The current state-of-the-art of spinal cord imaging: Methods." NeuroImage 84(0): 1070-1081.

Tan, M., Y. Zou and C. Zhou (2013). "A new inversion method for (T2, D) 2D NMR logging and fluid typing." Computers & Geosciences 51(0): 366-380.

Vasilescu, V., E. Katona, V. Simplaceanu and D. Demco (1978). "Water compartments in the myelinated nerve. III. Pulsed NMR result." Experientia 34(11): 1443-1444.

Wansapura, J. P., S. K. Holland, R. S. Dunn and W. S. Ball (1999). "NMR relaxation times in the human brain at 3.0 tesla." Journal of Magnetic Resonance Imaging 9(4): 531-538.

Webb, S., C. A. Munro, R. Midha and G. J. Stanisz (2003). "Is multicomponent T2 a good measure of myelin content in peripheral nerve?" Magnetic Resonance in Medicine 49(4): 638-645.

Whittall, K. P., A. L. Mackay, D. A. Graeb, R. A. Nugent, D. K. B. Li and D. W. Paty (1997). "In vivo measurement of T2 distributions and water contents in normal human brain." Magnetic Resonance in Medicine 37(1): 34-43.

Zheng, S. and Y. Xia (2010). "On the measurement of multi-component T2 relaxation in cartilage by MR spectroscopy and imaging." Magnetic Resonance Imaging 28(4): 537-545.

Chapter 6
Magnetization Transfer and z-spectra study of the Brachial Plexus

To further quantify MR properties of the brachial plexus, this chapter describes its magnetization transfer and z-spectra properties that have proven useful in previous investigations of soft-tissue damage.

6.1 Introduction

Magnetization Transfer (MT) MRI experiments study the transfer of saturated longitudinal magnetization associated with bound macromolecules (such as proteins and lipids) to the free water hydrogen nuclei, and thus can be used to create contrast between regions containing different amounts of bound macromolecules (Balaban *et al.* 1992, Henkelman *et al.* 1993, Henkelman *et al.* 2001). MT can be used to study the solutes and macromolecules present in the sample indirectly via the water signal (Graham *et al.* 1997, Filippi *et al.* 2000, Henkelman *et al.* 2001). Since the semi-solid tissues have very short T2 values (~μs), their frequency distributions are broad (~100ppm). Thus implementation of an RF irradiation at a frequency far from the water resonance can selectively saturate these protons without direct saturation of the water. Through spin diffusion and intra-/intermolecular energy exchange, the saturation is transferred to the surrounding water and results in observable signal attenuation. As a result, the MT effect is proportional to the relative amounts of water associated with macromolecules and water, and is therefore different in tissues and in CSF, and has been shown to be sensitive to the myelin concentration, degeneration and regeneration of myelin (Graham *et al.* 1997, Schmierer *et al.* 2004, Stanisz *et al.* 2005, Schmierer *et al.* 2007, McCreary *et al.* 2009, Brown *et al.* 2012).

By varying the irradiation frequencies the transfer processes can be further explored and represented by the z-spectrum (Balaban *et al.* 1992, Bryant 1996). Understanding the z-spectra processes are important for tissue characterizations and clinical purposes as they can help to provide different contrast for certain types of pathology. It has been generally assumed that the resonant frequency of the bulk water is the same as the solid like macromolecules which leads to symmetry in the z-spectra. However, several studies have demonstrated that the z-spectra associated with solid like macromolecules in different tissues are slightly asymmetric around the water proton resonance frequency (Pekar *et al.* 1996, Hua *et al.* 2007, Hua *et al.* 2007, Schmierer *et al.* 2007, Ng *et al.* 2009, Jones *et al.* 2013, Zaiss *et al.* 2013, Xu *et al.* 2014).

The asymmetry due to shifting of the centre of z-spectrum towards upfield (lower frequency) is associated with conventional MT and nuclear overhauser enhancement (NOE) attributed to solid-like macromolecules and aliphatic and olefinic protons in tissues (Liepinsh *et al.* 1996, Ling *et al.* 2008, Jones *et al.* 2011, Jin *et al.* 2013), and the asymmetry of the centre of z-spectrum towards lowfield (higher frequency) is associated with the chemical exchange saturation transfer (CEST) effect based on exchangeable protons (Wolff *et al.* 1989, Guivel-Scharen *et al.* 1998, van Zijl *et al.* 2011). Thus in general the z-spectra comprises the direct water saturation effect, the broad macromolecular MT effects which determines the baseline; and the effects of cross relaxation processes such as NOE due to dipolar coupling between the protons and CEST mediated by various water-exchangeable protons of macromolecules. Asymmetry in the z-spectra can explore and further characterize the biological tissues. For example, recent in vivo studies demonstrated that the asymmetry in WM is generally higher than those in the GM, indicating that the NOE is greater in WM than GM, showing the myelin content abundances in the WM (Liepinsh *et al.* 1996, Jones *et al.* 2013, Liu *et al.* 2013, Mougin *et al.* 2013, Zaiss *et al.* 2014). It is important to mention that all of these effects strongly depend on the static magnetic field strength (B_0), the RF irradiation amplitude (B_1) and other experimental parameters discussed in Section 3.3.

This Chapter aims to study the MT and z-spectra for brachial plexus. To measure the z-spectra in the peripheral nervous system such as the brachial plexus, there are two challenges, first obtaining sufficient contrast between the nerves and surrounding tissues, and second robustly characterising the z-spectra in this challenging circumstance. Tracking the peripheral nerves and the corresponding nerve roots can be difficult on MT imaging because of a lack of contrast with the surrounding tissues and breathing movements. The diffusion weighted whole body imaging with background suppression (DWIBS) technique provides a means of obtaining highlighted images of the peripheral nerves (discussed in Section 4.1). Thus to produce quantitative MT imaging of the brachial plexus by highlighting nerves, roots, root ganglions, spinal cord WM and GM etc. from surrounding tissues a novel combined diffusion weighted and magnetization transfer sequence has been developed. Furthermore, since DWIBS uses the EPI readout, the acquisition is fast, allowing data to be acquired at multiple frequency offsets or RF powers quickly.

The conventional magnetization transfer ratio (MTR) as discussed in Section 3.3 can be expressed as,

$$MTR(\Delta\omega) = 1 - \frac{S_{sat}(\Delta\omega)}{S_0} \qquad (6.1)$$

where $S_{sat}(\Delta\omega)$ is the signal measured with saturation of the magnetization at off-resonance ($\Delta\omega$), S_0 is the signal measured with non-saturated magnetization of the tissues. In many basic MT studies, the MT z-spectra profile is assumed to be symmetric around the water peak; however, several studies indicate that it shows asymmetry features such as NOE from aliphatic protons (Hua *et al.* 2007, Ng *et al.* 2009). The MT z-spectra standard asymmetry can be expressed as,

$$MTR_{asym}(\Delta\omega) = MTR(\Delta\omega) - MTR(-\Delta\omega) \qquad (6.2)$$

where the spectrum data is acquired only at two symmetric frequencies ($\pm\Delta\omega$). If the spectra data are truly symmetric $MTR_{asym}= 0$, otherwise when $MTR_{asym}<0$ the lowfield saturation exchange is greater (contributed by CEST and underlying MT) compared to the upfield saturation (contributed by NOE and underlying MT) and vice versa. Therefore standard asymmetry analysis assumes that there is only one process leading to asymmetry for example either NOE at negative frequency offsets or Amide proton transfer (APT a parametric form of CEST) at positive frequency offset. It also assumes that the sample is on resonance, whereas in practice this is unlikely, which will shift the spectrum up or down field as indicated in Figure 6.1.
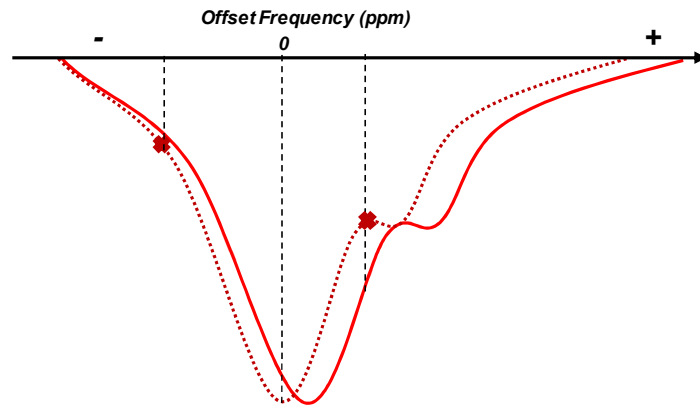

Figure 6.1 *Schematic plots of z-spectra and shifting of offset frequency, showing clear change in apparent asymmetry.*

Both these effects could confound such simple measures of asymmetry. An alternative approach for asymmetry analysis is to acquire the full z-spectra, which allows the data to be corrected for $\mathbf{B}_0$ offsets and other contributions, but this process takes longer. It is also then necessary to find ways of robustly characterizing the asymmetry in the z-

spectra. In this work several methods have been developed to characterise the asymmetry of the brachial plexus z-spectra.

Based on initial acquired z-spectra of the brachial plexus nerves and cord (shown in Figure 6.2), it was clear that the spectra from the brachial plexus were quite broad and noisy. The spectrum in Figure 6.2 clearly shifted to negative frequencies due to field inhomogeneities. To correct the z-spectrum for $\mathbf{B}_0$ field inhomogeneities, the water shift saturation referencing (WASSR) technique was used. In the WASSR technique the direct water saturation frequency was detected at very low power and then the z-spectra was re-centred independently of spatial $\mathbf{B}_0$ variations (Kim *et al.* 2009) (discussed in Section 3.3.4).
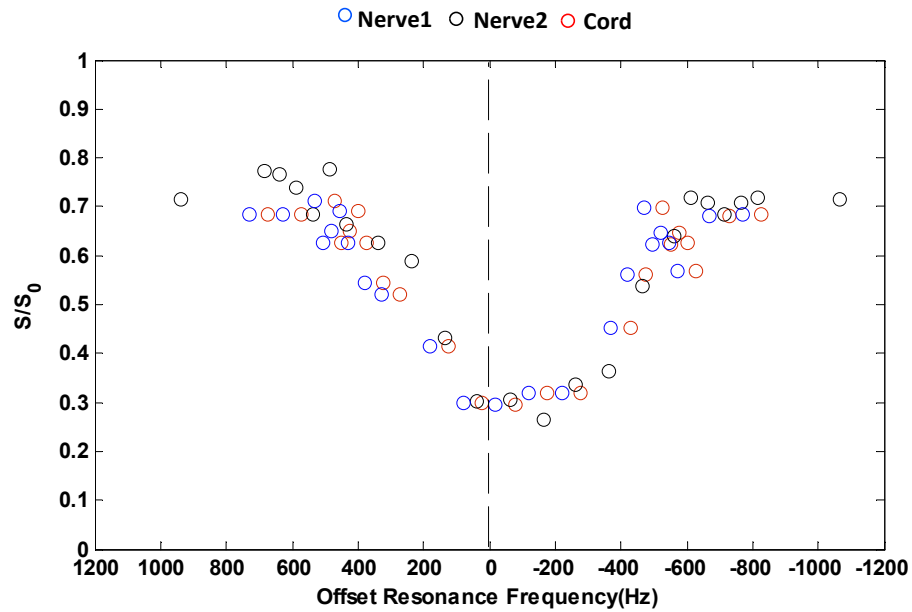

Figure 6.2 *Initial acquired z-spectra obtained from brachial plexus nerves and cord.*

The first approach used to characterise the asymmetry assuming that the underlying MT spectrum and direct water saturation had a Lorentzian line shape:

$$L_1 = 1 - \frac{A}{1 + (\frac{x - x_0}{W})^2} \tag{6.3}$$

where A is the amplitude, W is the full width at half maximum and x_o is the position of the central peak of the fitted lineshape. At the RF saturation pulse powers used here, the NOE can cause some asymmetry in the spectrum rather than a double peak (Mougin *et al.* 2010, Mougin *et al.* 2013) and CEST is assumed to be negligible. One simple way to characterise this asymmetry is to fit a single Lorentzian to both sides of

the spectrum separately and compare their widths. Alternatively the model could be extended to a double Lorentz equation with the second peak corresponding to NOE.

$$L_2 = 1 - \left[\frac{A_1}{1+\left(\frac{x-x_1}{W_1}\right)^2} - \frac{A_2}{1+\left(\frac{x-x_2}{W_2}\right)^2}\right] \tag{6.4}$$

where A_1 is the amplitude, x_1 is the position and W_1 is the full width at half maximum of the central peak; and A_2 is the amplitude, x_2 is the position and W_2 is the full width at half maximum of the second peak from the double Lorentz lineshape.

The aim of this chapter is to study the asymmetry of the z-spectrum in the brachial plexus nerves and cord using combined DWIBS MT sequence. Initially the nerve and cord MTR asymmetry at a symmetric pair of offset frequencies ($\pm\Delta\omega$) were measured and then it was extended to measure the nerve and cord z-spectra at two RF powers.

6.2 Methods

For the MT and z-spectra study, images were acquired from ***cohort D*** (page 126) subjects using the combined DWIBS-MT sequence shown in Figure 6.3.
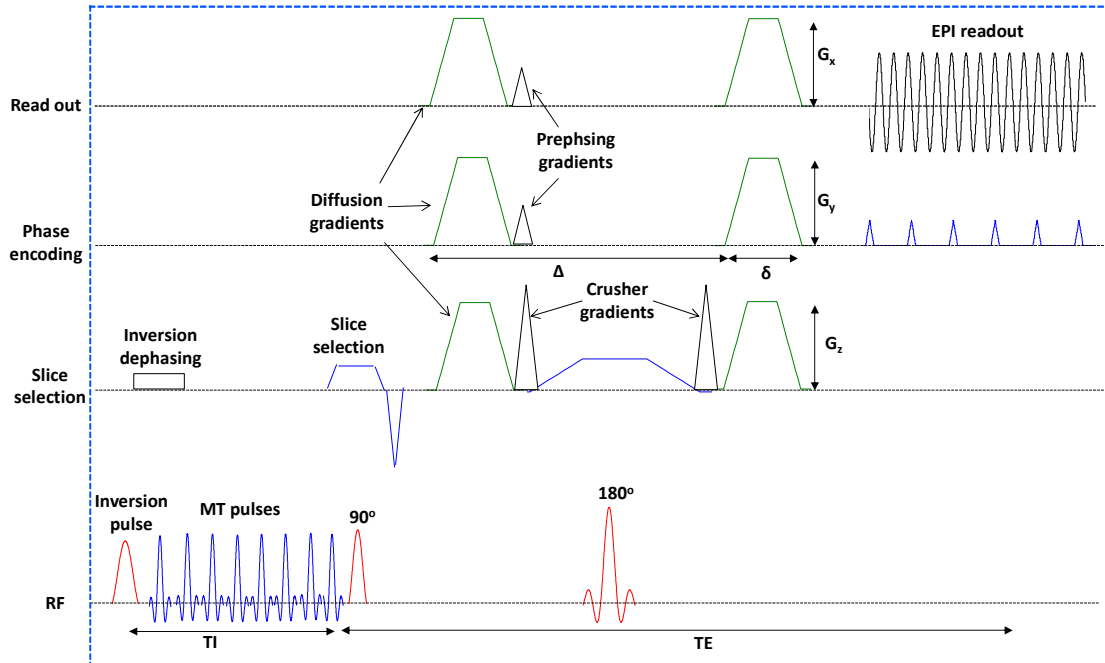

Figure 6.3 *Schematic diagram of combined diffusion and MT pulse sequence used in the Philips 3T scanner.*

This sequence was implemented in the patch to the standard Philips sequence code written by Dr. Andrew Peters and Dr. Olivier Mougin.

In this sequence the IR pulse suppresses the surrounding fat signal and diffusion gradients suppress soft tissue signals and hence highlight the nerves and cord. The MT saturation pulses were applied between the IR pulse and the readout pulse to minimize recovery of the saturation. As the MT pulses are phase cycled a spoiler gradient is not used. The combined MT diffusion sequence used PGSE, single shot EPI readout making it possible to vary $\Delta\omega$ and $\mathbf{B}_1$ in a reasonable equidistant time, the sequence parameters for fat suppression TI = 215 ms; for surrounding tissue and IVIM signal suppression TE = 75 ms, b = 300 s/mm², Δ = 56 ms, δ = 10 ms. ROIs for nerves and cord were selected using 2D Gaussian fitting with one pixel for each nerve in sagittal view and four pixels for cord in transverse view (discussed in Section 4.1).

Standard Asymmetry study:

To assess the asymmetry between lowfield and upfield MTR values, images were acquired from 15 subjects of **cohort D** by applying the presaturation using 8 sinc RF pulses with 300° flip angle and 20 ms pulse duration with power of 0.3 µT, and using symmetric pairs of off-resonance frequencies as ±600 Hz, ±500 Hz and ± 400 Hz and saturation at 10 kHz. The frequency used to observe the sensitivity to NOE effects at - 3.5 ppm (-448 Hz), the MTR values were measured according to Equation 6.1. To compare the possible statistical difference between MTR values at symmetric pair frequencies for nerves averaged from both sides and cord the Wilcoxon rank sum test was used to test the null hypothesis, H_0: MTR $_{+\omega}$=MTR $_{-\omega}$.

z-spectrum study:

To characterize the z-spectra brachial plexus images were acquired from 4 subjects out of 15 subjects of **cohort D** using the same presaturation applied at two saturation flip angles 300° and 200° where the corresponding powers are P1 = 0.18 µT, P2 = 0.3 µT respectively and using 24 off-resonance frequencies: 10 kHz (saturation), ±750 Hz, ±650 Hz, ±550 Hz, ±525 Hz, ±500 Hz, ±475 Hz, ±450 Hz, ±400 Hz, ±350 Hz, ±200 Hz, ±100 Hz and 0 Hz. For B_0 inhomogeneity correction the WASSR technique was used to identify the frequency offset of the water spectrum, which could then be used to correct the frequency offset of the z-spectrum (fig 6.2). A WASSR spectrum was acquired with low power presaturation (8, 20° Flip angle with 20 ms intervals and corresponding power B1 = 0.01 µT) to minimize any effects other than direct water saturation and using 16 off-resonance frequencies 10 kHz, ±120 Hz, ±100 Hz, ±80 Hz, ±60 Hz, ±40 Hz, ±20 Hz, ±10 Hz and 0 Hz. The WASSR spectrum was then non-linearly fitted to single Lorentz equation (Equation 6.3), to find the position of the minimum. Using the position of minimum as the reference ($\Delta\omega$=0) point, the z-spectra was shifted by interpolation to correct for B_0 inhomogeneities.

To assess the asymmetry firstly the WASSR corrected z-spectrum was fitted to the single Lorentzian equation centred on zero (x_0= 0),

$$L_1 = 1 - \frac{A}{1+(\frac{x}{W})^2} \qquad\qquad (6.5)$$

where *x* and *W* are in Hz. However, the lowfield (+) and upfield (-) sides of the z-spectra were fitted separately to the Equation 6.5. From the fitting the full width half

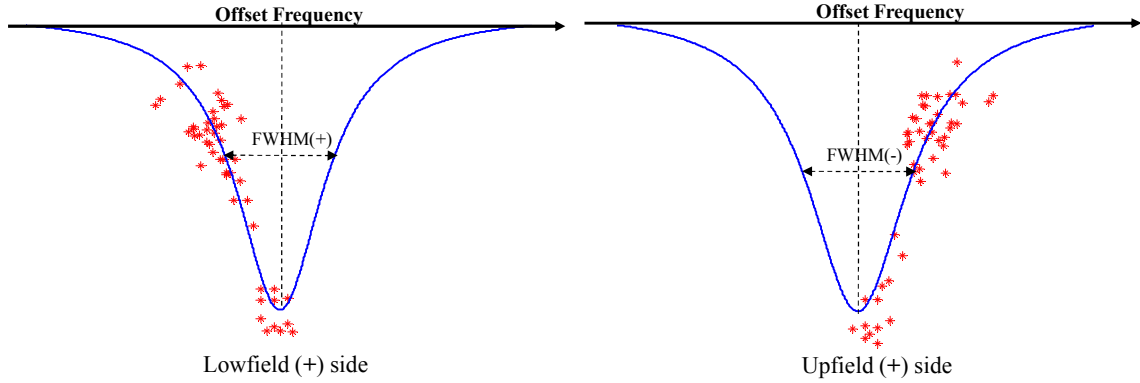maximum values were measured as FWHM (+) and FWHM (-) schematically shown in Figure 6.4.

Figure 6.4 *MT spectra fitted with single Lorentzian equation for lowfield (+) side and upfield (-) side. Red data points showing the MTR values acquired for the whole MT spectrum.*

If the z-spectra are truly symmetric, FWHM(+) = FWHM(-) otherwise the result suggests the presence of asymmetry. When FWHM(+) > FWHM(-) it assumes the lowfield saturation exchange is greater (due to CEST, APT and underlying MT) compared to the upfield saturation (due to NOE and underlying MT) in contrary when FWHM(+) < FWHM(-) the upfield saturation is greater compared to the lowfield saturation. This asymmetry was also studied using Wilcoxon rank sum test (Oyeka *et al.* 2012).

Another parameter, the difference between the widths of the single Lorentz fitting,

$$\Delta \text{FWHM} = \text{FWHM(-)} - \text{FWHM(+)} \tag{6.6}$$

was also used to monitor the effects of change in asymmetry with applied powers P1 and P2. The asymmetry of the MT spectra was also investigated using the double Lorentzian equation considering the central peak $x_1 = 0$, and the NOE peak $x_2 = -3.5ppm = -448Hz$ then from Equation 6.4,

$$L_2 = 1 - \left[\frac{A_1}{1+\left(\frac{x}{W_1}\right)^2} - \frac{A_2}{1+\left(\frac{x-(-448)}{W_2}\right)^2}\right] \tag{6.7}$$

where W1, W2 and A1, A2 are the FWHMs and amplitudes of the central peak and NOE peak at negative frequencies respectively as schematically shown in Figure 6.5.
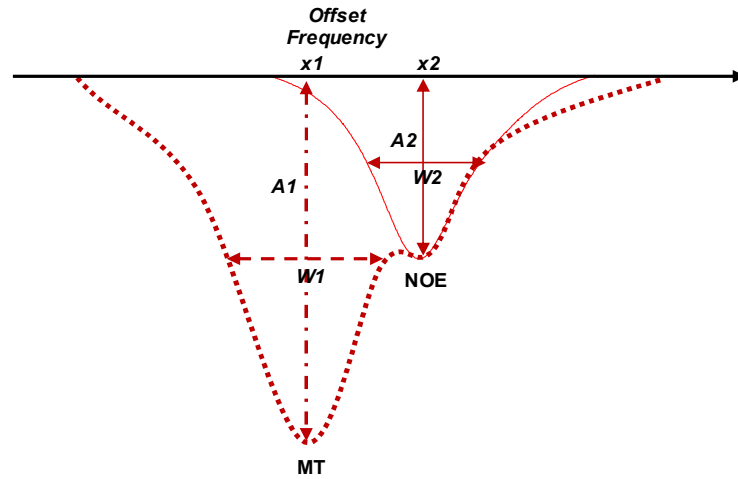
Figure 6.5 *MT spectra and double Lorentz equations fitting showing the width and amplitude of the central peak and second peak.*

A measurable value of width and amplitude of the second peak from the double Lorentzian equations confirms the presence of asymmetry. To compare the asymmetry at powers P1 and P2 the areas under the central peak and NOE peak were evaluated as, Γ_1=A1*W1 and Γ_2=A2*W2 respectively. The z-spectra were analysed both for individual subjects and for the averaged spectra.

6.3 Results

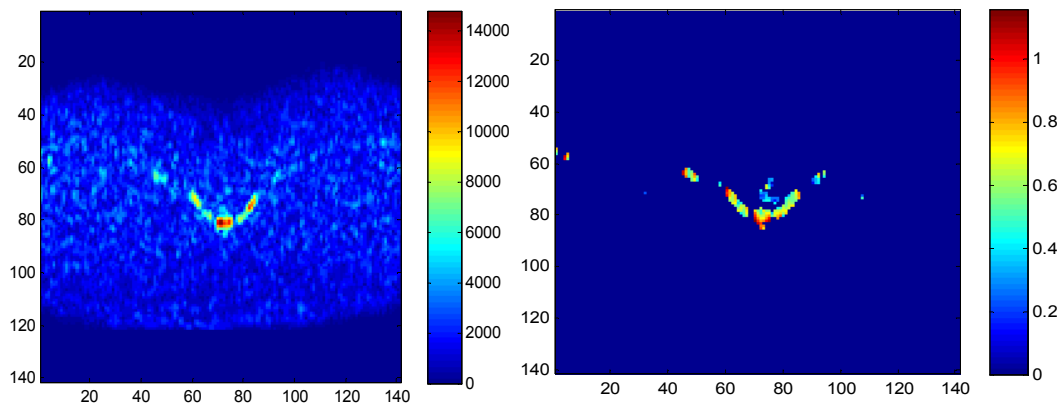Figure 6.6 shows the brachial plexus MT image and MTR map in the transverse view.

Figure 6.6 *Combined MT-DWIBS image of the Brachial plexus at a MT off resonance of 400Hz and b=300 s/mm², Δ=56.3, δ=10ms; Corresponding MTR map highlighting the spinal cord and nerve roots.*

Figure 6.7 shows the MTR values calculated at different single offset frequencies ±600, ±500, ±400 Hz from subjects of **cohort D**, which also shows the Wilcoxon rank test results.
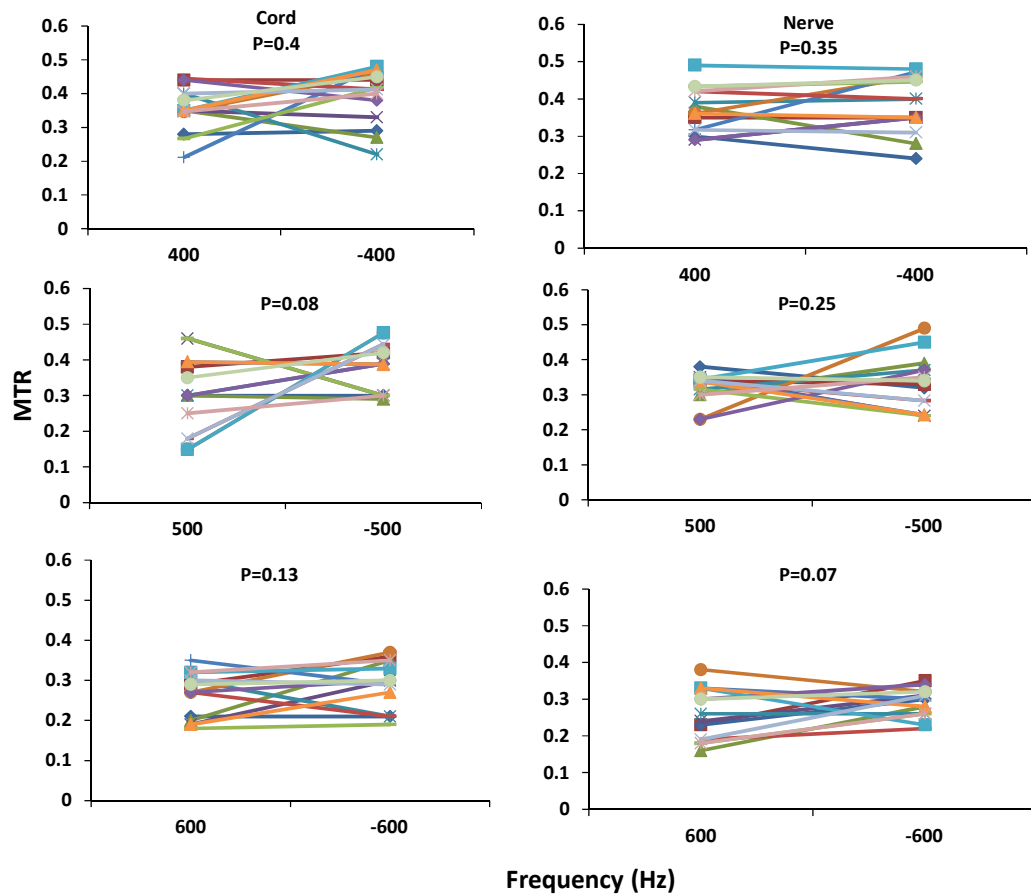

Figure 6.7 *MTR values at off-resonances ±400, ±500 and ±600 Hz from nerves and cord from 15 normal subjects each colour corresponds to individual data. The P value shows the results from Wilcoxon test for difference between positive and negative frequency offsets. Cords are showing asymmetry trend at ±500 Hz whereas nerves showing asymmetry trend at ±600 Hz.*

Figure 6.8 shows the WASSR correction shifting and z-spectra of brachial plexus nerves before and after the WASSR correction. Table 6.1 shows the WASSR correction frequencies for nerves and cord.
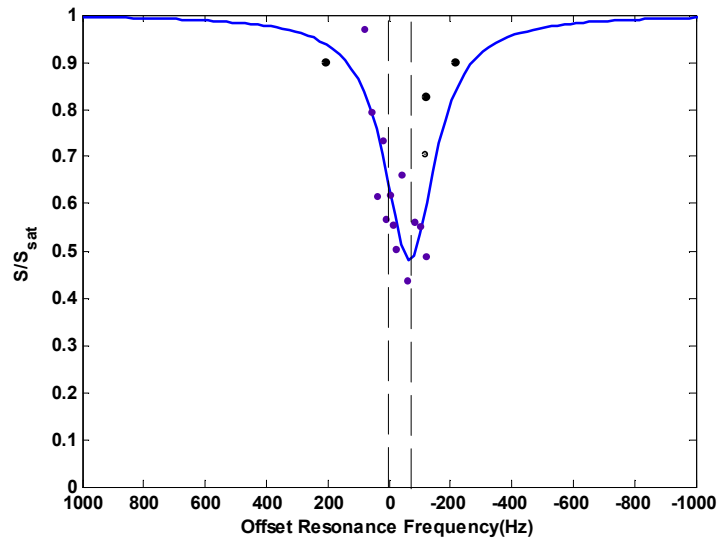
Figures 6.8 (a) *Example of WASSR corrections for brachial plexus nerve of subject 3, indicating the shifting of the central peak.*
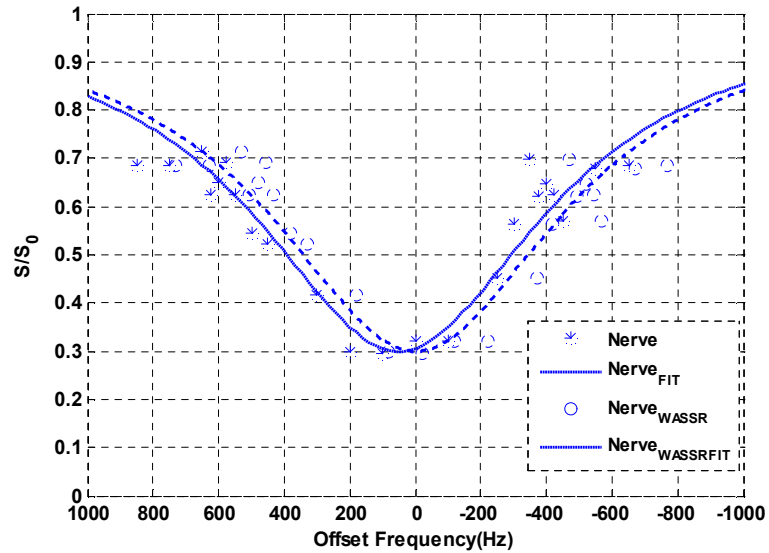

Figure 6.8 (b) *Nerve z-spectrum before and after the WASSR correction.*

Table 6.1: WASSR correction frequencies for nerves and cord are shown in table.

Subject	Right Nerve (Hz)	Left Nerve (Hz)	Cord (Hz)
Sub1	55	50	48
Sub2	-48	-40	-60
Sub3	20	20	80
Sub4	-30	-35	-50

Figures 6.9 shows the WASSR corrected z-spectra obtained from the nerves and cord from four subjects of ***cohort D*** at powers P1 = 0.18 µT and P2 = 0.3 µT.
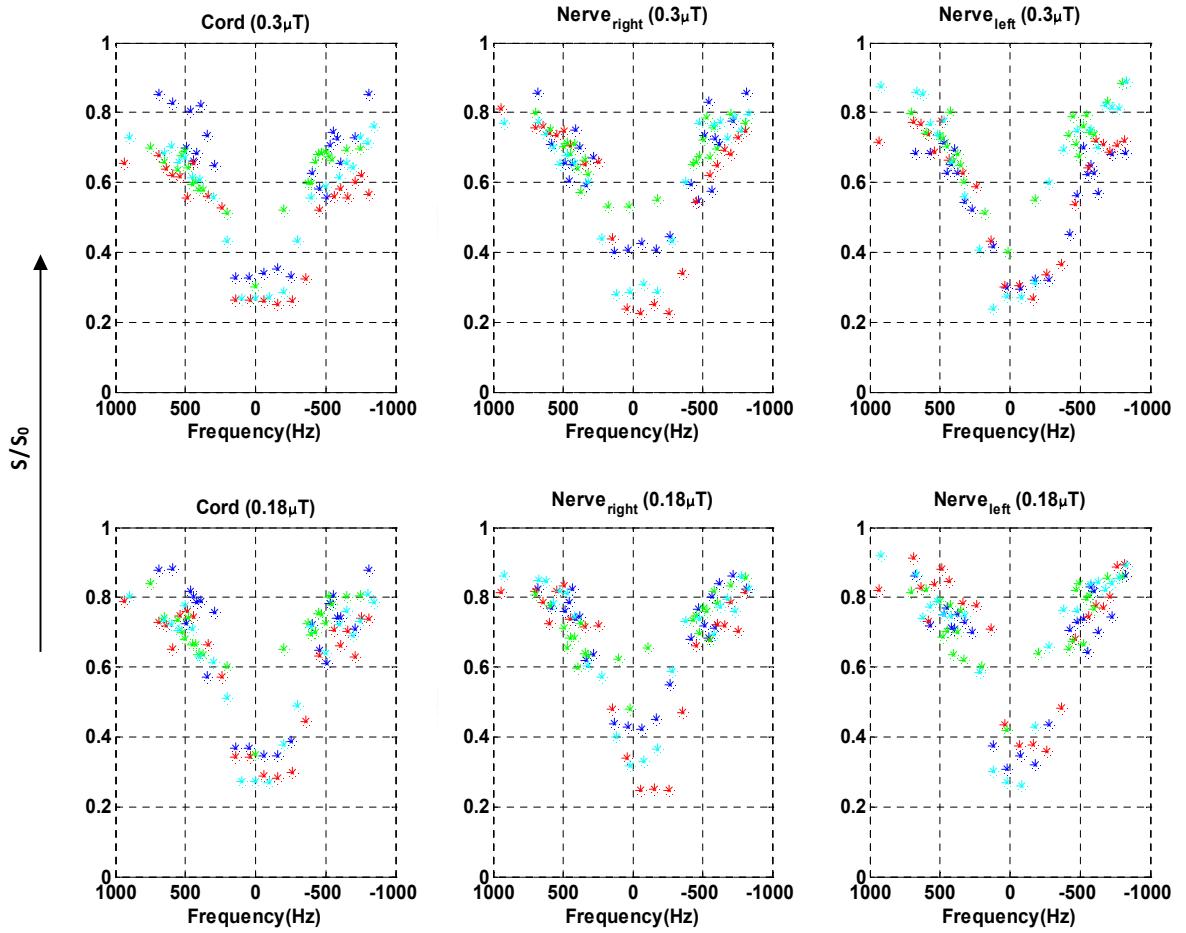

Figure: 6.9 *WASSR corrected z spectra of brachial plexus cord and nerves recorded. Each colour corresponds to a different subject.*

Figure 6.10 shows the single Lorentz equation fitting for lowfield (+) and upfield (-) sides of the subject average spectra at powers P1 and P2.
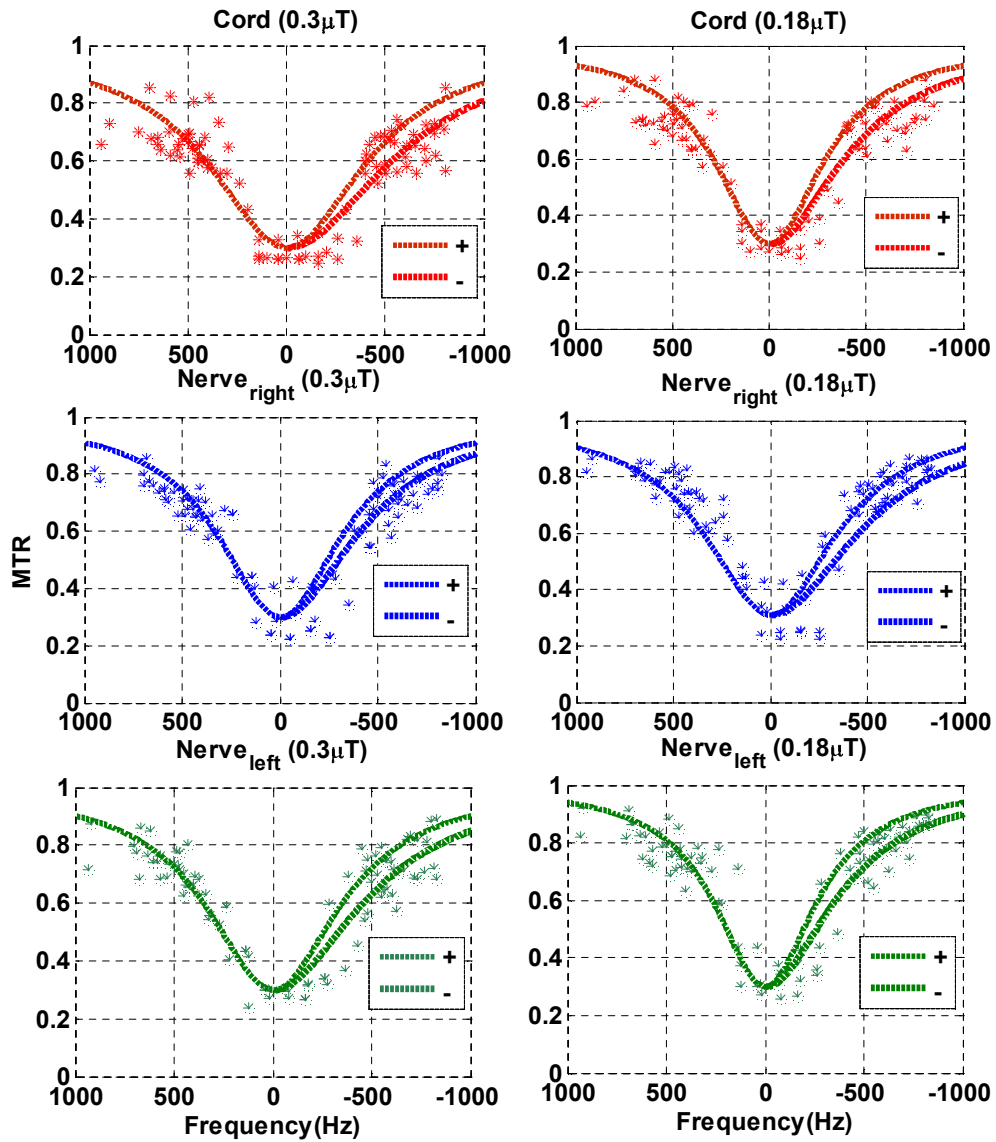

Figure 6.10 *MT spectra with single Lorentzian equation fitting for cord, right and left side nerves from four subject combined MT values. The dotted lines are showing upfield fitting and solid lines showing lowfield fitting. The upfield fit showed on lowfield side for comparison. The lowfield fitting are clearly showing presence of asymmetry both for nerves and cord at powers P1 and P2.*

Figure 6.11 shows the variations of FWHM MTR+ and MTR- values from single Lorentzian equation fittings for individual four subjects measured at powers P1 and P2.
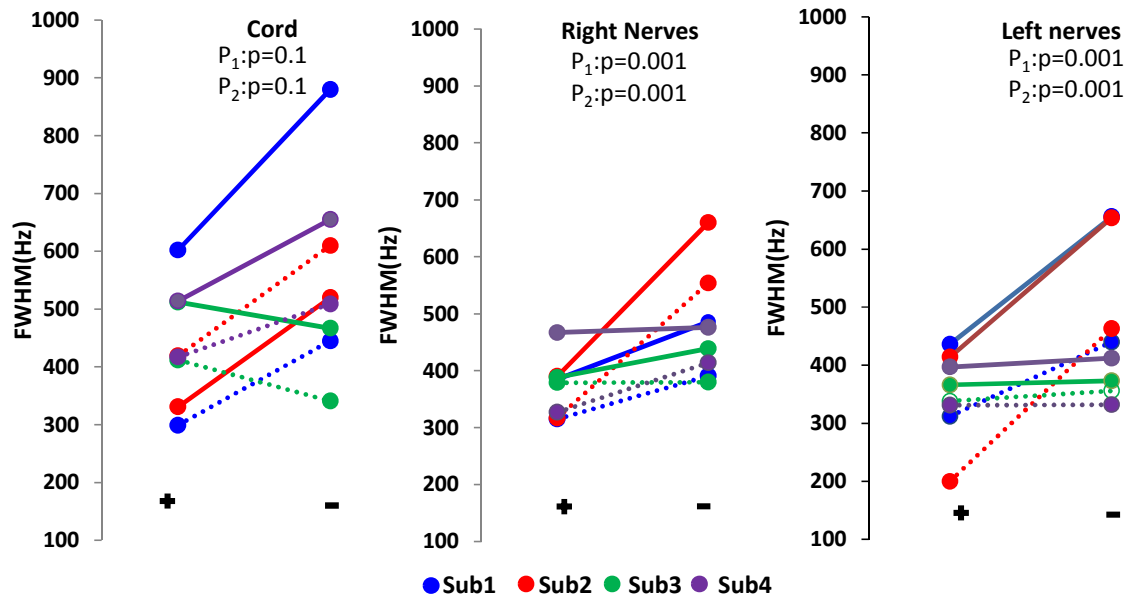
Figure 6.11 *FWHM values calculated from low field (+) and upfield (-) sides using single Lorentz fitting from 4 subjects (S1, S2, S3, S4) at two low power, P1 = 0.18 µT (dotted line) and high power, P2 = 0.3 µT (solid line). The Wilcoxon test p values are also shown for difference between offsets for different powers. For all cases except Sub3 cord FWHM are higher in the upfield (-) then the low field.*
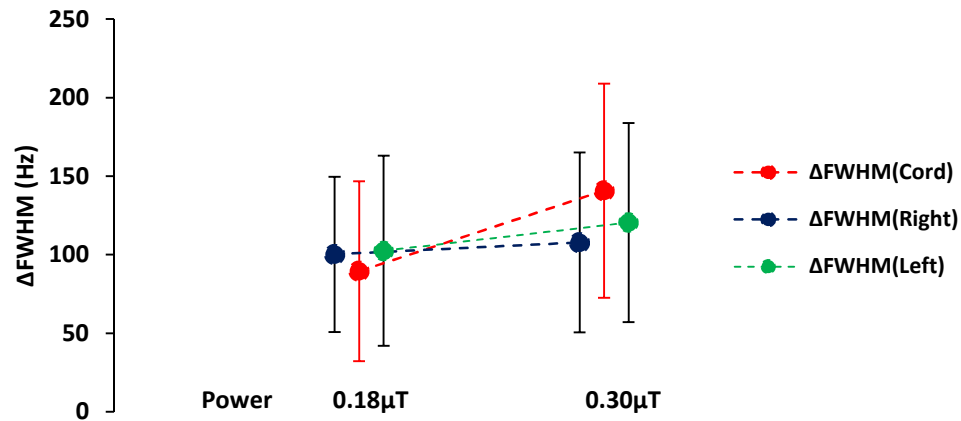
Figure 6.12 *Changes in ΔFWHM between upfield(-) and lowfield(+) sides from the averaged z-spectra for cord, right and left side nerves at P1 and P2 powers. ΔFWHM was lower at low power P1 compared to high power P2 and cord has higher asymmetry at high power.*

Figure 6.13 shows the double Lorentz equation fitting averaged four subject data sets at powers P1 and P2.
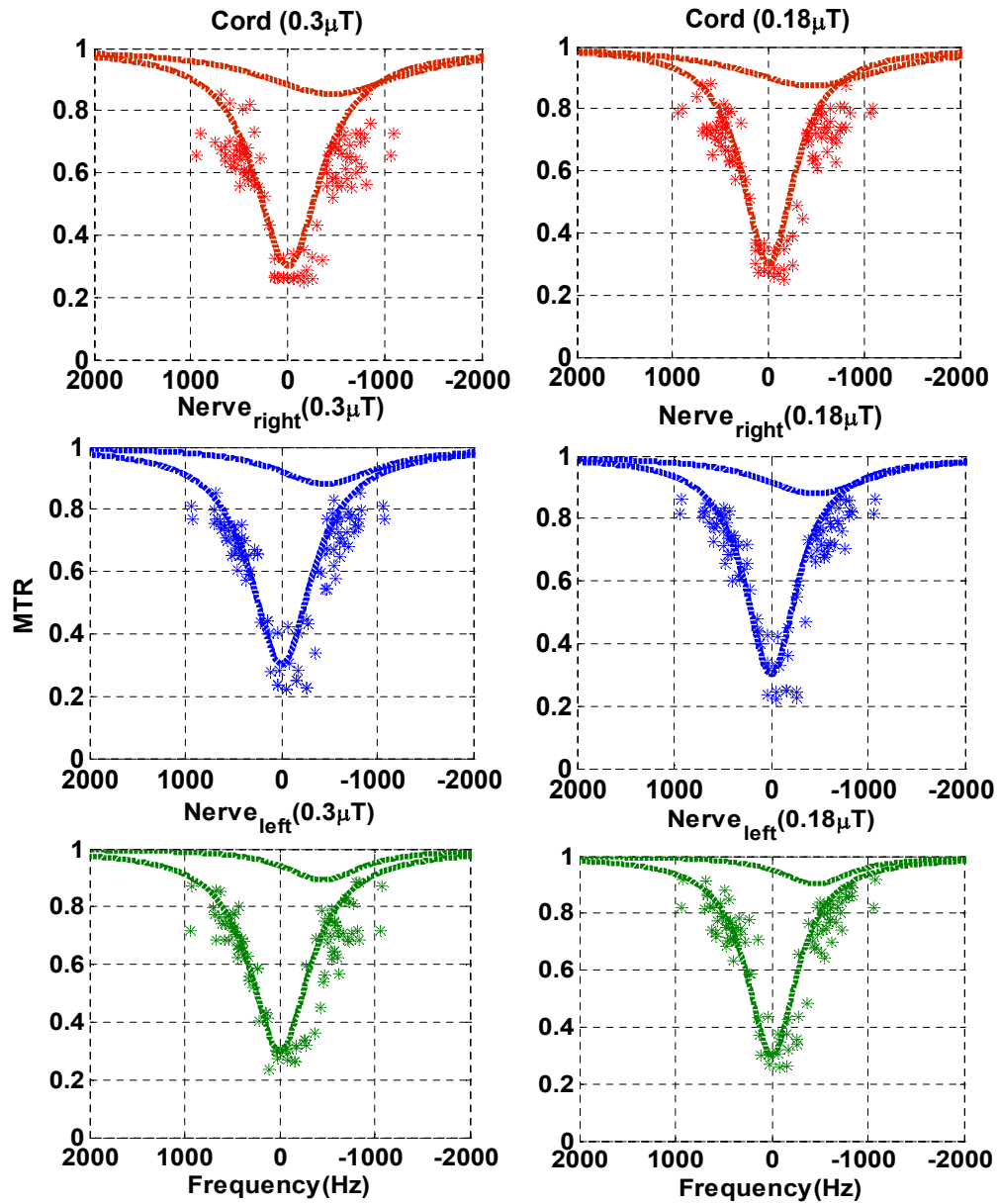
Figure 6.13 *z-spectra with double Lorentzian equation fitting for cord, right and left side nerves from averaged z-spectra. The dotted lines are showing central peak and solid lines are showing second peak at P1 and P2 powers.*

Figure 6.14 shows the double Lorentzian fitting areas under the central and secondary (NOE) peaks calculated from four individual's nerves and cord at powers P1 and P2.

Figure 6.14 *Parameters from double Lorentzian equation fitting on MT spectrum from individual subjects for low and high power. For central peak and secondary off-resonance (NOE) peak.*

Figure 6.15 showing the averaged areas under the central and NOE peaks from double Lorentzian fitting at powers P1 and P2.

Figure 6.15 (a) *Averaged areas from the central peak of fitting showing higher areas for power P1 compare to P2; (b) Averaged areas from the second (NOE) peak showing slight increasing tendencies at power P2 compare to P1.*

6.4 Discussion
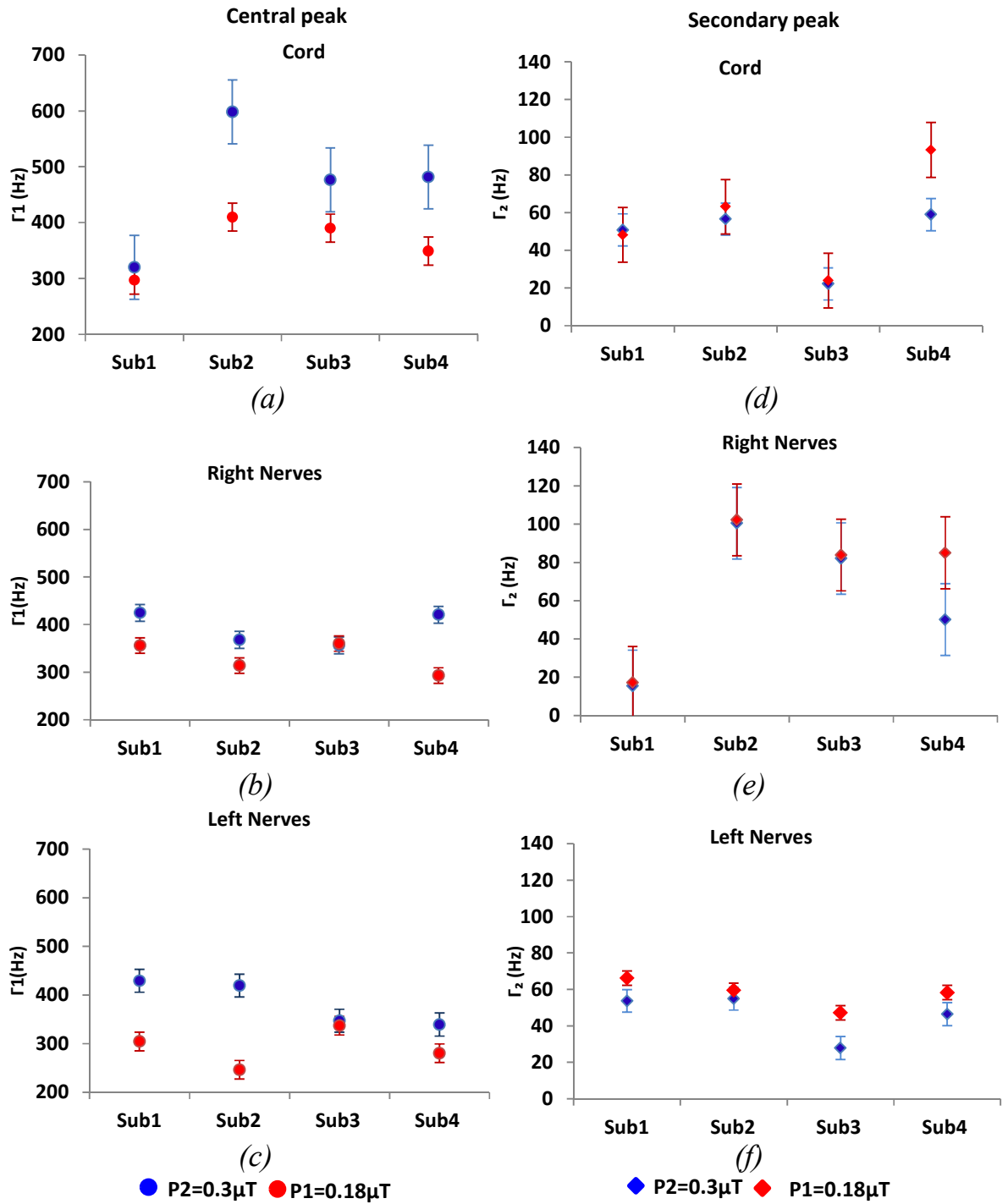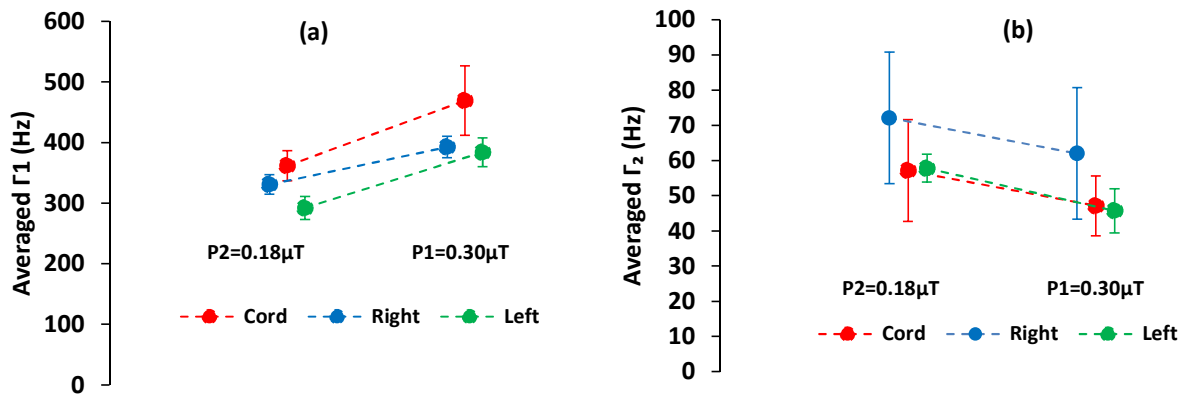
A protocol has been developed to allow the measurement of MT in the brachial plexus nerves and spinal cord. Contamination from CSF or blood flow has been suppressed by use of DWIBS technique which also allows the full z-spectrum to be acquired at multiple RF powers with SAR < 96% and within reasonable imaging time. This sequence offers a new imaging tool to characterise the brachial plexus both quantitatively and in clinical practice. From the standard asymmetry analysis which cannot be corrected for $\mathbf{B}_0$ inhomogeneities, asymmetry in the MTR is not significant. It shows trends of asymmetry at ±600 Hz for the cords and at ±500 Hz for the nerves. These asymmetries are consistent with NOE contributions (around -3.5 ppm), although without the full z-spectrum it is difficult to interpret these results, and they are noisy due to variable off resonance effects.

To study the asymmetry in more detail MT data were obtained at multiple offset frequencies and effects of $\mathbf{B}_0$ inhomogeneities were corrected using the WASSR technique. Although, there are no clear peaks on the wings of the spectra of the cord and nerves for individual data or combined data point MT spectra, when the WASSR corrected spectra were fitted to the single Lorentzian equation (L1) for lowfield and upfield sides separately, the widths (FWHM) on each side and difference of widths between sides (ΔFWHM) indicated an NOE contribution on the negative frequency

188

offset side of the spectrum, the NOE may be arise from the myelin in the cord, DRG and rami nerve fibres. From Figure 6.11 the individual FWHM are higher in upfield (-) compared to lowfield (+) both for nerves and cord, from Wilcoxon statistical values there are significant trends for nerves compare to cord. From Figure 6.12, the ΔFWHM values are in the same range for nerves and cord spectra may be due to similar sizes of their axons, and are higher at high power both for nerves and cord, thus more asymmetric at higher power.

Despite the fact that no clear secondary peak was visible, the double Lorentzian fit to the spectrum found significant second peaks at negative frequency offsets for both individual and subject averaged z-spectra for nerves and cord, which further confirms NOE effects. From Figure 6.13 and 6.14 the area under the central peak (Γ_1) was higher at high power than at low power for individual MT spectra cord and nerves, as expected for MT; whereas the area under the second peak (Γ_2) was lower at high power compare to low power as expected for NOE. From the averaged z-spectra asymmetry study in Figures 6.12 and 6.15 for single and double Lorentzian fitting both showed asymmetry in the z-spectra. Single Lorentz fittings showed more MT asymmetry compare to NOE asymmetry but are noisier than double Lorentzian fitting. Whereas, the double Lorentzian fittings showed clear MT and NOE asymmetry effects both for cord and nerve. MT asymmetry goes up for higher power, whereas, the NOE asymmetry goes down for higher power as expected (Liu *et al.* 2013, Zaiss *et al.* 2013). The detectable NOE in nerves and cord could be an area of active research for quantifying myelin content, demyelination and remyelination in brachial plexus.

The goal of this thesis is to study and measure the quantitative MR parameters ADC, T2 and MTR of brachial plexus discussed in Chapter 4, 5 and 6 respectively, the correlations between those parameters also have been observed from six subjects of **cohort D** and are shown in Figure 6.16 and Table 6.2.
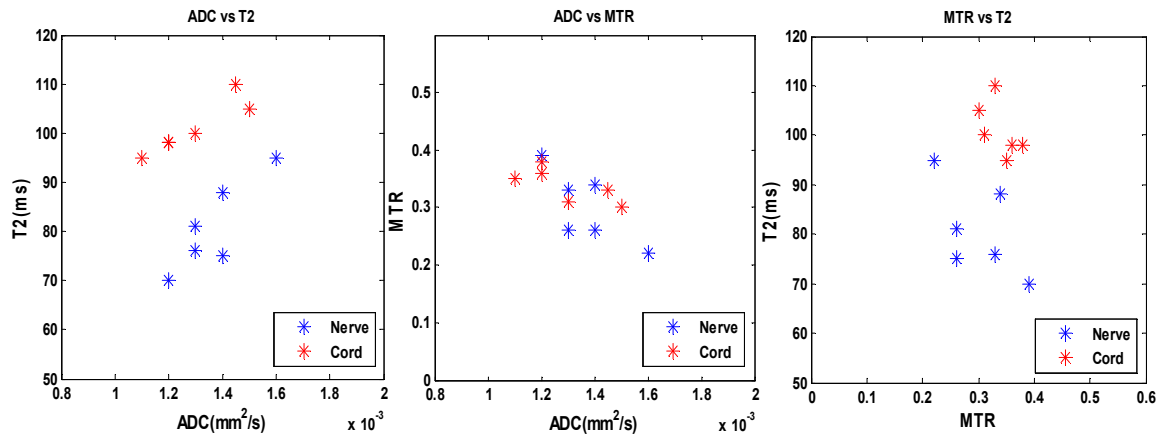
Figure 6.16 *Correlation between quantitative MRI parameters obtained from cohort D (6 subjects).*

Table 6.2 Correlation between quantitative MR parameters in brachial plexus

Correlation coefficient	Nerve	Cord
ADC vs T2	0.87	0.91
ADC vs MTR	-0.76	-0.74
MTR vs T2	-0.6	-0.55

Figure 6.16 shows that there are high positive correlations between ADC and T2 both for nerves and cord; this may be due to higher diffusivity regions having more mobile water content and hence higher T2. The ADC and MTR showed a trend of negative correlation, this may be due to more mobile water content with increased diffusivity relating to less magnetization transfer between bound and free protons. The T2 and MTR showed slight negative correlation which may be due to proton exchanges within the semi-solid tissues. The correlations between quantitative MR parameters can further characterise the biophysical properties of brachial plexus nerves and cord.

6.5 Conclusion

The magnetization transfer and z-spectra have been studied for brachial plexus using the DWIBS-MT sequence. The observed MT and z-spectra could produce information of microenvironments and tissue integrity in brachial plexus. The z-spectra showed asymmetry both for nerves and cord. The asymmetry in z-spectra corresponds to the NOE effects. These observations may give new insight into the interaction between semisolid tissue components and bulk water inside the nerves and cord of the brachial plexus and in future could provide a MR contrast for finding disorders in brachial plexus. We observed only the healthy group, thus no particular trends with pathology can be discussed. However, the combined DWIBS-MT sequences may provide an additional MR contrast for finding disorders in the brachial plexus.

References

Balaban, R. S. and T. L. Ceckler (1992). "Magnetization transfer contrast in magnetic resonance imaging." Magnetic resonance quarterly 8(2): 116-137.

Brown, R. A., S. Narayanan and D. L. Arnold (2012). "Segmentation of magnetization transfer ratio lesions for longitudinal analysis of demyelination and remyelination in multiple sclerosis." Neuroimage 66: 103-109.

Bryant, R. G. (1996). "The dynamics of water-protein interactions." Annual review of biophysics and biomolecular structure 25(1): 29-53.

Filippi, M., M. Bozzali, M. A. Horsfield, M. A. Rocca, M. P. Sormani, G. Iannucci, B. Colombo and G. Comi (2000). "A conventional and magnetization transfer MRI study of the cervical cord in patients with MS." Neurology 54(1): 207.

Graham, S. J. and R. M. Henkelman (1997). "Understanding pulsed magnetization transfer." Journal of Magnetic Resonance Imaging 7(5): 903-912.

Guivel-Scharen, V., T. Sinnwell, S. Wolff and R. Balaban (1998). "Detection of proton chemical exchange between metabolites and water in biological tissues." Journal of Magnetic Resonance 133(1): 36-45.

Henkelman, R. M., X. Huang, Q.-S. Xiang, G. J. Stanisz, S. D. Swanson and M. J. Bronskill (1993). "Quantitative interpretation of magnetization transfer." Magnetic Resonance in Medicine 29(6): 759-766.

Henkelman, R. M., G. J. Stanisz and S. J. Graham (2001). "Magnetization transfer in MRI: a review." NMR in Biomedicine 14(2): 57-64.

Hua, J., C. K. Jones, J. Blakeley, S. A. Smith, P. C. M. van Zijl and J. Zhou (2007). "Quantitative description of the asymmetry in magnetization transfer effects around the water resonance in the human brain." Magnetic Resonance in Medicine 58(4): 786-793.

Hua, J., P. van Zijl, P. Sun and J. Zhou (2007). Quantitative description of magnetization transfer (MT) asymmetry in experimental brain tumors. Proc Int Soc Mag Reson Med.

Jin, T., P. Wang, X. Zong and S. G. Kim (2013). "MR imaging of the amide-proton transfer effect and the pH-insensitive nuclear overhauser effect at 9.4 T." Magnetic Resonance in Medicine 69(3): 760-770.

Jones, C. K., A. Huang, J. Xu, R. A. E. Edden, M. Schaer, J. Hua, N. Oskolkov, D. Zaca, J. Zhou, M. T. McMahon, J. J. Pillai and P. C. M. van Zijl (2013). "Nuclear Overhauser enhancement (NOE) imaging in the human brain at 7 T." Neuroimage 77: 114-124.

Jones, C. K., A. J. Huang and P. C. Van Zijl (2011). "Exchange-relayed nuclear Overhauser effect MRI." Proceedings of the 19th Annual Meeting of ISMRM, Montreal.

Kim, M., J. Gillen, B. A. Landman, J. Zhou and P. C. M. van Zijl (2009). "Water Saturation Shift Referencing (WASSR) for Chemical Exchange Saturation Transfer (CEST) Experiments." Magnetic Resonance in Medicine 61(6): 1441-1450.

Liepinsh, E. and G. Otting (1996). "Proton exchange rates from amino acid side chains— implications for image contrast." Magnetic Resonance in Medicine 35(1): 30-42.

Ling, W., R. R. Regatte, G. Navon and A. Jerschow (2008). "Assessment of glycosaminoglycan concentration in vivo by chemical exchange-dependent saturation transfer (gagCEST)." Proceedings of the National Academy of Sciences of the United States of America 105(7): 2266-2270.

Liu, D., J. Zhou, R. Xue, Z. Zuo, J. An and D. J. Wang (2013). "Quantitative characterization of nuclear Overhauser enhancement and amide proton transfer effects in the human brain at 7 tesla." Magnetic Resonance in Medicine 70(4): 1070-1081.

Liu, G., X. Song, K. W. Y. Chan and M. T. McMahon (2013). "Nuts and bolts of chemical exchange saturation transfer MRI." NMR in Biomedicine 26(7): 810-828.

McCreary, C. R., T. A. Bjarnason, V. Skihar, J. R. Mitchell, V. W. Yong and J. F. Dunn (2009). "Multiexponential T2 and magnetization transfer MRI of demyelination and remyelination in murine spinal cord." Neuroimage 45(4): 1173-1182.

Mougin, O., M. Clemence, A. Peters, A. Pitiot and P. Gowland (2013). "High-resolution imaging of magnetisation transfer and nuclear Overhauser effect in the human visual cortex at 7 T." NMR in Biomedicine 26(11): 1508-1517.

Mougin, O. E., R. C. Coxon, A. Pitiot and P. A. Gowland (2010). "Magnetization transfer phenomenon in the human brain at 7 T." Neuroimage 49(1): 272-281.

Ng, M. C., J. Hua, Y. Hu, K. D. Luk and E. Y. Lam (2009). "Magnetization Transfer (MT) Asymmetry Around the Water Resonance in Human Cervical Spinal Cord." Journal of Magnetic Resonance Imaging 29(3): 523-528.

Oyeka, I. C. A. and G. U. Ebuh (2012). "Modified Wilcoxon Signed-Rank Test." Open Journal of Statistics 2: 172.

Pekar, J., P. Jezzard, D. A. Roberts, J. S. Leigh, J. A. Frank and A. C. McLaughlin (1996). "Perfusion imaging with compensation for asymmetric magnetization transfer effects." Magnetic Resonance in Medicine 35(1): 70-79.

Schmierer, K., F. Scaravilli, D. R. Altmann, G. J. Barker and D. H. Miller (2004). "Magnetization transfer ratio and myelin in postmortem multiple sclerosis brain." Annals of Neurology 56(3): 407-415.

Schmierer, K., D. J. Tozer, F. Scaravilli, D. R. Altmann, G. J. Barker, P. S. Tofts and D. H. Miller (2007). "Quantitative magnetization transfer imaging in postmortem multiple sclerosis brain." Journal of Magnetic Resonance Imaging 26(1): 41-51.

Stanisz, G. J., E. E. Odrobina, J. Pun, M. Escaravage, S. J. Graham, M. J. Bronskill and R. M. Henkelman (2005). "T1, T2 relaxation and magnetization transfer in tissue at 3T." Magnetic Resonance in Medicine 54(3): 507-512.

van Zijl, P. C. M. and N. N. Yadav (2011). "Chemical exchange saturation transfer (CEST): What is in a name and what isn't?" Magnetic Resonance in Medicine 65(4): 927-948.

Wolff, S. D. and R. S. Balaban (1989). "Magnetization transfer contrast (MTC) and tissue water proton relaxation in vivo." Magnetic Resonance in Medicine 10(1): 135-144.

Xu, J. Z., M. Zaiss, Z. L. Zu, H. Li, J. P. Xie, D. F. Gochberg, P. Bachert and J. C. Gore (2014). "On the origins of chemical exchange saturation transfer (CEST) contrast in tumors at 9.4 T." NMR in Biomedicine 27(4): 406-416.

Zaiss, M., P. Kunz, S. Goerke, A. Radbruch and P. Bachert (2013). "MR imaging of protein folding in vitro employing Nuclear-Overhauser-mediated saturation transfer." NMR in Biomedicine 26(12): 1815-1822.

Zaiss, M., J. Z. Xu, S. Goerke, I. S. Khan, R. J. Singer, J. C. Gore, D. F. Gochberg and P. Bachert (2014). "Inverse Z-spectrum analysis for spillover-, MT-, and T-1-corrected steady-state pulsed CEST-MRI - application to pH-weighted MRI of acute stroke." NMR in Biomedicine 27(3): 240-252.

Chapter 7
Distribution of F-latency (DFL) and MRI study of the Brachial Plexus

Brachial plexus imaging by MRI can efficiently detect disorders and study the microstructures qualitatively and quantitatively. EMG can detect the peripheral neuropathies using time dependent behaviour of nerve conduction. Thus the combination of EMG and MRI could provide important insight and information about the brachial plexus. The objective of this chapter is to measure the distribution of F-response latencies (DFL) as a new parameter in EMG and combine it with quantitative MRI studies.

7.1 Introduction

EMG and the nerve conduction velocity measurements using evoked or electrically stimulated responses are commonly used for studies of various peripheral neuropathies, radiculopathy, polyneuropathy, etc. (Aminoff 2006, Date *et al.* 2006, Massey 2006, Teener *et al.* 2006, Trojaborg *et al.* 2006, Pastore-Olmedo *et al.* 2009, Kimura 2013). Nerve conduction studies have the attraction that they are potentially low cost, non-invasive and can be made available widely. The objective of nerve conduction studies is to record the compound muscle action potential (CMAP) in various proximal nerves, and assess the direct and late response conduction properties across the nerve path, and measure the intrinsic electrical activity of the muscle.

When a motor nerve is electrically stimulated action potentials are generated within the individual fibres which travel to the connected muscle as orthodromic conduction eliciting CMAP or M-responses that can be recorded using surface electrodes. From the stimulation site the action potentials also travel in the antidromic direction to their respective cell bodies located in the spinal cord. In most of the motor nerve cells these antidromic potentials simply die down. However, a small percent of the cell bodies back-fire after a short delay and send fresh action potentials down the nerve fibres to the muscle. These produce a delayed compound muscle action potential called the F-response which is very much reduced in amplitude with respect to the M-response because of the small number of fibres involved. It has also been shown in Section 3.5.3 that F-response is different from a reflex.

M-responses, obtained with repeated supramaximal stimulation, always have the same shape and amplitude, and occur at the same latency, whereas the F-responses vary in shape, amplitude and latency on repeated stimulation, because of the participation of a

random number of backfiring cell bodies (shown in Figure 7.1). Which nerve cells will backfire is not known, it is entirely a random statistical process, and so depending on the conduction velocities of the backfiring nerve cells, the combined response that is recorded will vary. Sometimes there will be no backfiring, and then there is no F-response at all.
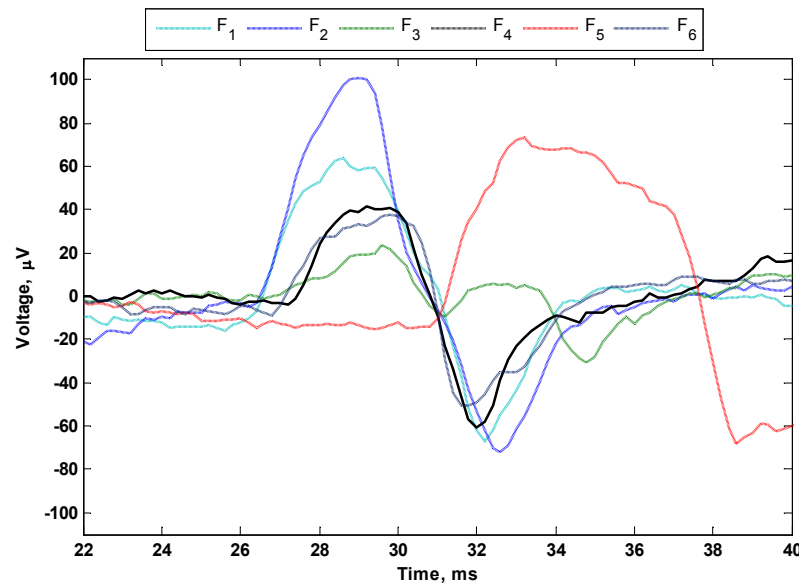

Figure 7.1 *Different F-responses with varying amplitude and latencies, recorded from the abductor-pollicis brevis (APB) muscle in the palm after stimulation over the median nerve from single subject.*

Despite this variability, the F-responses are one of the most sensitive parameters in nerve conduction studies in defining the polyneuropathies and can work as a meaningful physiological parameter (Mahmoudi *et al.* , Oberthuer *et al.* 2001, Kocer *et al.* 2005, Rabbani *et al.* 2007, Pastore-Olmedo *et al.* 2009). For the current research we focused on MRI and DFL for brachial plexus functions/structure studies.

7.1.1   Distribution of F-latencies (DFL)

Recently, a group in Dhaka University, Bangladesh comprehended and developed a new nerve conduction parameter based on neuro-physiological function named Distribution of F-Latency (DFL) (Rabbani *et al.* 2007). DFL handles the randomness of F-responses by considering a statistical frequency distribution of the F-latencies, schematic DFL shown in Figure 7.2. The hypothesis of DFL is described below:
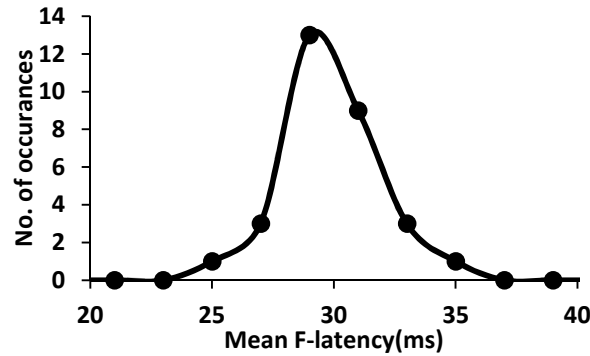

Figure 7.2 *Typical DFL from one healthy subject.*

The F-response latency for a motor unit potential on the connected muscle can be expressed as,

$$T_f = T_1 + \Delta T_c + T_2 + \Delta T_m + T_3 \tag{7.1}$$

where T_1 is the time taken by the potential to travel from the stimulation site (S) to the nerve root at the anterior horn cell in the spinal cord (C), ΔT_c is the time delay for backfiring at the cell body C, T_2 is the time taken by the backfired signal to travel from S to the neuromuscular junction (NMJ), ΔT_m is the time delay at the NMJ and T_3 is the time of travel from the NMJ to the recording electrode (R). Expression 7.1 is schematically shown in Figure 7.3.
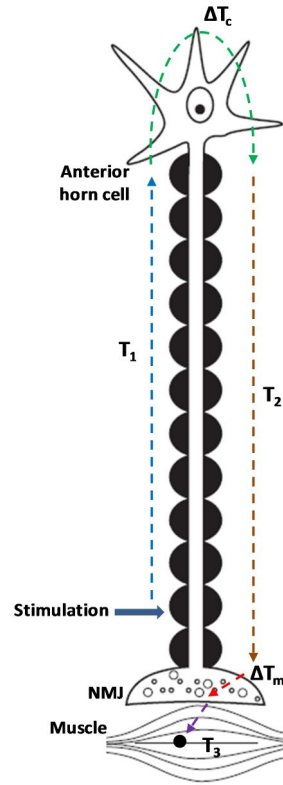
Figure 7.3 *F response circuitry with travelling time of the response. When a nerve is stimulated the F-response is derived by antidromic travel to the anterior horn cell in the spinal cord (T_1). Backfiring of some of the horn cells (ΔT_c) creates the late response that travels down (T_2) to the neuromuscular junction-NMJ (ΔT_m), which is then recorded from the muscle (T_3) as the F-response.*

Here T_1 and T_2 depend on the conduction velocity v_n of the particular nerve fibre and T_3 depends on the conduction velocity v_m of the short length between the *NMJ* and *R*. Assuming ΔT_c, ΔT_m and T_3 produce a constant delay of ~1ms for all nerve fibres and motor units (Kimura 2001), which compared to an F-latency of about 25ms can be ignored (Fisher 1982, Rajabally *et al.* 2013). Then Equation 7.1 simplifies to,

$$T_f = T_1 + T_2 + k = (d_1 + d_2)/v_n + k \qquad\qquad (7.2)$$

where d_1 and d_2 are the antidromic and orthodromic conduction nerve segment lengths and k is a constant period.

Now the distances d_1 and d_2 are almost constant for all fibres involved in an F-latency measurement; also considering $d_1 \approx d_2$ Equation 7.2 can be further simplified to,

$$T_f = (2L)/v_n + k \qquad\qquad (7.3)$$

where $2L$ is the total travelling distance for the F-responses. Thus the F-latency T_f for each nerve fibre is simply dependent on its velocity v_n.

For a single stimulation a single F-latency can be measured that depends on the random backfiring of the nerve cell bodies. This suggests that if multiple F-responses

are obtained at sufficient time intervals to allow the physiological processes to restore to normal condition, then the number of times that a particular F-latency is obtained will depend on the number of nerve fibres contributing to the F-response, because of simple statistical probability of chance. Therefore a frequency distribution of occurrence of F-latencies creates the DFL.

As latency is inversely proportional to the velocity, the DFL will depend on the distribution of conduction velocities (DCV) of the nerve fibres, specifically those motor nerve fibres in the nerve trunk that take part in the creation of the F-response (the backfiring nerves). From the description in section 2.2, the DCV of a myelinated nerve trunk has a bimodal distribution. From DCV the second and smaller peak which corresponds to the A-α fibres are present in the electrically stimulated motor nerves (Barker *et al.* 1979, Cummins *et al.* 1981, Dorfman 1984). Therefore for healthy nerves, the single peak DCV would be involved in any motor conduction study. Thus the DFL corresponds to a reflection of the DCV about the vertical axis (number of fibres) of the motor nerve fibres taking part in the F-responses. This simple inverse relationship between the DFL and the DCV allows an easy estimation of the DCV, and proposing the DFL as a valid physiological parameter. Figure 7.4 shows a schematic diagram of DCV and DFL comparison.
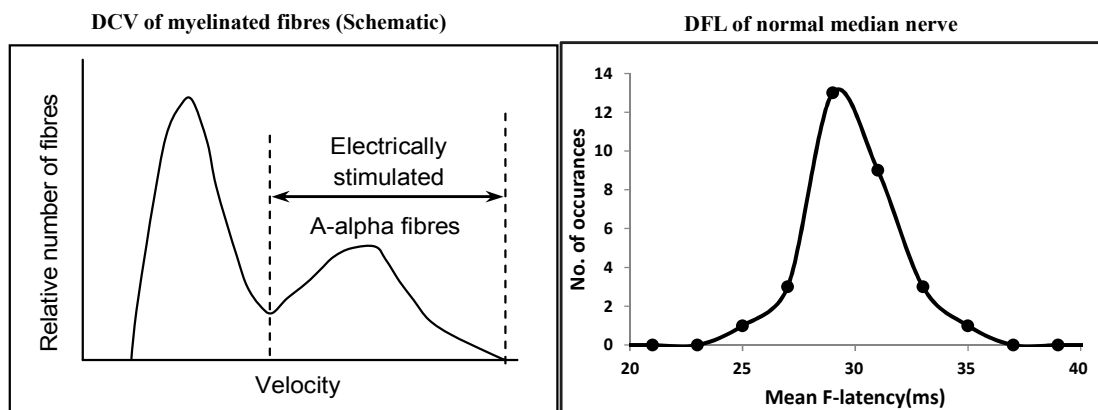

Figure 7.4 *Schematic DCV (left side) of normal myelinated nerve fibres and DFL (right side) for normal median nerve. A-α fibre DCV peak relates to the electrical stimulated nerve fibres which is like a mirror image of the DFL (Dorfman 1984, Rabbani et al. 2007).*

7.1.2   Observations from the DFL

From clinical studies in over more than one hundred subjects, it was observed that the DFL has a single peaked pattern similar to a 'Gaussian distribution shape' for normal healthy median and ulnar nerves in hands, and common peroneal and tibial nerves in the leg. The recorded DFL also demonstrated very good intra subject and intersubject repeatability and reproducibility for the same nerve (Rabbani *et al.* 2007). Changes in the DFL can be found not only for disordered nerves but also for the normal healthy nerves by creating temporary compression or extension states. The physiological basis for this observed changing in the DFL is briefly discussed below.

Different positions of the head can cause temporary compression or extension over the brachial plexus nerve roots. This artificial disorder causes clear shifting of the DFL (more than 1ms latency shifting) compared to the normal position of the head, due to distinctive changes in nerve fibre latencies. Such DFL shifting from normal healthy median nerve is shown in Figure 7.5.
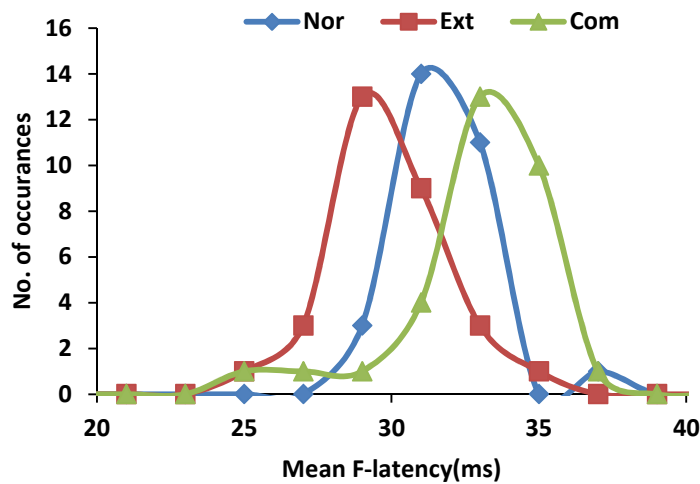

Figure 7.5 *DFL shifting with head movement recorded from a normal and healthy median nerve. Shows the normal head position DFL (blue line) is in the middle; the extended position of the head (red line) cause DFL shifting towards shorter F-latencies; and the compressed position of the head (green line) cause DFL shifting towards longer F-latencies.*

That amount of change cannot be accounted for by a change of 'length' of the nerve fibre. Since a normal fibre with a conduction velocity of 50m/s would have to traverse the nerve twice, a 1ms shift in F-latency would require a change of 25mm in length which is not possible with tolerable head movement. However, the cross section of

the nerve is also changed during the head movement. If the cross sectional area decreases it may cause a localised partial block and a corresponding delay in F-latency and delaying DFL to longer times. On the other hand, if the cross sectional area increases it may cause a 'release' of an existing partial block, resulting in a faster F-latency and making the DFL shift left to the normal DFL.

Using the resistance-capacitance (RC) model of the nerve (Binnie *et al.* 1995, Brown *et al.* 1998), the speed and transmission of a nerve impulse is determined by the capacitance of the membrane and myelin which separates the axon from the outside fluid, and the resistance of the axon schematically as shown in Figure 7.6. From the RC model the conduction time depends on the circuit time constant,

$$\tau = RC \tag{7.4}$$

Resistance of the nerve axon is given by,

$$R = \rho \frac{l}{A} \tag{7.5}$$

where A is the cross sectional area of the axon, ρ is the specific resistivity of the fluid inside the axon, and l is the length of the axon. Also, capacitance of the nerve as a parallel plate capacitor is given by,

$$C = \frac{\epsilon A_c}{d} \tag{7.6}$$

where d is the thickness of the membrane (about $0.005 \mu m$), ε is the dielectric constant of the membrane, and A_c is the membrane area of the axon.
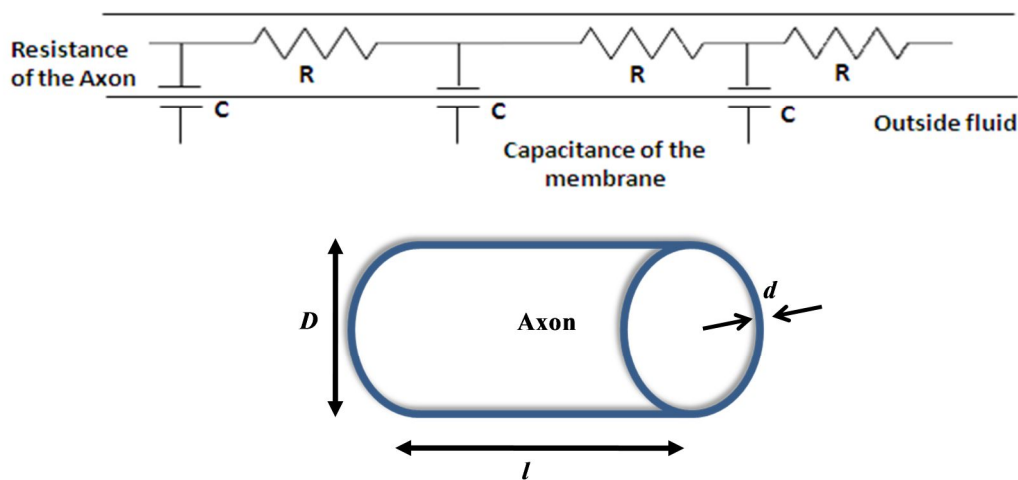

Figure 7.6 *RC model of an axon showing the resistance of the axon and capacitance created at the membrane between inside and outside fluid and a schematic axon indicating diameter D, length l and thickness d.*

If $r=D/2$ is the radius of the axon. Then

    Membrane area, $A_c=2\pi rl$ (7.7)

    Axon area, $A = \pi r^2$ (7.8)

Then from Equations (7.4) to (7.8)

$$\tau = \left(\frac{2\rho\epsilon l^2}{d}\right)\frac{1}{r} \tag{7.9}$$

For fixed thickness, d, and unchanged length, l, the conduction time inversely varies with the radius of the nerve,

$$\tau \propto \frac{1}{r} \tag{7.10}$$

Thus when the diameter of the axon is reduced the time constant will increase and vice versa.

From the above expression, it is clear that the nerve radius changing due to head movement should be inversely related to the F-latency. That means that the compressed position DFL will shift towards longer latency values and extended position DFL will shift towards shorter latency values. This can also explain why more than one peak and/or broad peaks in DFL are observed. It was understood that the measured DFL is contributed by the F-response from the whole propagating path along the nerve trunk up to the nerve roots at spinal cord. If any one or more paths are compressed, conduction through all the underlying fibres will decrease in a proportional way, and their contribution to the DFL will result in a delayed distribution from the relevant compressed nerve trunk. If the delay difference is large enough between the compressed and normal nerve trunk it will create two or more peaks in the DFL, while if the delay is less, as in mild compression, it will show a broad peak DFL. Changing of the DFL pattern and the production of more than one peak is schematically shown in Figure 7.7.
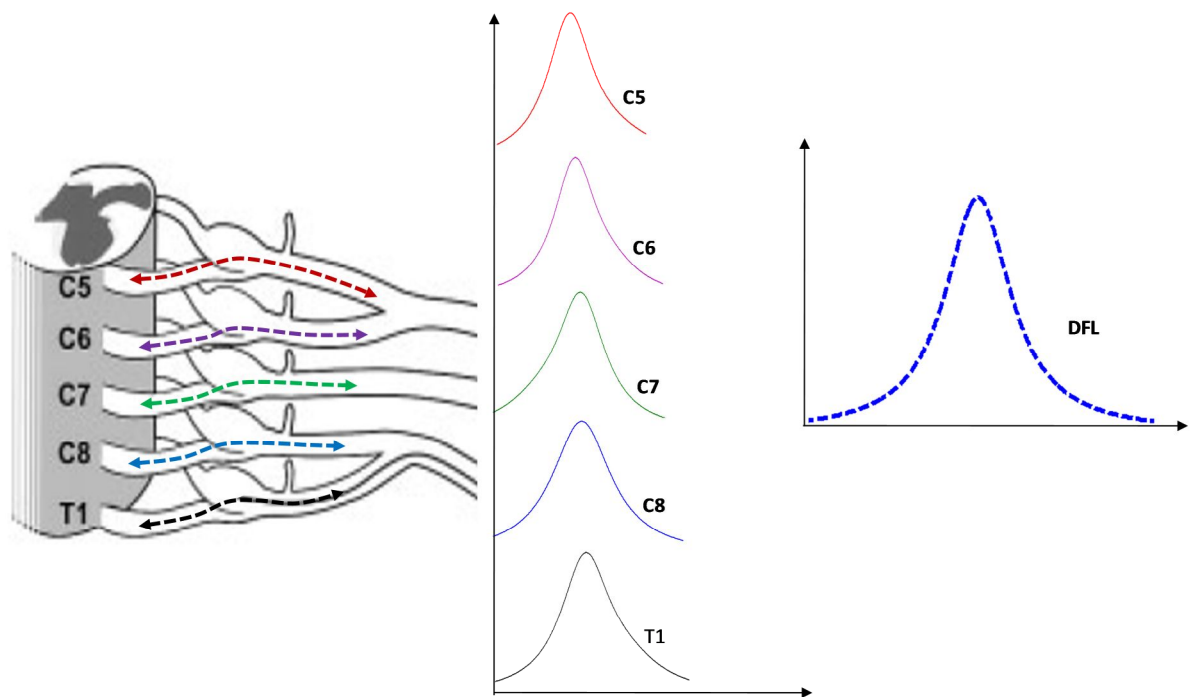
Figure 7.7a *Schematic diagram of DFL contribution from brachial plexus nerve roots, all the nerve roots appeared as normal and there is single peak in DFL.*
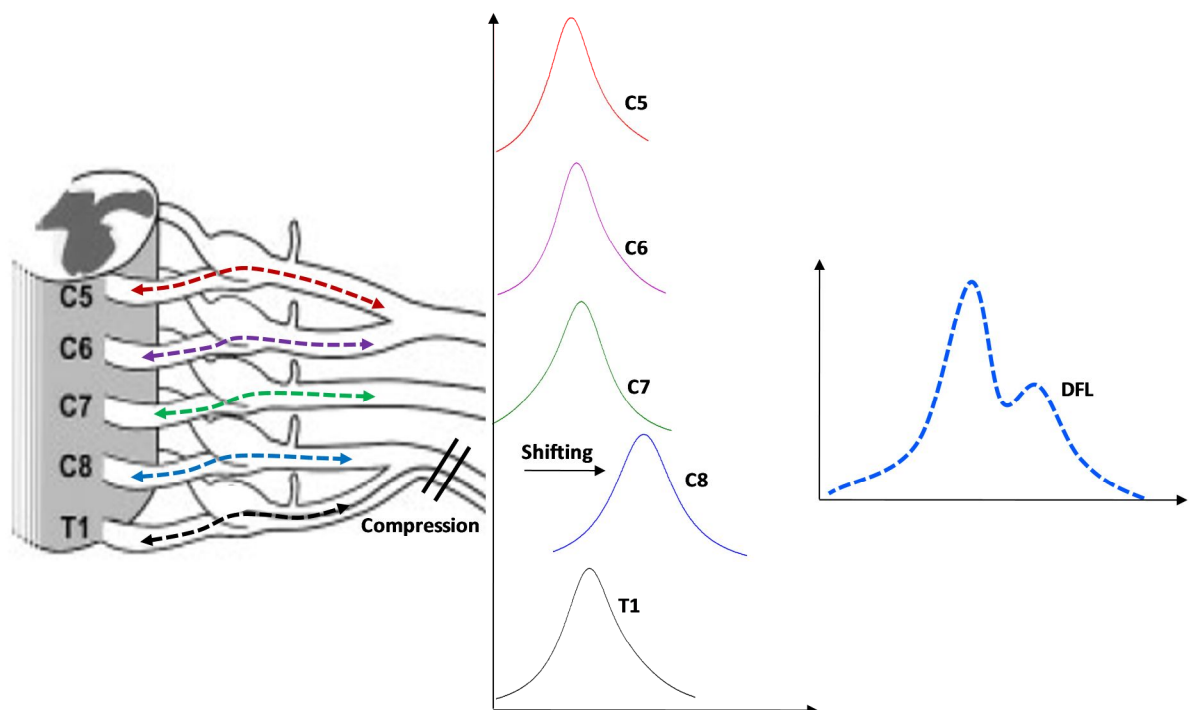

Figure 7.7b *Schematic diagram of DFL contribution from brachial plexus nerve roots, the nerves at C8 appeared to be compressed thus there is shifting of conduction which results in a double peak in the DFL.*

The above explanations are directly applicable with the DFL observations for different peripheral neurological disorders. From the EMG diagnostic observations

many patients have one side affected with some kind of neuropathy while the other side is normal. DFL obtained from the normal sides of these patients demonstrated single peak DFLs. That agrees with the DCV for the normal nerve trunk. However, the disordered side DFLs demonstrated more than one or delayed or broad peaks for different disorders such as cervical spondylosis, carpal tunnel syndrome (CTS), nerve damage and cut injury etc.

7.1.3   Cervical spondylotic neuropathy and DFL study

Cervical spondylotic neuropathy as myelopathy and radiculopathy are conditions involving a pathologic process affecting the spinal nerve root (discussed in section 2.10). Commonly, these disorders occur due to herniated nucleus pulposis anatomically which compresses nerve roots within the spinal canal. Another common cause of radiculopathy is spinal stenosis resulting from a combination of degenerative spondylosis and ligament hypertrophy. EMG and nerve conduction studies provide valuable information for such disorders and can help treatment planning and minimize other expensive diagnostic and therapeutic procedures.

Needle EMG is a straight forward diagnosis of cervical spondylotic radiculopathy that can also find the level of lesion of the disorders (Preston *et al.* 2012, Hakimi *et al.* 2013). However, being an invasive procedure such a technique has strict protocols to follow and requires an expert neurologist to locate the region for inserting the needle (Aminoff 1978). Depending on the underlying pathophysiology and the level of the lesion, such abnormalities also examined using conventional NCV tests, like the sensory nerve conduction velocity and/or the motor nerve conduction velocity test (Preston *et al.* 2012, Kimura 2013). The author of this thesis has studied the correlation between the shape of NCV M-responses and cervical spondylosis using FFT and wavelet transformation (Mahbub *et al.* 2007, Mahbub *et al.* 2013). The H-reflex is helpful in evaluating lower extremity radiculopathy, which is only possible to evaluate S1 radiculopathy (Pastore-Olmedo *et al.* 2009). Compared to other electrodiagnosis the F-response shows direct abnormalities with radiculopathies, because an abnormal F-response with normal distal nerve conduction studies suggests a proximal lesion, either in the plexus or roots. It is important to note that, the F-responses will show the abnormality only if the recorded muscle is innervated by the affected nerve roots (Guiloff 2006, Teener *et al.* 2006, Preston *et al.* 2012, Rajabally *et al.* 2013). The recently proposed F-response parameter, DFL, shows good clinical

results as a sensitive parameter for diagnosing cervical spondylotic neuropathy. For patients with cervical spondylotic disorders, the measured DFL from peripheral nerves shows double or triple peaks and/or a broad peak compared to the normal nerve DFL. The DFL observations are briefly discussed below.

In the case of cervical spondylotic radiculopathy, observations were explained as when a segment of a peripheral nerve trunk has a reduced velocity due to compression at its root(s) while the rest of the nerve trunks are normal, that leads to a double peak or broad peak in DFL depending on the delay difference between the nerve trunks. Patterns of DFL expected on this hypothesis have been observed in practice from cervical spondylotic radiculopathy patients (Alam *et al.* 2010, Rabbani 2011), shown in Figure 7.8.

Again, the DFL has more than one peak from the patients with cervical spondylotic myelopathy through disc bulging and compression in the cervical spinal cord. Since the spinal cord is surrounded by CSF in the spinal canal, disc compression will affect the local nerve fibres rather than the whole spinal cord. The compressions will cause some degeneration of the fibres and that will cause a reduction in conduction velocity; hence more than one peak or a broad peak is demonstrated in the resulting DFL. However, these trends may differ from person to person, depending on individual anatomical conditions and whether they have already other unknown neurological disorder or not (Alam *et al.* 2010, Rabbani 2011).
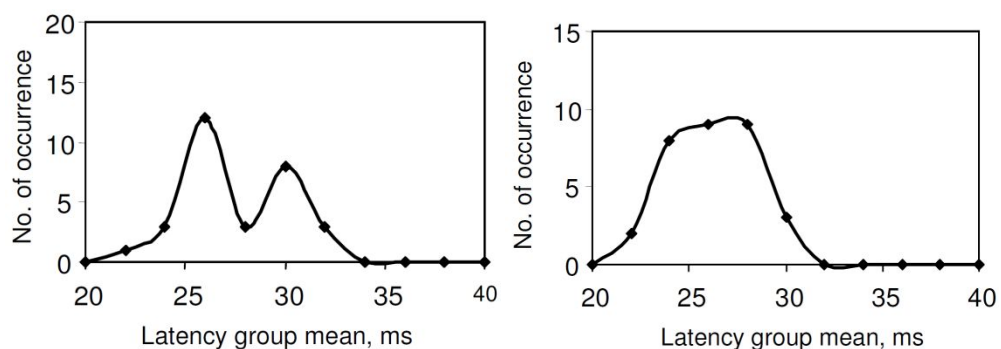

Figure 7.8 *Double peak DFL obtained and broad peak DFL from CS patient (Rabbani 2011).*

In addition the DFL also shows changes in positions with other peripheral nerve disorders such as carpal tunnel syndrome (CTS), a disorder due to nerve compression at the wrist. For CTS patients, the whole DFL pattern shifts laterally along the time axis, i.e. delayed, without significant change in the pattern (Alam *et al.* 2010, Rabbani 2011). This result can be explained as: the conduction velocities of the fibres remain

normal in the whole F-response pathway except at the region of local compression at the wrist; this compression slows down all the fibre conduction velocity, thus the DFL is shifted without much change in its pattern shown in Figure 7.9.
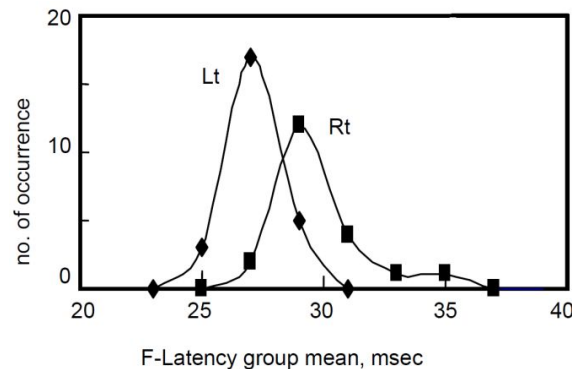

Figure 7.9 *DFL for median nerve for as subject with CTS on right hand (Rt), but normal left hand (Lt). Rt DFL peak shifted towards higher latencies compare to the normal Lt DFL (Alam et al. 2010).*

Thus DFL proved its sensitivity with brachial plexus and peripheral nerve disorders. As mentioned before, MRI has become a gold standard for imaging the anatomy of spinal cord and surrounding peripheral nerves and diagnosis of associated neuropathies such as cervical and lumbosacral spondylosis (NAGATA *et al.* 1990, Denno *et al.* 1991, Okada *et al.* 1993, Trojaborg *et al.* 2006, Waldrop 2006, Abbed 2007, Cook *et al.* 2008, Eubanks 2010). The aim of this chapter is to determine whether DFL correlates with MRI.

Hypothesis of combined DFL and MRI study:

From anatomical and physiological observations (discussed in Chapter 2) the F-responses are elicited from motor nerve fibres, which are not present in DRG. Thus practically DFL is related with the anatomy of rami and trunks. On the other hand, the quantitative MRI values ADC, MTR and T2 were calculated from selected ROIs of DRG and closest nerve roots, thus quantitative MRI values are related with the sensory nerve fibres. Thus it was assumed that the DFL and quantitative MRI parameters are not directly related.

Aims of this chapter: measurements of parameters from median nerve DFL; measurements of sizes of nerves from anatomical MRI and quantitative MRI; study the correlation between DFL shifting and MRI measurements at different postures of the subjects.

7.2 Methods

The DFL and MRI study is divided into three sections, measurement of DFL, measurement of MRI parameters and comparison of DFL and MRI at different positions of the head. These studies were carried out with the **cohort E** subjects (page 126).

7.2.1   DFL measurements

F-responses were elicited by stimulating the median nerve at the wrist using surface electrodes attached to a constant current, high voltage stimulator using the Digitimer stimulator, Model DS7A, Digitimer Ltd., Hertfordshire, England. The responses obtained were amplified using the amplifier and subsequently acquired using the dedicated software using the BrainAmp MR compatible EEG amplifier and Brain Vision Recorder software, Brain products, Munich, Germany.

F-responses recorded at room temperature ($\sim 20^0$ C) using stimulator setup: current 20~40 mA, voltage 220 V, duration 500 µS and recording setup: sampling rate 5 kHz, resolution 0.5 µV low cut-off=10 Hz, high cut-off = 1 kHz.

The active electrode was placed over the middle of the abductor-pollicis brevis (APB) muscle on the palm, the reference electrode was placed distally at the thumb, and the ground electrode at the back of the palm. The stimulator cathode was placed proximal to avoid anodal block. Before placing the electrodes the subject skin was cleaned and prepared. Conducting gel was used under the electrode to improve the conductivity and reduce the impedance. The resulting (M- and F-) responses were recorded with the relaxed muscle. The electrodes were fixed using tapes for stability shown in Figure 7.10.
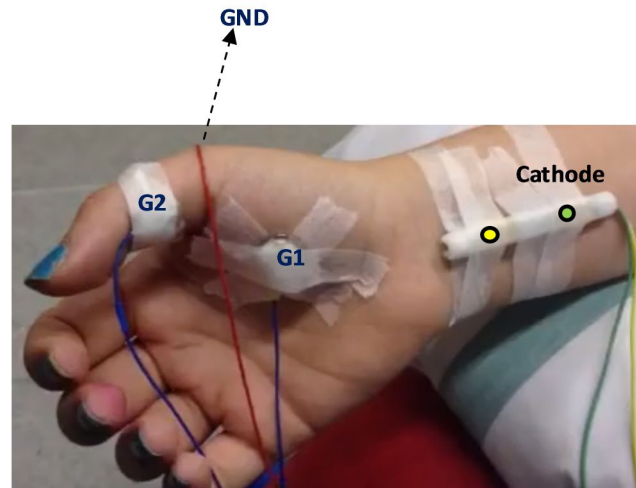
Figure 7.10 *F-response recording arrangement. G1 is the recording electrode over the APB muscle of the palm, G2 is the reference at the thumb and GND is the ground at the back. Stimulator placed over the median nerve with the cathode in proximal position.*

The strength of the stimulating current started from a low value of 5 mA and changing by 2 mA increments to elicit compound muscle action potentials (CMAP) of more underlying nerve fibres. When the current is increased to the point that the CMAP no longer increases in size that proves all nerve fibres have been excited and supramaximal stimulation has been achieved. The current was then increased by another 20% to ensure the supramaximal stimulation. However, before increasing the current steps, the subject's tolerance was observed carefully. A spare MRI scanner bed trolley was used to record the F-responses so that the subject lay in the same position for the DFL and MRI observations.

It is rather time consuming and difficult to find the F-latencies manually, because F-responses vary inherently, are low amplitude and generally arise from an unstable baseline on the prolonged slow negative decay line of M-response. F-latency determination software is available in most commercial NCS/EMG equipment which is based on first deflection from the trace baseline. These methods are suitable when the baseline is flat, free of mixing with noise and other sources of artefacts. However, required F-responses could be obscured by the external noise e.g. high frequency and line frequency (Krishnamachari *et al.* 2007), unstable baseline as terminal portion of M-responses (Han *et al.* 2007), effects of volume conduction from non-stimulated muscle action potentials (Tracey *et al.* 2006, Tracey *et al.* 2010), and unusual waveform from pathological nerves (Kong *et al.* 2006). For that reason an automated

program according to 'local' standard recording setup could be useful. Considering our stimulator-recorder setup and other computer based analysis of F-responses, an objective technique of F-latency determination was used and the corresponding DFL calculation was developed by writing MATLAB code.

To improve the F-latency detection the recorded CMAPs were segmented from 20ms to 60ms as standard F-latency range observed from median nerve with surface electrodes placed over the APB muscle for adult subjects (Buschbacher 1999, Oberthuer *et al.* 2001, Guiloff 2006). F-latencies are measured from the stimulus artefact to the beginning of the F-response determined with minimum amplitude of 20 µV. The baseline disturbances are estimated using a least square fit with the segmented signal, and then the fitted curve subtracted from the signal to ascertain the F-responses clearly. Figure 7.11 shows an example of segmented CMAP before and after the baseline corrections.
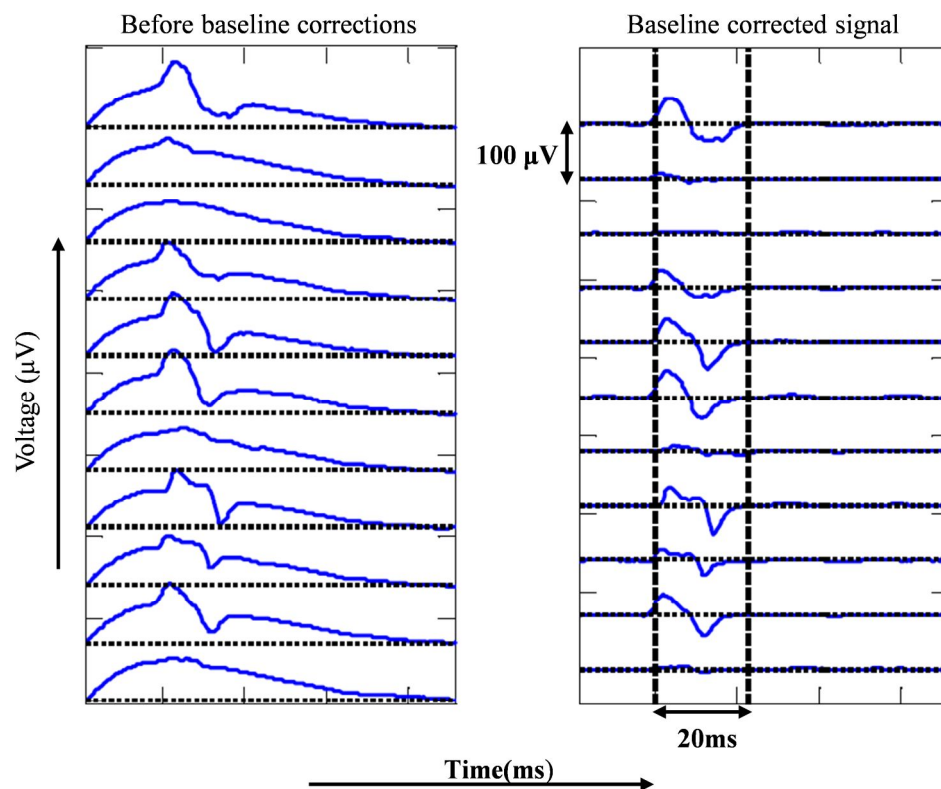

Figure 7.11 *Segmented CMAP before and after the baseline corrections.*

In order to calculate the DFL, about 30 F-responses were recorded at 5 second interval stimulations. However, the number of stimuli depends on the subject's tolerance of the stimulation. F-responses were saved and numbered according to the time sequence, and stimulations that did not produce any F-responses were rejected.

To obtain the DFL, latency groups (bins) were chosen at 2 ms intervals from 20 ms to 40 ms then a plot of the number of F-responses in each latency groups results the DFL of the respective nerve.

Long term repeatability of the DFL was observed from four subjects of *cohort E*. The F-responses were recorded three different days for each subject. From the corresponding DFLs (i) the correlation coefficients between different day's DFL were calculated; (ii) the DFL fitted to a Gaussian function and the peak and the width were compared between three experiments.

Short term reproducibility of the DFL was also observed from the same four subjects of *cohort E*. The total F-latency for each nerve were separated into odd and even data acquisitions in terms of time sequence of collection, and new DFLs were plotted for those two subsets of data. To check reproducibility another way, the first half and second half of the total F-latencies was separated as two different set data points to make new DFLs. The resulting DFLs were fitted to a Gaussian function then corresponding peak and width were calculated and compared between different sets.

For different head positions DFL and MRI study, first normal position F-responses were recorded from the median nerve, and then the subject was asked to bend their head in the coronal plane. When bent towards that side of the body (compressed position) F-responses were recorded, then the subject bent their head to the other side of the body (extension position) and F-responses were recorded again. The same procedure followed for the other side of the subject. The DFL obtained were fitted to a Gaussian equation and the position of the fitted peak was selected as the DFL parameter to compare with MRI observations.

7.2.2   MRI measurements

Anatomical and quantitative MR images of the brachial plexus were acquired from the *cohort E* subjects. The anatomical MRI measurement images were acquired using the STIR TSE sequence, as discussed in section 3.1, and the quantitative MRI measurements of ADC, T2 and MTR values images were acquired as discussed in sections 4, 5 and 6 respectively. For each subject, three scans were run to acquire the images, first at normal posture then head tilted towards right and then left shoulder with similar positioning as for DFL study. Padding was used to fix the head position in the scanner. Figure 7.12 shows the images of brachial plexus at two positions of the head.
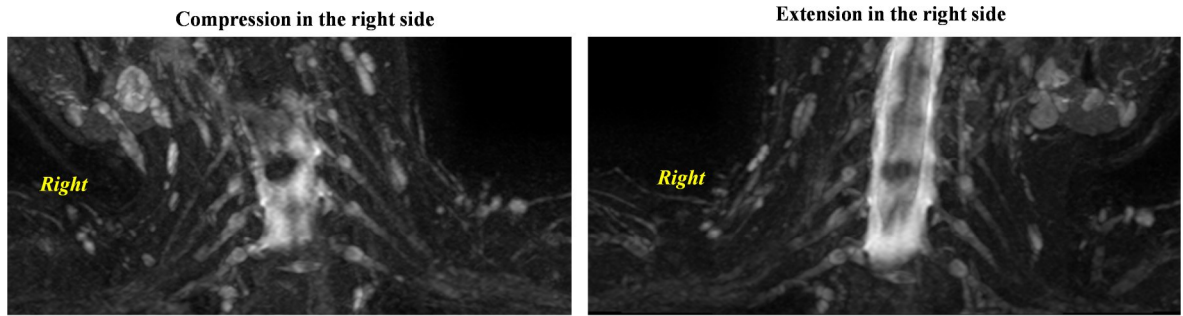
Figure 7.12 *Brachial plexus images at compression and extension positions with respect to the right side of the body.*

The anatomical measurements were carried out from the coronal view maximum intensity projection (MIP) of brachial plexus, created using the procedure discussed in section 4.1. Since the DFL calculations were carried out from the APB muscle through median nerve stimulations, corresponding anatomical regions were identified in the brachial plexus images for analysis. Thus from the coronal MIP view of the brachial plexus (i) the dorsal root ganglion (DRG) and (ii) the rami both at C7 and C8 levels, and (iii) the middle trunk (MT) and lower trunk (LT) were identified. Figure 7.13 shows the anatomical view of the trunks, DRG and rami on MRI.
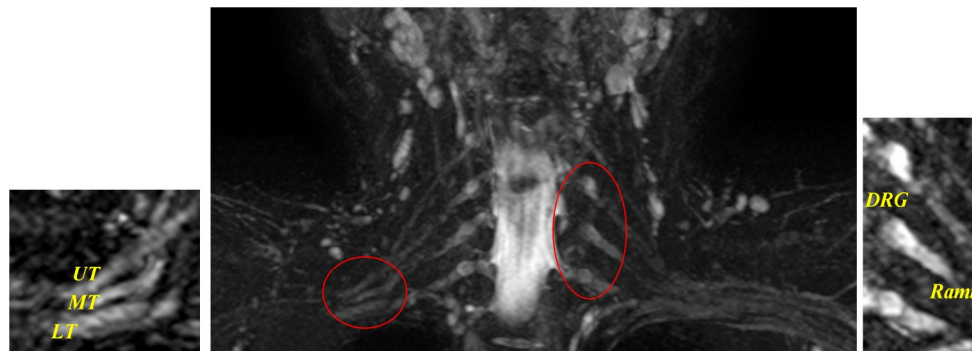

Figure 7.13 *Coronal MIP view of brachial plexus from STIR TSE sequence MRI. The trunks are marked as a smaller red circle and zoomed view of upper trunk (UT), middle trunk (MT) and lower trunk (LT) shown in the left inset; the DRG and Rami are marked as bigger red circle and zoomed view shown in the right inset.*

To measure the sizes of the DRG, Rami, MT and LT from the coronal MIP view intensity line profiles were drawn across the regions, and then fitted to a Gaussian function. The widths of each Gaussian peak correspond to the sizes of the anatomical regions. This was repeated at different positions across the nerve for measuring the trunk and rami diameters, and at different angles (Figure 7.14) to estimate the DRG diameters. The quantitative MRI values were calculated according to the procedures discussed in Sections 4.2, 5.2 and 6.2.
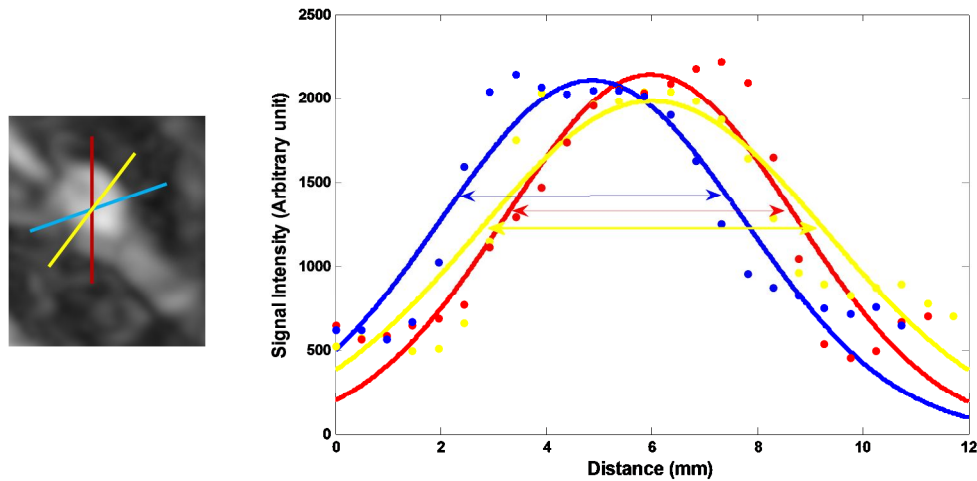
Figure 7.14 *View of DRG at C8 level and obtaining the intensity profiles at different angles, intensity profiles and Gaussian function fittings.*

7.2.3 Comparing DFL and MRI measurements

To observe the effects the different head positions, all the MRI measurements were also measured at normal position of the head and tipped to left and right. Page's L trend tests (Cuzick 1985) were used to assess the effects of head positioning on the DFL and MRI parameters for individual measurements. MRI sizes of the DRG, Rami and trunks; quantitative MRI values of ADC, T2 and MTR and DFL peak of the fitted Gaussian curves compared for individual subjects and values averaged from those subjects.

7.3 Results

Figure 7.15(a) shows an exmple from one subject DFL plots calculated from basline corrected F-responses at three different day tests; (b) shows the Gaussian equation fitting with DFL. Repeatability measures for four subjects are shown tables 7.1 and 7.2.
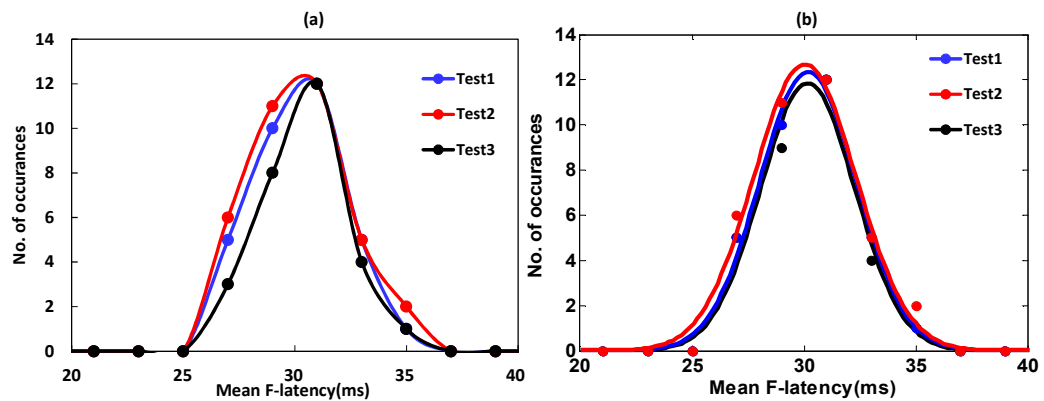

Figure 7.15 (a) *DFL from one subject median nerve tested at three different days;* (b) *DFL from one subject fitted to Gaussian equation at three different day experiments.*

Table 7.1 Correlation between repeated measures on three different days DFLs from 4 subjects

Sub1				Sub2			
	Test1	*Test2*	*Test3*		*Test1*	*Test2*	*Test3*
Test1	1			Test1	1		
Test2	0.94	1		Test2	0.9	1	
Test3	0.95	0.82	1	Test3	0.91	0.95	1
Sub3				Sub4			
	Test1	*Test2*	*Test3*		*Test1*	*Test2*	*Test3*
Test1	1			Test1	1		
Test2	0.85	1		Test2	0.85	1	
Test3	0.7	0.65	1	Test3	0.85	0.9	1

Table 7.2 Peak and width of the DFL are two parameters calculated and compared for 4 subjects at three different day experiments.

Peak and width of DFL measured at 3 tests (ms)								
Subject	*Test1*		*Test2*		*Test3*		*Mean width ± S.D. (ms)*	*Mean Peak ± S.D. (ms)*
	Width (ms)	*Peak (ms)*	*Width (ms)*	*Peak (ms)*	*Width (ms)*	*Peak (ms)*		
Sub1	2	30.48	2.4	28.84	2.6	30.18	2.3±0.3	30±0.3
Sub2	2.2	29.7	1.8	30.15	2.0	30	2.0±0.1	29±0.3
Sub3	1.6	32.3	1.8	30.2	1.5	30.5	1.6±0.2	31±0.2
Sub4	2.0	33.4	2.2	31.5	2.4	32.5	2.1±0.2	32±0.2

The short term reproducibility of DFL from two subjects is shown in Figures 7.16 and 7.17 and tables 7.3 and 7.4. DFL calculations were carried out from total, and interleaved (odd and even ordered) F-latencies, also from total, first half and second half of F-latencies.
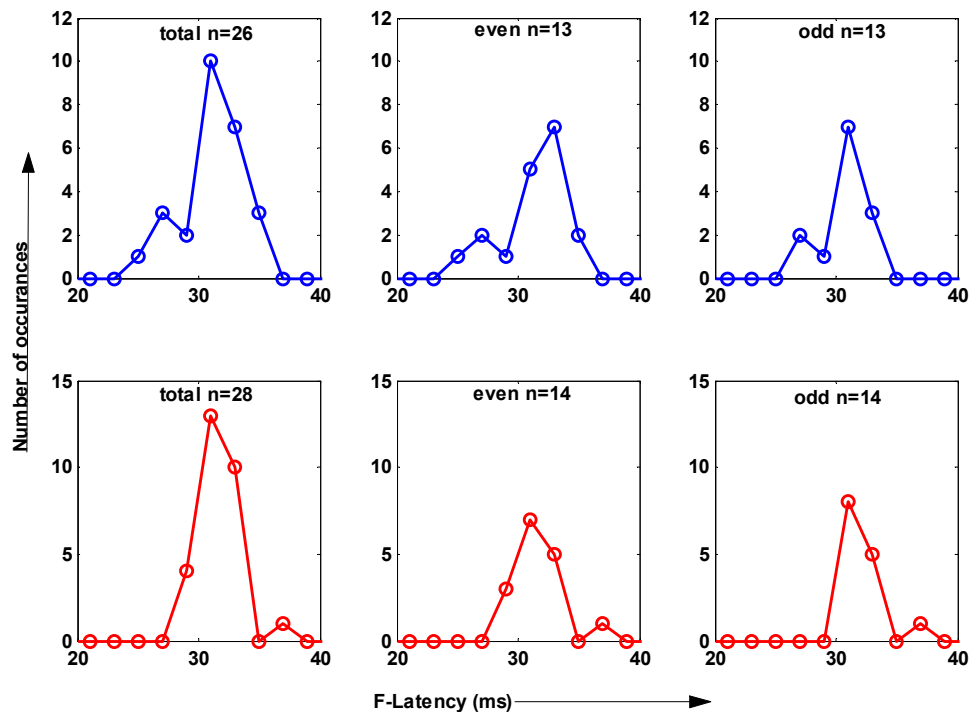

Figure 7.16 *DFL of median nerve for total, even and odd sequenced data from two subjects. The number of events (n) for each data set is also indicated. Both subjects DFL are showing clear similarity between total, even and odd sequenced DFL.*
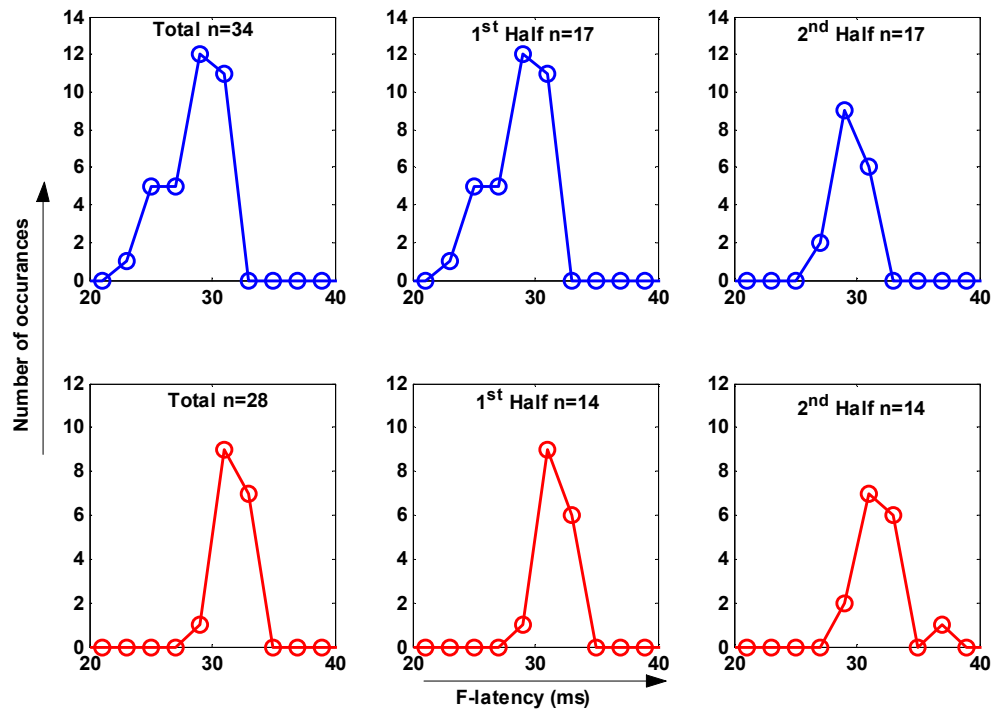
Figure 7.17 *DFL of median nerve for total, first and second half sequenced data from two subjects. The number of events (n) for each data set is also indicated. Both subjects DFL are showing clear similarity between total, first half and second half sequenced DFL.*

Table 7.3: Comparing the peak and width of DFL from odd and even sequenced F-latencies

Subject	Peak (ms)			Width (ms)		
	Total	Odd	Even	Total	Odd	Even
sub1	31.5	32.0	31.0	2.2	2.0	2.4
sub2	32.0	32.0	33.0	2.7	2.5	2.2
sub3	33.0	32.5	31.5	2.1	2.2	2.4
sub4	29.5	30.0	30.5	2.4	2.5	2.8

Table 7.4: Comparing the peak and width of DFL from first and second half of the sequenced F-latencies

Subject	Peak (ms)			Width (ms)		
	Total	First_half	Second_half	Total	First_half	Second_half
sub1	31.0	32.0	31.0	2.8	2.6	2.7
sub2	32.0	31.5	32.0	2.5	2.5	2.8
sub3	31.0	31.0	31.0	3.5	3.0	3.2
sub4	29.0	29.5	28.5	2.5	2.2	2.7

The DFL peak from Gaussian fitting at different head positions, for individual subjects and averaged over subjects are shown in Figure 7.18.
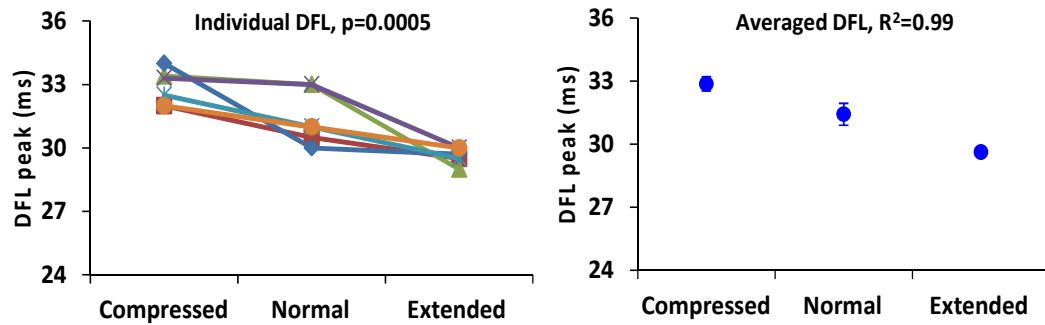
215

Figure 7.18 *DFL peaks at different positions of the head showing decreasing trends from compressed, normal and extended positions for individuals and averaged DFL. Each colour corresponds to one individual. For individual subjects Page's trend test predicted trend is present and for averaged DFL clear negative correlation.*

Figure 7.19 is showing anatomical MRI size measurement dependency with head movement.
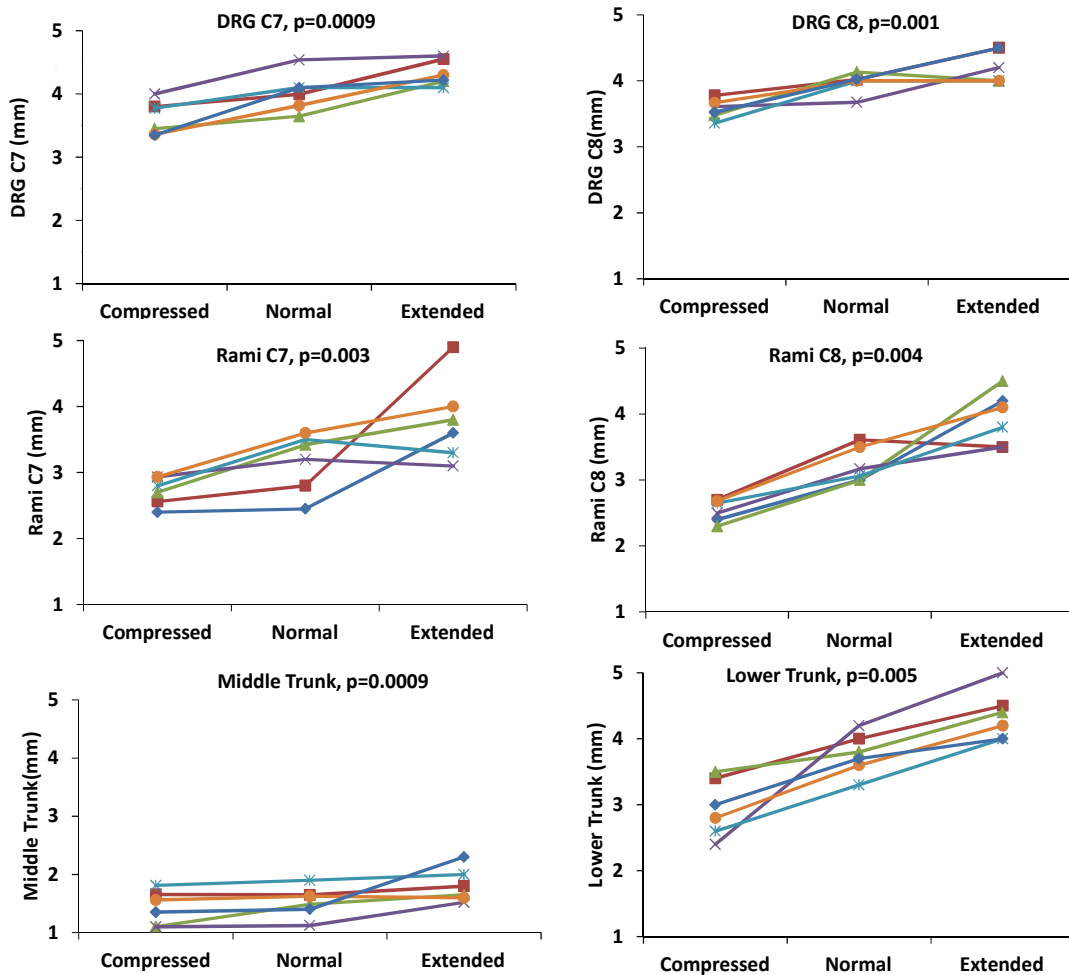

Figure 7.19 *Anatomical MRI measurements at different head positions with Page's statistical values. Variations of DRG C7 almost unchanged and C8 are showing slight positive trend; variations of Rami C7 and C8 are showing positive trend; variations of Middle Trunk almost unchanged and lower trunk showing a positive trend.*

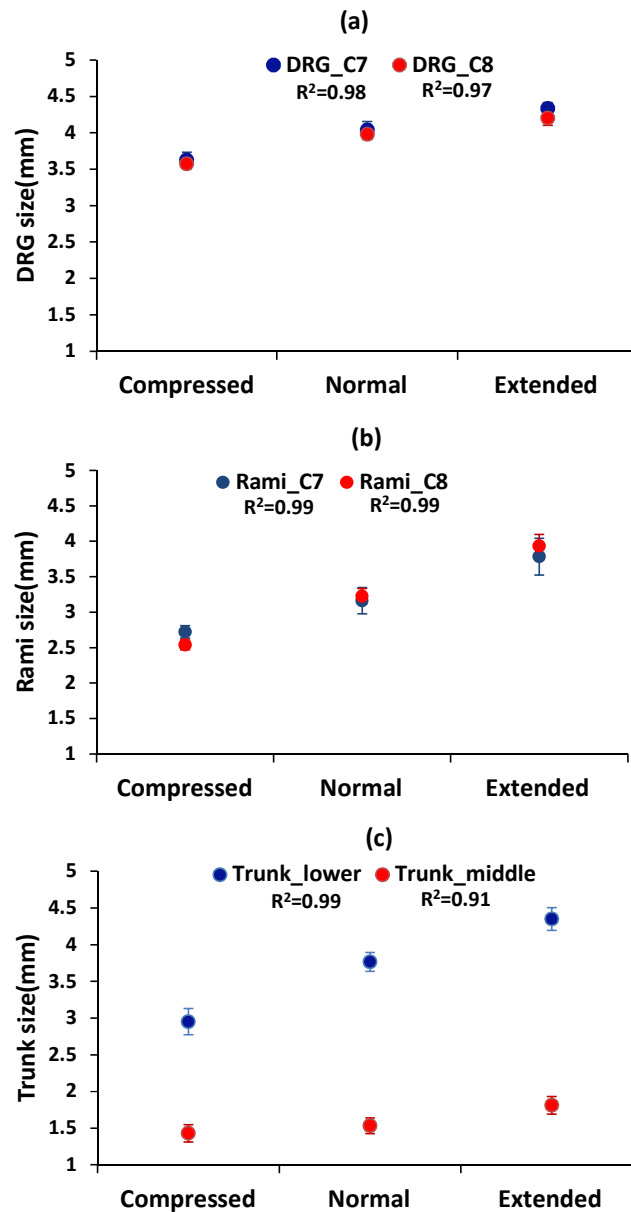Figure 7.20 shows the averaged values of anatomical MRI measurements at different positions of the head.

Figure 7.20 *Averaged values of anatomical MRI measurements at compressed, normal and extended positions and correlation coefficient of the measurements showing,* (a) *Averaged DRG C7 and C8 both showing positive trend;* (b) *Rami C7 and C8 both showing positive trend;* (c) *Middle trunk showing a positive trend, while lower trunk showing stronger positive trend.*

The T2 values from quantitative MRI measurements individual subjects and averaged values shown in Figure 7.21.
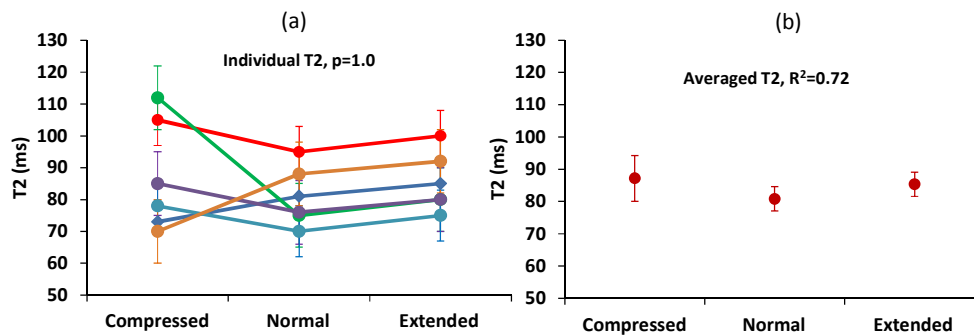
Figure 7.21 *(a) Variations of T2 with different head positions from individual subjects left and right side averaged with error bars and Page's trend test and (b) all subject averaged T2 values with error bars and correlation coefficients of measurements. Individual subjects T2 showing no trend and averaged T2 showing arbitrary changing.*

The MTR values from quantitative MRI measurements individual subjects and averaged values shown in Figure 7.22. The ADC values from quantitative MRI measurements individual subjects and averaged values shown in Figure 7.23.
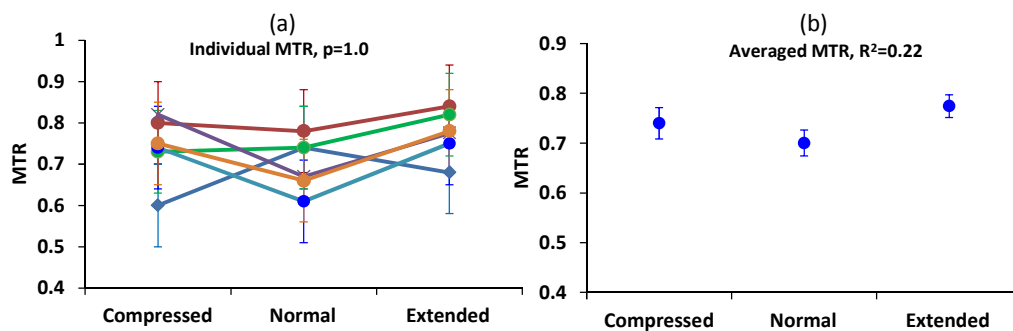

Figure 7.22 *(a) Variations of MTR with different head positions from individual subjects left and right side averaged with error bars and Page's trend test and (b) all subject averaged MTR values with error bars and correlation coefficients. Individual subjects MTR showing no trend and averaged T2 showing arbitrary changing.*
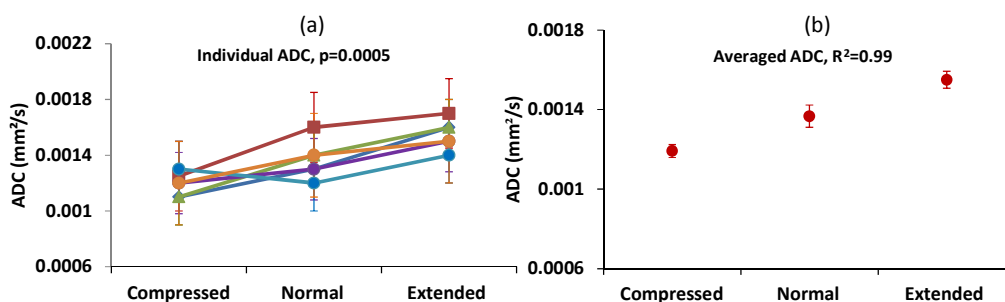

Figure 7.23 *(a) Variations of ADC with different head positions from individual subjects left and right side averaged with error bars and Page's trend test and (b) all subject averaged ADC values with error bars and correlation coefficients of measurements. Individual subjects ADC showing positive trend and averaged ADC showing clear positive trend.*

Figure 7.24 shows the relation between T2, MTR and ADC with anatomical MRI measurements of DRG C7 and C8.
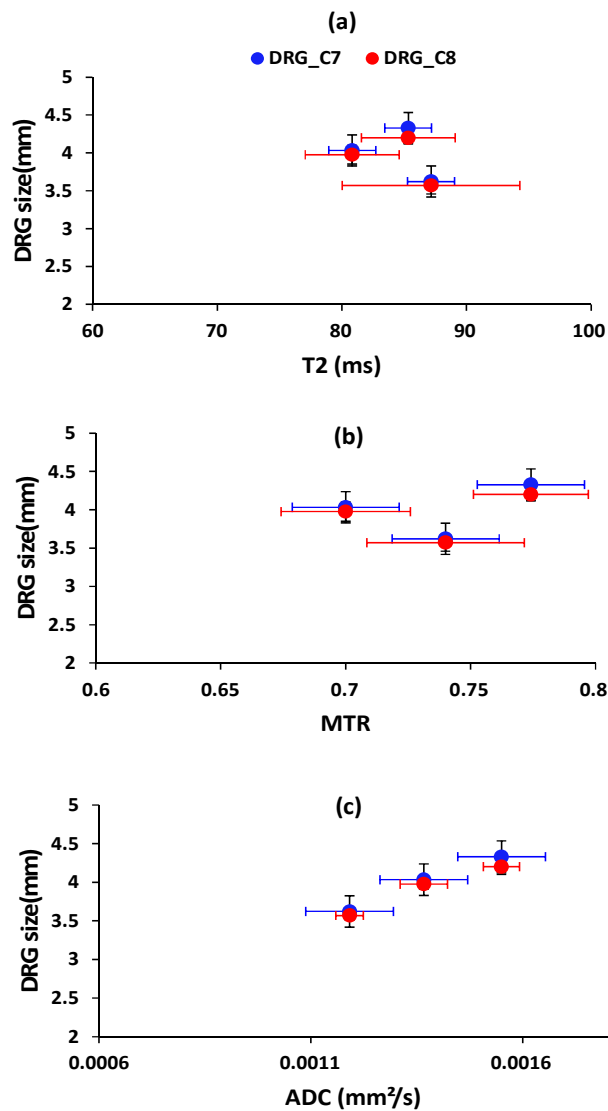
Figure 7.24 *DRG and quantitative MRI relations on brachial plexus measurements* (a) *T2 and DRG size variations showing no specific tendencies;* (b) *MTR and DRG size variations showing no specific tendencies;* (c) *ADC and DRG size variations showing increasing tendencies with sizes of DRG.*

Figure 7.25 shows the relationship between MRI measurements of DRG, rami and trunks diameters and DFL peak parameters averaged over all subjects.
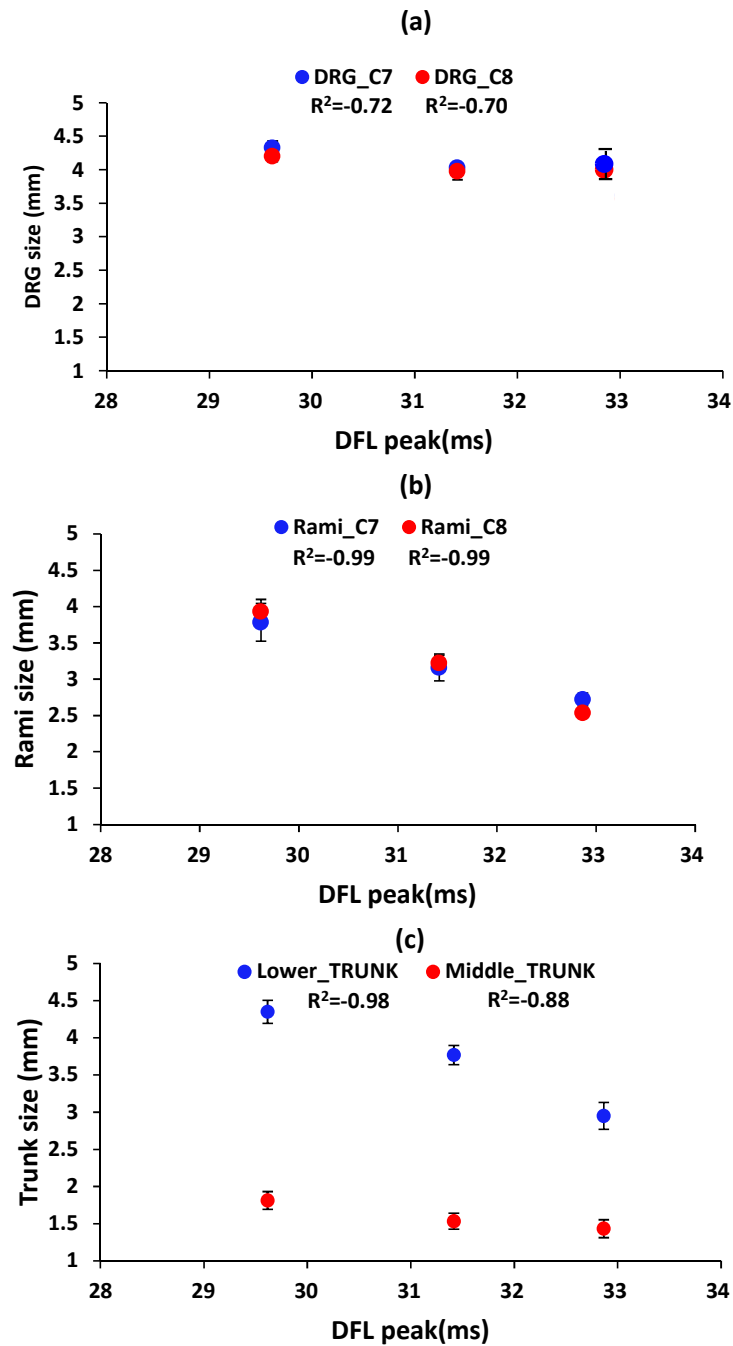
Figure 7.25 *DFL and anatomical MRI measurement relationships, all plots showing decreasing trends with longer latencies.* (a) *DRG C7 and DRG C8 both has negative correlation with DFL peak;* (b) *Rami C7 and Rami C8 both has negative correlation with DFL peak;* (c) *Lower trunk and middle trunk both showing negative correlation with DFL peak..*

7.4 Discussions

This study has shown important correlations between DFL and MRI parameters in normal and healthy median nerve. *Repeatability* of the DFL between different days from same subjects has shown high correlation of the DFL time course between different days and less than 10% variations in repeatability of peak and width of DFL from Gaussian fitting. *Reproducibility* with a single acquisition of the DFL showed in tables 7.3 and 7.4. From interleaved (even and odd numbered) F-responses DFL peaks and widths showed nice reproducibility with less than 2ms differences in peak (thus between the bin size) and less than 0.5ms differences in widths. Also the peak and width from first and second half sequence F-response DFLs showed similar reproducibility of DFL. Thus reproducibility and repeatability measurements indicate that DFL is a physiologically useful parameter. Furthermore, normal median nerve DFLs shows clear shifting with tipping of the head in the coronal plane. DFL peaks were shifted to longer latencies sequentially from extended to normal and then compressed positions of the neck that also showed from Page's L trend test. This dependency indicates the DFL shape sensitivity to nerve compression.

The DFL dependency with head positions was confirmed by anatomical MRI measurements (at compressed, normal and extended positions of the head) that showed the expected trends for sizes of DRG, rami and trunk, the vertebral bones press/release the DRG and rami, and the clavicle at shoulder press/release the trunks. DRG C7 and C8 showed slight increments in sizes with extended positions. As the DRG are placed in the intervertebral foramina (shown in Figures 2.15 and 2.16) a slight changing with head positioning would be expected. Rami C7 and C8 both showed increments in sizes with compressed to extended positions as expected by the squashed or extended states of the rami. The lower trunks showed clear increments in sizes with extended positions due to pressure of clavicle from bottom and release of middle, upper trunks from top. However, the middle trunks showed less change with different positions of the head, probably because of its position between the upper and lower trunks and thus not much affected with changed positions. The trends were also verified by Page's L trend test.

The quantitative MRI parameters show that the T2 and MTR did not change with head position. However, the ADC decreased from extended to compressed positions, due to the compression results less space for intracellular and intercellular fluid thus lower diffusivity compare to normal and extended positions and this was confirmed by the positive correlation between ADC and DRG sizes.

From the combined median nerve DFL and MRI study, the DFL was independent on the DRG C7 and C8 sizes which is expected since the DRG contains sensory nerve fibres and DFL depends on the motor nerve fibres. The position of the DFL peak varied systematically with the sizes of rami at C7 and C8 as expected because the ramus contains mixed motor and sensory fibres. The lower trunk size systematically decreases with longer DFL peaks, which again shows trunk motor nerve fibre dependencies on DFL. However, the DFL peak was almost independent of the sizes of the middle trunks, may be due to its anatomical positioning. These observations were expected according to the hypothesis.

The combined DFL and MRI data was also acquired from a single subject with no severe complains except sometimes pain in the neck and tingling effects in the fingers. The DFL recorded from this subject's median nerve showed double peaks. Also the anatomical MRI acquired (before knowing the DFL results) of the subject's neck showed disc bulging and pressure directly on the spinal cord at C6-C7 level that may cause cervical spondylotic myelopathy (Figure 7.26).
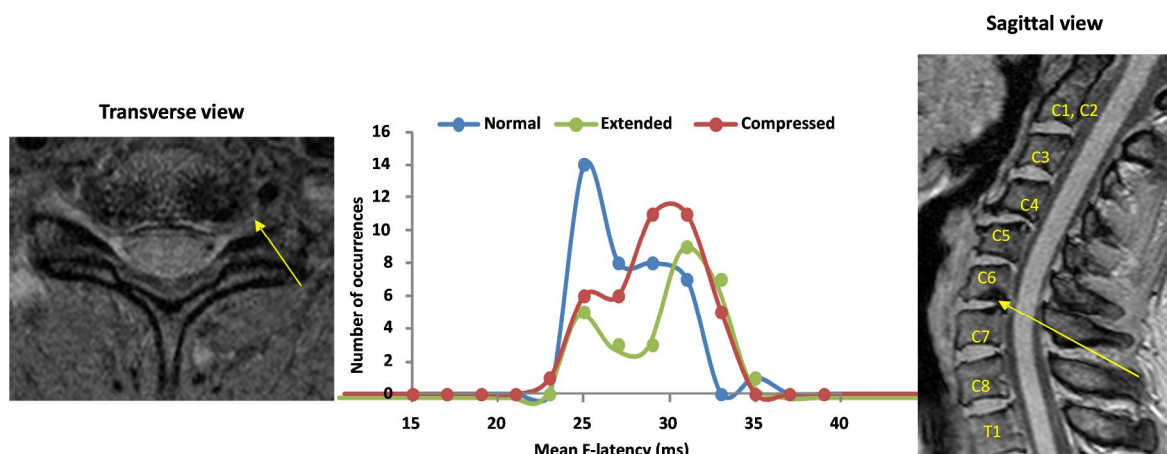

Figure 7.26 *DFL and anatomical MRI from one subject with suspected cervical myelopathy. The transverse view shows narrowing of the nerve root (indicated by yellow arrow); DFL of the subject shows double peaks for normal, extended and compressed positions of the head; sagittal view shows the compression of discs C6 and C7 on spinal cord (indicated by yellow arrow).*

This observation can be explained as: the localised pressure on the spinal cord at C6-C7 level may be causing degeneration of the descending nerve fibres. Now the degeneration of these descending nerves will in turn cause a degeneration of the peripheral motor nerves due to 'disuse atrophy'. This degeneration in the motor nerves will cause a reduction of the conduction velocity and contributing delay shifting in DFL. Since the rest of the median nerve roots (C8-T1) are unaffected the DFL due to these fibres will remain in the original positions. Therefore, on combination, double peaks of DFL are resulting from the median nerve observation. These results strengthened the confidence of correlation between DFL and MRI observations. Thus combined DFL and MRI experiments could provide a novel approach for nerve conduction observation. It can also be applicable for ulnar, radial nerves in the upper extremity and sciatic, tibial, peroneal nerves in the lower portion of the body.

7.5 Conclusion

From this study the DFL parameters showed that it has the potential to become a useful investigation method for peripheral neuropathy even without using other nerve conduction measurements. DFL is cost effective, easy to set up, risk free approach, and suitable globally. DFL can be an 'objective' screening experiment for peripheral neuropathies as it can suggest neurological pathology even before observation through imaging modalities such as MRI, CT etc. However, DFL is based on motor F-responses thus not able to study the sensory nerves. Also DFL is applicable for peripheral nerves from brachial plexus, lumber plexus, etc., but not suitable for other nerves such as cranial, facial nerves etc. On the other hand MRI is a gold standard for neurophysiology; it is versatile, and easily observable. Also MRI is faster, directly interpretable, and also diffusion weighted MRI relates to the fibre distribution both for motor and sensory nerves. Thus the combination of MRI and EMG based on DFL might provide a great combination for clinical applications in peripheral neurophysiology.

References:

Abbed, K. M. M. (2007). "CERVICAL RADICULOPATHY: PATHOPHYSIOLOGY, PRESENTATION, AND CLINICAL EVALUATION." Neurosurgery online 60(1): 28-34.

Alam, M. and K. Rabbani (2010). "Possible detection of cervical spondylotic neuropathy using Distribution of F-latency (DFL), a new neurophysiological parameter." BMC Research Notes 3(1): 112.

Aminoff, M. J. (1978). Electromyography in clinical practice, Addison-Wesley Publishing Company, Medical/Nursing Division.

Aminoff, M. J. (2006). Chapter 30 Lumbosacral radiculopathies. Handbook of Clinical Neurophysiology. K. Jun, Elsevier. Volume 7: 621-630.

Barker, A. T., B. H. Brown and I. L. Freeston (1979). "DETERMINATION OF THE DISTRIBUTION OF CONDUCTION VELOCITIES IN HUMAN NERVE TRUNKS." Ieee Transactions on Biomedical Engineering 26(2): 76-81.

Binnie, C. D. and J. W. Osselton (1995). Clinical neurophysiology: EMG, nerve conduction and evoked potentials, Butterworth-Heinemann.

Brown, B. H., R. Smallwood, D. Barber, P. Lawford and D. Hose (1998). Medical physics and biomedical engineering, CRC Press.

Buschbacher, R. M. (1999). "Median Nerve F-Wave Latencies Recorded From the Abductor Pollicis Brevis1." American Journal of Physical Medicine & Rehabilitation 78(6): S32-S37.

Cook, C., A. Braga-Baiak, R. Pietrobon, A. Shah, A. C. Neto and N. de Barros (2008). "Observer agreement of spine stenosis on magnetic resonance imaging analysis of patients with cervical spine myelopathy." Journal of Manipulative and Physiological Therapeutics 31(4): 271-276.

Cummins, K. L. and L. J. Dorfman (1981). "Nerve fibre conduction velocity distributions: Studies of normal and diabetic human nerves." Annals of Neurology 9(1): 67-74.

Cuzick, J. (1985). "A Wilcoxon-type test for trend." Statistics in medicine 4(4): 543-547.

Date, E. S. and B. J. Kim (2006). Chapter 28 Cervical and thoracic radiculopathies. Handbook of Clinical Neurophysiology. K. Jun, Elsevier. Volume 7: 601-611.

Denno, J. J. and G. R. Meadows (1991). "EARLY DIAGNOSIS OF CERVICAL SPONDYLOTIC MYELOPATHY - A USEFUL CLINICAL SIGN." Spine 16(12): 1353-1355.

Dorfman, L. J. (1984). "The distribution of conduction velocities (DCV) in peripheral nerves: A review." Muscle & Nerve 7(1): 2-11.

Eubanks, J. D. (2010). "Cervical Radiculopathy: Nonoperative Management of Neck Pain and Radicular Symptoms." American Family Physician 81(1): 33-40.

Fisher, M. A. (1982). "F-RESPONSE LATENCY DETERMINATION." Muscle & Nerve 5(9): 730-734.

Guiloff, R. J. (2006). Chapter 9 Late responses (F- and A-waves): methodology and techniques. Handbook of Clinical Neurophysiology. K. Jun, Elsevier. Volume 7: 189-235.

Guiloff, R. J. (2006). "Late responses (F-and A-waves): methodology and techniques." Handbook of clinical neurophysiology: peripheral nerve disease. Amsterdam, the Netherlands: Elsevier: 189-235.

Hakimi, K. and D. Spanier (2013). "Electrodiagnosis of Cervical Radiculopathy." Physical Medicine and Rehabilitation Clinics of North America 24(1): 1-12.

Han, Z. and X. Kong (2007). <u>F-Wave Decomposition for Time of Arrival Profile Estimation</u>. Engineering in Medicine and Biology Society, 2007. EMBS 2007. 29th Annual International Conference of the IEEE, IEEE.

Kimura, J. (2001). <u>Electrodiagnosis in diseases of nerve and muscle: principles and practice</u>, Oxford University Press.

Kimura, J. (2013). <u>Electrodiagnosis in diseases of nerve and muscle: principles and practice</u>, Oxford university press.

Kocer, A., E. Gozke, N. Dortcan and O. Us (2005). "A comparison of F waves in peripheral nerve disorders." <u>Electromyogr Clin Neurophysiol</u> 45(7-8): 417-423.

Kong, X. and S. Gozani (2006). <u>F-Wave</u>, John Wiley & Sons, Inc.

Krishnamachari, S., B. Tracey and D. Iyer (2007). <u>Detection and classification of motor nerve late-wave activity</u>. Engineering in Medicine and Biology Society, 2007. EMBS 2007. 29th Annual International Conference of the IEEE, IEEE.

Mahbub, Z. B., J. Karami and K. S.-e. Rabbani (2013). "Analysis of Evoked EMG using Wavelet Transformation." <u>Bangladesh Journal of Medical Physics</u> 5(1): 41-51.

Mahbub, Z. B. and K. Rabbani (2007). "Frequency domain analysis to identify neurological disorders from evoked EMG responses." <u>Journal of Biological Physics</u> 33(2): 99-108.

Mahmoudi, H., Z. Salehi, K. Azma, Z. Rezasoltani and M. Omidzohour "F wave to height or limb length ratios as rational alternatives for F wave latency in clinical electrodiagnostic medicine." <u>Clinical Neurophysiology</u> In Press, Corrected Proof.

Massey, J. M. (2006). Chapter 21 Electromyographic assessment of peripheral nerve diseases: an overview. <u>Handbook of Clinical Neurophysiology</u>. K. Jun, Elsevier. Volume 7: 467-486.

NAGATA, K., K. KIYONAGA, T. OHASHI, M. SAGARA, S. MIYAZAKI and A. INOUE (1990). "Clinical value of magnetic resonance imaging for cervical myelopathy." <u>Spine</u> 15(11): 1088-1096.

Oberthuer, A., P. Sagave, M. Dueck, C. Wedekind and C. Diefenbach (2001). "F-Wave recording:monitoring residual neuromuscular blockade." <u>European Journal of Anaesthesiology (EJA)</u> 18: 26.

Okada, Y., T. Ikata, H. Yamada, R. Sakamoto and S. Katoh (1993). "Magnetic resonance imaging study on the results of surgery for cervical compression myelopathy." <u>Spine</u> 18(14): 2024-2029.

Pastore-Olmedo, C., O. González and E. Geijo-Barrientos (2009). "A study of F-waves in patients with unilateral lumbosacral radiculopathy." <u>European Journal of Neurology</u> 16(11): 1233-1239.

Preston, D. C. and B. E. Shapiro (2012). <u>Electromyography and Neuromuscular Disorders: Clinical-Electrophysiologic Correlations (Expert Consult-Online)</u>, Elsevier Health Sciences.

Rabbani, K., M. Alam and M. Salam (2007). "Frequency Distribution of F-Latencies (DFL) has physiological significance and gives Distribution of Conduction Velocity (DCV) of motor nerve fibres with implications for diagnosis." <u>J of Biol Phys</u> 33: 291 - 303.

Rabbani, K. S.-e. (2011). "HYPOTHESES TO EXPLAIN THE OCCURRENCE OF MULTIPLE PEAKS OF DFL IN NERVE CONDUCTION MEASUREMENT." <u>Bangladesh Journal of Medical Physics</u> Vol 4(No 1): 27-36.

Rabbani, K. S., M. J. Alam and M. A. Salam (2007). "Frequency distribution of F-latencies (DFL) has physiological significance and gives distribution of conduction velocity (DCV) of motor nerve fibres with implications for diagnosis." Journal of Biological Physics 33(4): 291-303.

Rajabally, Y. A. and S. Varanasi (2013). "Practical electrodiagnostic value of F-wave studies in chronic inflammatory demyelinating polyneuropathy." Clinical Neurophysiology 124(1): 171-175.

Teener, J. W. and J. W. Albers (2006). Chapter 32 Neuropathies associated with medical conditions. Handbook of Clinical Neurophysiology. K. Jun, Elsevier. Volume 7: 647-668.

Tracey, B. H., D. Iyer, E. A. Lesser, F. J. Potts and S. N. Gozani (2010). "Comparison of expert and algorithm agreement in measurement of nerve conduction study parameters." Biomedical Signal Processing and Control 5(2): 158-163.

Tracey, B. H. and S. Krishnamachari (2006). Automated removal of stimulus artifact in nerve conduction studies. Engineering in Medicine and Biology Society, 2006. EMBS'06. 28th Annual International Conference of the IEEE, IEEE.

Trojaborg, W. and J. Payan (2006). Chapter 29 Brachial plexopathies. Handbook of Clinical Neurophysiology. K. Jun, Elsevier. Volume 7: 613-620.

Waldrop, M. A. (2006). "Diagnosis and treatment of cervical radiculopathy using a clinical prediction rule and a multimodal intervention approach: A case series." Journal of Orthopaedic & Sports Physical Therapy 36(3): 152-159.

Conclusion

This thesis has described different methods for studying the Brachial Plexus to provide quantitative and qualitative measures for use in peripheral neurophysiology. The goal of this thesis was to study the characteristics and microstructure of the brachial plexus nerves and spinal cord by developing the MRI and EMG techniques, which could be applied to the diagnosis of neuropathy associated with Cervical and Lumbosacral spondylosis.

In Chapter 3 high resolution qualitative anatomical MR images of the brachial plexus have been obtained using 3T Philips scanner to show the dorsal and ventral root ganglions, nerve roots, trunks and path of the nerves exiting from brachial plexus. These MRI imaging protocols can be used to measure geometric features of the brachial plexus.

Chapter 4 initially developed the DWIBS sequence and showed its potential for brachial plexus imaging by highlighting peripheral nerves against surrounding tissue to avoid partial volume effects in quantitative measures. These background signal suppression capabilities of the DWIBS sequence allowed the novel measurement of quantitative MRI parameters from brachial plexus as well, such as, study of diffusion time dependence of ADC, T2 relaxation time measurements, MTR measurements and z-spectra studies. In this work only one gradient direction was considered but in future data will be acquired with gradients in each direction in turn and then averaged to avoid any directional bias in the results.

In the second part of the Chapter 4, the DWIBS was successfully optimized for an accessible range of diffusion times at maximum diffusion gradients, for brachial plexus imaging, and corroborated with Monte Carlo simulation of restricted diffusion. From the in vivo data a clear reduction was observed in the ADCs as the diffusion time increases confirming the presence of restricted diffusion in the brachial plexus nerves and cord for the first time. These results were fitted to the porous media model of restricted diffusion. This model describes the nature of diffusion by measuring the tortousity and surface to volume ratio (S/V) and has been applied in vivo peripheral nerves for the first time. In future these parameters will be verified by changing the permeability of the cell membrane for post mortem nerves to confirm further the presence of diffusion compartments within the nerves. These observations are completely new in brachial plexus. In future this sequence will be applied to

individual nerves in the wrist and arm and also in the lumbar plexus nerves. To explore the nerve fibres size distribution in more detail, MRI restricted diffusion models for axon fibre distribution such as Ax-caliber and EMG based DFL, that proposes the distribution of nerve conduction velocity, will be compared in future. This imaging protocol can also be applied for studying other microstructures such as size bacterial colony, different types of grains and food items.

In Chapter 5, using DWIBS, the T2 relaxation time was measured for nerve and cord. Preliminary data showed diffusion weighting dependencies of T2 and TE dependencies of ADC, such observations are signatures of compartments within the nerves and cord axons. In future, multiexponential decays will be measured for further characterizing the sizes of compartments in the axons. To further quantify the relaxation processes T1 relaxation time will also be measured from brachial plexus.

In Chapter 6, a new DWIBS-MT sequence was successfully used to measure the MTR values for brachial plexus nerves and cord and has also been used for the z-spectra study of the brachial plexus. MTR values are similar to other studies of nerves. Both the nerves and cord showed asymmetry in z-spectra which probably corresponds to the NOE effects. NOE effects could give new insights into the interactions between the semisolid tissue components and bulk water inside the nerves and cord of brachial plexus and in future could provide a MR contrast for finding disorders in brachial plexus. In future NOE will be quantified by exploring the z-spectra asymmetry with several offset frequencies and RF powers to study the myelination. This will then be combined with other quantitative MRI studies.

In Chapter 7, the relation between the EMG measurements in the form of DFL and MRI parameters have been studied in the brachial plexus for the first time. DFL is cost effective, easy to set up, risk free approach, and suitable globally. From this study the DFL not combined with other nerve conduction measurements showed its potential to become a useful investigation technique of peripheral neuropathy. In future, DFL and MRI combined studies will be used to distinguish sensory and motor fibres in the brachial plexus. The combined study could relate the condition and content of each nerve root.

Further development of DWIBS for imaging the elbow, wrist, and lower regions of the body is possible; these observations will have important clinical applications in related degenerating neuropathies such as carpal tunnel syndrome, Gullean bery syndrome and spondylotic disorders. The combination of MRI and EMG based on DFL might provide a useful combination for clinical applications in peripheral neurophysiology. Furthermore MRI will provide validation of the DFL model, allowing DFL to be used as a cheap readily available method of monitoring peripheral nerves.

Appendix I

Monte Carlo simulation of restricted diffusion

Self-diffusion of water molecules based on Brownian motion within one dimensional restricted microstructures has been modeled by using Monte Carlo method (Haacke *et al.* 1999, Price 2009) and then the optimized DWIBS sequences that are suitable for MRI scanner applied and corresponding diffusion coefficients has been assessed.

Algorithm: The position of a molecule at a time *t* is given by: $x(t) = x(t) + R$ where $x(t)$ is the position at time *t* and **R** is the displacement vector, which mimics the molecule's interaction with its vicinity during the time increment *t*. The components of **R** obey the Einstein's diffusion equation $R = \sqrt{2Dt'}$ where D is the diffusion coefficient and t' is the corresponding diffusion time. The particles reflecting from the restricting boundaries according to the size and shape of the structure, such that $|x(t)| \leq$ Boundary range. Following the above algorithm one-dimensional random walks were set up within restricted boundaries. The step length of each walk was taken to be that for free water molecule and the restriction boundaries were considered in micron scales between 2~50μm.

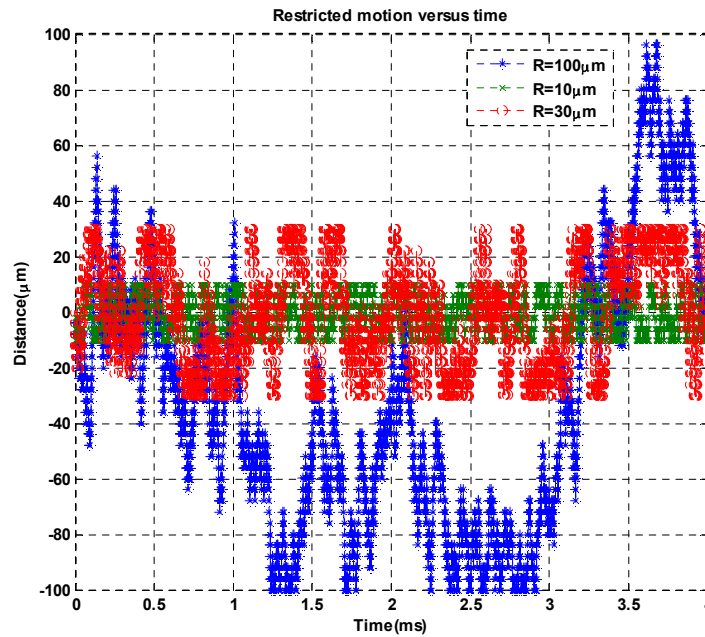Figure A-i shows a schematic diagram of one dimensional restricted molecular motion.

Figure A-i: *Random motion of water molecules in a restricted structure, where each colour corresponds to different restriction sizes 40μm, 20μm and 2μm.*

The effect of diffusion gradients on the random walk was estimated point by point. The frequencies corresponding to the diffusion gradient (G) and particle positions can be expressed as,

$$\Delta\omega = \gamma G x_i$$

Each particle assigned a phase accumulated after every time step t, then the phase for the ith particle,

$$\varphi_i = \varphi_{i-1} + \omega_s \Delta t = \varphi_{i-1} + \gamma G x_i \Delta t$$

Total phase after summed at the end of the diffusion gradient pulse can be expressed as,

$$\varphi = \int \gamma G x dt + \varphi_0.$$

To determine the phase shift distribution among the particles, $N = 5 \times 10^6$ trajectories were generated for each simulation. Then resulting signal due to phase changing was,

$$S = S_0 e^{-j\varphi}$$

S_0 is the signal at b=0.

The net signal must be summed over all particles,

$$S = \sum_{i=1}^{N} S_0 e^{-j\varphi_i}$$

This expression can be compared to the general diffusion signal,

$$S = S_0 e^{-bD}$$

From that we can estimate the apparent values of D using the linear relationship of lnS vs b.

Presence of restricted diffusion:

To study the effects of restrictions for free particle movement different boundaries were set in the range of *microns*; diffusion factors chosen for the subsequent diffusivity measurements lower b-value as $b_1 = 0$ s/mm^2 and higher b-value as one of each b_2=400, 600, 800, 1000, 1400 s/mm^2 with diffusion times between Δ_1=20 ms(short diffusion time) and Δ_2=80 ms(long diffusion time), with diffusion lobe δ=10 ms, and TE=100 ms.

From the simulated particles ADC vs Δ plots showing asymptotic decaying behavior of ADC with long diffusion times that resembles theory such as less restricted molecules result higher diffusion coefficients and more restricted molecules results lower diffusion coefficients. Using the ideal diffusion measurement conditions as, $\delta \ll \Delta$, Δ ranges from very short~0 to long enough 80ms values, the MC simulated particles diffusivity variations at R=20 μm plotted in Figure A-ii.
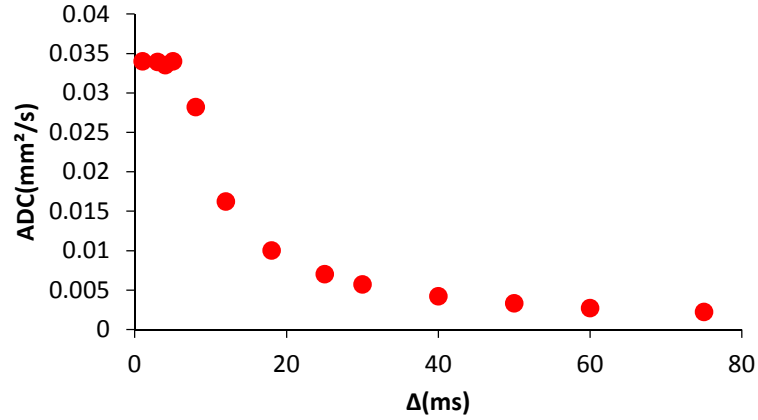
Figure A-ii *ADC variations with Δ showing restricted diffusion behavior*

When there are larger restriction boundaries particles can move freely thus signal decays rapidly and results in higher diffusion coefficients. On the other hand for tighter boundaries particles have less space to move thus signal decays slowly and results lower diffusion coefficients. The short diffusion time ADCs are lower compare to the long diffusion time ADCs as expected.

Figure A-ii shows the simulated logS vs b plots at Δ_1 and Δ_2 and using different restriction sizes.
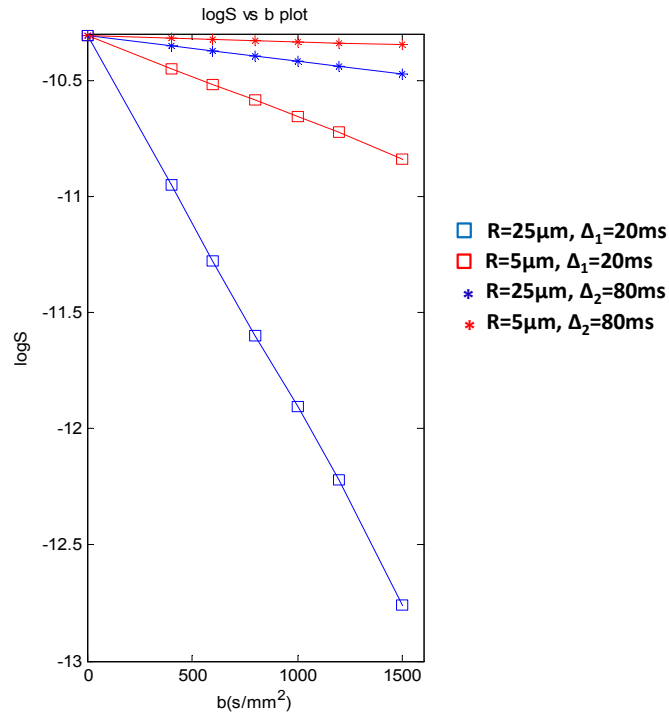

Figure A-ii: *logS vs b plot for different restriction sizes R=5 and 25μm at diffusion times Δ_1=20ms and Δ_2=80ms.*

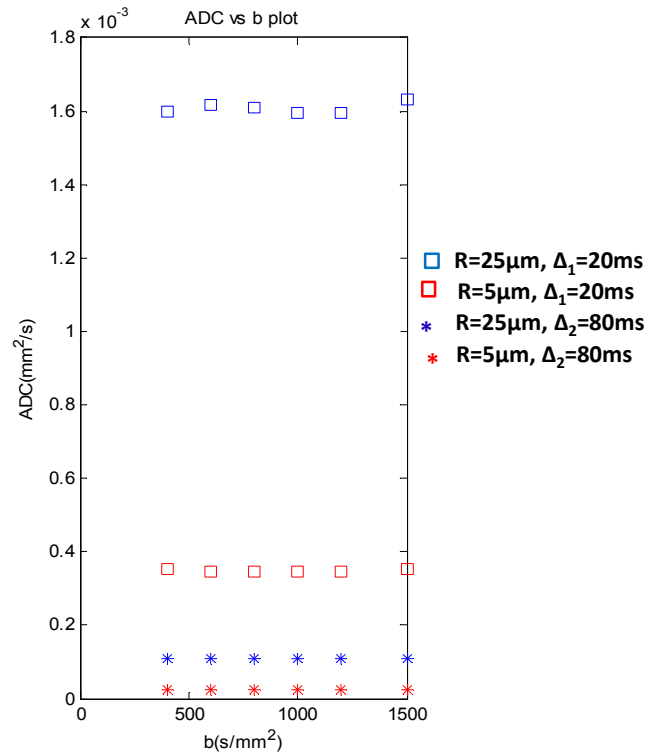Plots of simulated ADC vs b shows the results are independent of b values shown in Figure A-iii.

Figure A-iii: *ADC vs b plot for different restriction sizes R=5 and 25μm at diffusion times Δ₁=20ms and Δ₂=80ms.*

References:

Haacke, E. M., et al. (1999). Magnetic resonance imaging, Wiley-Liss New York:.

Price, W. S. (2009). NMR studies of translational motion: principles and applications, Cambridge University Press.